HOPKINSON BAR TESTING OF CELLULAR MATERIALS

A thesis submitted to The University of Manchester for the degree of

Doctor of Philosophy

in the Faculty of Engineering and Physical Science

2010

Elisavet Palamidi

School of Mechanical, Aerospace and Civil Engineering

List of Contents

List of Contents

Number of Words: 56,717

List of Figures

List of Tables

List of Tables

Abstract

The University of Manchester: Faculty of Engineering and Physical Science

Abstract of thesis submitted by Elisavet Palamidi

For the degree of Doctor of Philosophy (PhD)

and entitled HOPKINSON BAR TESTING OF CELLULAR MATERIALS

Date of Submittion: 26/11/2010

Cellular materials are often used as impact/blast attenuators due to their capacity to absorb kinetic energy when compressed to large strains. For such applications, three key material properties are the crushing stress, plateau stress and densification strain. The difficulties associated with obtaining these mechanical properties from dynamic/impact tests are outlined. The results of an experimental investigation of the quasi-static and dynamic mechanical properties of two types of cellular materials are reported.

The dynamic tests were carried out using Hopkinson pressure bars. Experimentally determined propagation coefficients are employed to represent both dispersion and attenuation effects as stress waves travel along the bars. Propagation coefficients were determined for 20 mm and 40 mm diameter viscoelastic PMMA pressure bars and for elastic Magnesium pressure bars. The use of the elementary wave theory is shown to give satisfactory results for frequencies of up to approximately 15 kHz, 8 kHz and 30 kHz for the 20 mm and 40 mm diameter PMMA bars and the 23 mm diameter Magnesium bars respectively. The use of low impedance, viscoelastic pressure bars is shown to be preferable for testing low density, low strength materials.

The quasi-static and dynamic compressive properties of balsa wood, Rohacell-51WF and Rohacell-110WF foams are investigated along all three principal directions. The dynamic properties were investigated by performing Split Hopkinson Pressure Bar (SHPB) and Direct Impact (DI) tests. In general, the crushing stress, the plateau stress and the densification strain remain constant with increasing strain rate of the SHPB tests. However, a dynamic enhancement of the crushing stress and plateau stress was revealed for balsa wood and Rohacell-51WF. In contrast, the plateau stresses of the Rohacell-110WF specimens are lower for SHPB than quasi-static tests.

From the DI tests, it is shown that compaction waves have negligible effect on the stresses during dynamic compaction of along and across the grain balsa wood at impact speeds between approximately 20 – 100 m/s. Alternatively, the proximal end stresses of both Rohacell-51WF and 110WF foams increase with increasing impact velocity, following the quadratic trend predicted by “shock theory”. This indicates that compaction waves are important for the case of Rohacell foam, even at low impact velocities.

Declaration

I declare that no portion of the work referred to in the thesis has been submitted in support of an application for another degree or qualification of this or any other university or other institute of learning.

Copyright Statement

Acknowledgements

First, I would like to express my sincere thanks and gratitude to my supervisors, Dr J. J. Harrigan and Dr Z. Zou for their expert advice and skilful guidance throughout the course of this work.

Further, I would like to express my thanks to Mr Bill Storey for his advice during the set-up of the various experiments, for his expert technical advice, for the skilful manufacture of the various test sections and for the excellent technical assistance he provided in all cases.

Thanks to all my friends that supported me during these years and especially to Diamantis Kounadis who helped me in preparing this thesis.

Finally, I would like to dedicate this thesis to my parents Maria and Christos and to my brother Ioannis for their moral and economical support in all these years of my stay in UK.

Nomenclature

Roman Symbols

A	Area of the pressure bars
A^+	Pseudoinverse of a matrix A
A^H	Hermitian matrix
A_o	Initial area of the specimen
$A(\omega)$	Coefficient matrix
C	Constant
E	Young's Modulus of the pressure bars
$E^*(\omega)$	Complex Young's Modulus
$F(t)$	Force at bar/specimen interface
$\tilde{F}(\omega)$	Fourier Transform of the force
G	Gain
G_S	Shear Modulus of the cell wall material
$G^*(\omega)$	Complex Shear Modulus
I	Second moment of area
$K^*(\omega)$	Complex Bulk Modulus
$M^*(\omega)$	Complex Moduli
N	Number of sampling points
P_B	Buckling load
$\tilde{N}(\omega)$	Fourier Transform of the backward travelling wave ($N(t)$)
$\tilde{P}(\omega)$	Fourier Transform of the forward travelling wave ($P(t)$)
S_G	Gauge factor
V	Change in velocity across the compaction wavefront
V_{in}	Input bridge voltage
V_{out}	Output bridge voltage
V_{IMP}	Impact velocity

Nomenclature

V_{cr} Critical impact velocity

$V(t)$ Velocity at bar/specimen interface

$\tilde{V}(\omega)$ Fourier Transforms of the particle velocity

$\tilde{X}(\omega)$ Matrix containing the unknown forward and backward waves

c Longitudinal wave velocity of the pressure bars

c_o Elastic wave speed of the foam

$c(\omega)$ Phase velocity

d Diameter of the pressure bars

f_h Highest frequency component present in a signal

$k(\omega)$ Wavenumber

l Length of the pressure bars

l_o Initial length of the specimen

p_{atm} Atmospheric pressure

p_o Initial pressure of the fluid within the cells of the foam

t Time

$\tan\delta_M(\omega)$, $\tan\delta_v(\omega)$ Loss factors

$u(x,t)$ Axial displacement at a position x

$v(x,t)$ Particle velocity at a position x

Greek Symbols

Δf Frequency spacing

Δt Time interval between two successive points

$\Delta\sigma$ Elevation in stress

$\Delta\omega$ Angular frequency increment

$\alpha(\omega)$ Attenuation coefficient

γ Ratio of specific heat capacities

$\gamma(\omega)$ Propagation coefficient

γ_y Yield strain of balsa wood in longitudinal shear

ε_{cr} Crushing strain

ε_d Densification or locking strain

Nomenclature

$\varepsilon_I(t)$ Incident strain

$\varepsilon_R(t)$ Reflected strain

$\varepsilon_T(t)$ Transmitted strain

$\varepsilon_s(t)$ Average strain in the specimen

$\tilde{\varepsilon}(x,\omega)$ Fourier transform of the longitudinal strain ($\varepsilon(x,t)$) at position x

$\dot{\varepsilon}_s(t)$ Average strain-rate in the specimen

$\tilde{\dot{\varepsilon}}(\omega)$ Fourier Transform of the strain rate

$\ddot{\varepsilon}$ Second derivative of strain (strain acceleration)

η Energy absorbing efficiency

θ_o Initial fibre misalignment angle

λ_{opt} Optimum slenderness ratio

$\lambda(\omega)$ Wavelength

μ Coefficient of friction

$\nu^*(\omega)$ Complex Poisson's ratio

ν_o Poisson's ratio of the foam

ρ Density of the pressure bars

ρ_o Density of the specimen

ρ_r Relative density

ρ_s Density of the cell wall material

σ Real positive constant

σ^* Stress at the front of the compaction wave

σ_{cr} Crushing stress

σ_{pl} Plateau stress

σ_{ys} Yield stress of the cell wall material

$\sigma(x,t)$ Normal stress at a position x

$\sigma_s(t)$ Average stress in the specimen

$\tilde{\sigma}(\omega)$ Fourier Transform of the stress

φ Fraction of the solid material in the cell edges

ω Angular frequency

CHAPTER 1

Introduction

1.1 Aims

Cellular materials are often used as energy absorbers in impact applications due to their low cost, good strength to weight ratio and their ability to dissipate energy under an optimum safe load/displacement level. It is therefore important to know their response under high strain rates. The main objectives of this study include the investigation of the difficulties involved when testing soft materials using the conventional Split Hopkinson Pressure Bar (SHPB) technique that utilises high impedance elastic pressure bars. In order to achieve this aim, experimental techniques that can be used to obtain high strain rate properties of cellular materials to large strains were explored: The goal being to generate stress-strain curves up to full densification for balsa wood and Rohacell foam. Both SHPB techniques that utilised low impedance elastic pressure bars and viscoelastic pressure bars were investigated. As well as SHPB tests, Direct Impact (DI) tests were carried out in order to characterise the dynamic properties of the cellular materials.

1.2 Background of the Split Hopkinson Pressure Bar technique

Cellular materials, including wood, polymeric foams and honeycomb structures, possess unique characteristics such as the ability to undergo large deformation under constant load as well as high strength to weight ratios. Due to low cost manufacturing processes, they are used in various impact and blast damage protection applications. For example they are used in the automobile industry, for occupant protection under impact or in new car bumper designs, in the sports industry for the design of new helmets and various protective equipment. Clearly, it is important to know the properties of these materials under high rates of strain.

Several techniques have been developed for studying the response of materials under low, medium and high strain rates.

The Split Hopkinson Pressure Bar (SHPB) is one of the most popular and reliable devices used to study the dynamic behaviour of materials up to strain rates of approximately 10^4 s^{-1}. It finds its origin in 1914 when B. Hopkinson used a single elastic pressure bar for measurements of dynamic pressure by means of momentum traps at the end of the bar. The pressures were generated by the detonation of explosives or by the impact of bullets. Major advances on the Hopkison's design were made by Davies [1] who discussed the limitations involved in the Hopkinson's pressure bar and introduced the use of electrical measurement techniques which enabled direct measurements of the pressure-time pulse travelling through the bar. In 1949 Kolsky [2] introduced the use of two pressure bars. The SHPB consists of two pressure bars of uniform cross-sectional area made of the same elastic material, which are referred to as the incident (or input) and transmitter (or output) bars. A short specimen is placed between the two bars. A projectile or striker made of the same material and the same diameter as the pressure bars is fired at the incident bar and imposes an elastic compressive pulse on it, i.e. the *incident wave*. The incident compressive wave propagates until it reaches the specimen. At the interface, part of the incident wave is reflected back through the bar, i.e. the *reflected wave*, while a portion of it is transmitted through the specimen to the transmitter bar, i.e. the *transmitted wave*. Measurements of these three pulses are taken by two pairs of strain gauges, which are attached usually in the middle of each bar. According to one-dimensional stress wave propagation, the signals picked up from each strain gauge station are time shifted and are known in every point on the bar. In this way the conditions at both faces of the specimen in contact with the bars can be determined.

The applied forces ($F(t)$) and the velocities ($V(t)$) at both ends of the specimen (Figure 1.1) are given by

$$F_1(t) = AE\left(\varepsilon_I(t) + \varepsilon_R(t)\right) ; \qquad (1.1)$$

$$F_2(t) = AE\varepsilon_T(t) \ ; \tag{1.2}$$

$$V_1(t) = c\left(\varepsilon_I(t) - \varepsilon_R(t)\right) \ ; \tag{1.3}$$

$$V_2(t) = c\varepsilon_T(t) \ , \tag{1.4}$$

where A, E, c are the area, Young's Modulus and longitudinal wave velocity of the pressure bars and subscripts *1*and *2* are explained in Figure 1.1. $\varepsilon_I(t)$, $\varepsilon_R(t)$ and $\varepsilon_T(t)$ are the incident, reflected and transmitted strains respectively.

The average stress, strain and strain-rate in the specimen can be obtained as:

$$\sigma_s(t) = \frac{EA}{2A_o}\left(\varepsilon_I(t) + \varepsilon_R(t) + \varepsilon_T(t)\right) \ ; \tag{1.5}$$

$$\varepsilon_s(t) = \frac{c}{l_o}\int_0^t \left(\varepsilon_I(t) - \varepsilon_R(t) - \varepsilon_T(t)\right)dt \ ; \tag{1.6}$$

$$\dot{\varepsilon}_s(t) = \frac{c}{l_o}\left(\varepsilon_I(t) - \varepsilon_R(t) - \varepsilon_T(t)\right) \ , \tag{1.7}$$

where l_o and A_o are the initial length and area of the specimen respectively.

One of the main assumptions for the specimens involved in the SHPB analysis is that the stress and strain state throughout the specimen is uniform [3, 4] (note that the presence of friction and/or the effects of radial and axial inertia can violate this assumption). Details of the assumptions involved in the SHPB technique have been presented in a number of review papers such as [3, 4].

If the stress and strain fields are assumed uniform throughout the specimen then the stress-strain relationship of the specimen can be obtained from:

$$\sigma_s(t) = \frac{EA}{A_o}\varepsilon_T(t) \ ; \tag{1.8}$$

$$\varepsilon_s(t) = \frac{2c}{l_o}\int_0^t \varepsilon_R(t)dt \ . \tag{1.9}$$

Experimental results can be processed using a one, two or three-wave analysis, depending on the number of stress waves used to calculate the stress in the specimen. For the one-wave analysis uniformity of the stress is assumed rather than checked, with the stress and strain calculated from Equations (1.8) and (1.9) respectively. Similarly, for the two-wave analysis, the waves in the incident bar only are used to determine stresses (Equation (1.1)). The three-wave analysis uses the average stress calculated from Equation (1.5).

1.3 Report Outline

In the second chapter the limitations of using steel (or other high mechanical impedance) SHPB set ups to test soft materials are discussed. Then a review is presented of the existing methods that are used to test cellular materials utilising the SHPB technique. Furthermore, the validity of the assumption of stress uniformity within the tested specimen is discussed in detail.

In the next chapter the details of the instrumentation that was used are given. Also, the two different SHPB arrangements and the DI set up are described.

The following chapter involves the “calibration” procedure followed for the 20 mm and 40 mm diameter PMMA pressure bars. This includes a discussion of the wave propagation in viscoelastic media as well as the validation for the accuracy of the “calibration” method that was carried out. Also, the mechanical properties of the PMMA material are investigated and results are presented.

The fifth chapter includes a discussion of existing wave propagation techniques. Numerical and experimental results are presented for the case of the PMMA pressure bars.

In Chapter Six an experimental propagation coefficient is determined for the case of the Magnesium pressure bars. The accuracy of the method is verified and results of the wave separation in the case of the Magnesium pressure bars are presented.

In the seventh chapter the properties of balsa wood are investigated under quasi-static and dynamic conditions. Balsa wood is compressed under high strain rates along its three principal axis utilising both the Magnesium and PMMA SHPB set ups. In addition DI tests are performed for both along and across the grain balsa wood specimens. It is worth mentioning that the data obtained from the SHPB tests for the across the grain balsa are new.

In the eighth chapter new data is presented of the dynamic properties of Rohacell-51WF and Rohacell-110WF foam in all three directions by performing SHPB and DI tests.

Finally, in the last chapter the concluding remarks of this study are presented. Furthermore, suggestions are given for future research in this field.

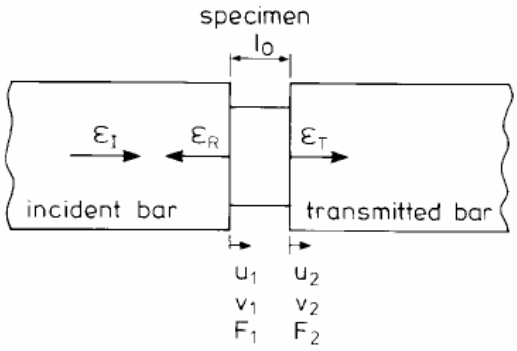

Figure 1.1 Specimen between the incident and transmitter pressure bars [3].

CHAPTER 2

Literature Review

2.1 Introduction

The knowledge of the properties of soft materials under dynamic conditions is essential since they are often utilised as energy absorbers. One of the most widely used devices for the determination of a material's dynamic properties is the SHPB. However, testing of soft materials using a conventional SHPB set up, which usually consists of steel pressure bars, leads to inaccuracies due to the low strength of the specimen. Hence, testing of soft materials such as cellular solids has often been carried out using modified SHPB arrangements.

In this chapter the limitations of the classical, high impedance, elastic SHPB arrangement for testing low density, soft materials are investigated. Then a review of the existing modified SHPB methods is given. Finally, the validity of one of the fundamental assumptions of the SHPB technique is discussed in detail.

2.2 Limitations of the classic SHPB technique when testing soft materials

The SHPB technique is the standard method used to obtain dynamic properties of materials at strain rates of the order of 1000 s^{-1}. However, the conventional SHPB system consists of pressure bars whose mechanical impedance is higher than that of the low impedance and low strength materials considered here. This mismatch in the mechanical impedance can lead to inaccuracies.

Some understanding of this can be gained by considering the magnitude of the transmitted ($\sigma_{T,E}$) and reflected ($\sigma_{R,E}$) elastic stress waves at the interface of two

rods with different mechanical impedances. The magnitude of the elastic incident stress wave at the interface is defined as $\sigma_{I,E}$. According to the wave propagation in linear elastic solids the magnitude of the reflected and transmitted wave depends on the impedance mismatch of the two rods [3]:

$$\sigma_{T,E}(t)=\frac{2\rho_o c_o A_o}{(A_o\rho_o c_o + A\rho c)}\frac{A}{A_o}\sigma_{I,E}(t)\ ; \tag{2.1}$$

$$\sigma_{R,E}(t)=\frac{A_o\rho_o c_o - A\rho c}{A_o\rho_o c_o + A\rho c}\sigma_{I,E}(t)\ . \tag{2.2}$$

If the mechanical impedance of the second rod $(A_o\rho_o c_o)$ is very small compared to that of the first rod $(A\rho c)$, the magnitude of the reflected stress wave will be approximately equal to that of the incident stress wave (Equation (2.2)) leading to a very low amplitude transmitted pulse (Equation (2.1)).

Now consider the case when the specimen has a low strength, defined by a yield stress σ_Y. The maximum stress at the back face of the specimen (i.e. specimen/transmitter bar interface) is limited by the yield stress of the specimen. If this stress is low, the accurate measurement of the transmitted pulse becomes difficult for high impedance bars. The maximum stress at the incident bar/specimen interface is also limited by this yield stress and once yielding occurs, the difference between the magnitudes of the incident and reflected waves is proportional to the yield stress in the specimen. The aim here is to measure this low strength accurately, and at strain rates of the order of 1000 s^{-1} and to large strains of up to 0.9. Large specimen strains require large displacements in the incident pressure bar. The combination of large displacements in the bar and high strain rates in the specimen can only be achieved when the incident wave in the high impedance input bar has a large stress magnitude relative to the yield stress in the specimen. In these circumstances, the incident wave and the reflected wave are almost equal in magnitude (the difference in magnitude is proportional to σ_Y). This is the fundamental difficulty associated with testing low strength materials using elastic bars with relatively high mechanical impedance. The incident and reflected waves

have almost equal magnitude so that the experimental noise and oscillations in the stress waves make it extremely difficult to determine the stress at the incident bar/specimen interface. It therefore becomes impossible to check for stress uniformity in the specimen by using either the two-wave or three-wave analysis.

Furthermore, when soft materials are tested using an elastic SHPB, it is essential that a uniform stress state within the specimen is checked experimentally. It should not simply be assumed that Equations (1.8) and (1.9) can be applied. Stress waves within the specimen can result in differences in stress across the specimen and since soft materials tend to have low wave speeds, the time required to achieve stress equilibrium will be significantly greater than that for metallic specimens. For example, consider the effect of an incident wave in a conventional SHPB with a short rise time (approximately 10μs) if the specimen is a soft material with a low wave speed. If the amplitude of the stress of the loading pulse exceeds the yield stress within the rise time, then plastic yielding will occur at the front face of the specimen, while the stress at the back face may be small, resulting in a non-uniform stress and strain state [5, 6, 7]. The limitations of the assumption of stress uniformity within the specimen will be discussed in more detail in Section 2.4.

2.3 SHPB arrangements for testing soft materials

The difficulties encountered when testing soft materials have been overcome by either modifying the SHPB set up in order to increase the sensitivity of the transmitter bar or by using lower impedance pressure bars so as to increase the signal to noise ratio of the strain signals and overcome the limitations discussed in section 2.2.

2.3.1 Modified SHPB arrangements

For a given stress in the specimen, the strain in the transmitter bar can be increased by reducing either the Young's Modulus or the cross-sectional area of the bar (Equation (1.5) and (1.8)). Based on this observation Chen et al. [7] modified the

classic SHPB set up by using lower impedance Aluminium alloy bars with a hollow output bar to test RTV630 silicone rubber. An end cap of the same material as the bar was placed at the specimen/transmitter interface in order to keep the sample in place. A pulse shaping technique was employed to control the rise time of the incident pulse, in order to ensure homogeneous deformation of the specimen. Furthermore, this pulse shaping eliminated any high frequency components in the loading pulse and so dispersion effects were assumed negligible. It was argued that the pulse shaper ensured that the presence of the end cap did not violate the one dimensional wave propagation in the transmitter bar. In order to examine the effects of the end cap on the transmitter bar signal, two experiments were conducted using identical incident waves. It was argued that as the two transmitter bar signals had similar shapes, the effect of the end cap could be ignored. Gray et al. [8] argued that both a one-wave and two-wave analyses should have been carried out by Chen et al. [7] in order to check correctly the effect of the end cap. In addition, Mahfuz et al. [9] pointed out that it is doubtful whether the end cap would not interfere with the wave propagation in the hollow bar.

The use of a hollow transmitter bar was regarded as adequate for testing rubber materials, such as silicone rubber RTV630 specimens [7], and was also applied in SHPB tension experiments of epoxy and Polymethylmethacrylate (PMMA) specimens [10]. However, for even lower impedance materials such as foams a new technique was introduced by Chen et al. [6], which provided an increase of the measured transmitted signal by three orders of magnitude when compared with the conventional technique of employing strain gauges. Instead of reducing the cross-sectional area of the transmitter bar, a piezoelectric transducer was placed in the middle of the output bar to increase the sensitivity of the measurements. The quartz crystal had the same cross-sectional area and approximately the same mechanical impedance as the bars to ensure one-dimensional wave propagation by minimising reflections at the bar/specimen interface.

Neither of the above methods [7, 6] can overcome the problem that when testing soft materials with higher impedance pressure bars most of the incident wave will be reflected back to the input bar. Therefore, the specimen’s stress equilibrium cannot be checked by simply comparing the one and two wave analysis [5, 11, 12], since the

input force (force at incident bar/specimen interface) will be difficult to measure, i.e. the incident and reflected strains of Equation (1.1) are almost equal in magnitude but of opposite sign so that the result of adding them together produces a very noisy signal. In order to overcome this problem piezoelectric transducers were placed near the specimen's interfaces to monitor both the front and back forces [5, 11, 12]. The transducers could not be placed at the interfaces as the lateral expansion of the specimen during compression would destroy the quartz crystals. Therefore, thin aluminium disks were placed between the transducers and the specimen. The presence of additional interfaces in both pressure bars can interfere with the stress wave propagation and obscure the reflected and transmitted waves that are used to calculate the nominal stress, strain and strain rate of the specimen. Further investigations of this experimental arrangement were carried out by Casem et al. [13], who concluded that the force measurements made by the quartz gauges may need to be corrected for errors associated with inertial effects in the quartz and aluminium discs.

Mahfuz et al. [9] replaced the elastic steel transmitter pressure bar with a low impedance, viscoelastic, polycarbonate bar in order to increase the magnitude of the transmitted signal. An increase of one order of magnitude in the sensitivity of the transmitter bar signal was achieved by using the polycarbonate output bar. However, stress waves disperse and attenuate as they travel along a viscoelastic bar. Although these effects were recognised by the authors, they were assumed negligible and both the phase velocity and Young's Modulus were assumed constant. Errors associated with these simplifying assumptions were not quantified. The same SHPB arrangement was used by Deshpande and Fleck [14] to test aluminium foam (Alulight and Duocel Foam). Again viscoleastic effects were disregarded. Furthermore, since the pressure bars are made out of different materials Equations (1.5)-(1.9) were modified. This was identified by both Mahfuz et al. [9] and by Deshpande and Fleck [14] However, the results from both investigations are questionable, since the assumption of stress equilibrium within the specimen was not checked. A fuller discussion of the effects of frequency on the viscoelastic properties of polymer materials and the stress wave propagation in viscoelastic rods is provided in Chapter 4.

2.3.2 Low impedance SHPB arrangements

The advantage of large impedance mismatch between the bars and specimen is that stress equilibrium can be achieved more rapidly [5, 11, 12]. Elastic bars have the additional advantage of simple processing of strain records. The disadvantages are the low sensitivity in the output bar and the difficulty in determining the input force as previously discussed. In order to achieve an appropriate balance between these advantages and disadvantages, pressure bars made out of metals, which have lower Young's Modulus than steel, such as Titanium alloys or Magnesium alloys, have been employed [15, 16, 17, 18] in preference to viscoelastic pressure bars. In addition, the mechanical properties of these low impedance metallic bars are unaffected by various environmental factors such as temperature, aging and moisture. It should be noted that even if metallic bars are used dispersion effects should be taken into account if the stress waves contain frequencies wherein the ratio of the wavelength to bar diameter is not large. However, there is a class of materials that includes certain foams, some types of wood and polymers for which even low impedance metallic bars will not provide sufficient sensitivity when used in the SHPB [8]. Table 2.1 shows the relative impedance of materials used as Hopkinson bars as a percentage of that of steel. Lower impedance materials give greater sensitivity in the measurements. Just as magnesium alloy is preferable to steel as a Hopkinson bar material for testing certain materials, so PMMA is preferable to magnesium alloy for increasingly soft materials. Using bars with lower impedance allows the stresses at both bar/specimen interfaces to be calculated. The uniformity of stress within the specimen can be checked by comparing the results of the one- and two-wave analyses. The increase in sensitivity that is gained by employing PMMA rather than magnesium alloy bars is also illustrated in Figure 2.1. SHPB tests utilising PMMA and Magnesium alloy pressure bars were performed on two aluminium foam specimens with a thickness of 10 mm. The forces shown in Figure 2.1 (a) follow similar shapes, while in Figure 2.1 (b) the difference between the front face and back face forces makes it difficult to assess whether stress uniformity within the specimen has been achieved. This is further discussed in later chapters.

During the last decade, the use of polymer bars (Polymethylmethacrylate (PMMA), Polycarbonate (PC)) has become very popular [19, 20, 21, 22, 23, 24, 25, 26, 27, 28]. However, stress waves propagating in viscoelastic bars attenuate due to material damping and disperse due to the geometric effects of radial inertia and due to the fact that the material properties depend on frequency [19, 26]. Both effects have to be considered in order to obtain valid SHPB data. It has been shown experimentally [23] that if these effects are assumed negligible, the magnitude of stress in the specimen can be underpredicted by 15%, while the specimen strain can be overpredicted by more than 26%. In addition, the viscoelastic material properties depend on several environmental factors such as temperature, moisture content and ageing [8]. Therefore, the use of polymer pressure bars at various temperatures requires additional effort compared with elastic pressure bars whose mechanical properties can be assumed to be constant for small changes in room temperature. Bacon et al. [29] suggested the experimental determination of a transfer matrix whose properties depend on temperature. However, if soft materials have to be tested at various temperature levels, a transfer matrix has to be determined for every temperature.

Wang et al. [25] developed a viscoelastic SHPB model based on the Zhu-Wang-Tan (ZWT) non-linear constitutive equation (Equation 2.3) and the method of characteristics. The mechanical properties of polymers are strain rate dependent and this was incorporated using the rheological model of Figure 2.2. In a viscoelastic SHPB system, the bars are subjected to impact loading conditions and therefore it was suggested that the wave propagation in a viscoelastic SHPB should be treated according to the high strain rate behaviour of polymers. Based on experimental observations it was argued that the Zhu-Wang-Tan equation (Equation (2.3)) can be used to describe the non-linear behaviour of polymers at high strain rates:

$$\sigma = E_o\varepsilon + \alpha\varepsilon^2 + \beta\varepsilon^3 + E_1\int_0^t \dot{\varepsilon}(\tau)e^{\left(-\frac{t-\tau}{\theta_1}\right)}d\tau + E_2\int_0^t \dot{\varepsilon}(\tau)e^{\left(-\frac{t-\tau}{\theta_2}\right)}d\tau \ , \qquad (2.3)$$

where the first three terms describe the non-linear elastic response and E_o, α, β are elastic constants, the first integral describes the viscoelastic response at low strain

rates with E_1, θ_1 being the elastic constant and relaxation time respectively and the last term corresponds to the viscoelastic response at high strain rates and E_2, θ_2 are the elastic constant and relaxation time respectively.

The low frequency Maxwell element with E_1 and η_1 can be reduced to a single elastic element under high strain rates. Furthermore, because the deformation of the bars is small the second and the third terms of Equation (2.3) were ignored. Hence, for Hopkinson pressure bars Equation (2.3) reduces to:

$$\sigma = E_o\varepsilon + E_1\varepsilon + E_2\int_0^t \dot{\varepsilon}(\tau)e^{\left(-\frac{t-\tau}{\theta_2}\right)}d\tau \ . \qquad (2.4)$$

Considering the above equation (Equation (2.4)) and the equations of motion and continuity for a thin bar a solution for the wave equation in viscoelastic bars was obtained. It should be pointed out that Wang et al. [25] suggested that in the case of high strain rate conditions for the high frequency waves the phase velocity was assumed to be constant, as was the attenuation coefficient. Neither of these assumptions are accurate for practical Hopkinson bar set-ups, as is illustrated in Chapter 4. Gary et al. [30] argued that the predictions of the viscoelastic model used by Wang et al [25] are not generally applicable to Hopkinson bars. It was accepted by the same authors [27] as well as in [21] that the proposed method [25] would give satisfactory results for a narrow frequency range. It is worth pointing out that the method presented by Wang et al. [25] has never been used in an actual SHPB test in the open literature.

Zhao et al. [26] considered both attenuation and dispersion effects by generalising the Pochhammer-Chree frequency equation for elastic bars in the case of viscoelastic bars, where the elastic constants were replaced by complex properties. The Fourier stationary wave analysis was employed for the viscoelastic model because the numerical efficiency and the precision were independent of the distance between the strain gauge and the specimen/bar interface [27]. Also, the three dimensional effects (the bar diameter effects), which become important as the ratio of the wavelength to diameter of the bar reduces, could be considered without additional computational

efforts. The solution of the frequency equation gives the phase velocity and attenuation coefficient, which both depend on the frequency and the diameter of the bar [26, 27]. However, in order to obtain the solution, the material properties must be known a priori. As a result a rheological model was employed and the unknown viscoelastic parameters were determined by comparing a predicted wave and a measured wave at another point on the bar. It should be mentioned that the details of the solution scheme that is required to determine the nine constants in the rheological model used were not published.

The technique has been used to test honeycombs [31] and metallic tubes as well as polymeric foams and satisfactory results were obtained [32]. However, it is mathematically rather complex and additional computational time is required to solve the Pochhammer-Chree equation, since an iteration procedure is required. Also, it was assumed that the Poisson's ratio was constant which is not exactly true for viscoelastic materials as will be shown in Chapter 4.

Sawas et al. [23] used two strain measurements at two different locations on a polymeric pressure bar and determined experimentally an auxiliary function in the time domain in order to establish the relaxation and creep functions. Those functions where then used to determine the stress-strain and stress-particle velocity relationships at the specimen/bar interfaces. However, the constitutive relationship of the linear viscoelastic material is required to be known before the technique is applied. Furthermore, the starting time of each signal had to be identified accurately to avoid errors, which is difficult since real signals are often corrupted with noise. Polycarbonate, polyurethane foam and Styrofoam samples were tested using the viscoelastic analysis that was proposed at different strain rates. It should be pointed out that the specimens were assumed to be in equilibrium without comparing the results from the one and two wave analyses. In addition high-strength titanium alloy anvils were placed at the specimen/bar interfaces to avoid any damage of the bars and to diminish localised elastic deformation at the interfaces.

Bacon [33], following the work by Lundeberg and Blanc [22], presented an experimental method for the dispersion correction in viscoelastic bars due to both the bar geometry and the viscoelastic properties. Based on the one-dimensional wave

propagation it was shown that measurements of the longitudinal strain could lead to the determination of a propagation coefficient. This coefficient $\gamma(\omega)$ is representative of both attenuation and dispersion effects in a viscoelastic bar and is defined as:

$$\gamma(\omega) = \alpha(\omega) + ik(\omega) = \alpha(\omega) + i\frac{\omega}{c(\omega)} , \tag{2.5}$$

where $\alpha(\omega)$, $k(\omega)$ and $c(\omega)$ are the attenuation coefficient, the wavenumber and the phase velocity respectively, and ω is the angular frequency.

The one-dimensional equation of axial motion of the viscoelastic bars is given by

$$\left(\frac{\partial^2}{\partial x^2} - \gamma^2\right)\tilde{\varepsilon}(x,\omega) = 0 . \tag{2.6}$$

The general solution of Equation (2.6) gives the strain at any point on the bar,

$$\tilde{\varepsilon}(x,\omega) = \tilde{P}(\omega)e^{-\gamma x} + \tilde{N}(\omega)e^{\gamma x} , \tag{2.7}$$

where $\tilde{P}(\omega)$ and $\tilde{N}(\omega)$ are the Fourier transforms of the forward ($P(t)$) and backward ($N(t)$) travelling waves respectively and $\tilde{\varepsilon}(x,\omega)$ is the Fourier transform of the longitudinal strain at any cross section x. From a series of impact tests on a 20 mm and a 40 mm diameter viscoelastic pressure bars and by use of Equation (2.7) the propagation coefficient was determined and used to calculate the axial particle velocity and normal force at any point of the bar. As the propagation coefficient was determined experimentally, it incorporates all dispersion and attenuation effects in the propagating wave that are present as a result of both the bar geometry and material properties. As such, the strains calculated at the end of the bar include inherently all material and geometric effects of the bar. However, in order to determine the complex elastic modulus of the bar or the stress at the bar ends, it is necessary to employ a rod wave theory together with the propagation coefficient. In contrast to the method used by Zhao et al. [26, 27], Bacon [33] employed the one-

dimensional wave model. Although, this can lead to inaccuracies when the wavelength is of the same order or less than the lateral dimensions of the bar, it is considered to lead to sufficiently accurate results in the case of SHPB tests (the frequency range of a typical SHPB test does not exceeds the 10-15 kHz [33,20]). The method is regarded as rather advantageous, since it is simple from a mathematical point of view and easy to implement. It can also be applied to pressure bars of any cross sectional shape and the properties of the viscoelastic material are not required a priori [33]. The method described was used successfully for the determination of the high strain-rate properties of balsa wood [34].

A simple technique to predict the strains at certain positions along a viscoelastic bar was employed by Cheng et al. [21], whereby a transfer function was used to relate the strain measurements at two positions along the bar. Using this technique the strain can then be predicted at integer multiples of the distance between the two strain readings.

In order to determine the strain in a specimen when using viscoelastic bars usually involves measurements of the strain on both bars using strain gauges. In this case the correction for the dispersion and attenuation effects is essential. In order to avoid the viscoelastic wave analysis needed when using strain gauges, Casem et al. [20] used electromagnetic velocity gauges, which were placed between the specimen/bar interfaces, to measure directly the velocity at both faces of the specimen. For the case of a 19 mm diameter polycarbonate bar, it was shown that errors of less than 5% arise for frequencies up to 20 kHz when calculating the stress from the velocity measurements and without taking into account dispersion and attenuation effects. The main drawback that exists with this technique is that a single measurement of the velocity at the input bar/specimen interface is not sufficient to calculate both the incident and reflected waves. An impact pre-test on the incident bar is required so as to calculate the velocity of the loading pulse. The incident bar has to be impacted at the same velocity in order to generate an identical incident pulse to that occurring in an actual test with the specimen. Therefore, the accuracy of this method relies on the repeatability of the incident pulse during every test [20]. Nevertheless, the measuring test duration is doubled without the need of the waves to be separated. The method was applied successfully for testing low-density foam at various strain rates (1500 s^{-1}

to 10000s^{-1}). It should be noted that the method cannot be used to test magnetic materials or when the pressure bars are magnetic due to the effects of the induced magnetic field on the velocity readings.

Sharma et al. [24] proposed the use of high-speed photography in combination with a viscoelastic SHPB. The high-speed camera was used to measure the axial and transverse strains of the specimen. The viscoelastic properties of the bars were described using a three parameter Kelvin model (see Figure 2.3) and the method of characteristics was applied to determine the forces and the particle velocities at both faces of the specimen.

However, as in the case of the techniques by Wang et al. [25] the geometric effects were not considered and the material constants needed to be determined before the application of the method. Also, the time steps used in the method of characteristics were approximate, since the wave speed was assumed to be independent of frequency (as was the attenuation coefficient). Tests were performed on sorbothane, clay and bologna and it was revealed that the viscoelastic analysis underestimated the strain values of the specimens by approximately 15%, when compared with the strain measurements that were obtained using the high-speed camera. Therefore, it was suggested that the values of the material constants should be changed in order to reduce the discrepancies between the two methods to ±5%. Nevertheless, the stress values were validated by comparing the results of tests on polyurethane samples with previous results on the same material.

More recently Liu and Subhash [28] developed a new method to describe the wave propagation in viscoelastic bars. Two strain measurements were used to define an impulse response function. One-dimensional wave propagation was assumed and the constants of a universal linear viscoelastic model with multiple Maxwell elements were determined by a least squares fit. The method is therefore similar in some respects to that of Zhao et al. [26], but employs a simpler wave theory. The method has been used to test the high strain-rate properties of polymeric foams [35].

2.4 Stress uniformity in the specimen

One of the fundamental assumptions of the SHPB is that the stress and strain state throughout the specimen is uniform (Note that for cellular materials the strain will never be uniform due to localised deformation and this is discussed further in e.g. Chapter 7). This assumption can be violated by inertia or friction effects. Strictly speaking the above assumption is never true at the early stages of loading (for several μs) especially for thicker specimens, since as the incident wave arrives at the front specimen/bar interface the generated stress wave loads only the front face of the specimen. At this instant the back face remains at rest. Until the stress wave propagates to reach the back face of the specimen the difference in stresses between the front and the back specimen's face is great [5, 12]. Although this is inevitable the assumption of stress equilibrium will not lead to significant errors for the case of metal specimens [36] of appropriate aspect ratio [37]. The achievement of a uniform stress and strain state within the specimen is more difficult in the case of brittle and soft materials. Brittle materials usually fail during the initial stage of loading, while soft materials require a longer time to achieve stress equilibrium due to their lower stress wave speeds [6, 5, 12, 8,38,39].

Therefore stress uniformity of the specimen, especially for brittle and soft materials, must not be assumed at any time and should always be checked. This can be done by checking the forces/stresses at both faces of the specimen (referred to as two-wave and one-wave analysis). The two-wave analysis represents the force/stress at the front face of the specimen, while the one-wave analysis represents the force/stress at the back face of the specimen. The result obtained from the two-wave analysis will be always more oscillating than the result from the one-wave analysis. This is due to the fact that as the transmitted pulse travels though the tested sample the high frequency oscillations will be eliminated leading to a smoother pulse in the transmitter pressure bar. If the specimen reaches stress equilibrium, the two-wave result will oscillate equally above and below the one-wave result [4,8]. The achievement of a constant strain rate can be used as another validation of stress uniformity within the specimen [4, 8], at-least for metal specimens as explained later (Equation (2.8)). Note that caution should be applied when using strain rate as a

check for stress uniformity in soft or cellular materials. Particularly when the pressure bars are high impedance, the strain-rate is dominated by the displacement history of the input bar/specimen interface. When the specimen is soft, the reflected wave is so similar to that for a free-ended bar that strain rates will always tend to appear to be approximately constant.

The establishment of a uniform stress and strain state within the tested sample depends mainly on:

- The existence of radial and axial inertia effects;
- The presence of friction at the bar/specimen interfaces;
- The rise time of the incident loading pulse, which controls the initial stress state in the specimen [12];
- The sample thickness, which controls stress equilibrium after the initial stage [12];
- The mechanical impedance mismatch between the specimen and the pressure bars;
- The quality of the specimens.

Radial and axial inertia effects can be minimised by a suitable choice of the sample size. The majority of the guidance in the literature on the choice of optimal specimen size refers to metallic specimens. However, it can be used to guide the choice of dimensions of non-metallic specimens [40]. The diameter of the specimen is chosen usually to be 80% of the bar diameter [4]. In this way the maximum desirable strain in the sample is achieved without its diameter exceeding the bar's diameter. On the other hand, the specimen must be large enough for its bulk properties to be measurable. For example in the case of polycrystalline metals and alloys the sample diameter should be at least ten times the representative microstructure unit size [4].

Davies and Hunter [41] adopted an energy balance approach to minimise axial and radial inertia effects. Their analysis leads to the result:

$$\sigma_s(t) = \sigma_o(t) + \rho_s \left(\frac{l_s^{\,2}}{6} - \nu_s^2 \frac{d_s^{\,2}}{8} \right) \ddot{\varepsilon} \ , \qquad (2.8)$$

where σ_s is the axial stress required for the specimen to deform in a one-dimensional stress state, σ_o is the stress measured at the transmitter bar/specimen interface, l_s, d_s, ρ_s and ν_s are the length, diameter, density and Poisson's ratio of the specimen under investigation respectively and $\ddot{\varepsilon}$ is the second derivative of strain often referred as strain acceleration [42]. Errors due to inertia are minimised when a constant strain rate has been achieved or when the parenthesis of Equation (2.8) is zero, which gives the optimum slenderness ratio for metal specimens as:

$$\lambda_{opt} = \frac{l_s}{d_s} = \frac{\sqrt{3}}{2}\nu_s \ . \qquad (2.9)$$

It should be mentioned that the above equation is valid only when the stress is calculated using the transmitted pulse, i.e. when stress equilibrium is assumed and the stress is calculated by use of Equation (1.8) [43]. Numerical studies [37, 40] suggested that the use of Equation (2.9) gives reasonable results for metal specimens when the effect of friction is small. It was proven in [37, 40] that for metal specimens with $\lambda<\lambda_{opt}$, stress uniformity is affected by radial inertia, while for $\lambda>\lambda_{opt}$, stress uniformity is influenced by axial inertia. Hence, radial inertia limits the maximum strain rate that can be achieved by the SHPB technique, since the strain rate is inversely proportional to the specimen's length.

Another problem that arises in the case of very thin samples is friction. The effects of friction were investigated numerically by Bertholf and Karnes [37] as well as by Meng and Li [40]. It was demonstrated that even if both inertia effects are eliminated by a suitable choice of sample size, the presence of friction at the bar/specimen interface will lead to inaccurate results. As a consequence of friction, the calculated value of the flow stress of the tested material will be enhanced due to the presence of shear stresses at the interfaces that will violate the assumption of a uniaxial stress state in the specimen [37, 40, 44]. This can be wrongly interpreted as a strain rate effect especially when the quasi-static and dynamic results are compared directly. Therefore, lubrication at the bar/specimen interfaces is essential. Moreover, extreme care should be taken to ensure that both quasi-static and dynamic tests are performed

under the same conditions regarding friction in order to make qualitative comparisons [37, 42, 45].

It has been suggested [4, 42] that for dynamic testing of metals at room temperatures an oil-based lubricant is suitable to minimise friction, since there is not sufficient time for the lubricant to flow out from the interfaces. At elevated temperatures the use of a thin layer of fine boron nitride powder is more effective, while for example petroleum jelly [46] and PTFE spray [14] have been used as lubricants for SHPB tests on polymeric and aluminium foams. In all cases care must be taken that only a thin layer of lubricant is applied at the interfaces, in order to avoid any delays of the strain recordings on both pressure bars due to its presence. Also, velocity-dependant frictional constraints should be avoided, since they can affect the measurements especially for thicker specimens [4, 47]. It was pointed out [47] that thicker specimens deformed at the same strain rate as thinner specimens, will contain larger radial displacements and hence lubricant breakdown is more likely to occur.

Based on an energy balance approach, Malinowski and Klepaczko [42] following their earlier investigation [45] suggested an optimum specimen size that would reduce the effects of both inertia and friction (Equation 2.10). This optimum slenderness ratio is

$$\lambda_{opt} = \frac{l_s}{d_s} = \left(\frac{2\mu\sigma_z}{\rho d_s^2 (\dot{\varepsilon}^2 + \ddot{\varepsilon})} \right)^{1/3}, \qquad (2.10)$$

where μ is the coefficient of friction, $\ddot{\varepsilon}$ is the strain acceleration, ρ is the specimen density and σ_z is the experimental compressive stress. However, this slenderness ratio has to be checked always since both the strain and strain rate change for different experiments. Furthermore, the calculation of the second derivative of strain may be difficult to define accurately due to the problems associated with performing numerical differentiations, especially on noisy strain signals [43, 48]. As already mentioned, both works by Malinowski et al. [42] and Davies and Hunter [41] considered only metal specimens. However, they can be used as a reference for testing soft materials [40].

Gorham [43] and Zencker [44] argued that Equation (2.9) cannot eliminate inertia. It was suggested that no optimum sample size exists that would eliminate completely inertia effects, apart from very thin specimens (1 mm thick), which can only be tested using miniature impact apparatus [49]. The benefits of a miniature SHPB have been presented by Jia and Ramesh [50]. Apart from the fact that strain rates up to 50000 s^{-1} can be achieved, the effects of both inertia and friction are less pronounced in a miniature SHPB. Furthermore, waves are less dispersive in smaller diameter bars. Following the work by Gorham [43] a limiting strain rate was presented [50] for a selected error, *r*, due to the inertia effects:

$$\dot{\varepsilon}_{\lim} = \frac{1}{l_s}\sqrt{\frac{\sigma_y}{\rho} r\left(\frac{192}{32+\frac{3}{\left(\frac{l_s}{d_s}\right)^2}}\right)}, \qquad (2.11)$$

where σ_y is the yield stress of the tested material. From Equation (2.11) it is evident that for a given (acceptable) error, materials with high yield stresses and low densities can attain higher strain rates than that for low strength, high density materials. However, Equation (2.11) as well as Equation (2.10) can only be used as an approximation since the material properties are often not known prior to testing.

The thickness effect in the case of dynamic compression of polymers has been investigated experimentally [51] and numerically [52, 36]. Dioh et al. [51] examined polymers of different thicknesses (l_s/d_s= *0.12, 0.35*) at different strain rates and concluded that their response at high strain rates depends on the sample size. Particularly, thicker specimens showed an enhancement of the flow stress at high strain rates. In the numerical study reported by Dioh et al. [52] a rate independent bilinear material model was used. The absence of stress enhancement for thinner specimens was attributed to the lower impact velocities that were used to achieve the same strain rate as for the thicker specimens. It was demonstrated that the use of high impact velocities in SHPB tests violates the assumption of stress uniformity due to

the generation of large plastic wave fronts within the specimen. On the other hand, Zhao [36] used a rate sensitive polymer-like model and concluded that the observations of Dioh et al. [51, 52] were not valid, since his results showed no sample size dependence. It was suggested that any thickness effect was due to inertia and friction and not due to wave propagation effects as suggested by Dioh [51, 52].

A more detailed finite element analysis on stress uniformity within the specimen was performed by Meng and Li [40], who relate the stress equilibrium to the accuracy of the SHPB results. Considering both axial and radial inertia as well as friction effects, two coefficients representative of the stress uniformity and a method to correct errors on SHPB results were introduced. A metallic material was used to demonstrate the method. However, the method cannot be used when materials of unknown properties are tested, since a constitutive law describing the material is needed a *priori*. Furthermore, the method requires further developments if the pressure bars are viscoelastic in order to simulate the SHPB tests.

Other factors that influence the specimen stress uniformity include the incident pulse rise time. In the case of metallic specimens the length of the incident wavefront must be large compared to the specimen's length to ensure stress equilibrium before the plastic deformation begins [38, 53]. Therefore, an incident pulse with a suitable rise time is required, in order to ensure that the elastic region in a stress-strain curve represents the true material response. Yang et al. [39] used the method of characteristics and according to the relative mechanical impedance of the specimen and the bars, determined the number of reverberations of the stress pulse required to achieve stress equilibrium within the specimen. Previously, Ravichandran and Subhash [38] had considered a linear ramp in the incident pulse and suggested that four reverberations of the stress wave were sufficient to achieve stress uniformity. However, Yang et al. [39] showed that the number of reverberations was greater. It was also shown that the time to reach equilibrium is strongly dependent on the shape of the incident pulse. For example samples which are loaded with an incident wave of finite rise time reach equilibrium faster than the ones loaded by a rectangular stress pulse.

There are several techniques that can be used in order to control the rise time of the incident wave. A brief overview of the existing pulse shaping techniques is given in [4]. Song et al. [11, 12] as well as Chen et al. [5, 6], have performed extensive investigations into the conditions that are required for soft materials to reach equilibrium. In all four of these studies, the incident wave was "triangular" in form and typically with a long rise-time of approximately 100 to 200 μs in order to achieve the stress equilibrium in the soft, rubber materials. An examination of the loading rate and specimen thickness effect [12] revealed that the thinner samples, which were compressed under lower loading rates, achieved equilibrium for almost the entire test duration. Similar "triangular" waveforms have been used to test ceramics and it was suggested [54] that the desirable loading pulse could be obtained by placing thin copper disks on the impact end of the incident bar. By doing so, the sample deformed uniformly and at a constant strain rate [54].

2.5 General remarks of the literature review

Testing of soft, low strength materials with high mechanical impedance pressure bars encounters two main difficulties. The first problem is the low magnitude transmitted pulse which cannot be measured accurately using strain gauges. The second problem is that the stress uniformity within the specimen cannot be checked by simply comparing the forces from the incident bar/specimen and transmitter bar/specimen interfaces. A review has been presented of previously reported attempts to overcome the above limitations when testing soft, low strength materials. The use of low impedance pressure bars (elastic or viscoleastic) is regarded as an ideal solution. The use of elastic low impedance bars is attractive due to the simple analysis involved in the processing of the results. However, there exists a class of materials (e.g. Rohacell foam) wherein the use of viscoelastic (e.g. PMMA) pressure bars is regarded as essential to perform SHPB tests. The main reason being that stress uniformity within the specimen can be checked with confidence. The main disadvantage when using viscoelastic pressure bars is the complicated analysis that is required to describe the wave propagation. Different approaches to achieve accurate results when using viscoelastic SHPB set ups where presented in Section 2.3.2. It can be concluded that the method proposed by Bacon [33] is advantageous over the other techniques, since

it is easy to implement and accurate results can be achieved when applied to impact tests that involve the use of viscoelastic bars (this is further discussed in Chapter 4). In fact the simplicity of the method presented by Bacon [33] is comparable to that when using elastic bars.

A discussion of the validity of the assumption of stress uniformity within the specimen in SHPB tests was presented in Section 2.4. It can be concluded that stress equilibrium within the specimen should never be assumed for soft materials and should always be checked during SHPB testing, even if using the proposed optimal lengths presented in Section 2.4. Furthermore, the results obtained by SHPB testing are influenced by the specimen dimensions, suggesting that tests should be carried out on a range of specimen sizes when testing unknown material properties. Finally, the shape of the loading wave can affect the achievement of stress uniformity. When impacting an elastic bar with a projectile of the same material without the use a pulse shaper a rectangular pulse is produced with a sharp rise time. On the other hand the impact of a viscoelastic rod with a projectile of the same material tends to create a loading pulse with longer rise times due to the damping of the material. This facilitates the achievement of stress equilibrium more quickly within the specimen, adding to the advantage of using viscoelastic pressure bars in SHPB tests.

Material	**Young's Modulus (E in GPa)**	**Density (ρ in kgm^{-3})**	**Mechanical impedance relative to steel (%)**
Steel	≈205	≈7870	100
Titanium Alloy (Ti-6Al-4V)	114	4430	56
Magnesium Alloy (AZ31B)	45	1770	22
PMMA	≈5	1190	6

Table 2.1 Comparison of the mechanical impedance of different materials.

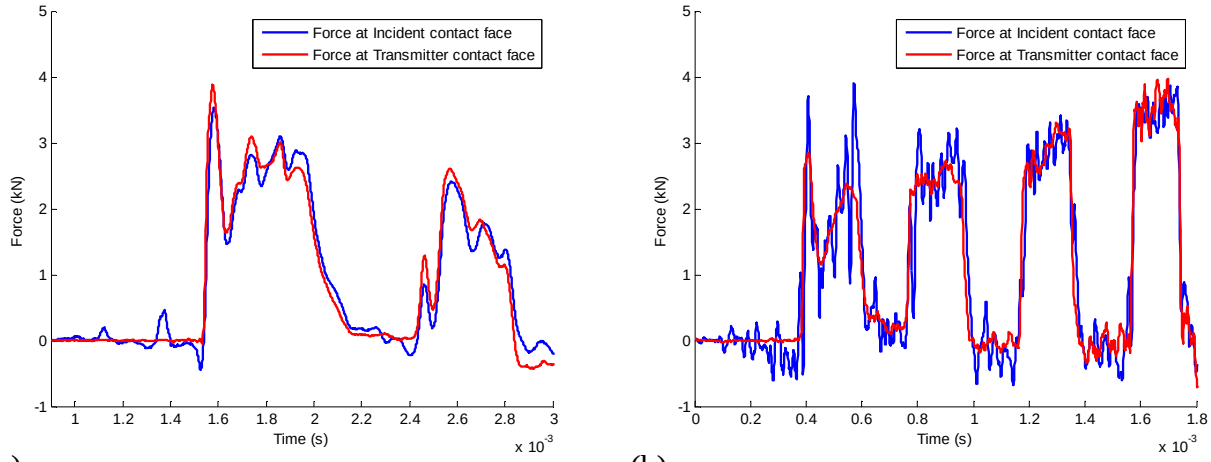

Figure 2.1 Forces at the incident/specimen and transmitter/specimen interfaces from SHPB tests on aluminium foam specimen with a thickness of 10 mm length utilising (a) PMMA and (b) Magnesium pressure bars.

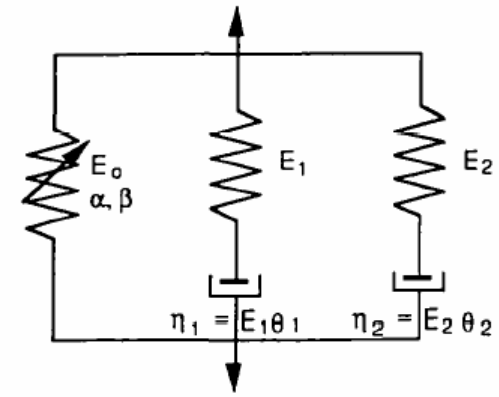

Figure 2.2 Model of the ZWT constitutive equation (Equation (2.3)) [25].

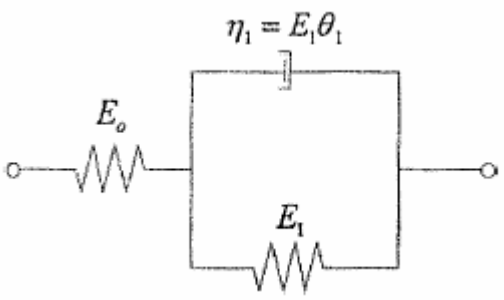

Figure 2.3 Three parameter Kelvin model [24].

CHAPTER 3

Experimental Set-up

3.1 Introduction

The main aim of this study was to examine the dynamic properties of soft materials by performing SHPB tests and Direct Impact (DI) tests. For the case of the SHPB tests two different configurations were used, one consisting of Magnesium alloy pressure bars and another consisting of PMMA pressure bars. The purpose of using pressure bars made out of different materials was to compare the two set-ups and to make recommendations for future SHPB testing of soft materials. For the DI tests a large diameter PMMA pressure bar was used.

In general a SHPB consists of two pressure bars known as input/incident and output/transmitter bars, where a specimen is sandwiched between them. A projectile made of the same material and having the same diameter as the pressure bars is fired using an airgun at the first bar and a compressive pulse is created. Strain measurements from both the pressure bars are sufficient to reveal the properties of the material.

Two types of DI tests were carried out in order to measure forces at the impacted and non-impacted faces of the specimen. The forces were measured using a single strain-gauged PMMA pressure bar.

In this chapter the details of the SHPB and the DI test arrangements are presented.

3.2 Description of the pressure bars

The first set of pressure bars used for the SHPB tests consisted of bars made out of Magnesium alloy (AZ31B). The second set of SHPB pressure bars as well as the pressure bar used in the DI tests was made out of Polymethylmethacrylate known as PMMA. A summary of the main material properties for each material is given in Table 3.1.

The two Magnesium bars had a diameter of 23 mm and the PMMA bars used for SHPB tests were 20 mm in diameter. Both types of bars were approximately 1m long. The PMMA bar that was used for the DI tests had a diameter of 40mm and length of approximately 2 m.

The strain pulses on each bar were recorded using resistance strain gauges. For the Magnesium bars FLA-3-23 foil strain gauges were used with a gauge length of 3 mm, nominal resistance 120 Ω and a gauge factor of 2.15 (±1%). For the PMMA bars Tokyo Sokki Kenkyujo Co. Ltd strain gauges were used (Model GFLA-3-70), which are suitable for plastic materials only, having a gauge length of 3mm, a gauge factor of 2.12 (±1%) and again a resistance of 120 Ω. In general, the strain gauges were attached in the longitudinal direction. However, certain strain gauges were attached to a 20 mm PMMA bar in the circumferential direction in order to take measurements of the circumferential strain. For the Magnesium bars the strain gauges were bonded using epoxy resin (AE10). Elevated temperatures are required when bonding with epoxy. This is unsuitable for PMMA. Therefore, cynoacrylic was used to bond the gauges to the polymer bars.

Pairs of strain gauges were connected with dummy resistors to form a Wheatstone bridge (Figure 3.2). This involved two active arms (R1, R2) and two dummy resistors (R3, R4). The two active arms were cemented in the direction of the strain that was desired to be measured (i.e. for measurements of the axial or the hoop strain they were placed parallel or perpendicular to the axis of the bars respectively). In this way, all strain gauges were insensitive to bending and the hoop stations gave no output for axial strain.

All Wheatstone bridges were connected to strain gauge amplifiers type 359 TA voltage amplifiers (FYLDE Electronics Laboratories Limited) and before each test the balance of each bridge was checked. The outputs from each amplifier were fed into a Digital Acquisition System, which in turn was connected to a PC that uses the Nicolet software. Nicolet software uses the recorded data and produces plots of voltage against time for every captured pulse. The strain was calculated from the strain gauge output voltage using the relationship

$$\varepsilon = \frac{4 \cdot V_{out}}{2 \cdot S_G \cdot G \cdot V_{in}}, \tag{3.1}$$

where ε is the strain to be measured, V_{in} and V_{out} are the input and output bridge voltages respectively (V_{in} was 2.5 V), S_G is the gauge factor and G is the gain.

Each pressure bar was instrumented with gauges at three or four positions along the bar. The position of the strain gauges were measured accurately using a vertical vernier. All measurements were taken from the impact end or the end closest to the impact for every bar. It should be pointed out that during testing some of the gauges were damaged and the bars had to be regauged. Table 3.2 shows the position of the strain gauges for the majority of the tests that were performed in this study.

For the 20 mm diameter PMMA pressure bars, the propagation coefficient and the Poisson's ratio were calculated using measurements of the axial and hoop strain at a location 492.54 mm from the left end of the bar. This strain gauge location was not subsequently used for SHPB testing and is not listed in the above Table 3.2.

3.3 Description of the SHPB arrangement

Details of the background of the SHPB set up were given in Chapter 1 (Section 1.1). Delrin guides were used to support each of the bars in the SHPB arrangement (Figure 3.2) in such a way that the bars were aligned accurately with the axis of the gun barrel, in order to ensure that the conditions for one dimensional wave

propagation theory are not violated [4]. Both the input and output bars were free to move along the bar axis. A shock-absorbing block was placed a short distance from the free end of the transmitter bar to prevent the bars from sliding so far as to damage of the strain gauges. The input Magnesium bar was earthed to reduce electrical noise that occurred on contact with the striker.

Each of the compressive waves was generated by the impact of a striker/projectile onto the incident bar using an airgun (Figure 3.2). The details of the air gun used are given in [3]. Different impact velocities could be achieved by adjusting either the pressure level in the reservoir or the position of the striker bar in the gun barrel. The gun barrel had an internal diameter of 23.15 mm. The level of the air pressure was recorded using three pressure gauges. At the end of the gun barrel two laser photoelectric detectors were placed 120 mm apart. As the striker travels along the gun barrel it cuts both laser beams giving an output. Measurements of the time taken for the projectile to travel the distance between the two photodiodes provided the impact velocity.

For both SHPB arrangements the striker length was 250 mm, 450 mm and 500 mm. Also, a slight radius was machined to the front face of the projectile. This was done in order to achieve good alignment with the input bar as well as a finite rise time of the incident loading wave.

The maximum safe impact velocity of the projectile and the strain generated on both Magnesium and PMMA bars had to be determined, in order to avoid any yielding at the impact end. For convenience it was assumed that the stress wave velocity was constant for both bars. The maximum impact velocities (V_{IMP}) and strains that were calculated are shown in Table 3.3 for both materials.

As an approximation the strain rate and the strain applied to a specimen can be calculated using the following equations:

$$\dot{\varepsilon} = \frac{V_{IMP}}{l_o} \text{ and } \varepsilon = 2\dot{\varepsilon}\frac{l_{striker}}{c}. \qquad (3.2)$$

It is worth noticing from the above an advantage of the PMMA bars over the Magnesium bars. Since the strain rate is approximately directly proportional to the impact velocity, from Table 3.3 it can be deduced that higher strain rates are achievable using PMMA bars compared with the Magnesium ones for a specimen of the same length. It follows from Equation (3.2) that the strain experienced by a specimen using a projectile of the same length is again higher when using PMMA bars.

3.4 Description of the Direct Impact (DI) test arrangement

Two types of DI tests were carried out in order to measure the proximal and distal loads of the specimens tested. The forces were measured using a strain gauged 40mm diameter PMMA pressure bar, which was supported using three Delrin rings similar to those utilised for the SHPB bars (Figure 3.2). The two different arrangements that were used to determine the proximal and distal loads are similar to those used by Harrigan et al. [55] and shown in Figure 3.3.

Masses were used either as a backing mass (Figure 3.3(a)) or as projectiles (Figure 3.3 (b)). The purpose of the backing mass was to provide additional kinetic energy and it also ensured better alignment of the specimen in the gun barrel. Two masses were used. One mass was a 65 gr, 35 mm long aluminium alloy cylinder. The other mass was a cylinder made out of Derlin with an aluminium disk attached to its front end. This two-part cylinder had a total mass of 24 gr and a total length of 38 mm. In order to measure proximal end forces, a backing mass was attached to the rear face of the specimen (Figure 3.3 (a)) before the mass and specimen were fired at the pressure bar. As illustrated in Figure 3.3 (b) the distal end loads were measured by firing a projectile at the specimen that was positioned in such a way that its distal end was in contact with the end of the PMMA bar. For both types of tests the crushing of the specimens took place within the gun barrel which provided lateral constrain. Also, cushioning of the projectile was minimised by use of the air vents situated near the end of the gun barrel. The impact velocities were measured as in the case of the SHPB tests by use the two light beams. A small clearance was kept between the end

of the gun barrel and the pressure bar so that signals were not transmitted from the barrel to the bar.

Type of material	**Young's Modulus (Gpa) (E)**	**Compressive yield strength (MPa) (σ_y)**	**Density (kgm^{-3}) (ρ)**	**Poisson's Ratio (ν)**
Magnesium Alloy (AZ31B)	≈45	97	1770	0.35
PMMA	≈5	≈110	1190	≈0.33

Table 3.1 Mechanical properties of Magnesium alloy and PMMA.

Bar Material	**Test**	**Bar Position**	**Total length (m)**	**Position of Strain Gauges (mm)**			
				A	**B**	**C**	**D**
Magnesium	SHPB	Incident	0.98346	326.96	373.6	491.68	700.58
Magnesium	SHPB	Transmitter	0.9836	327.7	374.34	700.6	
PMMA	SHPB	Incident	0.99778	145.4	323.16	540.18	801.18
PMMA	SHPB	Transmitter	1.00068	324.03	540.36	800.92	
PMMA	DI	-	1.9772	279.7	1036.8	1565.2	

Table 3.2 Position of the strain gauges.

Bar Material	**Stress Wave Velocity (m/s)** $(c = \sqrt{E/\rho})$	**Maximum Impact Velocity (m/s)** $(V_{IMP\max} = (2\sigma_y / \rho c))$	**Maximum Elastic Strain** $(\varepsilon_{y(\max)} = \sigma_y / E)$
Magnesium	5042.2	21.73	0.002155
PMMA	≈2050	≈90.18	0.022

Table 3.3 Maximum impact velocity of the projectile and maximum elastic strain for the Magnesium alloy and PMMA pressure bars.

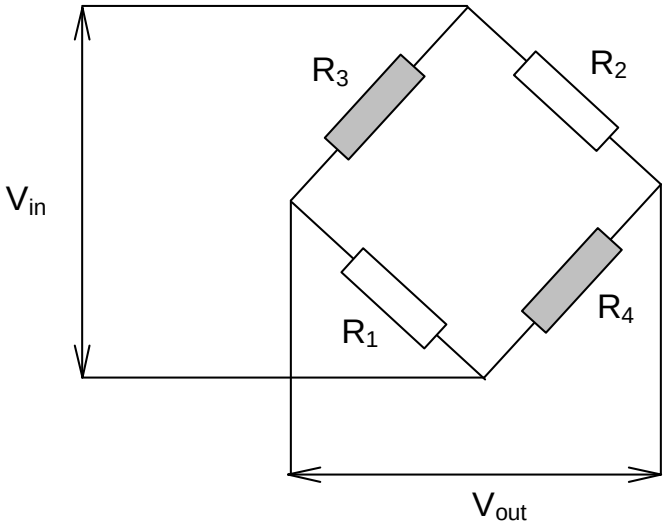

Figure 3.1 Wheatstone Bridge arrangement.

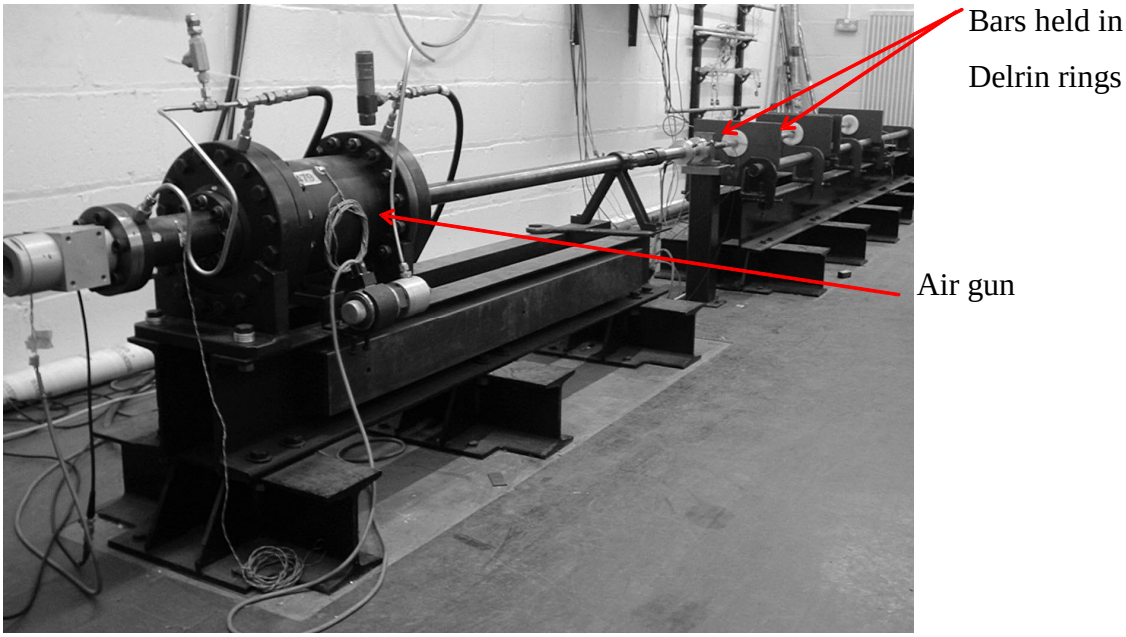

Figure 3.2 SHPB arrangement.

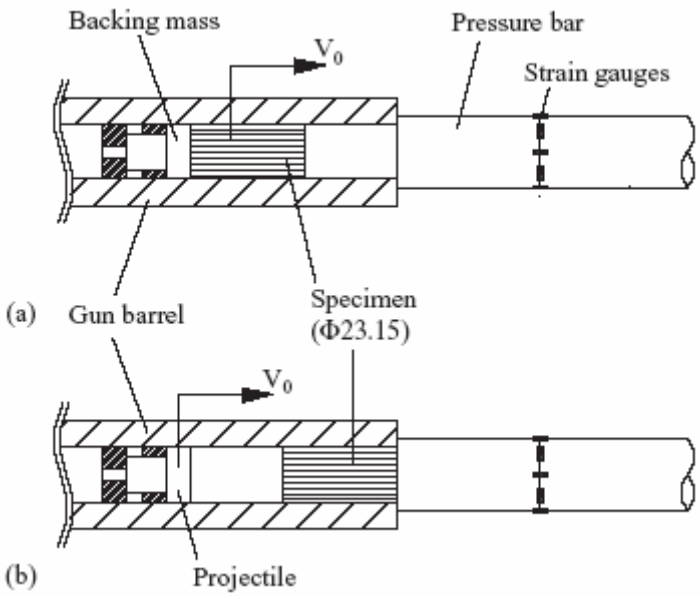

Figure 3.3 Arrangements used to measure (a) proximal and (b) distal end forces [55].

CHAPTER 4

Determining the Propagation Coefficient and the Material Properties of the PMMA Pressure Bars

4.1 Introduction

In a classical SHPB apparatus the forces and displacements at the specimen/bar interfaces are evaluated using strain measurements that are not taken directly at the interfaces but from strain gauges that are placed away from the specimen. Under the assumption of the one-dimensional stress wave propagation the measured strains can be time shifted and be known at any point on the pressure bars. This is true in the case of elastic bars for wavelengths that are long compared to the diameter of the bars. However, if high frequency waves are present or if the bar diameter is large, then radial inertia becomes significant. This results in geometric wave dispersion.

The importance of using low impedance pressure bars for SHPB testing of soft materials was discussed in Sections 2.2 and 2.3. Unfortunately, the wave propagation in viscoelastic media is complicated since waves disperse and attenuate. Both the attenuation and dispersion are defined herein using an experimentally determined propagation coefficient.

The procedure that was followed to determine the propagation coefficients for the 20 mm and 40 mm diameter PMMA pressure bars is outlined in this chapter. This includes a discussion of the wave propagation in viscoelastic media. The accuracy of the experimentally determined propagation coefficient is validated. Also, the mechanical properties of the PMMA material are investigated and results are presented.

4.2 Wave propagation in viscoelastic bars

The analysis involved in the classical SHPB method is often based on the assumption that the propagation of the stress waves along the bar is governed by the one-dimensional wave theory. In the case of the elastic bars this is not always true, since stress waves change shape as their higher frequency components travel slower than their lower frequency components. This leads to the characteristic oscillations in the measured strain histories that are often apparent in the evaluated stress-strain curves [56]. Therefore, the phase velocity is frequency dependent and decreases as frequency increases. This phenomenon is referred to as geometric dispersion and is particularly important when the wavelength of the loading wave is of the same order of magnitude or less than the diameter of the bar, i.e. when the effects of the radial inertia become important. In order to correct for this dispersion, the Pochhammer-Chree equation of motion has been used [3, 33, 57, 4, 26]. Although, its solution is exact only for infinite circular bars it can be used for finite length bars without introducing significant errors [58].

In the case of viscoelastic bars the wave propagation is rather more complex than in elastic media. Apart from the wave dispersion due to the lateral motion in the bars, dispersion occurs as a result of the dependency of the viscoelastic material properties on frequency (material dispersion), which causes the phase velocity to increase as frequency increases. In addition, waves attenuate owing to material damping [33, 57, 26]. Zhao and Gary [26] have taken into account both dispersion and attenuation effects by generalising the Pochhammer-Chree equation for elastic bars to viscoelastic bars. However, this approach is mathematically and computationally complex and requires as *a priori* the knowledge of the material properties (section 2.3.2). Benatar et al. [57] simplified the Pochhammer-Chree equation for the case of viscoelastic bars in order to correct for both attenuation and geometric dispersion in the phase velocity. For low and intermediate loss viscoelastic materials, this approach extends the usable frequency range as compared with the one-dimensional theory and only requires the knowledge of the Poisson's ratio. More recently Anderson [59] presented the four-mode rod equation whose accuracy is comparable with Pochhammer-Chree equation. Its advantage over the Pochhammer-Chree

equation is its computational efficiency, since it can be solved without using any iteration theme. Furthermore it can be applied to cross-sectional areas other than solid circular sections.

On the other hand, methods based on experimental techniques for the determination of a propagation coefficient, which is representative of both the attenuation and dispersion are simpler and do not need prior knowledge of the material properties [33, 60, 61, 62, 63, 64, 65]. Despite the advantage of the simplicity involved in these methods, they are accurate up to a narrow frequency range, since they are based on the one-dimensional theory of motion, which neglects the lateral motion of the bar. However, it has been proven that they can lead to sufficiently accurate results up to approximately 10-15 kHz for 20 mm diameter viscoelastic bars. This is adequate for SHPB tests if no energy is detected at frequencies higher than 10-15 kHz in the strain gauge histories [33]. Figure 4.4 shows the frequency spectrum of two strain gauge measurements for a pressure bar impacted by the shortest striker bar used in this investigation. Accurate results using the elementary theory have been obtained at frequencies up to 15 kHz for a 20 mm diameter PMMA bar [62] and up to 10 kHz for a 40 mm diameter bar [33]. In the case of smaller diameter PMMA bars (10 mm) accurate results were obtained up to 40 kHz [62].

Waves propagating in viscoelastic media can be described using the one-dimensional theory in the frequency domain if three complex functions of frequency are known (see Equation (4.10)). These functions are the propagation coefficient, $\gamma(\omega)$, which is representative of the attenuation and dispersion of waves, and the two waves that propagate in opposite directions in the bar [33, 61, 62]. Therefore, three independent strain measurements are required (or two if a boundary condition is utilised, e.g. a free end), in order to determine the three unknown complex functions and thereby to obtain the properties of a viscoelastic material. From the propagation coefficient the complex Young's Modulus of Elasticity can be determined when the density of the material is known (Equation (4.7)). However, if the two waves that propagate in opposite directions are measured separately, i.e. avoiding wave superposition, then only two or one strain measurement and a boundary condition are required. Methods that utilise a reduced number of measurements have been adopted in the past [33, 29,

66, 34] and have the advantage that they are simple and easy to implement. Furthermore, in the case where the free end boundary condition is used the solution benefits from the use of a noise free measurement. However, these methods require long bars and some skill to ensure that the waves do not overlap.

Alternatively, methods exist that allow the determination of the propagation coefficient (and hence the complex Young's Modulus) without requiring the waves to be measured separately [61, 67, 68, 62]. Therefore, short bars can be used. The main disadvantage of these methods is that they require at least two strain measurements and a boundary condition and their accuracy is limited by the position of the strain gauges. This is due to the fact that the propagation coefficient cannot be determined at some critical frequencies. These frequencies correspond to the cases when the distance between two strain gauges is a multiple of half the wavelength [61, 67, 68, 62]. Hillström et al. [61] suggested that the gauges should be positioned non-uniformly at more than three strain gauge stations in order to minimise the number of critical frequencies and proposed the use of the least square method so as to obtain an approximate value of the propagation coefficient at the possible critical frequencies. However, the above technique is rather complex mathematically and computationally. It should also be noted that although an advantage of these techniques is that they are applicable to short bars, they have only been applied to relatively long bars to date, for example the length of the bar that was used in [61] and [62] was 2 m.

4.3 Experimental determination of the viscoelastic properties of the pressure bars

4.3.1 Principle

The properties of the PMMA bars were determined experimentally by means of a series of impact tests on the input pressure bar, utilising one strain gauge station and a free end boundary condition. When a spherical projectile impacts the bar it generates a compressive pulse, which propagates in the direction of increasing x (Figure 4.1). When it reaches the free end, it is reflected back as a tensile wave. Provided that the wavelengths within the pulse are greater than the diameter of the bar and assuming that the plane cross-sections remains plane and a uniaxial stress state exists, the wave motion can be described as one-dimensional. The relationships for the longitudinal strain ($\varepsilon(x,t)$) and particle velocity ($v(x,t)$) are defined with respect to the axial displacement ($u(x,t)$) at a position x and time t by:

$$\varepsilon(x,t) = \frac{\partial u(x,t)}{\partial x}; \tag{4.1}$$

$$v(x,t) = \frac{\partial u(x,t)}{\partial t}. \tag{4.2}$$

From the equation of motion of a small volume element, the following relationship for the normal stress ($\sigma(x,t)$) can be derived:

$$\frac{\partial \sigma(x,t)}{\partial x} = \rho \frac{\partial v(x,t)}{\partial t}, \tag{4.3}$$

where ρ is the density of the bar.

From Equations (4.1)-(4.3) the equation below can easily be derived [2]:

$$\frac{\partial^2 \sigma(x,t)}{\partial x^2} = \rho \frac{\partial^2 \varepsilon(x,t)}{\partial t^2}. \tag{4.4}$$

Equation (4.4) can be transformed to the frequency domain:

$$\frac{\partial^2}{\partial x^2} \tilde{\sigma}(x,\omega) = -\rho\omega^2 \tilde{\varepsilon}(x,\omega), \tag{4.5}$$

where $\tilde{\sigma}(x,\omega)$, $\tilde{\varepsilon}(x,\omega)$ are the Fourier transforms of the stress and strain respectively. The stress and the strain of a linear viscoelastic material are related by the following equation:

$$\tilde{\sigma}(x,\omega) = E^*(\omega)\tilde{\varepsilon}(x,\omega), \tag{4.6}$$

where $E^*(\omega)$ is the complex Young's modulus and is a function of the frequency due to the viscoelastic characteristics of the material.

The propagation coefficient is defined as

$$\gamma(\omega)^2 = -\frac{\rho\omega^2}{E^*(\omega)}. \tag{4.7}$$

By twice differentiating Equation (4.6) with respect to x, one obtains the following relationship:

$$\frac{\partial^2 \tilde{\sigma}}{\partial x^2}(x,\omega) = E^* \frac{\partial^2 \tilde{\varepsilon}}{\partial x^2}(x,\omega). \tag{4.8}$$

Comparing Equations (4.5) and (4.8) and substituting $(-\rho\omega^2)$ from Equation (4.7) the following relation (first encountered in Equation (2.6)) is obtained:

$$\left(\frac{\partial^2}{\partial x^2} - \gamma^2\right)\tilde{\varepsilon}(x,\omega) = 0. \tag{4.9}$$

The general solution of Equation (4.9) gives the strain measured at any position x:

$$\tilde{\varepsilon}(x,\omega) = \tilde{P}(\omega)e^{-\gamma x} + \tilde{N}(\omega)e^{\gamma x}, \tag{4.10}$$

where $\tilde{P}(\omega)$ and $\tilde{N}(\omega)$ are the Fourier transforms of the waves propagating in the positive and negative direction respectively. If the forward and backward waves do not overlap at $x = 0$ (Figure 4.1), they can be defined as the incident strain, $\varepsilon_I(t)$, and reflected strain, $\varepsilon_R(t)$, of a single pulse, i.e.

$$\tilde{\varepsilon}_I(\omega) = \tilde{P}(\omega) \text{ and } \tilde{\varepsilon}_R(\omega) = \tilde{N}(\omega). \tag{4.11}$$

Both ends of the bar are free and hence the force at the non-impacted end will be zero. For $x = d$ (Figure 4.1) Equation (4.10) becomes:

$$0 = \left[\tilde{\varepsilon}_I(\omega)e^{-\gamma d} + \tilde{\varepsilon}_R(\omega)e^{\gamma d}\right]. \tag{4.12}$$

Rearranging Equation (4.12), the ratio of the strains can be expressed in terms of a transfer function or the propagation coefficient.

$$\tilde{H}(\omega) = -\frac{\tilde{\varepsilon}_R(\omega)}{\tilde{\varepsilon}_I(\omega)} = e^{-2\gamma d}. \tag{4.13}$$

The propagation coefficient can be obtained by taking the natural logarithm of the Equation (4.13). The logarithm's real part (i.e. the attenuation coefficient, $\alpha(\omega)$) and its imaginary part (i.e. the wave number, $k(\omega)$) are equal to the amplitude and the phase of the transfer function respectively (see Equation (2.5)). The attenuation coefficient represents the damping of the material and is an even function, positive for both positive and negative frequencies, while the wave number represents the

wave dispersion and is an odd function, positive only for $\omega > 0$. Both functions are continuous with $\alpha(0) = k(0) = 0$ and increase monotonically as positive frequency increases. It should be noted that calculations are performed in the frequency domain. As such all calculated phase angles have an infinite number of solutions at intervals of 2π. In order to obtain the correct phase a numerical procedure known as unwrapping is performed. This allows the actual continuous phase angle to be approximated by the calculated discrete phase angle [33].

4.4 Complex viscoelastic material properties

The components of any complex moduli ($M^*(\omega)$) and the complex Poisson's ratio ($\nu^*(\omega)$) are defined in the frequency domain as follows [69, 70, 71, 72]:

$$M^*(\omega) = M'(\omega) + iM''(\omega) = M'(\omega)(1 + i\tan\delta_M(\omega)); \tag{4.14}$$

$$\tan\delta_M(\omega) = \frac{M''(\omega)}{M'(\omega)}; \tag{4.15}$$

$$\nu^*(\omega) = -\frac{\tilde{\varepsilon}_y(\omega)}{\tilde{\varepsilon}_x(\omega)} = \nu'(\omega) - i\nu''(\omega) = \nu'(\omega)(1 - i\tan\delta_\nu(\omega)); \tag{4.16}$$

$$\tan\delta_\nu(\omega) = \frac{\nu''(\omega)}{\nu'(\omega)}, \tag{4.17}$$

where the symbols $\tan\delta_M(\omega)$ and $\tan\delta_\nu(\omega)$ are referred to as the loss factors and $\tan\delta_\nu(\omega)$ represents the lag of the lateral strain to the axial strain which occurs due to material damping [70]. The prime superscript (′) and the double prime superscript (″) refer to the real and imaginary parts respectively. The lateral strain lags behind the axial strain due to damping and the Poisson's ratio is defined as the negative of the ratio of the lateral strain to the axial strain under a uniaxial stress state (see Equation 4.16) [69, 70, 71, 72].

The experimental methods used for the determination of the complex Poisson ratio of viscoelastic materials are categorised as (a) *direct*, (b) *secondary effect* and (c) *two moduli methods* [70]. Direct methods are based on experimental measurement of the axial and lateral strains of the specimen (often using strain gauges) when it is excited into axial vibration. Although, direct methods are easily implemented, extreme care has to be taken when calculating the phase angle of the Poisson's ratio. For secondary methods, the Poisson's ratio is determined by use of its effect on vibration e.g. the dispersion of the wave propagation. These methods lead to results accurate up to a very narrow frequency range where the wavelength is much larger than the lateral dimensions of the specimen. The most effective method for the determination of Poisson's ratio is the measurement of two other complex moduli. According to Pritz [70] the best approach is to measure the complex Shear ($G^*(\omega)$) and Bulk ($K^*(\omega)$) moduli. Caracciolo et al. [72] measured the complex Poisson's ratio and Young's Modulus ($E^*(\omega)$) by subjecting a beam-like viscoelastic specimen to seismic excitation at different temperatures taking into account the plate effect. By applying a reduced variable method they broaden the frequency range and obtained a master curve up to 108 and 104 Hz for the complex Poisson's ratio and Young's Modulus respectively.

4.5 Experiments, results and discussion of the propagation coefficient and complex properties of 20 mm and 40 mm diameter PMMA bars

Direct measurements of both axial and lateral strains on an impacted PMMA rod can lead to the determination of both the Poisson's ratio and the Elastic Modulus of the PMMA bar. The complex Young's modulus can be determined using Equation (4.7) as long as the propagation coefficient has been determined for the viscoelastic rod under consideration. The Poisson's ratio can be calculated with the use of Equation (4.16).

In this study the procedure presented by Bacon [33] was used to determine experimentally the propagation coefficients for both the 20 mm and 40 mm diameter PMMA bars. As already mentioned, the only limitation of this technique is that

superposition of waves should be avoided when determining the propagation coefficient. The propagation coefficient and the Poisson's ratio for the 20 mm diameter PMMA bar were evaluated by impacting the PMMA bar with a 6 mm diameter spherical projectile between 26 to 56 m/s using an air gun and taking measurements of the axial and lateral strains from strain gauges that were positioned 492.54 mm away from the impact end of the bar. In total twelve tests were performed. For the case of the 40 mm diameter PMMA bar impact tests were performed using a 35 mm long and 20 mm diameter PMMA projectile. Seven tests were performed at impact velocities between 23 to 42 m/s again using an air gun and axial strain measurements were taken from position B (see Table 3.1). For both bars the use of smaller diameter projectiles provides data over a wider frequency range [33]. The propagation coefficient was determined by using axial strain measurements according to Equation (4.13). Figure 4.2 shows the attenuation and phase velocity derived from all the tests that were performed on both 20 mm and 40 mm diameter PMMA bars together with an overall average for each bar.

From Figure 4.2 it can be observed that the results obtained for both the attenuation coefficient and phase velocity show good repeatability up to approximately 20 kHz. The attenuation coefficient increases with frequency for both bars (Figure 4.2 (a)). Both geometric and material dispersion effects are evident in Figure 4.2 (b). The material effect is seen in the increasing phase velocity at the lower frequency range plotted in Figure 4.2 (b) [33, 57]. As expected, the geometric dispersion is particularly evident in the larger diameter bar, for which the phase velocity reaches a maximum and then decreases with frequency. Figure 4.2 (b) shows that the phase velocities plateau at approximately 20 kHz and 8 kHz for the 20 mm and 40 mm diameter bars respectively. Above 8 kHz, the phase velocity of the 40 mm diameter bar decreases indicating that the effects of the lateral motion of the bar become the dominant effect and hence the one-dimensional theory becomes less accurate [33]. When comparing the values of the phase velocity for both bars it can be seen that for frequencies below about 10 kHz the phase velocity of the smaller diameter bar is lower than that of the larger diameter bar, indicating that the mechanical properties of the two bars are not identical. This can be attributed to the extrusion process during manufacture of the bars [33].

In order to set an upper bound frequency for the validity of the one-dimensional theory, the wavelength ($\lambda(\omega)$) was calculated as a function of frequency for both 20 mm and 40 mm diameter PMMA bars using Equation (4.18), and is plotted in Figure 4.3.

$$\lambda(\omega) = \frac{2\pi}{k(\omega)}. \tag{4.18}$$

Since the wavelength is inversely proportional to the wavenumber (Equation (4.18)) it will be a continuous function, which decreases monotonically with frequency and approaches infinity as frequency tends to zero. The properties of the viscoelastic material can be determined using the elementary theory for frequencies where the wavelength is greater than approximately 7 to 10 times the bar diameter [62]. At higher frequencies the radial inertia effects are dominant. From Figure 4.3 (a) the wavelength of longitudinal waves in the 20 mm diameter PMMA bar is 0.22 m (i.e. 11D) at 10 kHz and approximately 0.15 m (7.5D) at 15 kHz, where D is the diameter of the bar. For the 40 mm diameter PMMA bar (Figure 4.3 (b)) the wavelength has values of approximately 0.4 m (10D) at 6 kHz and 0.28 m (7D) at 8 kHz. It can be concluded that the elementary theory is accurate for frequencies up to between 10 to 15 kHz and 6 to 8 kHz for the 20 mm and 40 mm diameter PMMA bars respectively. Figures 4.4 and 4.5 show the frequency spectrums of strain signals from impact tests performed on both diameter bars. The frequency spectrums in Figure 4.4 were obtained by firing a 95 mm long PMMA projectile onto the 20 mm diameter PMMA bar at a velocity of 22 m/s. From Figure 4.4 it can be observed that negligible energy is detected for frequencies above 10 kHz. It should be noted that during SHPB tests the shortest projectile that was used was 250 mm long. The shorter the length of the projectile the shorter the duration of the stress wave that will be produced. Hence higher frequency components will be present in the strain signals. For the 40 mm diameter PMMA bar, the frequency spectrums plotted in Figure 4.5 were generated from strain measurements taken during a DI test on Rohacell foam. It is clear that no energy is detected above 4 kHz. Hence the elementary theory can be used with accuracy in both SHPB and DI tests.

The dependence on frequency of the complex properties of viscoelastic materials has been investigated thoroughly by Pritz [69]. The real part of the complex Young's modulus should increase monotonically with increasing frequency and the slope of this increase indicates the amount of damping within the material [69]. The real and imaginary parts of the Young's modulus as well as the loss angle ($\arctan(E''(\omega)/E'(\omega))$) obtained from the average propagation coefficient (Equation 4.7) for both diameter PMMA bars are illustrated in Figure 4.6.

Observing Figure 4.6 (a) the real part of the complex Young's modulus for the 20 mm diameter PMMA bar increases with frequency but with a reducing slope as the frequency increases. At frequencies greater than 4 kHz, the real part could be said to be approximately constant. For the 40 mm PMMA bar, the real part of the complex Young's modulus increases up to a frequency of about 4 kHz and then remains roughly constant until a frequency of 8 to 10 kHz and subsequently decreases at higher frequencies. These observations further support the conclusions that were made previously regarding the frequency range over which Equation (4.7) is valid. The imaginary part of the Young's modulus is proportional to the slope of increase of the real part and that is why it has largest magnitudes at low frequencies and then remains approximately constant and low-valued at higher frequencies for both PMMA bars [69]. The loss angles for the two bar materials are plotted in Figure 4.6 (b). The loss angles have their highest values at the lowest frequencies, 10° and 6° for the 20 mm and 40 mm diameter bars respectively. For both bars the loss angles decrease to approximately 2° with increasing frequency. The low values of the loss angle and the fact that the slope of increase of the real part of the Young's modulus is small, indicates that the damping within the material is at a low level [69].

Pritz [69] reported that theoretically the real part of the complex Poisson's ratio decreases with increasing frequency. Also, as is the case for any complex moduli, the imaginary part of the complex Poisson's ratio is proportional to slope of the real part and together with the loss angle it should have at least one maximum at low frequencies [69]. Figure 4.7 illustrates the components of the Poisson ratio as a function of frequency for the 20 mm diameter PMMA bar. No experiments were performed for the 40 mm diameter bar. It can be observed (Figure 4.7 (a)) that the

real part of the Poisson ratio has an almost constant value of 0.33 while its imaginary component is approximately zero throughout the whole frequency range up to 20 kHz. The very small values of the loss angle (Figure 4.7 (b)) along with the almost zero imaginary part indicate that the Poisson's ratio of PMMA is frequency independent. The Poisson ratio can not be truly constant for viscoelastic materials [70, 71]. However, direct methods are not sufficient to measure the small variations in the Poisson ratio with sufficient accuracy [70, 71].

The results for both the complex Young's Modulus and Poisson's ratio agree well with the data reported up to 15 kHz by Mousavi et al. [62] for a 20 mm diameter PMMA bar (see Figure 4.8). However, the method that was followed here was simpler than that described in reference [62], where a least square method was used to minimise errors from measurements made using four strain gauges and a boundary condition. Although the method followed by Mousavi et al. [62] allows for wave superposition, the bar that was used was 2 m long. In this study, the length of the bar was approximately 1 m indicating that the technique presented in this study is suitable for *in situ* determination of viscoelastic properties for bars used in SHPB tests. Furthermore, no experimental results of the loss angle of the Poisson ratio are presented in [62]. Consequently, errors associated with the direct method to calculate the complex Poisson's ratio are not shown. Also, Mousawi et al. [62] used impact velocities up to 500 m/s. In this author's opinion, such high impact speeds are likely to produce plastic deformation at the impact surface of the pressure bar.

Assuming that the material is isotropic, the knowledge of any two material properties is sufficient to estimate any of the remaining complex moduli. Hence, both the complex Shear ($G^*(\omega)$) and complex Bulk ($K^*(\omega)$) moduli can be calculated by using the following well-known equations:

$$G^*(\omega) = \frac{E^*(\omega)}{2(1+\nu^*(\omega))}, \qquad K^*(\omega) = \frac{E^*(\omega)}{3(1-2\nu^*(\omega))} \tag{4.19}$$

The accuracy with which the complex Shear and Bulk moduli can be calculated using Equation (4.19) depends on the accuracy with which both the complex

Poisson's ratio and Young's Modulus have been determined. If the product of the loss factors of the complex Poisson's ratio and Young's Modulus is negligible when compared to unity, an error of 1% in the real parts of the Poisson's ratio and Young's Modulus will lead errors of ±1.25% and ±3% in the determination of the real parts of the Shear and Bulk moduli respectively [73]. Figure 4.9 shows that the product of the loss angles of the complex Poisson's ratio and Young's Modulus is small compared to unity for frequencies up to 20 kHz. The real and imaginary parts and loss angles of both the complex Shear and Bulk moduli are presented in Figures 4.10 and 4.11 respectively.

The behaviour of both real and imaginary components and loss angles of the complex Shear and Bulk moduli should follow similar trends to those of the complex Young's Modulus [69]. The real part of the complex Shear Modulus increases up to 4 kHz and then remains approximately constant up to approximately 20 kHz (Figure 4.10 (a)). The largest value of the imaginary part of the complex Shear Modulus occurs at the lowest frequency. The imaginary part remains approximately constant (Figure 4.10 (a)) for most of the frequency range. The Shear Modulus loss angle starts at a value of 10.5° but reduces rapidly with frequency to approximately 2° (Figure 4.10 (b)). Note that the values obtained for the complex Shear Modulus agree well with those reported by Mousavi et al. [62] for the same material, but obtained from a series of torsion tests (Figure 4.8). From Equation (4.19) it can be concluded that the accuracy of the evaluation of the Bulk modulus is influenced to a much larger degree by the accuracy of the complex Poisson's ratio. This is the reason for the fluctuations observed in Figure 4.11 especially for the loss angle of complex Bulk Modulus. However, the magnitudes for the real part are in line with those obtained by Read et al. [73] using a different technique.

4.6 Accuracy of the experimentally determined propagation coefficient for the PMMA bars

The accuracy of the experimentally determined propagation coefficient was verified by performing two impact tests on both 20 mm and 40 mm diameter PMMA

pressure bars. The 20mm diameter PMMA pressure bar was impacted with a 410 mm long PMMA projectile at an impact velocity of 10 m/s, while the 40 mm diameter bar was impacted with a 200 mm long projectile at an impact velocity of 17 m/s. In both cases the projectiles had a diameter of 20 mm.

During SHPB testing, the conditions of the specimen/bar interfaces are calculated in two stages. In the first stage the strain at this interface is calculated using the experimentally determined propagation coefficient (Equation 4.10). In order to verify the accuracy at which the propagation coefficients can be used for this stage, the strain measurements at a point x_A were used to predict the strain in another point (x_B) on the bars. The results shown in Figures 4.12 (a) and 4.13 (a) for the 20 mm and 40 mm diameter bars respectively reveal very high accuracy when comparing the predicted and measured strains.

In the second stage the stresses at the specimen/bar interfaces are calculated using the one-dimensional theory. The accuracy of the use of Equation (4.7) has been evaluated by calculating the forces at the free end of the bars. It has been shown [56] that for the conditions of a typical Spilt Hopkinson test the longitudinal stress, the longitudinal strain and the axial displacement vary negligibly over the cross section area and hence, the stress state can be assumed one-dimensional, indicating that strain gauges can measure the axial strain with sufficient accuracy. The above has been accepted by many researchers including Bacon [33, 74]. The longitudinal strain (and hence the force) should be zero at the non-impacted end of the bar and the maximum error of the method was defined as the accuracy to determine the zero strain at the free end of the bar as indicated by Bacon [33, 74]. Observing Figures 4.12 (b) and 4.13 (b), the absolute errors of the force predictions are calculated by comparing the maximum error at the free end with the value at the impacted end. The errors are estimated to be of the order of 3.9 % and 1.9% for the 20 mm and 40 mm diameter bars respectively.

4.7 Concluding remarks

The validity of Bacon's technique [33] for determining the propagation coefficient of longitudinal waves in polymer rods has been verified experimentally. In order to achieve large strains in the specimens during SHPB tests, wave separation techniques are required as the incident and reflected waves will tend to overlap at the strain gauge stations. This is considered in the next chapter where a fuller discussion of the analysis required to generate Figures 4.12 (b) and 4.13 (b) will be provided.

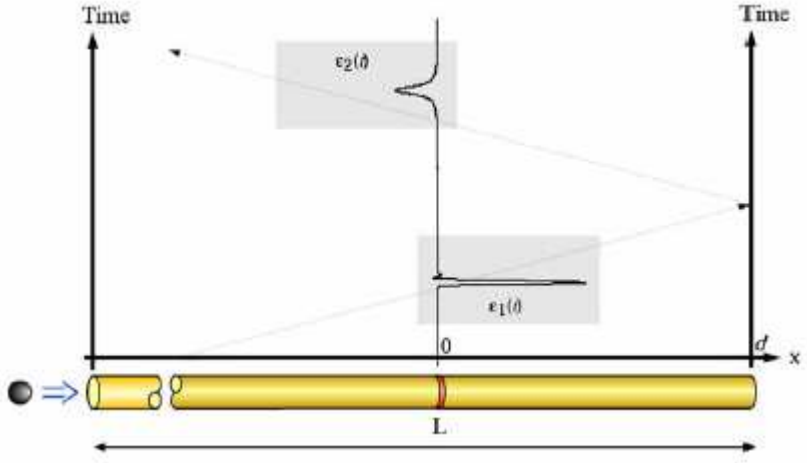

Figure 4.1 Non-overlapping incident and reflected waves generated by impact [33, 66].

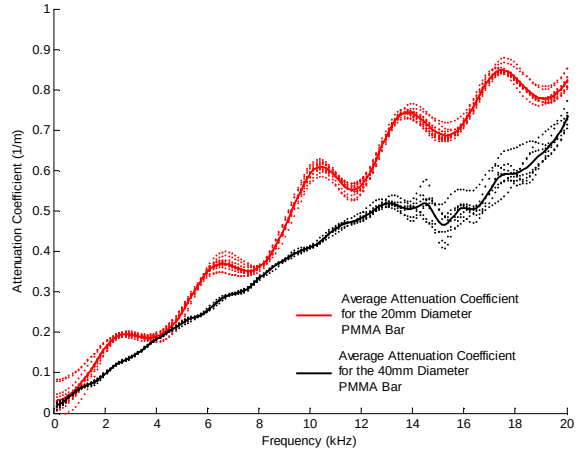

(a)

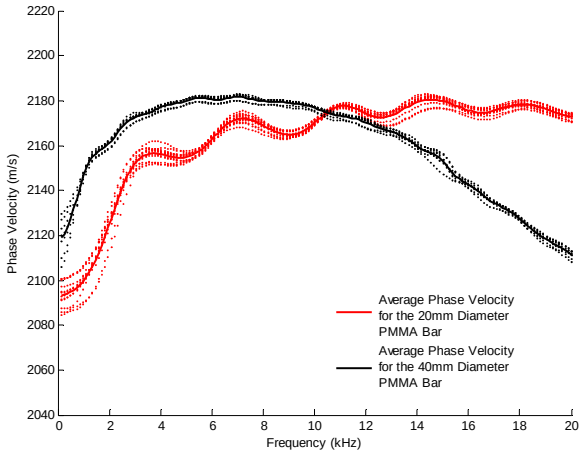

(b)

Figure 4.2 Experimental (a) Attenuation coefficient and (b) Phase velocity for the 20 mm and 40 mm diameter PMMA pressure bars.

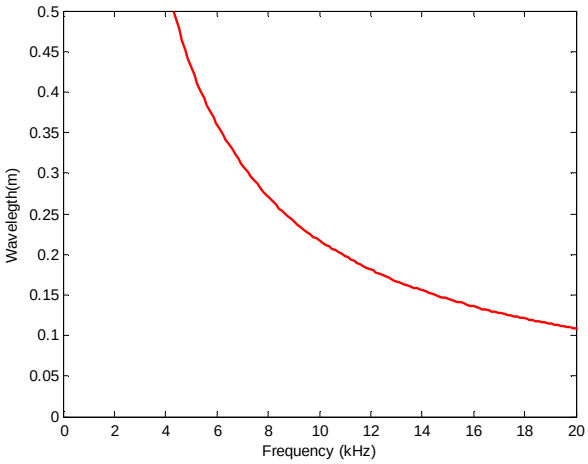

(a)

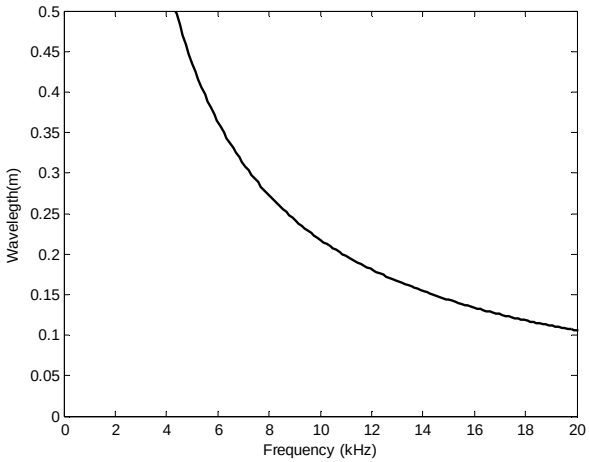

(b)

Figure 4.3 Wavelegth against frequency for the (a) 20 mm diameter and (b) 40 mm diameter PMMA bars.

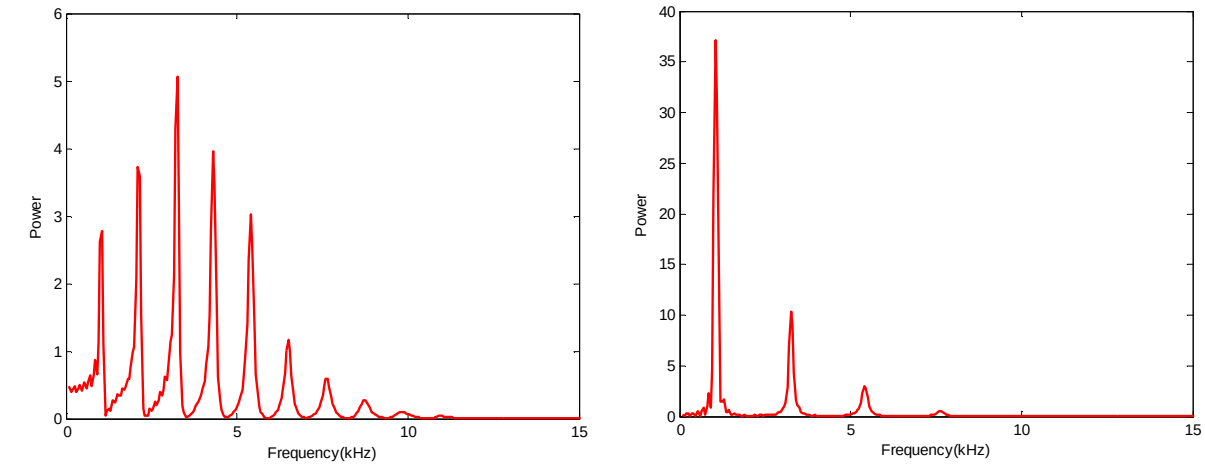

(a) (b)

Figure 4.4 Frequency spectrum of (a) the first and (b) the second strain gauge from an impact test on the 20mm diameter PMMA bar using a 95mm long PMMA projectile.

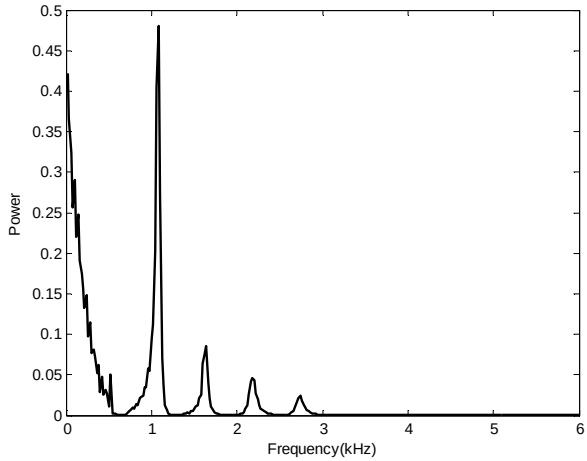

(a)

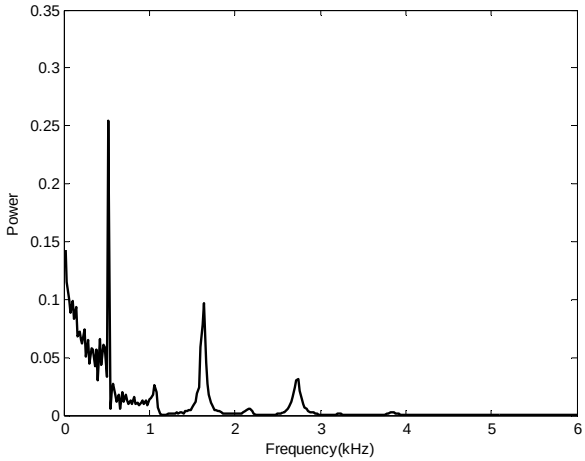

(b)

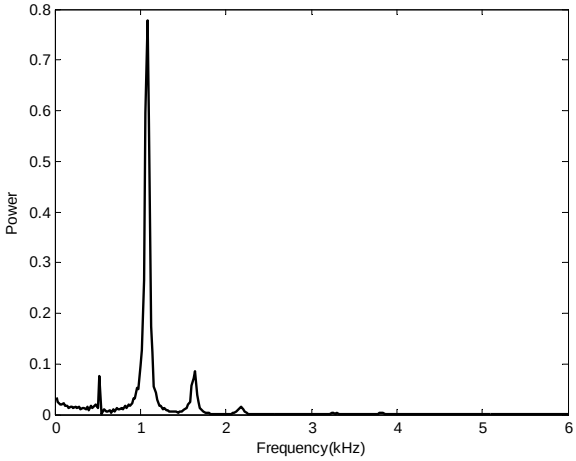

(c)

Figure 4.5 Frequency spectrum of (a) the first, (b) the second and (c) the third strain gauge used to calculate the distal end force on Rohacell foam from a direct impact test using a 35mm long projectile.

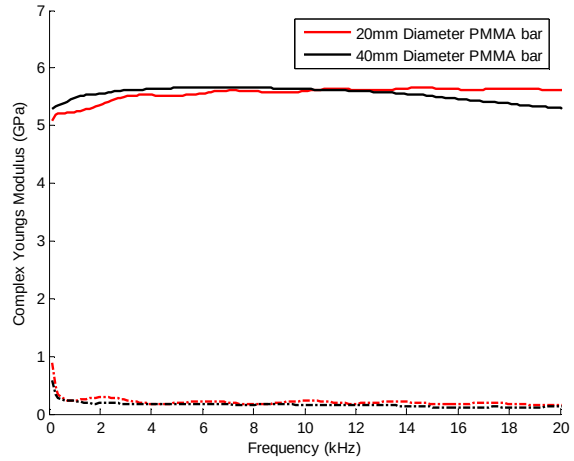

(a)

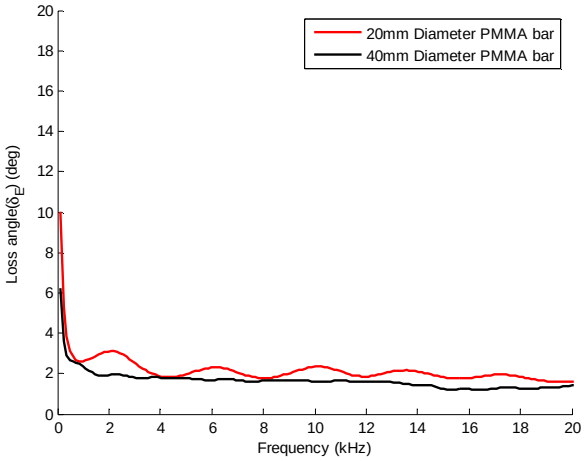

(b)

Figure 4.6 (a) Real (solid line) and imaginary (dash line) parts and (b) Loss angle of the complex Young's Modulus versus frequency for the 20 mm and 40 mm diameter PMMA bars.

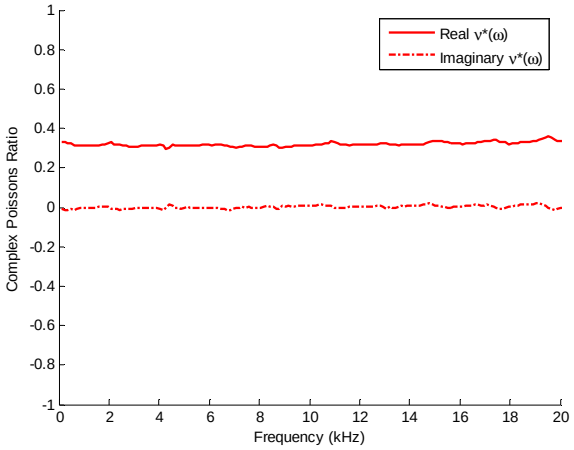

(a)

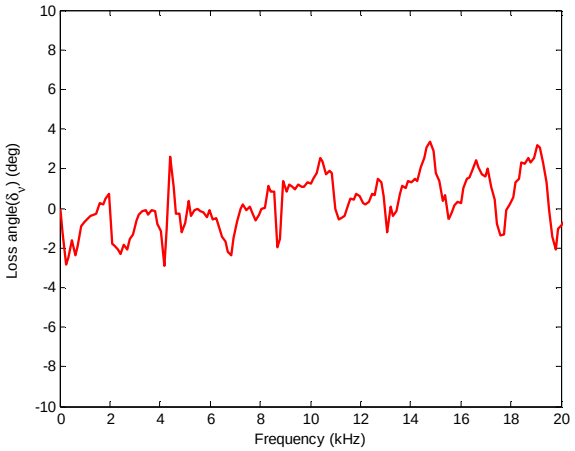

(b)

Figure 4.7 (a) Real (solid line) and imaginary (dash line) parts and (b) Loss angle of the complex Poisson's ratio versus frequency for the 20 mm diameter PMMA bar.

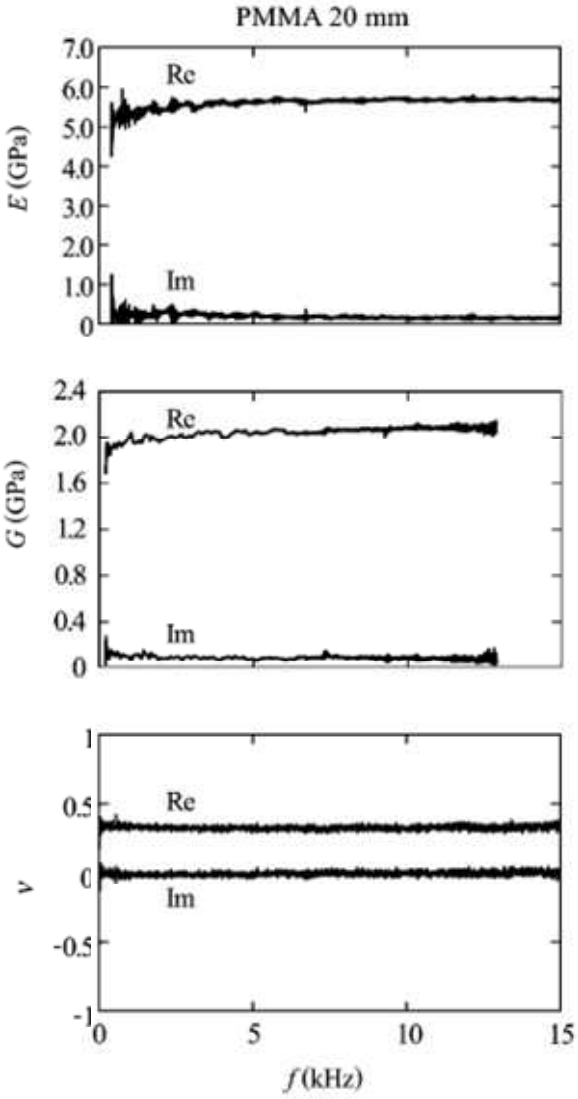

Figure 4.8 Complex Young's modulus, Complex Shear modulus and Poisson's ratio of a 20mm diameter PMMA bar from reference [62].

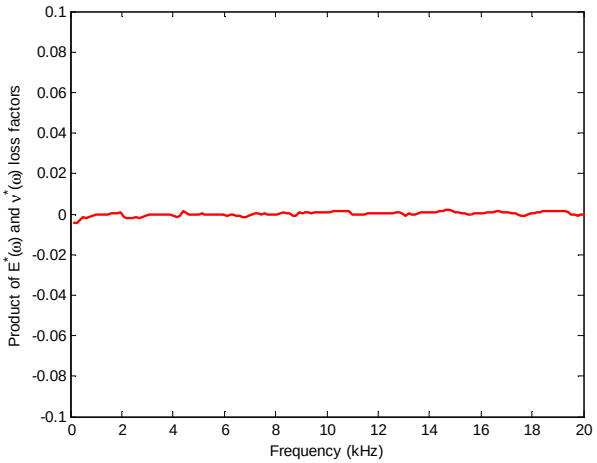

Figure 4.9 Product of the loss factors of the complex Poisson's ratio and the complex Young's Modulus for the 20mm diameter PMMA bar.

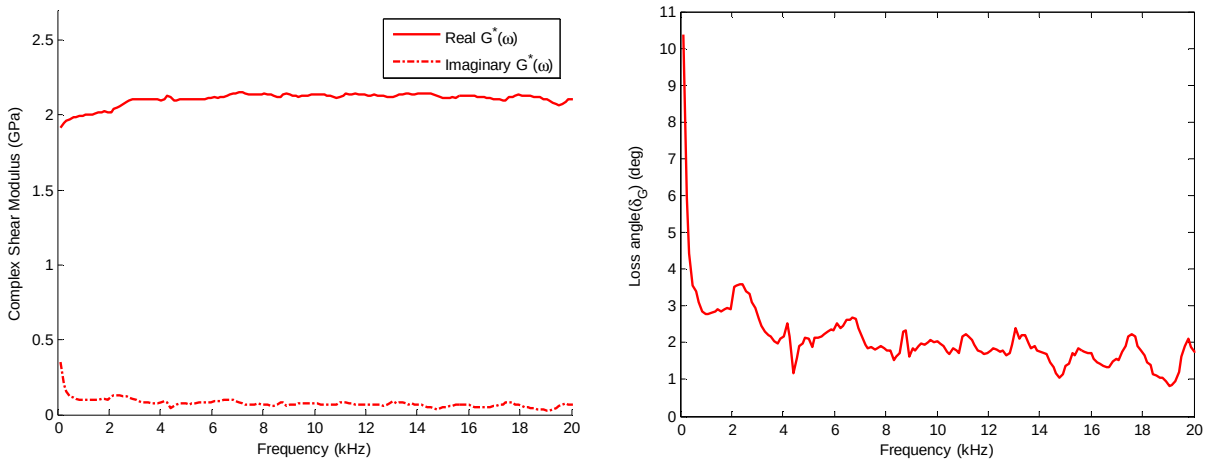

(a) (b)

Figure 4.10 (a) Real (solid line) and imaginary (dash line) parts and (b) Loss angle of the complex Shear Modulus versus frequency for the 20 mm diameter PMMA bar.

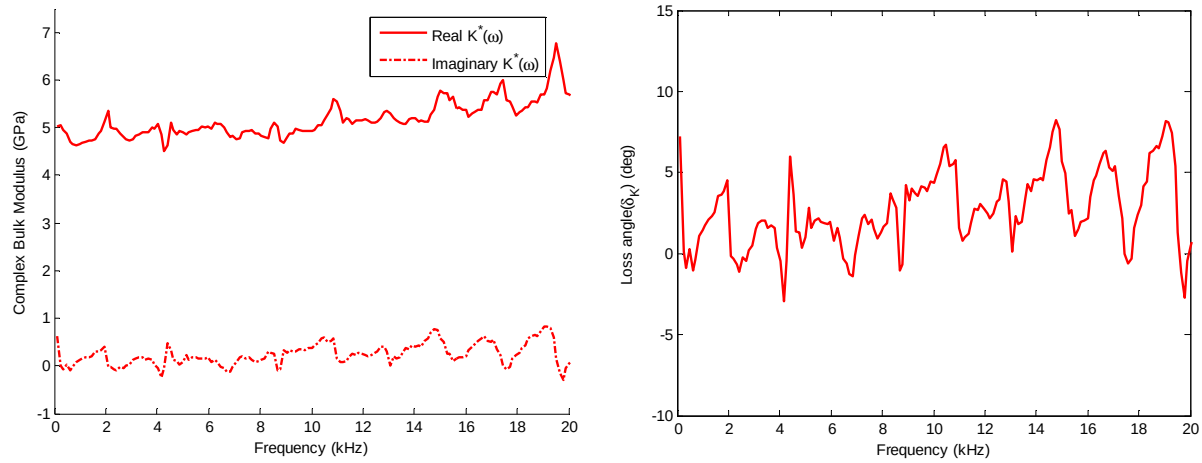

(a) (b)

Figure 4.11 (a) Real (solid line) and imaginary (dash line) parts and (b) Loss angle of the complex Bulk Modulus versus frequency for the 20 mm diameter PMMA bar.

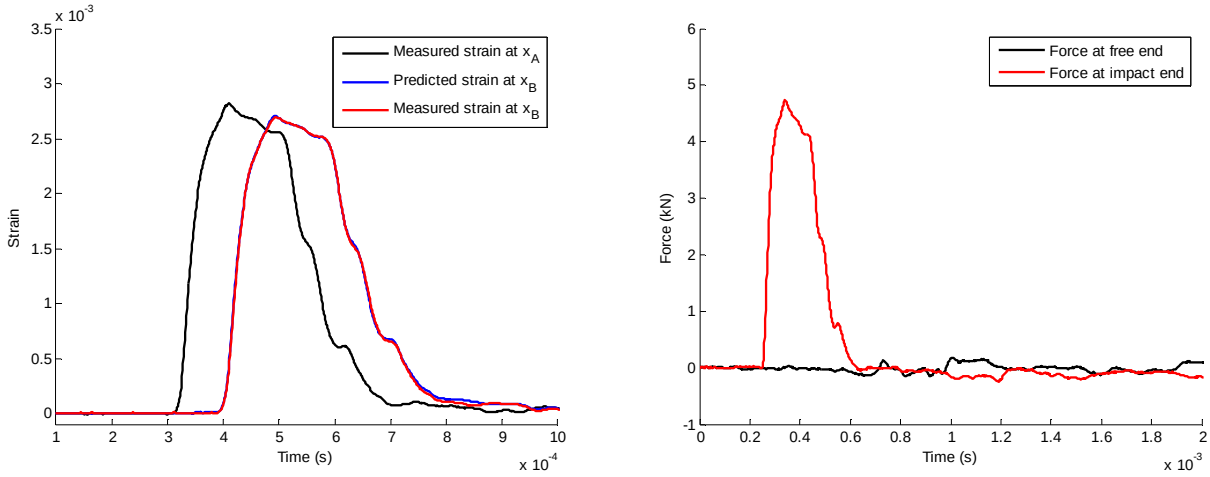

(a) (b)

Figure 4.12 (a) Measured and predicted strain (b) Forces calculated at the impact and free end using an experimentally determined propagation coefficient for the 20mm diameter PMMA bar.

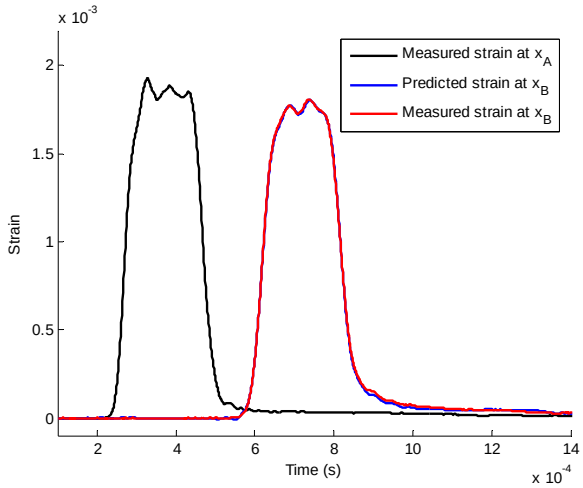

(a)

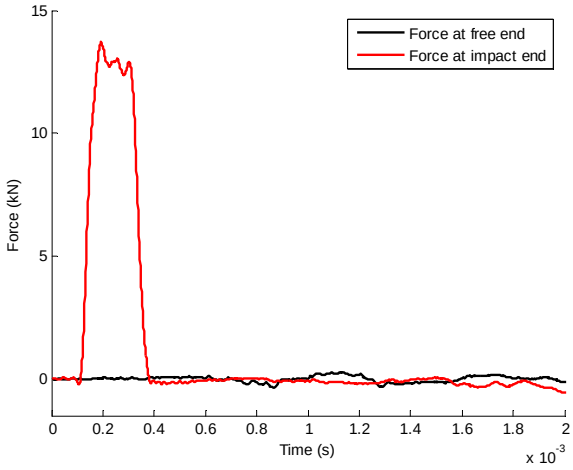

(b)

Figure 4.13 (a) Measured and predicted strain (b) Forces calculated at the impact and free end using an experimentally determined propagation coefficient for the 40mm diameter PMMA bar.

CHAPTER 5

Wave Separation Techniques

5.1 Introduction

In the conventional SHPB apparatus, the maximum strain that can be achieved in the specimens depends on the lengths of the striker bar and pressure bars, since this maximum strain depends on the length of the incident wave. Both the incident and transmitter pressure bars have one strain gauge station, in order for the incident, reflected and transmitted pulses to be captured. The position of the strain gauges is chosen so that each of the three pulses is recorded separately avoiding any overlapping with their reflections. In the case of the elastic bars an optimal position is regarded to be the midpoint of the input bar. The length of the incident pulse is twice the length of the projectile, hence the projectile length is limited to be less than half of the incident bar length. In order to avoid superposition of the stress waves at the strain gauges, there is a limitation on the period of the incident/reflected pulse (Δt),i.e. $\Delta t \leq \frac{l}{c}$, where l is the length of the input bar. Hence, there is a maximum displacement at the input bar/specimen interface and consequently a maximum specimen strain at a given strain rate [75]. It has been reported [75, 31] that in order to determine the densification strain of metallic or polymer foams, specimen strains beyond 80% may be required. This is not practical with the conventional SHPB set up, unless very long pressure bars are employed.

In order to measure to larger strains without the need for impractically long bars, wave separation is required. Both time-domain and frequency-domain wave separation are possible. The difficulties arising from frequency-domain separation are associated with the limitations of the Fourier Transform. In this chapter the background theory of the Fourier Transforms are presented and the

problems involved with its application are discussed. Then, a review of the existing wave separation techniques is given together with the advantages and disadvantages of each method. Finally, some numerical and experimental results of separated waves are shown for the case of the PMMA pressure bars.

5.2 Fourier Transforms

The dispersion and attenuation effects that are characteristic to stress waves in pressure bars can be treated in the frequency domain using the Fourier Transforms (FT) defined as:

$$\tilde{F}(\omega) = \int_{-\infty}^{+\infty} f(t) e^{-i\omega t} dt \,. \tag{5.1}$$

The inverse of the above function is

$$f(t) = \frac{1}{2\pi} \int_{-\infty}^{+\infty} \tilde{F}(\omega) e^{i\omega t} d\omega \,. \tag{5.2}$$

Experimental data is usually obtained by the use of digital electronics and computers. The recorded signals have specified values at discrete times only and they are referred to as sampled-data signals. The frequency and time domain expression for the sampled-data signals, are given by the Discrete Fourier Transform (DFT), which approximates closely the continuous Fourier Transform [76]:

$$\tilde{F}\left(n\Delta\omega\right) = \sum_{\kappa=0}^{N-1} f(\kappa\Delta t) e^{-2\pi i \kappa n/N} \,, \; n = 0,1 \ldots N-1 \,. \tag{5.3}$$

The inverse DFT is then

$$f(\kappa\Delta t) = \frac{1}{N} \sum_{n=0}^{N-1} \tilde{F}(n\Delta\omega) e^{2\pi i \kappa n/N} \,, \; \kappa = 0,1 \ldots N-1 \,, \tag{5.4}$$

where N is the number of sampling points and Δt is the time interval between two successive points. The angular frequency increment, $\Delta\omega$, is given by

$$\Delta\omega = 2\pi\Delta f = 2\pi\frac{1}{N\Delta t}, \tag{5.5}$$

where Δf is the frequency spacing.

The DFT evaluation of an N sampled signal requires the calculation of N^2 products. The efficiency of the DFT can be improved by adopting the Fast Fourier Transform (FFT) algorithm, which reduces the computation time for N samples to the order of $N\log_2 N$. It should be noted that the FFT algorithm is more efficient when the number of the sampled data (N) is an integer of power of two [76, 77, 78, 79]. The resolution of the FFT depends on the frequency spacing and can be increased by increasing either N or Δt (i.e. decreasing the frequency spacing) [78]. However, increasing of Δt is likely to cause aliasing.

5.3 Aliasing

Aliasing occurs when the time sampling interval Δt is too high (i.e. the sampling rate is too low). As a result the frequency function of the signal will overlap on itself and the higher frequency signal components will be represented wrongly as lower frequency components. In order to avoid aliasing the Shannon sampling theorem states that the time sampling interval must be:

$$\Delta t \le \frac{1}{2 f_h}, \tag{5.6}$$

where f_h is the highest frequency component present in the signal [76, 77, 78, 79].

In a typical SHPB or DI test the signals measured have negligible components above approximately 10-15 kHz [33] as illustrated in Figures 4.4, 4.5 and 6.3. All the

experiments were performed with a time increment Δt of 1 μs, which correspond to a Nyquist frequency of 500 kHz. Hence, errors due to aliasing are unlikely to be present.

5.4 Time-Domain Truncation

In SHPB tests the strain signals are recorded only for a limited period of time. When computing the FFT of these time definite non-periodic signals, errors will be introduced since the FFT assumes that the signals are periodic. As a result, the spectrum of the signal will spread at all frequencies forming a series of peaks, which are called sidelobes. This spreading of the spectrum is known as spectrum leakage [77, 78, 79, 76]. Errors due to leakage can be reduced by increasing the frequency resolution [79]. Mathematically direct truncation of the signal is equivalent to the multiplication of the signal with a rectangular window [79]. Leakage can be reduced if the measured signal is multiplied with a window function in the time domain so that the signal approaches zero smoothly at the end of the recording time and by forcing the signal to appear more periodic to the Fourier transform. There exist a number of window functions, including Hamming, Hanning and Keiser, which reduce leakage errors. However, in the case of dynamic testing exponential windows are regarded to be more efficient [80].

5.5 Exponential Window

The problem of assumed periodicity associated with performing an FFT on a non-periodic time signal can be solved effectively by the use of an exponential window. The multiplication of a time signal with an exponential window forces the signal to attenuate towards the end of the recorded time and hence makes the signal appear more periodic before application of the FFT. In fact the Fourier transform of the product of a time signal $f(t)$ with the exponential window ($e^{(-\sigma t)}$) is actually equivalent to the double-sided Laplace transform of $f(t)$ as shown below (Equation (5.7)) [79]. According to Equation (5.1) the Fourier transform of a time signal $f(t)$ multiplied by the exponential window is given as:

$$\tilde{F}(\omega) = \int_{-\infty}^{+\infty} f(t) e^{-\sigma t} e^{-i\omega t} dt = \int_{-\infty}^{+\infty} f(t) e^{-(\sigma + i\omega)t} dt, \tag{5.7}$$

where σ is a real positive constant. Defining the complex variable as $s = \sigma + i\omega$, the definition of the double-sided Laplace transform is

$$F(s) = \int_{-\infty}^{+\infty} f(t) e^{-st} dt. \tag{5.8}$$

The above equation is the Fourier transform of $f(t)e^{(-\sigma t)}$ written as a function of the complex variable s. The inverse double-sided Laplace transform can also be derived using the inverse Fourier transform. From Equation (5.2) the inverse Fourier transform of $f(t)e^{(-\sigma t)}$ is evaluated as

$$e^{-\sigma t} f(t) = \frac{1}{2\pi} \int_{-\infty}^{+\infty} \tilde{F}\left[f(t) e^{-\sigma t} \right] e^{i\omega t} d\omega. \tag{5.9}$$

Multiplying both sides of the above equation with ($e^{(\sigma t)}$) gives

$$f(t) = \frac{1}{2\pi} \int_{-\infty}^{+\infty} \tilde{F}[f(t) e^{-\sigma t}] e^{(\sigma + i\omega)t} d\omega. \tag{5.10}$$

Since $s = \sigma + i\omega$, then $ds = id\omega$, and as $\omega \to +\infty$, $s \to \sigma + i\infty$, hence

$$f(t) = \frac{1}{2\pi i} \int_{\sigma - i\infty}^{\sigma + i\infty} F(s) e^{st} ds. \tag{5.11}$$

In the case of causal systems the single-sided Laplace transform is used and has the same form of the double-sided (Equations (5.8) and (5.11)) with the difference that the limits are from *0* to ∞ in Equation (5.8) [79]. This makes no difference to the integration as $f(t) = 0$ for all $t \le 0$.

A suggestion for the correct choice of the constant σ is given as $4/N\Delta t$ [80]. There is no restriction on the choice of σ as it's optimum value varies from case to case [81]. However, two main errors should be kept to a minimum. When a very small value of the constant σ is chosen then this will result in insufficient attenuation of the signal towards the end of the time record and the free (or residual) response will fold over to the next time window. On the other hand, when the value of σ is too large the errors towards the end of the time window are magnified when computing the inverse Laplase transform. Wilcox [81] suggested as a rule of thumb a value for σ equal to $2\pi/N\Delta t$, which gives almost always satisfactory results as will be shown in the following sections. It should be pointed out that the exponential window should always start at time *t=0* independent of the pretriggering time that has been used [80].

5.6 Wave Separation Techniques

In order to increase the maximum measurable duration in a SHPB test, wave separation methods have been developed which are mainly categorised into two groups: The two-point method and the one-point method. The two-point method developed by Lundberg and Henchoz [82] separates the forward and backward moving waves in the time domain using strain signals from two different locations on the bar. Similarly, Yanagihara [83] independently proposed the two-point method using a similar numerical method as the one given by Lundberg and Henchoz [82] to measure impact forces. The one-point method proposed by Park and Zhou [84] replaced the second strain measurement by the condition of the zero strain at the free end. However, the one-point method only extends the test duration by a factor of two compared with the conventional SHPB duration [85]. One dimensional wave propagation in elastic bars was assumed for both of these methods, i.e. both dispersion and attenuation effects were assumed negligible.

Zhao and Gary [75] proposed a new method for separating waves propagating in opposite directions, which utilises the two-point measurement technique. The method takes into account both dispersion and attenuation effects and can be applied to both elastic and viscoelastic bars. With this technique wave shifting is performed

in the frequency domain and subsequently all the calculations regarding the separation of waves at a strain gauge location are then performed in the time domain. The authors [75] used a pressure bar with two strain gauges cemented at two different locations (e.g. SG2 ($x_B = d_1$) and SG3 ($x_C = d_2$) in Figure 5.1), in order to record the strain histories at these points. Both strain measurements were divided into equal time intervals Δt_{BC} , which is twice the time needed for waves to travel the distance between the two gauges. The first measured incident wave from the first strain gauge (SG2 ($x_B = d_1$), see Figure 5.1) is contained in the first time interval. Then the magnitude of the first incident wave at position $x_C = d_2$ (Figure 5.1) is predicted by time shifting the measured strain from point $x_B = d_1$ (Figure 5.1) using a Fourier transform. Since the strain at every cross section of the bar is equal to the sum of the stains due to both incident and reflected waves, the reflected wave at point $x_C = d_2$ (Figure 5.1) can be calculated.

The above method leads to the evaluation of all waves propagating in both directions for all the time intervals by means of an iterative process. This method allows tests to be performed on a SHPB with increased observation time. In order to obtain more accurate results, dispersion effects were taken into account using the generalised Pochhammer-Chree wave equation [26]. This technique was used for both elastic and viscoelastic SHPB arrangements for the determination of the dynamic behaviour of several materials including metallic tubes, polymeric foams [75] and aluminium honeycombs [31]. It was shown that the measured duration can be increased by a factor of 100 compared with the conventional SHPB set up [75] due to repeated loading of the specimen.

The method proposed above can be applied only if the first incident wave is fully measured before the reflected wave has reached the first strain gauge. Hence, the duration of the incident wave is limited. This is important especially in cases where a viscoelastic projectile is used, since as it has been reported the duration of the incident pulse is extended compared with the duration produced when using an elastic projectile [27]. Furthermore, the time intervals Δt_{BC} are approximate, since they are calculated without taking into account dispersion effects.

Zhao and Gary [75] first discussed the possibility of wave separation in the frequency domain and stated the problems involved when adopting this approach. The forward wave at position x_A in the frequency domain is given by:

$$\tilde{P}(\omega) = \frac{\tilde{\varepsilon}_A(\omega) - \tilde{\varepsilon}_B(\omega) e^{-\gamma(\omega)(x_B - x_A)}}{e^{-\gamma(\omega)x_A} - e^{-\gamma(\omega)(2x_B - x_A)}}. \quad (5.12)$$

This equation cannot be defined when the denominator is zero, which occurs at certain frequencies for both elastic and viscoelastic bars, as discussed in Section 2.7. Also, errors are caused when the recorded strain signals do not attenuate completely at the end of the test duration due to the finite time limits of the integration involved when performing a Fourier transform [75, 74, 86, 87]. To overcome this different testing procedures [86, 87, 88, 89, 90] and different approaches to solving Equation (5.12) have been proposed [85, 74, 86].

Bacon extended the two-point method for separating waves for both elastic and viscoelastic bars, where dispersion and attenuation effects are encountered [74]. The proposed technique involved an iterative calculation in the time domain when Equation (5.12) was not defined or could not be used i.e. when the strain signals were truncated. Details of this approach are provided in Section 2.7.

The separation of waves in large diameter elastic bars was investigated by Zhao and Lok [85]. Dispersion effects were taken into account by solving numerically the Pochhammer-Chree frequency equation. For frequencies ($\omega = \omega_0$) where Equation (5.12) could not be defined, Equation (5.12) becomes an undefined fraction of type 0/0 and was calculated using L'Hospital's rule. Outside these frequencies Equation (5.12) was used directly to determine the forward moving wave. The problem is that the application of L'Hospital's rule involves the determination of the spectral derivatives of the measured strain signals and the wave number. In particular, the calculation of the wave number's derivative was considered rather complex as pointed out by the authors [85]. Furthermore, it is not clear if problems due to truncation of the signals are overcome with this method. Also, the case of viscoelastic pressure bars, where waves attenuate and disperse, was not examined.

However, the method was validated both numerically and experimentally for 75 mm diameter steel SHPB.

A modified SHPB set-up was introduced by Meng and Li [90] where an iterative algorithm was performed in the time domain to separate the overlapping waves using measurements from two strain gauges. Based on the fact that the dispersion and attenuation effects become important only if the wave travels over a considerable length of the bar, two strain gauges having a small distance between them were placed near the bar/specimen interface. Therefore, both effects could be disregarded. A detailed finite element analysis revealed that a minimum distance of *1.5D* (where *D* is the bar diameter) ensures a uniform strain state on the cross-section of the elastic bar. Hence, a reduction in the time shift of the waves was introduced and the shape of the pulses was considered unchanged. The accuracy of the method was confirmed using both numerical and experimental examples. However, an error analysis needed to be employed in order to improve the accuracy of the results. Also, although the presented method has the advantage of minimising the time shift and the dispersion and attenuation effects in elastic bars, further investigation is needed before the technique can be employed for viscoelastic SHPB arrangements.

Velocity measurements have been utilised by many researchers when separating waves in SHPB set-ups [86, 88]. The main advantage is that the use of direct velocity measurements minimises errors due to noise, which are important when using strain signals [75, 86, 89, 87]. Casem et al. [88] proposed a method to separate overlapping waves and could be applied to both elastic and viscoelastic bars where dispersion and attenuation effects are important. A strain gauge is employed together with an electromagnetic velocity gauge to measure both the axial strain and velocity at a single point. The forward and backward waves were separated in the frequency domain by solving a system of two simultaneous equations. It was suggested that by this method unlimited test duration is achieved and there is no restriction for the position of the gauge stations. The accuracy of the technique was validated by evaluating the stress at the impact and free ends of a 19.1 mm diameter polycarbonate bar from an impact test of the bar with an aluminium projectile. Additionally, SHPB tests on foams at strain rates of approximately 280 to 1200 s^{-1} were performed. However, a more careful examination of this technique suggests

that the signals have to attenuate completely in order to avoid truncation errors. Also, questions arise in whether the magnetic field induced by the velocity gauges will affect the operation of the strain gauges. Lastly limitations exist when using velocity gauges on magnetic materials.

A detailed work on the factors that influence the accuracy of the separated strain signals has been performed by Bussac et al. [86]. It was suggested that when using the two-point method in the frequency domain, the presence of noise in the measured strain signals, the imprecise knowledge of the amplifier gain, the inaccurate measurements of the strain gauge positions and the incorrect null strain, will introduce errors when calculating forces and displacements at any cross-section of the bar. Using the Maximum Likelihood Principle both the forward and backward waves were expressed as functions of the strain signals and the bar dispersion relation. It was concluded that only a set-up consisting of three strain gauges and two velocity stations will be able to minimise any source of errors. Although, this solution is optimal regarding the elimination of errors, the mathematics involved are rather complex as pointed out by other researchers [87]. Furthermore, the fact that each pressure bar in a SHPB set-up requires to be implemented with five different measuring stations makes this technique rather expensive.

5.7 Wave separation in the time and frequency domain

Consider a linear viscoelastic bar that is impacted at its left hand side (see Figure 5. 1). The resulting stress waves that are generated in the bar are recorded by *N* stain gauge stations as shown in Figure 5.1. Viscoelastic wave propagation is characterised by both attenuation and dispersion. In Chapter 4, both effects were taken into account by calculating the experimental wave propagation coefficient, $\gamma(\omega)$ (Equation (2.5)). Recalling Equation (4.10), the Fourier transform (FT) of the longitudinal strain at any cross section x, $\tilde{\varepsilon}(x,\omega)$,on the bar is

$$\tilde{\varepsilon}(x,\omega) = \tilde{P}(\omega)e^{-\gamma(\omega)x} + \tilde{N}(\omega)e^{\gamma(\omega)x}. \qquad (5.13)$$

Then the Fourier Transforms of the axial strains at positions $x_A, x_B \cdots x_N$ with $x_A < x_B < \cdots < x_N$ as shown in Figure 5.1 can be expressed as follows:

$$\begin{bmatrix} \tilde{\varepsilon}_A(\omega) \\ \tilde{\varepsilon}_B(\omega) \\ \vdots \\ \tilde{\varepsilon}_N(\omega) \end{bmatrix} = \begin{bmatrix} e^{-\gamma(\omega)x_A} & e^{\gamma(\omega)x_A} \\ e^{-\gamma(\omega)x_B} & e^{\gamma(\omega)x_B} \\ \vdots & \vdots \\ e^{-\gamma(\omega)x_N} & e^{\gamma(\omega)x_N} \end{bmatrix} \begin{bmatrix} \tilde{P}(\omega) \\ \tilde{N}(\omega) \end{bmatrix}, \tag{5.14}$$

$$\text{or } \tilde{\varepsilon}(\omega) = A(\omega)\tilde{X}(\omega), \tag{5.15}$$

where the matrix A is defined as the coefficient matrix and X is the matrix containing the unknown forward and backward waves.

It is clear that the number of the measured strains should be greater than or equal to two, in order to determine the forward and backward moving waves at position x_A. For the case where only two strain gauges are used (e.g. *S.G.1* and *S.G.2* (Figure 5.1)) the Fourier Transform of the forward wave at $x_A = 0$ can be found from Equation (5.12) as:

$$\tilde{P}(\omega) = \frac{\tilde{\varepsilon}_A(\omega) - \tilde{\varepsilon}_B(\omega)e^{-\gamma(\omega)d_1}}{1 - e^{-2\gamma(\omega)d_1}}. \tag{5.16}$$

Since the longitudinal strain at any cross section on the bar equals to the sum of the forward and backward waves, the backward moving wave is determined in the time domain as:

$$N(t) = \varepsilon_A(t) - P(t). \tag{5.17}$$

As already mentioned Equation (5.16) cannot be defined when the denominator is zero. This occurs when the wave propagation is equal to $\gamma(\omega) = \frac{in\pi}{d}$, where *n* is an integer and *d* is the distance between the two strain gauges. In the case of elastic

bars, where the attenuation coefficient can be assumed to be zero, this occurs at frequencies such that $f_0 = \frac{nc(\omega)}{2d}$. Therefore, the limitation of using Equations (5.12) or (5.16) is directly related to the position of the strain gauges [74, 86, 88, 89, 87, 75,85]. In the case of viscoelastic bars, Equation (5.16) is defined at all frequencies except at zero frequency where $\gamma(0) = 0$. It should be noted that if the strain signals do not contain any noise, then at frequencies where Equation (5.16) cannot be calculated, the FT of the forward moving wave ($\tilde{P}(\omega)$) can be determined by continuity [87]. Unfortunately, in real tests strain signals are always affected by noise. Furthermore, for both elastic and viscoelastic bars the wave separation in the frequency domain cannot be performed if the strain recordings do not attenuate completely by the end of the test duration.

Errors due to the truncation of signals and problems related to critical frequencies can be overcome, for both elastic and viscoelastic bars, by performing the wave separation in the frequency domain with the application of a suitable exponential window and utilising more that two strain gauge stations. From Equation (5.14) it can be seen that this would lead to an over-determined system of equations whose solution can be evaluated using the least squares method. The least squares method provides some redundancy by utilising extra measurements taken at extra locations so as to reduce any errors involved (e.g. noise) and hence improve the accuracy of the identified forward and backward moving waves. The approximate solution of X (Equation (5.15)) given by the least squares method, is the one that minimises the error: $\|r\|_2 = \|\varepsilon - AX\|_2$. If the columns of the coefficient matrix A are linearly independent then the solution X can be determined as:

$$X = A^{+}\varepsilon = \left[A^H A\right]^{-1} A^H \varepsilon , \qquad (5.18)$$

where A^{+} is the pseudoinverse of the matrix A and A^H is the hermitian i.e. complex conjugate and transpose of A.

By multiplying the time signals by an exponential window, the propagation coefficient ($\gamma(\omega)$), has to be defined in the complex domain, i.e. $\gamma(\omega - i\sigma)$. The determination of $\gamma(\omega)$ was performed by use of an experimentally determined transfer function, defined as the negative ratio of the FFT of the backward to forward wave from a single strain recording (see Equation (4.13)). The application of an exponential window to both forward and backward waves will result in a transfer function in the Laplace domain [80]. Hence, by using the same exponential window for $\gamma(\omega)$ as the one that is going to be used for the determination of the forward moving wave, all components of Equation (5.15) are defined as a function of $(\omega - i\sigma)$. Therefore the linear independence of the matrix *A* is guaranteed and the approximate solution of the X can be defined by Equation (5.18). Even for the case of purely elastic materials the use of the exponential window ensures some artificial attenuation in all strain histories so that the denominator of Equation (5.16) is non zero.

The use of the exponential window for wave separation was first suggested by Bussac et al. [86]. However, a theoretical propagation coefficient was used that was determined using the generalised Pochhammer-Chree equation for viscoelastic bars [26]. Although, Bussac et al. [86] argued that the imprecise knowledge of the dispersion relation will lead to significant errors, approximations were made for the bar's material properties when calculating the propagation coefficient. Furthermore, despite the fact that the experimentally determined propagation coefficient used herein is valid for a lower frequency range (approximately up to 20 kHz) than the one derived by Bussac et al. [86] it is determined under dynamic conditions that are representative of the real SHPB tests.

Errors due to the truncation of signals and problems related to critical frequencies (f_0) can be overcome, for both elastic and viscoelastic bars, by performing the wave separation in the time domain [74]. Bacon [74] introduced an iterative algorithm, which treats the whole spectrum of the forward moving wave, $P_{\omega_0}(t)$, in the time domain using Equation (5.19):

$$P_{\omega_0}(t) = \varepsilon_A(t) - \varepsilon_B\left(t - \frac{d}{c(\omega_0)}\right)e^{-\alpha(\omega_0)d} + P_{\omega_0}\left(t - \frac{2d}{c(\omega_0)}\right)e^{-2\alpha(\omega_0)d}. \qquad (5.19)$$

One essential condition of the above iteration process is that both strain signals $\varepsilon_A(t)$ and $\varepsilon_B(t)$ are causal. This is true for all SHPB tests, since no strain measurements can exist before the instant of the impact (i.e. $\varepsilon_A(t) = \varepsilon_B(t) = 0$ for $t<0$). Equation (5.19) is extremely computationally expensive since the calculation has to be carried out at all times and for all frequency components. In contrast to the method that was proposed by Zhao and Gary [75], the above process does not depend on the duration of the incident loading pulse. Moreover, both the attenuation and dispersion effects are taken into account. Its main disadvantage is that it requires extensive computation time, a fact that makes this method impractical.

5.8 Wave Separation results

5.8.1 Numerical Example

The wave separation was first performed in the time domain according to Equation (5.19). In order to check the accuracy of the algorithm, it was first applied to a numerical example. A hypothetical elastic bar was assumed whose length was 1 m and had a constant phase velocity of 5000 m/s. The distance between the two strain gauges was 0.25 m and it was assumed that the stress waves propagate without changing their shapes (i.e. dispersion effects were negligible). Figure 5.2 (a) shows the numerically generated strains at the first ($x_A = 0$ m) and second strain gauges ($x_B = 0.25$ m). The forward and backward waves which were obtained from the wave separation in the time domain (Equation 5.19) are shown in Figure 5.2 (b). The black lines indicate the incident and reflected waves that were used in order to generate strain measurement at the first strain gauge. It should be noted that they have been shifted upwards and downwards to make the figure more readable. The good agreement between the forward and backward moving waves with the

numerically generated incident and reflected waves indicates that the algorithm can be used with confidence.

5.8.2 Experimental Example

In order to compare the accuracy of the wave separation in the time and frequency domain, both methods were applied to two different experiments. The 20 mm diameter PMMA input pressure bar (Table 3.2) was impacted with a 410 mm long projectile at an impact velocity of 10 m/s. The 40 mm diameter PMMA pressure bar (Table 3.2) was impacted with a 200 mm long projectile at an impact velocity of 17 m/s. For both cases the projectiles were made of PMMA and had a diameter of 20 mm. The separated waves that were obtained using wave separation in the time (Equation (5.19)) and frequency (Equation (5.18)) domains are illustrated in Figures 5.3 and 5.4 for the two PMMA bars. For clarity, the results obtained are shown in Figures 5.3 and 5.4 together with only the strain measurements from the first strain gauges on each bar.

Due to the fact that the first strain gauge is positioned close to the impact end (Table 3.2) the measurement taken at this station involves the full length of the first forward moving wave. This can be used to verify the accuracy of the time and frequency domain wave separation techniques for both PMMA bars. In Figures 5.3 and 5.4 the black and blue lines (i.e. the measured and predicted strains) are overlapping until the first backward wave arrives. This is true for both the time and frequency domain wave separation, thus verifying the accuracy of both techniques. However, the frequency domain wave separation appears more accurate as time increases. The predictions are smoother and follow the expected pattern for waves that should attenuate with time. The background oscillations in the predictions are fewer and of lower amplitude for the frequency domain wave separation. Bacon [74] suggested that the wave separation executed in the time domain would overcome the problems arising due signal truncation. Nevertheless, since the propagation coefficient is frequency dependent, Equation (5.19) is carried out for every frequency in the signal. Therefore, in order to determine the forward moving wave an FFT of Equation (5.19) still has to be performed and hence problems with signal truncation still exist.

To obtain the results in Figures 5.3 (a) and 5.4 (a), an exponential window was applied with a value of σ equal to $2\pi / N\Delta t$ to minimise these errors. In addition, the computation time that is required so as to perform the wave separation in the time domain is much longer than the one needed for the wave separation in the frequency domain. The frequency domain method is therefore preferable both in terms of accuracy and in terms of efficiency.

The accuracy of the wave separation method in the frequency domain was checked by evaluating the forces and the particle velocities at the free and impact ends of the 20 mm and 40 mm diameter PMMA pressure bars. The force and the velocity at any point *x* are given by the following equations:

$$\tilde{F}(\omega) = \frac{-\rho A \omega^2}{\gamma(\omega)^2} (\tilde{P}(\omega) e^{-\gamma(\omega)x} + \tilde{N}(\omega) e^{\gamma(\omega)x}) ; \qquad (5.20$$

$$\tilde{V}(\omega) = \frac{i\omega}{\gamma(\omega)} (\tilde{P}(\omega) e^{-\gamma(\omega)x} - \tilde{N}(\omega) e^{\gamma(\omega)x}) , \qquad (5.21)$$

where $\tilde{F}(\omega)$ and $\tilde{V}(\omega)$ are the Fourier Transforms of the force and the particle velocity respectively, ρ is the density of the bar material and A is the diameter of the pressure bar. It should be pointed out that the same exponential window that was applied for the wave separation in the frequency domain was used for the evaluation of both the force and particle velocity. The use of this window is implied in all future frequency domain calculations.

The magnitudes of the forces and particle velocities at both ends of the bars (Figures 5.5 and 5.6) were calculated using the forward and backward waves plotted in Figure 5.3 (b) and 5.4 (b). For each bar, the force at the free end is close to zero, while the velocity at the free end is almost double that at the impact end. This validates the accuracy of the wave separation in the frequency domain as described previously. From the forces plotted in Figures 5.5(a) and 5.6(a), the absolute errors are of the order of 3.9% and 1.9% for the 20 mm and 40 mm diameter bars respectively.

The accuracy of both the propagation coefficient and the wave separation technique in the frequency domain was validated for both the 20mm diameter PMMA pressure bars (i.e. incident and transmitter bar) with an impact test. The two bars were placed in contact having no specimen between them and the forces and displacements were calculated at the interface, from the strain measurements taken from both bars. The bars were impacted with a 410 mm long projectile at an impact velocity of 14 m/s. From Figure 5.7 it can be observed that the calculated forces and displacements are in excellent agreement for both contact faces of the pressure bars. This demonstrates the ability of the method to calculate forces and displacements at the interfaces of a specimen in the case of a SHPB test.

5.9 Conclusion

Wave separation techniques were presented which can be applied to either elastic or viscoelastic pressure bars. The majority of these methods utilise two strain measurements and the wave separation is performed in the time or frequency domain. Performing the wave separation in the frequency domain using two strain signals involves difficulties associated with truncation of the signals and critical frequencies. On the other hand, the main disadvantage of the wave separation in the time domain is the fact that it requires long computational times. A method that is computationally efficient and avoids problems associated with truncation of the measured signals and critical frequencies is the use of more than two strain measurements and the application of a suitable exponential window. The method was applied successfully to both 20 mm and 40 mm diameter PMMA pressure bars.

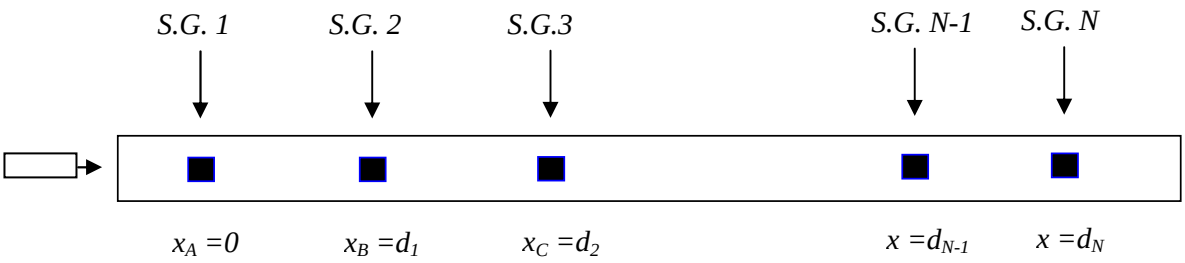

Figure 5.1 Pressure bar implemented with N strain gauges (S.G.).

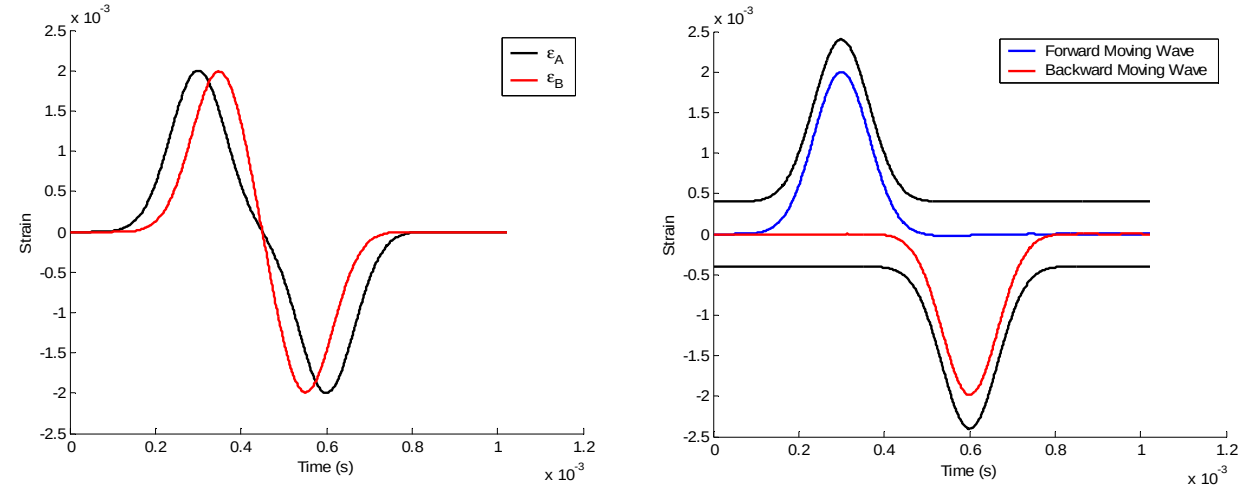

(a) (b)

Figure 5.2 (a) Numerical strains at x_A and x_B (b) Forward and backward moving waves obtained from wave separation in the time domain at position x_A=0.

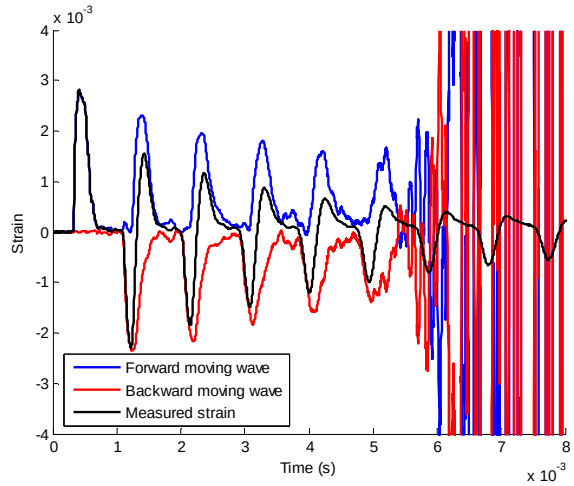

(a)

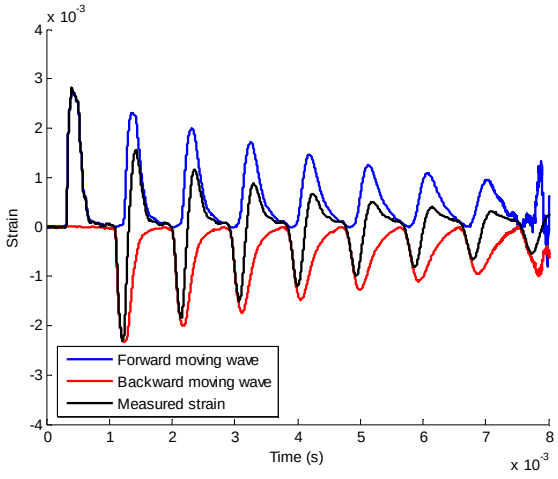

(b)

Figure 5.3 Waves separated in (a) time and (b) frequency domain for the case of the 20 mm diameter PMMA Pressure Bars.

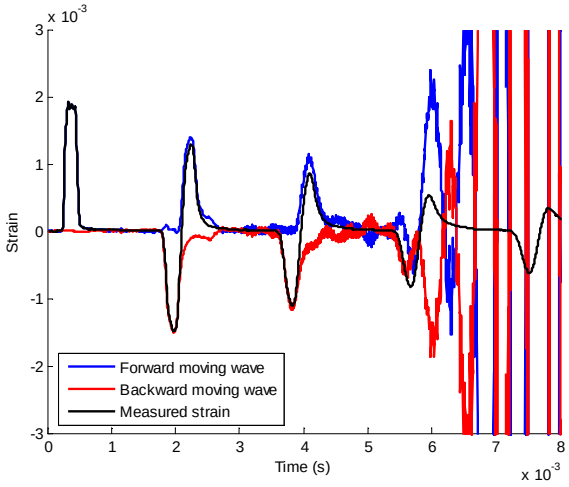

(a)

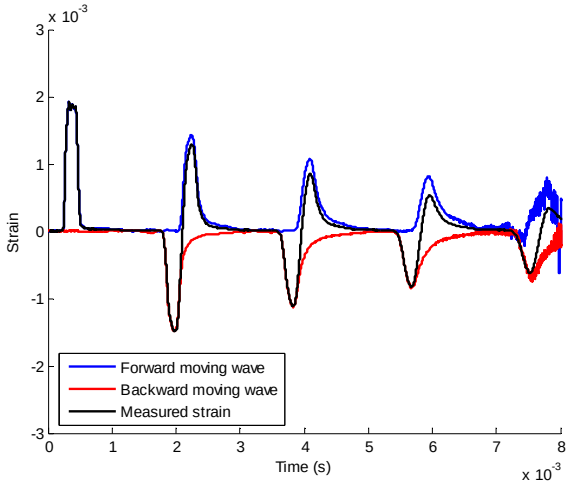

(b)

Figure 5.4 Waves separated in (a) time and (b) frequency domain for the case of the 40 mm diameter PMMA Pressure Bars.

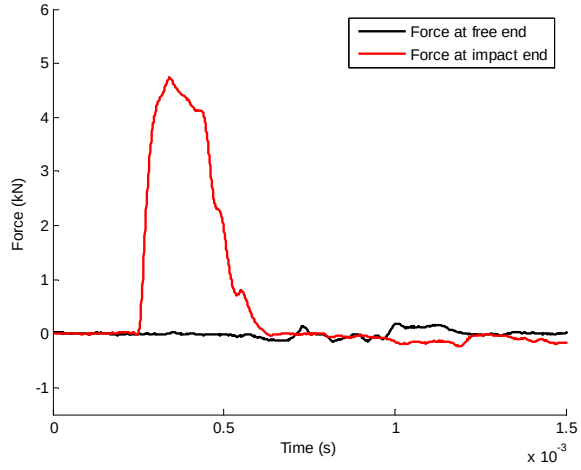

(a)

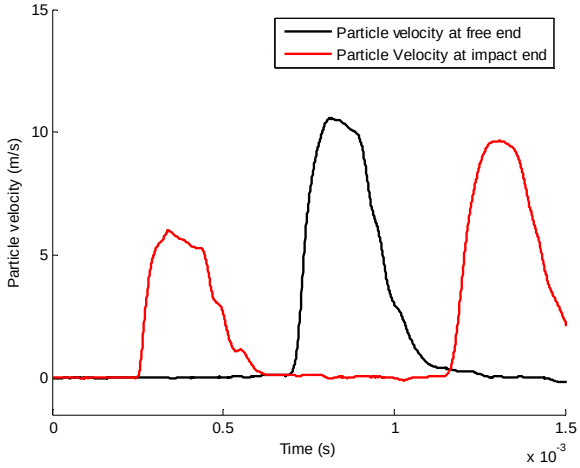

(b)

Figure 5.5 (a) Forces and (b) Particle velocities calculated at the impact and free ends using the wave separation in the frequency domain for the 20 mm diameter PMMA bar.

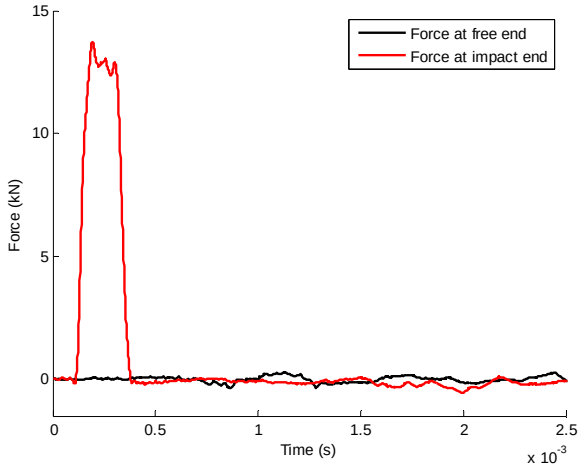

(a)

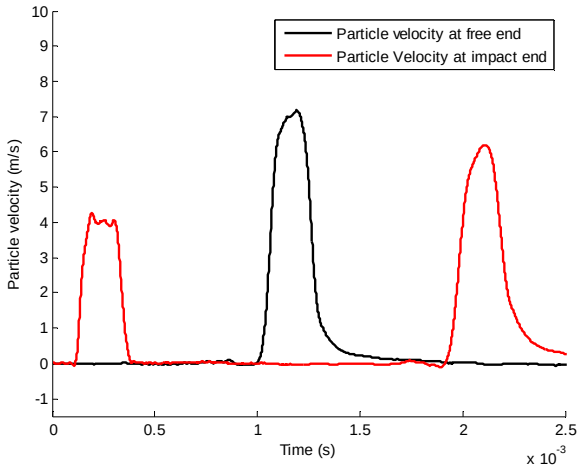

(b)

Figure 5.6 (a) Forces and (b) Particle velocities calculated at the impact and free ends using the wave separation in the frequency domain for the 40 mm diameter PMMA bar.

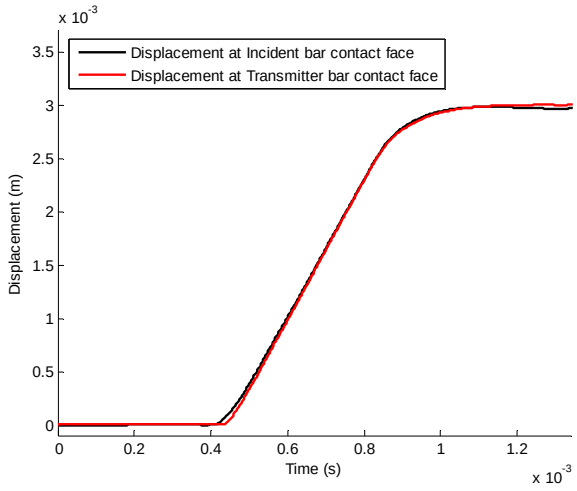

(a)

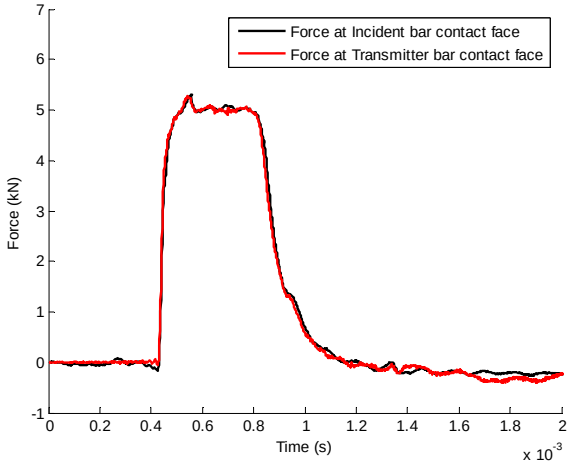

(b)

Figure 5.7 Contact (a) Displacements and (b) Forces calculated from strain measurements for the incident and transmitter 20mm diameter PMMA pressure bars.

CHAPTER 6

Wave Propagation in Magnesium Alloy Pressure Bars

6.1 Introduction

Lower impedance elastic pressure bars such as Titanium and Magnesium alloys are often employed in SHPB arrangements [15, 16, 17, 18]. Waves propagating in elastic media disperse due to the lateral motion in the bars. Furthermore, as will be shown in the following sections, a very small amount of damping can be observed. The accuracy of the stress-strain curve that is obtained from a SHPB test is improved by considering these effects.

In this chapter the method and results from the "calibration" of the Magnesium pressure bars will be presented and validated. Furthermore, results of the wave separation in the frequency and time domains are shown for the case of the Magnesium pressure bars.

6.2 Accuracy of the strain gauge stations

The first step for the "calibration" of the Magnesium pressure bars involves a check of the accuracy of the strain gauges and the measuring units such as the amplifiers that were later used in SHPB tests. This first "calibration" was performed by compressing both bars at a crosshead rate of 0.5 mm/min using an INSTRON machine (model 4507) and taking recordings of the load against the output voltage from all strain gauge stations. In order to avoid any overloading of the bars, the buckling load (P_B) was determined to be 6.2 kN using Equation (6.1).

$$P_B = \frac{\pi^2 EI}{l^2}, \qquad (6.1)$$

where I is the second moment of area of the bar defined as: $I = \frac{\pi d^4}{64}$ and l and d are the length and the diameter of the pressure bars respectively.

The output voltage (V_{out}) from the strain gauges is directly proportional to the applied force, i.e.

$$V_{out} = C \cdot Force, \tag{6.2}$$

where C is a constant. This constant was determined from the gradient of the plots of the load against the output voltage. The results obtained from four tests on both input and output pressure bars are shown in Table 6.1.

Rearranging Equation (3.1) one can obtain the analytical constant C as:

$$C = \frac{V_{out}}{Force} = \frac{S_G G V_{in}}{2AE} \quad . \tag{6.3}$$

From Equation (6.3) the analytical value of the constant *C* was calculated to be 0.143744 V/kN. Comparing this value with the average values of the constant *C* obtained from the static calibration (Table 6.1) the maximum difference is of the order of 0.24% which suggests the experimental values are of good accuracy. Experimentally derived values were used to convert from voltage readings to axial strains.

6.3 Dispersion correction for the Magnesium Pressure Bars

One of the assumptions often made when analysing SHPB data is that stress waves propagating in elastic cylindrical bars obey the one dimensional stress wave theory. However, as discussed in Chapter 4, during impact tests the generated waves often contain high frequency components for which the wavelength is of the order of the bar's diameter. In these cases geometric dispersion should be taken into account.

Pochhammer [91] and Chree [92] were the first to develop a dispersion relationship for the propagation of waves in cylindrical bars, often referred to us as Pochhammer-Chree equation. Numerical solutions of the Pochhammer-Chree equation have been presented by various authors including Bancroft [93], who presented numerical data for the first mode of vibration for different values of Poisson's ratio. In 1948 Davies [58] evaluated results for higher modes of vibration using a Poisson's ratio of 0.29. Using the numerical results of the Pochhammer-Chree equation appropriate phase shifts can be applied to frequency components of the measured strain signals in order to correct for dispersion [56, 94, 95, 96]. However, these methods give satisfactory results only for small amounts of dispersion [95, 48].

In this study the dispersion effects were taken into account by determining an experimental propagation coefficient following the same procedure as in the case of the PMMA pressure bars (see Section 4.3.1). The method for determining the experimental propagation coefficient requires that no overlapping of the waves occurs at the position where the strain measurements are taken. For this reason the input Magnesium pressure bar was impacted using an air gun with a 50 mm long projectile made out of the same material. Strain measurements were taken from a strain gauge positioned approximately in the middle of the pressure bar (position C (Table 3.2)). In total six tests were performed at impact velocities varying from 10 to 18 m/s. Figure 6.1 shows the attenuation and phase velocity derived from all the tests together with an overall average.

In the case of elastic bars the attenuation coefficient is expected it be zero or to have a very small value. From Figure 6.1 (a) it can be observed that the value of the attenuation coefficient is very close to zero up to 20 kHz. It is worth noticing that the value of the attenuation coefficient in the case of the PMMA pressure bars was 0.74 and 0.8 at 20 kHz for the 20mm and 40mm diameter bars respectively (see Figure 4.1 (a)). The phase velocity shows a small dependency on frequency. It is almost constant up to 10 kHz and then slightly increases up to 30 kHz (Figure 6.1(b)). The technique followed in this study although not optimum, can be characterised as satisfactory for the case of the SHPB, as will be shown in Section 6.4.

In order to examine the frequency range where radial inertia effects become important and hence, the one-dimensional theory is not valid, the wavelength was calculated (Equation (4.18)) and compared with the diameter of the bar. Again as in the case of the PMMA pressure bars, the wavelength is a continuous monotonically decreasing function with frequency and approaches infinity as frequency tends to zero. From Figure 6.2 it was found that the wavelength of the longitudinal waves is 497 mm (21.6D) at 10 kHz, 251 mm (10.91D) at 20 kHz and 166 mm (7.21D) at 30 kHz. Hence, it can be concluded that the elementary theory is accurate for frequencies up to between 20 to 30 kHz. Figure 6.3 shows the frequency spectrum of the four strain signals on the incident bar from an impact test with a 50mm long projectile. It can be observed that almost no energy is detected above 20 kHz.

In contrast to the PMMA pressure bars, the properties of the Magnesium bars do not depend on frequency. This was validated by calculating the Young's Modulus using Equation (4.7). From Figure 6.4 it can be seen that the calculated value of the real part of the Young's Modulus is almost constant and the calculated value of the imaginary part is approximately zero throughout the whole frequency range up to 30 kHz. Furthermore, the real part of the Young's Modulus has a value of approximately 44 GPa, which agrees well with the value given by the manufacturer (Table 3.1).

It has been demonstrated experimentally that the attenuation coefficient is approximately zero, that the phase velocity is approximately constant and that the elastic modulus is real and approximately frequency independent. This is to be expected for small diameter elastic bars. Nonetheless, the experimentally derived propagation coefficient is employed for all tests with Magnesium bars, rather than simple wave shifting using a single phase velocity and no attenuation. The experimentally determined propagation coefficient allowed slight changes in pulse shapes to be approximated in a way that is not possible by employing a simple analytical propagation coefficient. This may be due to the fact that real bars are not "ideal" (i.e. have zero curvature etc.). The advantage of the experimentally derived propagation coefficient is illustrated for example in Figure 6.6 (b), where the small changes in wave shape are well predicted using the experimental propagation coefficient.

6.4 Accuracy of the experimentally determined propagation coefficient for the Magnesium bars

The accuracy of the experimentally determined propagation coefficient was verified by performing an impact test on a Magnesium pressure bar. The pressure bar was impacted with a 250 mm long projectile at an impact velocity of 7.6 m/s. The projectile was made out of the same material as the pressure bar and had a diameter of 20 mm. As already mentioned in Section 4.3 during SHPB testing the conditions of the specimen/bar interfaces are calculated in two stages. In order to validate the accuracy with which the propagation coefficient can be used for stage one, the strain measurement at a point x_A was used to predict the strain at another point (x_B) on the bars. When comparing the predicted and measured strains (Figure 6.5(a)) it can be seen that the experimentally determined propagation coefficient can be used with accuracy so as to reconstruct a strain pulse at any point on the pressure bar.

In the second stage the stresses at the specimen/bar interfaces are calculated using the one-dimensional theory. The accuracy of the method was evaluated by calculating the forces at the free and impact ends of the bar. Observing Figure 6.5 (b) the absolute error involved is of the order of 4% .

6.5 Examples of wave separation in the time and frequency domain for the Magnesium Pressure Bars

As was the case with the PMMA bars (see Section 5.8), the separation of the waves was performed in the time domain (Equation (5.19)) and in the frequency domain (Equation (5.18)) with the use of a suitable exponential window. The input Magnesium pressure bar was impacted with a 250 mm long projectile of the same material at an impact velocity of 15 m/s. The total number of the sampling points was $N=2^{10}$ and 2^{12} for the wave separation in the time and frequency domain respectively, while the sampling rate was Δt=1 μs for both cases.

Figure 6.6 (a) shows the forward and backward waves at position C (Table 3.2) while Figure 6.6 (b) shows the separated waves at position B (Table 3.2). This is due

to the fact that three strain measurements were used in order to separate the waves in the frequency domain, while only two for the case of the wave separation in the time domain.

Due to the fact that the damping is low in the case of elastic pressure bars, any errors associated with noise when separating the waves will be more severe than in the case of the viscoelastic bars. This is the reason why the separated waves shown in Figure 6.6 contain more oscillations than the ones shown in Figures 5.3 and 5.4. A comparison between Figures 6.6 (a) and (b) reveals that the waves separated in the frequency domain are less oscillatory than the ones separated in the time domain. Hence, it can be concluded that, as was the case for the PMMA pressure bars, the wave separation in the frequency domain is preferable, since it gives more accurate results and also it requires less computational time.

The accuracy of the wave separation in the frequency domain was validated by evaluating the forces and the velocities at the free and impacted ends of the pressure bar, using Equations (5.20) and (5.21) respectively (Figure 6.7). Note that for all calculations an exponential window was used with a value of σ to be equal to $2\pi / N\Delta t$.

From Figure 6.7 it can be seen that the force at the free end is close to zero. Also, as expected the value of the velocity at the free end due to the incident and reflected waves is almost double that at the impact end due to the incident wave. From Figure 6.7 (a) the absolute error involved is calculated to be of the order of 3.2% .Hence, the separation of the waves in the frequency domain with the use of an exponential window is regarded as accurate for the case of Magnesium pressure bars.

As a last validation for both the propagation coefficient and the wave separation technique in the frequency domain, an impact test was performed on both pressure bars (i.e. incident and transmitter bar). Both bars were placed in contact having no specimen between them. The forces and displacements were calculated for each interface, from the strain measurements taken from both bars. The bars were impacted with a 250 mm long projectile at an impact velocity of 11 m/s. From Figure 6.8 it can be observed that the calculated forces and displacements are very

close for both contact faces of the pressure bars. This demonstrates the ability of the method to calculate forces and displacements at the interfaces of a specimen in the case of a SHPB test where Magnesium bars are employed.

6.6 Conclusion

A propagation coefficient was determined for the case of the Magnesium pressure bars following the method described in Chapter 4. The accuracy of the method was evaluated experimentally. Furthermore, wave separation was performed in both the frequency and time domains. Frequency domain wave separation is preferred due to better accuracy and efficiency. It was demonstrated that good accuracy is achievable via wave separation in the frequency domain with the use of an exponential window and more than two strain measurements. The method is regarded to give accurate results and so can be used with confidence in the analysis of the SHPB data utilising Magnesium pressure bars.

Magnesium Incident Pressure Bar					
Constant C (V/kN)					**Average C (V/kN)**
Strain gauge	**Test 1**	**Test 2**	**Test 3**	**Test 4**	
A	0.1434	0.1435	0.1433	0.1434	0.1434
B	0.1435	0.1436	0.1437	0.1437	0.143675
C	0.1433	0.1434	0.1434	0.1435	0.1434
D	0.1435	0.1435	0.1436	0.1437	0.143575
Magnesium Transmitter Pressure Bar					
Constant C (V/kN					**Average C (V/kN)**
Strain gauge	**Test 1**	**Test 2**	**Test 3**	**Test 4**	
A	0.1434	0.1436	0.1435	0.1434	0.143475
B	0.1435	0.1436	0.1437	0.1436	0.1436
C	0.1435	0.1436	0.1435	0.1437	0.143575

Table 6.1 Values of the constant C (V/kN) as obtained from the static calibration of the incident and transmitter Magnesium pressure bars.

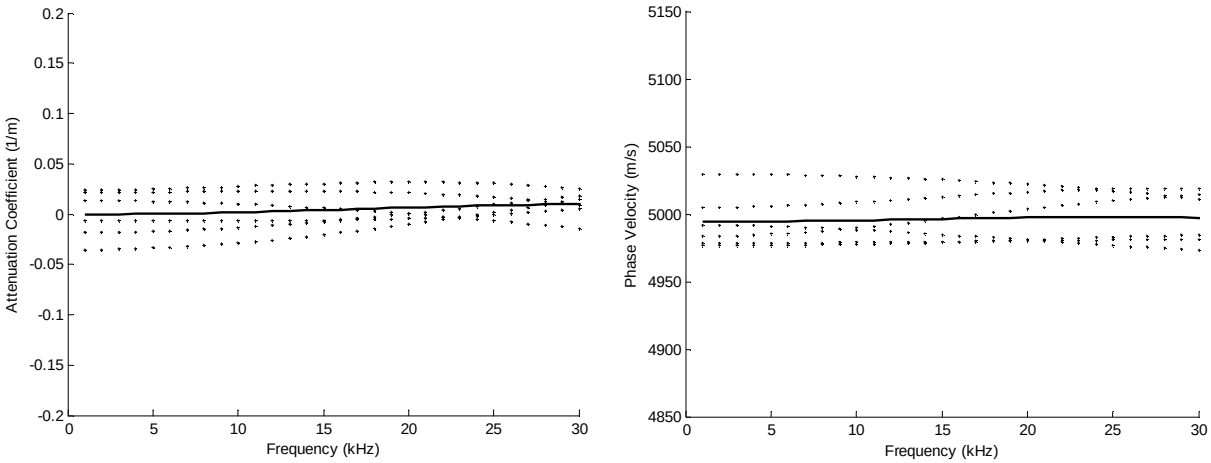

(a) (b)

Figure 6.1 Experimental (a) Attenuation Coefficient and (b) Phase Velocity for the Magnesium bars.

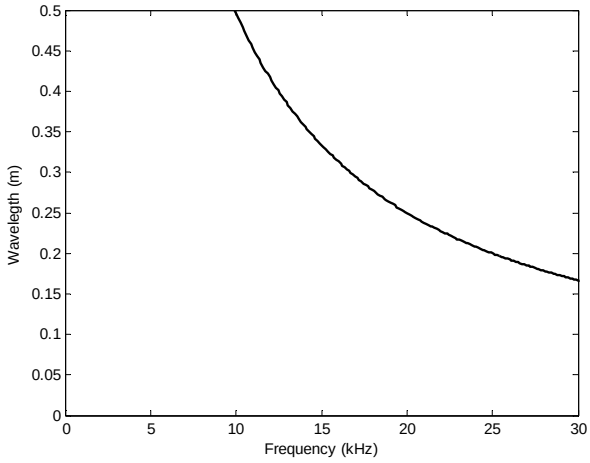

Figure 6.2 Wavelength against frequency for the Magnesium bars.

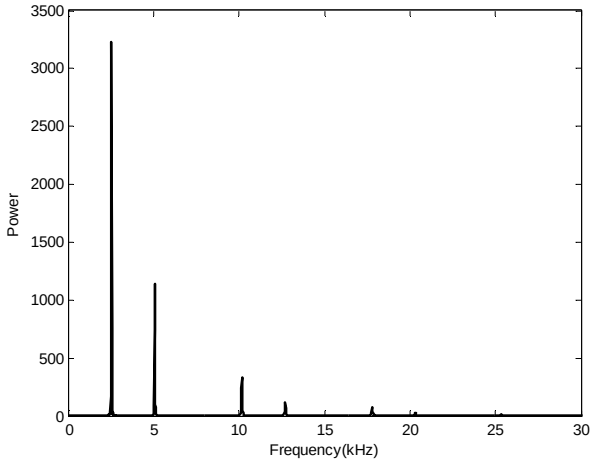

(a)

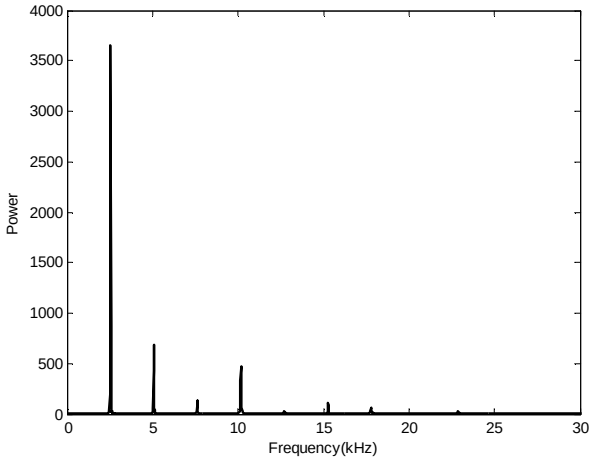

(b)

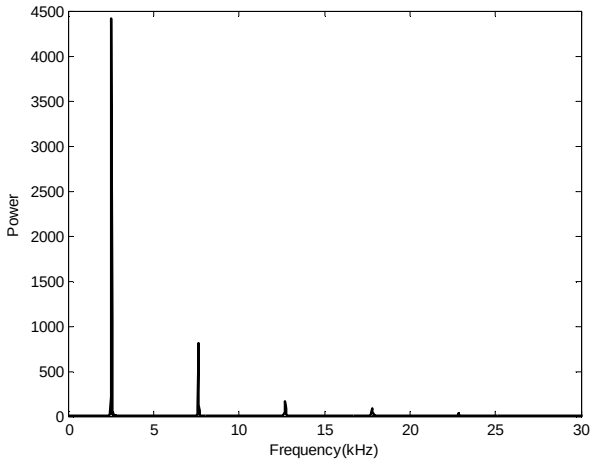

(c)

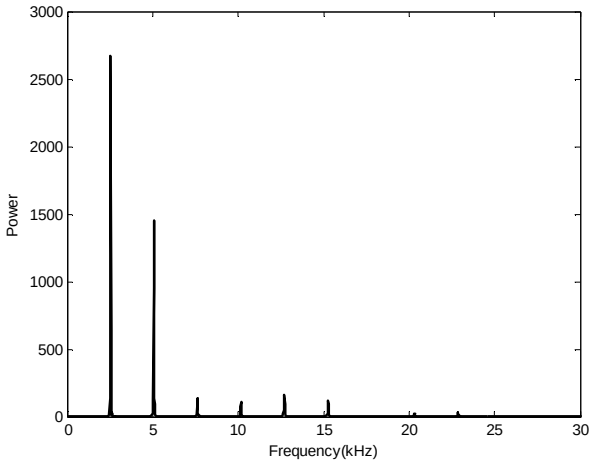

(d)

Figure 6.3 Frequency spectrum of (a) the first, (b) the second, (c) the third and (d) the fourth strain gauge from an impact test on the 23mm diameter Magnesium bar using a 50mm long Magnesium projectile.

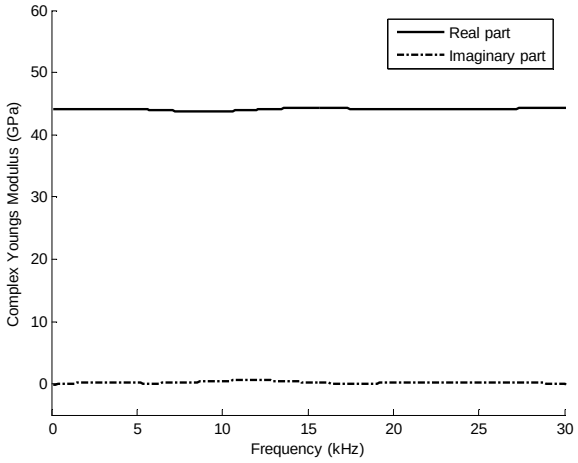

Figure 6.4 Real (solid line) and imaginary (dash line) parts of the Young's Modulus for the Magnesium bars.

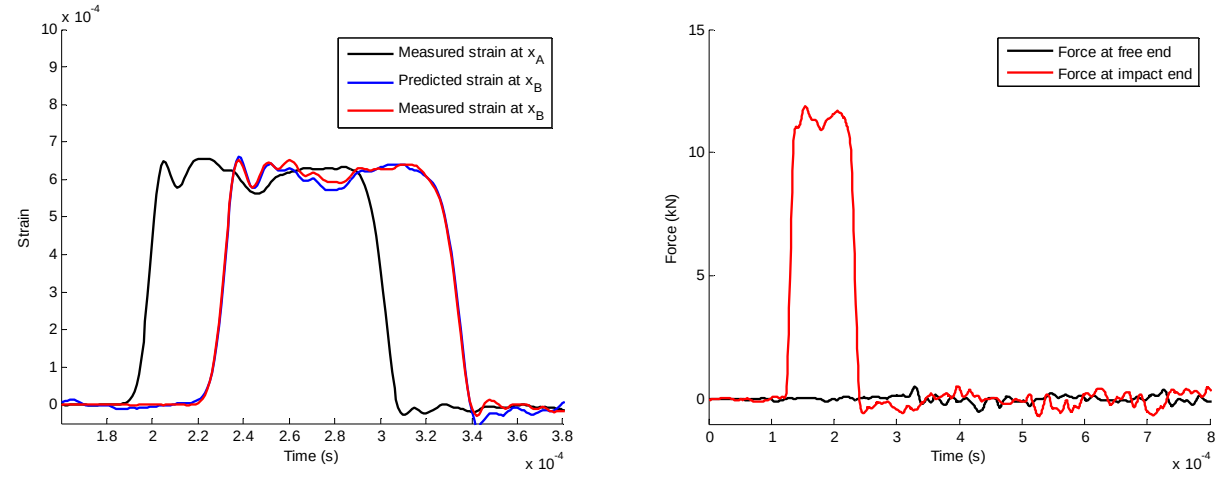

(a) (b)

Figure 6.5 (a) Measured and predicted strain (b) Forces calculated at the impact and free end using an experimentally determined propagation coefficient for the Magnesium bar.

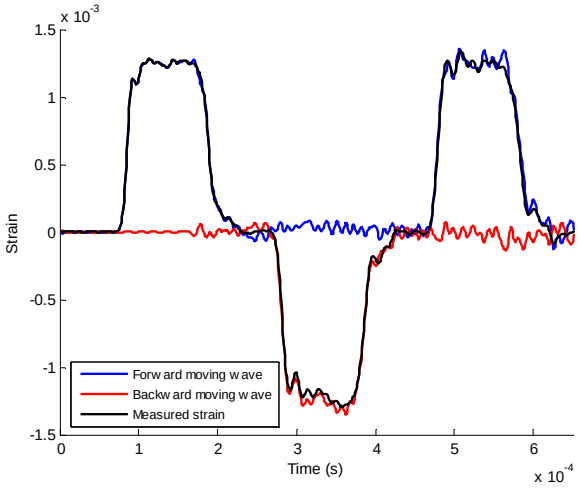

(a)

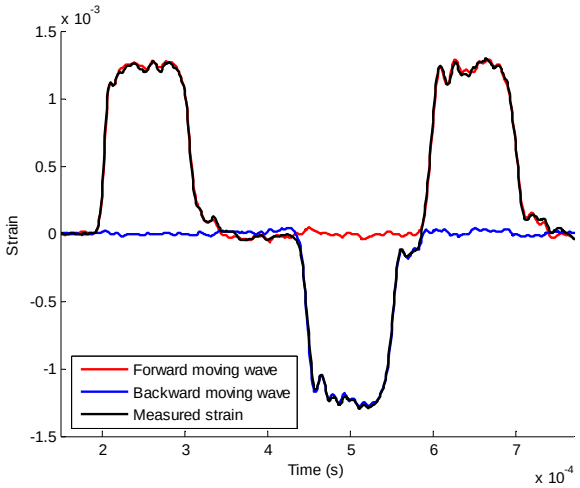

(b)

Figure 6.6 Waves separated in (a) time and (b) frequency domain for the case of the Magnesium Pressure Bars.

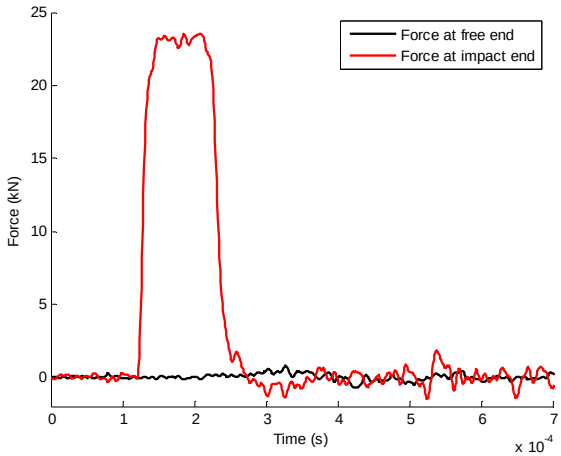

(a)

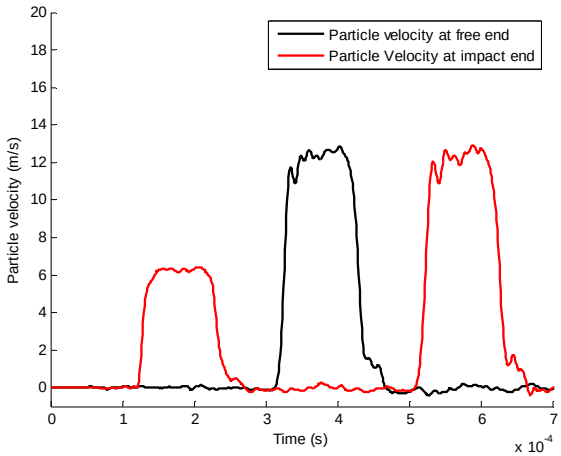

(b)

Figure 6.7 (a) Forces and (b) Particle velocities calculated at the impact and free ends using the wave separation in the frequency domain for the Magnesium pressure bar.

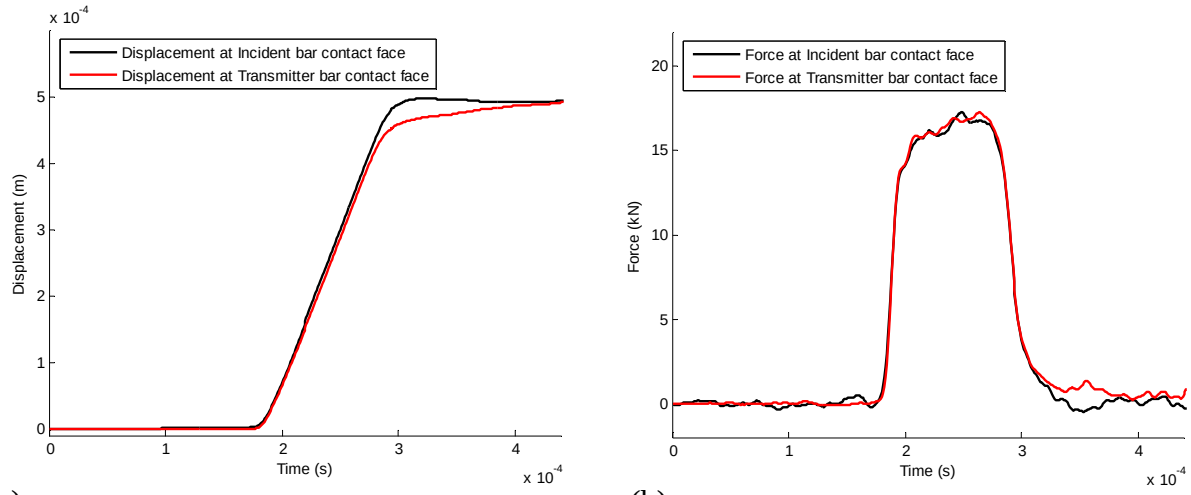

(a) (b)

Figure 6.8 Contact (a) Displacements and (b) Forces calculated from strain measurements on the incident and transmitter Magnesium pressure bars.

CHAPTER 7

An Investigation of Balsa Wood under Quasi-static and Dynamic Conditions

7.1 Introduction

The structure of many man made cellular materials is very similar to the structure of some natural porous composites, which originate from either the plant or animal kingdoms. Further advances and improvements in these materials are possible by investigating the structure and response of these natural systems in an attempt to mimic their designs [97]. Wood belongs to those natural composites and is one of the most ancient and commonly used materials as an energy absorber in many applications including packaging or in aircraft, ship and vehicle designs due to its low cost and good strength to weight ratio. The properties of wood such as strength, toughness, and density vary from one type of wood on another.

In an impact event an ideal energy absorber should have the ability to dissipate as much energy as possible under an optimum safe load/displacement level and also to have a high strength to weight ratio. Balsa wood belongs to one of lightest types of woods with a density varying form 40 to 320 kgm^{-3} and possesses excellent mechanical properties [97, 98, 99, 100]. However, as in every wood its properties depend on various factors such as the age of the tree, the moisture content, the temperature and the strain rate [101]. In this chapter the quasi-static and dynamic compression behaviour of balsa wood is investigated utilising two different SHPB arrangements, i.e. one consisting of Magnesium and another of PMMA pressure bars, and by performing Direct Impact (DI) tests using a 40 mm diameter PMMA pressure bar.

7.2 Failure mechanisms of balsa wood under quasi-static and dynamic compression loading

Balsa wood is one of the lightest types of wood available and its properties as an energy absorber are comparable to these of axially loaded hexagonal honeycombs [98]. Easterling et al. [102] was among the first who examined the deformation modes involved when compressing balsa wood quasi-statically along the three principal directions. Vural and Ravichandran [99, 100] have investigated thoroughly the quasi-static and dynamic compression response of balsa wood in the axial direction covering a wide range of density and have identified the possible failure mechanisms. The dynamic tests were carried out using a steel SHPB set-up with a quartz crystal embedded in the transmitter bar in order to increase the bar's sensitivity. Reid and Peng [103] investigated the dynamic response of five different types of wood, including balsa wood, by firing specimens at a steel Hopkinson pressure bar load cell at impact velocities up to approximately 300 m/s. A shock model was proposed which was based upon a rate-independent, rigid, perfectly-plastic, locking (r-p-p-l) idealisation of the quasi-static stress-strain properties of the woods. This model proved less successful for the along the grain specimens at lower velocities and the need for further investigation was highlighted. However, no distinction was made between the two transverse directions, i.e. tangential and radial directions. More recently Da Silva and Kyriakides [98] performed a comprehensive investigation on the microstructure and the deformation modes of balsa wood by performing a series of quasi-static uniaxial compression tests covering a variety of densities for the three principal directions.

Balsa wood is a highly anisotropic porous material whose main cells (tracheids) are very similar in shape to that of honeycombs, i.e. prismatic hexagonal [97, 98, 99, 100, 102]. These cells are distributed uniformly in the grain cross-section and have an aspect ratio (length to diameter) of approximately 16:1 [97, 100, 99, 102]. Radially arranged group of rays separate each block of the tracheids where the cells are smaller and have different cross section shape. Sap channels run parallel to the axis of the tree throughout the entire structure [97, 100, 99, 98, 102], (see Figure 7.1).

As in every type of wood there exist three principal axes (Figure 7.2) [98, 102, 101]:

- Longitudinal or axial (along-the-grain or end-grain, *L*);
- Radial (across the grain, along the rays and transverse to the growth of the rings, *R*);
- Tangential (across the grain, transverse to the rays and along the growth of the rings, *T*).

Despite the fact that the mechanical properties and densities differ for different types of wood, the density and properties of the cell wall material are regarded to be approximately the same for all types of woods [102, 101]. All woods are made of crystalline cellulose embedded in a matrix of amorphous homocellulose and lignin whose density is approximately 1500 kgm^{-3} [101, 97, 98]. The lay up of the cellulose fibres is rather complicated and is responsible to some degree for the anisotropy present in wood. However, the cell orientation plays a more important role for wood's anisotropy [101]. Due to the anisotropy of balsa wood its properties depend on the direction of loading. The compressive strength in the longitudinal direction is much higher than the strength in either transverse direction, while the difference in strength between the radial and tangential directions is relatively small.

As in most cellular materials both quasi-static and dynamic stress-strain curves of balsa wood follow the same trend. For small strains the response of the material is linear elastic. Permanent deformation (crushing) starts at a stress termed the *crushing stress* (σ_{cr}) with the corresponding strain termed the *crushing strain* (ε_{cr}), i.e. "*crushing*" is used here to abbreviate "initiation of crushing". At the crushing stress, initiation of the inelastic deformation occurs within the cells of the material. When wood is compressed in the longitudinal (*L*) direction a drop in stress then occurs (strain softening) and the deformation continues under an approximately constant stress known as the plateau stress (σ_{pl}) (Figure 7.3 (a)). In the case of the radial (*R*) and tangential (*T*) loaded wood specimens deformation progresses under a smooth rising plateau stress (strain hardening) (Figures 7.3 (b) and 7.3 (c)). For the radially compressed wood sometimes a small drop in stress is observed before the plateau region. The densification or locking strain (ε_d) is associated with compression of the

cell wall material. This occurs at large strains, and is denoted on the stress-strain curve by a sharp increase in the stress.

As already mentioned balsa wood is an anisotropic material indicating that its properties depend on the direction of loading. These differences indicate a number of possible deformation mechanisms that initiate when balsa wood is compressed in its three principal axes. The collapse mechanisms involved when balsa wood is loaded axially are more complex than the ones present in the other two directions. In addition, even if a specimen is compressed along the same axis different deformation modes exist, which depend on density. Vural and Ravichandran [99, 100] reported that when balsa wood is compressed along the grain, mainly elastic or plastic buckling of the cell walls occurs for the lower density specimens. On the other hand for the case of higher density specimens failure is initiated by either or both of the plastic collapse of the end caps and the formation kink bands [99, 100, 102]. Kink bands are responsible for the presence of a larger stress drop after the linear-elastic region for the case of higher density balsa wood. The creation of these bands is attributed to the increase of fibre misalignment, mainly in the longitudinal-tangential (*LT*) direction due to the existence of ray cells penetrating radially the structure [97, 99, 100, 101, 102].

In the case of balsa wood that is compressed in either the tangential or radial directions, failure occurs due to plastic bending of cell walls (similar to the compression of laterally loaded tubes) and deformation is uniform only for the tangentially compressed specimens. The fact that the plastic collapse of the cell walls is not uniform for the radially compressed specimens is responsible for the possible presence of the small drop in stress after the crushing stress. The rays in this direction of loading act as reinforcement [98, 101]. For this reason the radially compressed balsa wood specimens are stronger than the tangential. In both transverse directions the crushing stress is proportional to square of the relative density (Equation (7.1)) [101, 102]:

$$\sigma_{cr}^{R} = 1.4\sigma_{cr}^{T} = C_1\sigma_{ys}\left(\frac{\rho_o}{\rho_S}\right)^2, \qquad (7.1)$$

where ρ_o and ρ_s are the densities of the specimen and the cell wall material respectively, their ratio defines the relative density (ρ_r), C_1 is a constant and σ_{ys} is the yield stress of wood cell wall, having a value of 350 MPa as given by Cave [104].

When balsa wood is compressed axially, the cell walls are compressed rather than bent as in the case of the transversely loaded specimens, indicating that higher magnitude forces are required to initiate failure. For the end-grain balsa wood, when failure is initiated by the plastic collapse of the end-caps the crushing stress is directly proportional to the relative density [101, 102]:

$$\sigma_{cr}^{L} = C_2 \sigma_{ys} \left(\frac{\rho_o}{\rho_S} \right), \tag{7.2}$$

where C_2 is again a constant.

Vural and Ravichandran [99, 100] suggested different relationships for predicting the crushing stress according to the failure mode involved. For the case where failure is initiated by plastic buckling or kink band formation of the cells the crushing stress is given by Equations (7.3) and (7.4) respectively [99, 100]:

$$\sigma_{cr}^{L} = C_3 \sigma_{ys} \left(\frac{\rho_o}{\rho_S} \right)^{5/3}; \tag{7.3}$$

$$\sigma_{cr}^{L} = \frac{0.5 G_S \left(\rho_o \diagup \rho_S \right)}{1 + \frac{\theta_o}{\gamma_y}}, \tag{7.4}$$

where C_3 is a constant and is equal to 2 according to Vural and Ravichandran [100], G_S is the shear modulus of the cell wall equal to 2.6 GPa, γ_y is the yield strain of balsa wood in longitudinal shear equal to 0.023 and θ_o is the initial fibre

misalignment angle having an average value of 9^o. The above values are provided by Vural and Ravichandran [100].

Densification of any cellular material occurs at a strain where the cell walls crush together and compression of the cell wall material itself begins [101]. This indicates that the densification strain would be equal to the porosity of the material i.e. $1-\rho_r$, but in fact densification occurs at lower values of strain given by [99, 105]:

$$\varepsilon_d = 1 - C_4 \frac{\rho_o}{\rho_S}; \tag{7.5}$$

or

$$\varepsilon_d = C_5 (1 - \frac{\rho_o}{\rho_S}). \tag{7.6}$$

Maiti et al. [105] proposed a value of 2 for the constant C_4 in Equation (7.5), suggesting that densification occurs when the relative density of wood reaches a value of 0.5. This value agreed well with the experimental data for balsa wood presented by Reid and Peng [103]. However, Vural and Ravichandran [99] reported that Equation (7.5) did not compare well with their experimental data and they suggested the use of Equation (7.6) with a value of C_5 equal to 0.87 for the along the grain balsa.

Tan et al. [106] performed dynamic tests on aluminium alloy foam at high impact velocities and gave a more consistent definition for both the locking strain and plateau stress. The densification strain was defined as the global maximum of the energy absorbing efficiency (η) when plotted against strain, where the efficiency is defined as

$$\eta(\varepsilon_a) = \frac{1}{\left[\sigma_c(\varepsilon)\right]_{\varepsilon=\varepsilon_a}} \int_0^{\varepsilon_a} \sigma_c(\varepsilon) d\varepsilon. \tag{7.7}$$

The plateau stress can be obtained, after the crushing stress, crushing strain and locking strain have been identified, as follows:

$$\sigma_{pl} = \frac{1}{\varepsilon_d - \varepsilon_{cr}} \int_{\varepsilon_{cr}}^{\varepsilon_d} \sigma_C(\varepsilon) d\varepsilon \,. \tag{7.8}$$

7.3 Quasi-Static tests on Balsa wood

7.3.1 Specimens

Cylindrical balsa wood specimens were cut from big blocks of balsa wood along all three directions for the quasi-static tests. Specimens that were free from any visible defects and rough ends were chosen for testing. Prior to testing, their density was calculated, by weighing the specimens using a high precision weighing machine (accuracy ± 0.001g) and measuring their dimensions by the use of a vernier (accuracy ± 0.01 mm). All the specimens had a diameter of approximately 45 mm and lengths varying between 10 to 45 mm (see Tables 7.1-7.6). Particular attention was paid to measure their moisture content using a moisture meter, since it can affect both the density and the properties of balsa wood [107]. It was found that the moisture content of all specimens was less than 7%, which is a typical value for dry woods. It should be noted that all the above measurements as well as the testing of the specimens were conducted under conditions of atmospheric pressure and ambient temperature.

7.3.2 Experiments

All cylindrical specimens were compressed along and across the grain, in both radial and tangential directions, at a constant crosshead speed of 4 mm/min using an INSTRON machine (model 4507). Some specimens were constrained laterally while others were not. The unconstrained specimens were compressed between two flat parallel platens to eliminate any shear forces on the specimens [100]. In order to

investigate the behaviour of balsa wood under uniaxial compression, lateral constraint was applied by the use of a hollow steel cylinder, 45.15 mm in diameter. Small air bleeds in the hollow cylinder allowed air to escape. For these tests a loading rod was used to compress the specimen within the constraining barrel. Special care was taken to ensure the end face of the loading rod was parallel to the lower platen. Due to the fact that the strength and elastic modulus of the steel cylinder is much greater than that of balsa wood, the stresses within the cylinder remain elastic throughout the duration of the test.

7.3.3 Quasi-static compression of balsa wood results

Load-displacement curves were obtained for every test, which were then converted to stress-strain curves by defining the stress as the load divided by the original cross-sectional area and the strain as the change in length divided by the original undeformed length of the specimen. In all cases the displacement recordings were corrected to eliminate the machine compliance. The stress-strain curves that were obtained for every case are shown in the Figures 7.4-7.6.

At this point it is necessary to clarify the way that the key material properties have been extracted from the stress-strain curves obtained from both the quasi-static and dynamic experiments. For cases with an initial peak stress, the crushing stress (σ_{cr}) is defined as the first peak just after the end of the elastic region and the crushing strain (ε_{cr}) is the corresponding strain value at this peak. For cases with no peak stress, the crushing stress is denoted by the start of the plateau region of the stress-strain curve. The densification strain (ε_d) and plateau stress (σ_{pl}) are specified by the use of Equations (7.7) and (7.8) respectively.

Figures 7.8 (a) and (b) show the experimentally and theoretically determined values (using Equations (7.4) and (7.9)-(7.12) defined later) of the crushing stresses against density for all the along and across the grain specimens compressed quasi-statically. Overall, Figure 7.8 (a) indicates that the constraint has little effect. This is particularly clear for along the grain specimens with densities of approximately 125

kgm^{-3}. This is in agreement with the findings of Vural and Ravichandran [100]. The physical explanation is that the local buckles do not require large lateral expansion of the specimen [100].

The effect of the lateral constraint has not been reported previously for radially or tangentially compressed balsa wood. Figure 7.8 (b) illustrates that the constraint has little effect on the crushing stress of the radial and tangential specimens. The constraint then affects the crushing stress of neither along (discussed above) nor across the grain compression of balsa wood. It is proposed that the reason is the same for any direction i.e. the plastic compression of the cells takes place in the loading direction without the need of gross expansion in the perpendicular to loading direction.

Furthermore, the difference in lengths does not affect the crushing stress values although it affects the crushing strain. It is expected that the onset of crushing occurs at larger strains for the shorter specimens. This is the result of the nonuniform deformation in a cellular material. Crushing is associated with displacements and rotations at the scale of the cells. Where few cells are present these displacements will be interpreted as larger strains for short specimens. The fact that the difference in length does not affect the stress values but affects the crushing strain values can be verified by comparing for example:

- for the along the grain test 1 ($l_o = 46.53$ mm, $\sigma_{cr} = 12.6$ MPa, $\varepsilon_{cr} = 0.032$) with test 6 ($l_o = 10.26$ mm, $\sigma_{cr} = 12.8$ MPa, $\varepsilon_{cr} = 0.124$) (see Figure 7.4);
- for the radial test 19 ($l_o = 28.82$ mm, $\sigma_{cr} = 1.8$ MPa, $\varepsilon_{cr} = 0.016$) with test 23 ($l_o = 13.4$ mm, $\sigma_{cr} = 1.86$ MPa, $\varepsilon_{cr} = 0.0455$) (see Figure 7.6) ;
- for the tangential test 28 ($l_o = 45.39$ mm, $\sigma_{cr} = 1.5$ MPa, $\varepsilon_{cr} = 0.065$) with test 39 ($l_o = 12.66$ mm, $\sigma_{cr} = 1.57$ MPa, $\varepsilon_{cr} = 0.097$) (see Figure 7.7).

The experimental data for the crushing stresses was fitted into Equations (7.1), (7.2) and (7.3) in order to obtain the average values for the constants C_1, C_2 and C_3 respectively, without making any distinction on the confinement that was used and the specimens geometry. The following equations were obtained:

$$\sigma_{cr}^{R} = 0.2744\sigma_{YS}\left(\frac{\rho_o}{\rho_S}\right)^2; \quad (7.9)$$

$$\sigma_{cr}^{T} = 0.2373\sigma_{YS}\left(\frac{\rho_o}{\rho_S}\right)^2; \quad (7.10)$$

$$\sigma_{cr}^{L} = 0.4075\sigma_{YS}\left(\frac{\rho_o}{\rho_S}\right); \quad (7.11)$$

$$\sigma_{cr}^{L} = 2.23\sigma_{YS}\left(\frac{\rho_o}{\rho_S}\right)^{5/3}. \quad (7.12)$$

Equation (7.1) has been used by Reid and Peng [103] and Gibson and Ashby [101] using a value of C_1 equal to 0.2 and 0.14 for the radially and tangentially compressed specimens respectively. It was suggested [101, 103] that the wood specimens compressed in the radial direction are 1.4 times stronger that the ones compressed in the tangential direction. Equations (7.9) and (7.10) indicate that the radially compressed specimens are approximately 1.156 times stronger than the tangential. The above differences can be attributed to the fact that Equation (7.1) has been used in [101] in order to cover a wide range of woods. For the case of the along the grain specimens Vural and Ravichandran [100] proposed a value of C_2 equal to 0.5 which was derived analytically by considering the compression of the end cap. On the other hand, Gibson and Ashby used an empirical value of 0.35 for the same collapse mechanisms. The value of C_2 obtained here is between the values suggested in [100] and [101]. Lastly, the value of C_3 agrees well with the value given by Vural and Ravichandran (where $C_3 = 2$) [100].

The general trend observed in Figures 7.8 (a) and (b) is that for balsa wood when compressed in any of the three principal directions the crushing stress increases with density. This is in accordance to the findings in [98, 100, 101, 102, 103]. Also, the along the grain samples are stronger than both the radial and tangential specimens

due to the elongated shape of the cells in this direction. Initiation of failure requires the cell walls to be compressed rather than bent as in the case of the across the grain specimens (see Section7.2) [101, 102]. Furthermore, the fact that the radial specimens are stronger than the tangential is attributed to the existence of rays that act as reinforcement in this direction [101, 98].

Figure 7.8 (a) indicates that for specimens having a density between 95 to 105 kgm^{-3} failure is initiated due to plastic buckling of the cell walls, i.e. according to Equations (7.3) and (7.12). This was verified by Vural and Ravichandran [100] for low density balsa wood. For the highest density specimens tested, the values of the crushing stress are well approximated by all of Equations (7.4), (7.11) and (7.12). It should be noted that Equations (7.11) and (7.12), corresponding to end cap collapse and plastic buckling of the cell walls respectively, have been fitted to the experimental obtained data. Only Equation (7.12) follows the trend for all the density range considered herein. This agrees with the findings of Vural and Ravichandran [100], who reported that plastic buckling was the dominant mechanism to initiate failure for up to densities of approximately 170 to 200 kgm^{-3} . It is worth mentioning that the values shown in Figure 7.8 (a) agree well with the values obtained by Vural and Ravichandran [100] for same density range tested in this study.

Observing Figure 7.8 (b) it can be said that for the radially compressed specimens, Equation (7.9) can be used to obtain the values of the crushing stress for the density range shown. On the other hand, Equation (7.10) predicts fairly well the crushing stress for the specimens loaded in the tangential direction. However, it is worth noticing that the tangential specimens cover a smaller density range compared to the radial specimens and this may be the reason for the better agreement of Equation (7.10) with the experimental data.

The experimental data obtained for the densification strain with the use of Equation (7.7) was fitted into Equations (7.5) and (7.6) and the following values for the constants C_4 and C_5 were evaluated for the along and across the grain balsa:

$$\varepsilon_d^L = 1 - 3.12\frac{\rho_o}{\rho_S}; \tag{7.13}$$

$$\varepsilon_d^L = 0.82(1 - \frac{\rho_o}{\rho_S}); \tag{7.14}$$

$$\varepsilon_d^R = 1 - 3.19\frac{\rho_o}{\rho_S}; \tag{7.15}$$

$$\varepsilon_d^T = 1 - 3.32\frac{\rho_o}{\rho_S}; \tag{7.16}$$

$$\varepsilon_d^{R,T} = 0.64(1 - \frac{\rho_o}{\rho_S}). \tag{7.17}$$

It is worth mentioning that for the along the grain specimens the value obtained here for the constant C_5 is very close to the one used by Vural and Ravichandran [99] (i.e. compare 0.82 in Equation (7.14) with 0.87 in ref. [99]). However, Vural and Ravichandran [100, 99] extracted their experimental values of the densification strain directly from the stress strain curves by defining the densification strain as the strain at the local minimum before the stress starts to rise steeply. Despite the fact that this can be regarded adequate for the case of the along the grain specimens, for the across the grain specimens it is not possible to obtain accurately the densification strain in such a manner due to the shape of the stress strain curve (Figure 7.3). This indicates the importance for the use of Equation (7.7) in order to define the densification strain accurately.

The experimental values of the densification strain and those obtained from Equations (7.13)-(7.17) are illustrated in Figure 7.9. The values of the densification strain vary between 0.72 to 0.8 and 0.53 to 0.57 for the along and across the grain balsa respectively for the density range shown in Figure 7.9. Observing Figure 7.9 it can be concluded that the predictions of Equation (7.6) (i.e. that leads to Equations (7.14) and (7.17)) are closer to the general trends of the experimental densification strains for the along and across the grain balsa, especially for the radially compressed

specimens. Also, as was the case for the crushing stress, the values of the densification strain are again independent of the confinement used, which is in agreement with Vural and Ravichandran [100]. It is expected for the higher density wood to densify at lower strains, as the porosity level is lower. Due to the fact that the tested specimens cover a small range of density, this underlying trend cannot be observed too clearly in Figure 7.9.

Figure 7.10 illustrates the plateau stress obtained using Equation (7.8) for the along and across the grain balsa wood samples. The solid lines represent the best linear fits to the data obtained. As was the case for the crushing stress, the plateau stress tends to increase with increasing density. This is attributed to the fact that for denser wood the ratio of the cell wall material to cell diameter will be higher contributing to its strengthening [99].

It is worth mentioning that for the across the grain balsa wood there is no published data showing values of neither the densification strain nor the plateau stress. On the other hand, for the along the grain balsa the data presented in Figure 7.10 (a) agrees well with the findings of Vural and Ravichandran [99]. Again, the constraint has negligible effect on the experimental results.

A constant stress in the plateau region is considered to be ideal for energy absorbing purposes [101]. The ratio of the crushing stress to plateau stress is therefore equal to one for an ideal energy absorbing cellular material. This ratio has been used, e.g. in ref. [100], as a measure of the deviation of the material from an ideal energy absorber. For both along and across the grain balsa specimens the ratio of the crushing to plateau stresses is plotted in Figure 7.11. This ratio for the along the grain balsa is closer to one indicating that its properties are closer to those of an ideal energy absorber. In general, for along the grain samples the ratio is greater than one due to the initial stress drop at the onset of crushing. For the across the grain specimens the ratio is always less than one due to their monotonically increasing stress strain curves.

7.4 SHPB tests on Balsa Wood

As already mentioned, balsa wood belongs to one of the lightest types of wood. The limitations when testing soft materials with SHPB arrangements that consist of high mechanical impedance pressure bars have been discussed thoroughly in Chapter 2 (see Section 2.2). Dynamic testing of balsa wood was performed utilising two different SHPB arrangements, one consisting of Magnesium Alloy pressure bars and another consisting of PMMA pressure bars. Both experimental set-ups have been described in Chapter 3.

7.4.1 Specimens

For the SHPB tests cylindrical specimens were cut from big blocks of balsa wood along the three principal directions paying extreme care to ensure good specimen surface quality. Prior to testing their moisture content and relative dimensions were measured accurately as in the case of the quasi-static tests (see Section 7.3.1). The moisture content was found again to be less than 7%. The details of the specimens used for both SHPB and DI tests are shown in Appendix A (Tables A.1-A.7).

In the case of balsa wood, no lubrication could be used between the pressure bars/specimens interfaces so as to reduce any friction effects. This is due to the fact that balsa wood is a porous material, and any added fluid substance at the end faces would be absorbed resulting in a change of its mechanical behaviour. Hence, in order to minimise any friction effects, (which would result in the violation of the assumption of the uniaxial stress state in the specimen as well as in an enhancement of the flow stress (see Section 2.4)) the end faces of all the specimens were polished. Friction effects would be more severe in the case of the shorter specimens. However, all the samples for both quasi-static and SHPB tests had similar surface conditions and friction effects (if any) would be the same for all experiments. Hence, a comparison between the quasi-static and dynamic properties of balsa wood should reveal with accuracy any possible strain rate effects.

As already mentioned (see Section 2.4) the diameter of the specimens tested in a SHPB arrangement should in general have a diameter of approximately 80% of the bar diameter so that the maximum desirable strain in the sample can be achieved without its diameter expanding beyond the bar's diameter [4]. Furthermore, the tested sample must be large enough to represent the bulk properties of the material. As a rule of thumb, it has been proposed that the specimen size should be at least ten times the representative microstructure unit size [4] . For the tests performed in this study the balsa wood specimens had lengths off 3 mm, 6 mm and 8 mm. Their diameters were 16 mm and 19 mm for tests carried out using the PMMA and Magnesium SHPB set-ups respectively. The average cell diameter and length of the tracheids are approximately 45 μm and 650 μm respectively [98, 100]. It is obvious that the shorter along the grain specimens do not have a representative number of cells in the loading direction. However, the deformation mechanisms within the specimens (e.g. micro-buckling) have length scales of the order of the lateral dimensions [55]. This is comparable to out-of-plane honeycombs, wherein the fold lengths are similar to in-plane dimensions rather than the out-of-plane cell length, which is the specimen length in this case. The characteristic lengths of the specimens are therefore associated with the lateral dimension of the cells. In addition, the difference in dimensions of the specimens for the quasi-static tests did not affect the values of neither the crushing nor the plateau stress.

7.4.2 Experiments

For both Magnesium and PMMA SHPB arrangements an experimental propagation coefficient had been determined in order to take into account dispersion and attenuation effects (see Chapter 4 and 6). Furthermore, the waves that were used to calculate the properties of balsa wood were separated in the frequency domain by the use of a suitable chosen exponential window (see Chapter 5). The average stress, strain and strain rate of the specimens were calculated using the following equations:

$$\tilde{\sigma}(\omega)=\frac{-\rho\omega^2}{\gamma(\omega)^2}\frac{A}{2A_o}\left(\tilde{P}_I(\omega)e^{-\gamma(\omega)x}+\tilde{N}_I(\omega)e^{\gamma(\omega)x}+\tilde{P}_T(\omega)e^{\gamma(\omega)x}+\tilde{N}_T(\omega)e^{-\gamma(\omega)x}\right);$$

$$\tilde{\varepsilon}(\omega)=\frac{-1}{\gamma(\omega)\cdot l_o}\left(\tilde{P}_T(\omega)e^{\gamma(\omega)x}-\tilde{N}_T(\omega)e^{-\gamma(\omega)x}-\tilde{P}_I(\omega)e^{-\gamma(\omega)x}+\tilde{N}_I(\omega)e^{\gamma(\omega)x}\right); \tag{7.18}$$

$$\tilde{\dot{\varepsilon}}(\omega)=\frac{-i\omega}{\gamma(\omega)\cdot l_o}\left(\tilde{P}_T(\omega)e^{\gamma(\omega)x}-\tilde{N}_T(\omega)e^{-\gamma(\omega)x}-\tilde{P}_I(\omega)e^{-\gamma(\omega)x}+\tilde{N}_I(\omega)e^{\gamma(\omega)x}\right), \tag{7.19}$$

where ρ, A are the density and cross-sectional area of the pressure bars, ω is the angular frequency, $\gamma(\omega)$ is the wave propagation coefficient, l_o, A_o are the initial length and cross-sectional area of the specimen, x is the distance between the strain gauge and the specimen/bar interface and $\tilde{P}(\omega)$, $\tilde{N}(\omega)$ are the forward and backward waves respectively at the reference strain gauge. Note that the subscripts I and T refer to the incident and transmitter pressure bars respectively (i.e. $\tilde{P}_I(\omega)$, $\tilde{P}_T(\omega)$ are the forward waves in the incident and transmitter pressure bars respectively).

In the case where stress equilibrium has been achieved within the specimen the stress is given by:

$$\tilde{\sigma}(\omega)=\frac{-\rho\omega^2}{\gamma(\omega)^2}\frac{A}{A_o}\left(\tilde{P}_T(\omega)e^{\gamma(\omega)x}+\tilde{N}_T(\omega)e^{-\gamma(\omega)x}\right). \tag{7.21}$$

The use of Equation (7.21) will lead to a smoother stress-strain curve than the one obtained using Equation (7.18), due to the fact that the high frequency components of the incident loading wave will be damped as they pass through the specimen. This is important in the case of the Magnesium SHPB, since the damping in the bar material is low (Section 6.3) and the stress waves have more high frequency oscillations than is the case for the PMMA pressure bars. In particular, when the incident and reflected waves are added together to calculate the stress/force at the incident bar/specimen interface or when they are used in Equation (7.18), they lead

to an oscillating stress curve and little information is available about the response of the specimen. This is more pronounced in the case of the weaker specimens (e.g. tangential balsa wood shown in Figure 7.13). Hence, the use of Equation (7.21) especially in the case of the Magnesium SHPB is preferable. However, Equation (7.21) is valid only when stress equilibrium has been achieved within the specimen. In order to define the thickness of the specimen where Equation (7.21) leads to accurate results, the forces at both faces of the specimen were calculated and compared for different lengths, for both PMMA and Magnesium SHPB set ups.

Note that in Figures (7.12) - (7.15) the blue and red lines indicate the forces at the incident bar/specimen (front face) and transmitter bar/specimen (back face) interfaces respectively. Figures (7.12) illustrates the calculated forces at both faces of an along the grain balsa wood specimen obtained using a Magnesium SHPB arrangement. The strength of the along the grain balsa is higher than that of the across the grain, as was shown in the quasi-static results. There are no exact rules that can be applied to quantify the validity of the assumption of stress equilibrium. As a general rule, the forces at the front face of the sample exhibit larger fluctuations than those at the rear face. It is argued in [4, 8] that stress equilibrium is achieved if the force at the front face oscillates about the value of the force at the rear face. In Figures 7.12 (a) and 7.12(b) it can be seen that the force pulses follow similar patterns, with the front face force oscillating about the value of the rear face force. It is possible therefore to have some confidence in the results obtained from tests shown in Figures 7.12 (a) and 7.12 (b). However, for the force pulses shown in Figures 7.12 (c) and 7.13, the differences between the front face and back face forces are considered to be too great to have any confidence in the data obtained. For crushing forces of approximately 2 to 3 kN and samples of 6 mm in length the Magnesium bar set up is sufficient. In other words, the Magnesium pressure bars were suitable only for along the grain specimens with a maximum length of 6 mm.

Front and back face force pulses obtained from the PMMA bar set up are shown in Figures 7.14 and 7.15. Excellent agreement between the two forces was achieved for certain tests, e.g. Figures 7.14 (a) and 7.14 (b). As was the case for the Magnesium bar arrangement, the agreement is better for shorter specimens (up to 6 mm) and

higher crushing stresses. Nonetheless, good agreement was still achieved for the longest tangential samples as can be seen in Figure 7.15. Figures 7.14 and 7.15 illustrate that accurate data could be obtained using the PMMA SHPB set up for all the directions and lengths of balsa specimens. This indicates the superiority of the use of viscoleastic pressure bars for testing soft materials to large strains.

As already mentioned, before calculating the stress-strain curves of all balsa wood specimens using Equations (7.19) and (7.21), the waves from both the Magnesium and PMMA incident and transmitter pressure bars were separated. Figure 7.16 (a) and 7.17 (a) show the measured strain histories from the third strain gauge on the input bar and the first strain gauge from the output bar from the Magnesium and PMMA SHPB arrangements respectively (see Table 3.2). Note that for clarity only two strain histories for each SHPB set up are shown in Figure 7.16 (a) and 7.17 (a), although the wave separation was performed using all the strain gauges listed in Table 3.2. For both cases wave superposition is observed although the strain gauge in the incident bar was placed approximately in the middle of each bar. For the experiment conducted using the Magnesium SHPB set up the length of the projectile was 450 mm and was not sufficient to cause densification during the propagation of the first pulse. However, the second pulse reloaded the specimen from a strain of approximately 0.5 up to densification at a strain of 0.8 (Figure 7.16 (b)). The tested specimen was loaded at a nearly constant strain rate of 2800 s^{-1} and 2200 s^{-1} during the first and second pulses respectively (see Figure 7.16 (c)). The plateau stress was observed to be nearly constant at 8.5 MPa (Figure 7.16 (b)). The unloading and the reloading of the along the grain specimen shown in Figure 7.16 (b) follow slightly different paths. There is little experimental data in this area, however the unloading and reloading of the crushed balsa is not a simple linear elastic case. Similar observations were made on polymeric foams in [75]. A flow chart and the Matlab program that was used to produce the stress-strain curve shown in Figure 7.16 (b) are provided in Appendix B. For the case of the experiment using the PMMA SHPB set up, after wave separation the stress-strain curve shown in Figure 7.17 (b) was produced. Densification occurred at a strain of 0.78 and the plateau stress value was calculated to be 14 MPa. The average strain rate was approximate 2250 s^{-1}. Strain rates are never truly constant for tests carried out using the PMMA SHPB

arrangement. This is due to the shape of the incident wave that reaches the incident/specimen interface. Wave dispersion leads to longer rise times in the pulse seen at this interface. As this incident pulse deviates from an ideal "rectangular" waveform, constant strain rates are not possible. Neither of the stress-strain curves plotted in Figures 7.16 (b) and 7.17 (b) could be produced without wave separation.

7.4.3 Results

Typical stress-strain curves from the compression of balsa wood using the Magnesium and PMMA SHPB arrangements are shown in Figures 7.18 and 7.19 respectively. It should be noted that not all specimens were compressed to densification. The along the grain, radial and tangential samples were compressed over a range of strain rates. The along the grain specimens were compressed covering a strain rate range of 874-3426 s^{-1}, while the radial and tangential specimens were compressed under 1127-4510 s^{-1} and 1670-3802 s^{-1} respectively. The strain rates were calculated as the average strain rate obtained using Equation (7.20).

In the case of honeycombs compressed in the longitudinal (out-of-plane) direction, end effects in the specimen (due to machining etc.) can result in the loss of the initial peak (just before strain softening) in the stress-strain curve, resulting in a monotonous stress-strain curve [99], similar to that for across the grain. The same implies for the along the grain balsa wood. The shape of the stress-strain curves for the end-grain balsa wood samples (see Figure 7.18 and 7.19 (a)) verifies the fact that end effects were negligible.

Figure 7.20 shows the experimental values of the crushing stress as obtained from the SHPB and quasi-static tests along with the predictions of Equations (7.4) , (7.22)-(7.25), (7.9), (7.10) and (7.12). It has been reported in ref. [99] that the loading rate is not expected to influence the deformation modes for balsa wood. Hence, the experimental values of the crushing stress were fitted into Equations (7.1), (7.2) and (7.3) and the following expressions were obtained:

$$\sigma^{R}_{cr(SHPB)} = 0.47186\sigma_{YS}\left(\frac{\rho_o}{\rho_S}\right)^2; \quad (7.22)$$

$$\sigma^{T}_{cr(SHPB)} = 0.33887\sigma_{YS}\left(\frac{\rho_o}{\rho_S}\right)^2; \quad (7.23)$$

$$\sigma^{L}_{cr(SHPB)} = 0.50517\sigma_{YS}\left(\frac{\rho_o}{\rho_S}\right); \quad (7.24)$$

$$\sigma^{L}_{cr(SHPB)} = 2.5919\sigma_{YS}\left(\frac{\rho_o}{\rho_S}\right)^{5/3}. \quad (7.25)$$

It should be mentioned that the above expressions do not take into account the variation of the strain rate over which the SHPB tests were performed. Hence, it will be assumed that they are valid within a certain range of strain rates, i.e. Equation (7.22) is valid for a strain rate range of 1127-4510 s^{-1}, Equation (7.23) for 1670-3802 s^{-1} and Equations (7.24) and (7.25) are valid for a strain rate range of 874-3426 s^{-1}.

Inspection of Figure 7.20 (a) suggests that plastic buckling (Equation (7.25)) is the dominant mechanism for initiation of failure for the dynamically loaded specimens in the longitudinal direction, as was the case for the quasi-static tests. The highest density specimens crushed at lower stresses than those predicted by Equation (7.25). This may indicate a change in the deformation mode to kink band formation (Equation (7.4)) or plastic collapse of end caps (Equation (7.24)). All the test data in Figure 7.20 reveal an increase in the initial dynamic crushing stress when compared to the quasi-static values. This is shown if one compares the magnitudes of the constants from Equations (7.9-7.12) with Equations (7.22-7.25) respectively. From this comparison it can be said that for the along the grain specimens the value of the crushing stress increases by approximately 16%. This increase is less than that suggested by Vural and Ravichandran [99] of between 50-130%. However, the good agreement between the peak forces measured from either specimen/pressure bar interfaces (see for example Figure 7.14) gives confidence in the data presented in

Figure 7.20. To the author's knowledge these forces have not been checked to any previous SHPB studies of balsa wood.

The crushing stresses for dynamically loaded radial specimens are notably larger than those for quasi-static loading (Figure 7.20 (b)). Comparing Equations (7.22) and (7.9) the increase is 72%. However, a large spread is present in the data of Figure 7.20 (b), possibly due to the presence of rays in this direction. In the tangential direction the dynamic increase of the crushing stress is 43% (Figure 7.20 (c)). The general trend observed for all the dynamically compressed balsa wood specimens is that the crushing stress increases with density.

In order to minimise the variation of density and observe the effects of the strain-rate individually, the crushing stresses were normalised by the relative density (see Equations (7.1) and (7.3) for across and along the grain respectively). In Figure 7.21 the normalised stresses are plotted against strain rate. The mean quasi-static and dynamic normalised crushing stresses and a straight line best fit to the SHPB data are also shown in each of Figure 7.21 (a)-(c). The SHPB mean and the straight line best fit in Figure 7.21 (a) are almost identical. This indicates that although the strain rate causes an increase in the crushing stress, the effect is constant for strain rates between 870 s^{-1} to 3400 s^{-1}. In other words, the crushing stress remains constant as the strain rate increases form 870 s^{-1} to 3400 s^{-1}. Figure 7.21 (b) suggests that the radial crushing stress increases with strain rate. However, as previously mentioned the spread in the data is very large so no conclusive statements can be made about the trend. Figure 7.21 (c) indicates that the tangential crushing stress is approximately constant over strain rates between 1600 s^{-1} to 3800 s^{-1}. In summary, the crushing stress appears to be unaffected by the value of the strain rate, as shown in Figure 7.21, although there is possibly a strain-rate dependency for the radial direction.

As the strain rate is a function of the impact velocity of the striker bar and the length of the specimen, a check was carried out to ensure that the impact velocity was not incorrectly interpreted as a strain-rate effect. The normalised crushing stresses for all the three directions are plotted against impact velocity in Figure 7.22. A straight line

best fit is shown in each of Figure 7.22 (a)-(c). The results indicate strongly that the crushing stress is not a function of the impact velocity.

The plateau stresses for the three principal directions were plotted against density in Figure 7.23. A best fit straight line is fitted to the experimental data for each direction and for both quasi-static and SHPB loading scenarios. The results of Vural and Ravichandran [99] suggested no increase in the plateau stress with strain rate for along the grain balsa. This was attributed to the reduction in the inertia effect associated with the progressive deformation rather than the initiation the deformation mechanism. The results presented herein indicate an increase for the SHPB tests. Surprisingly, the radial and tangential SHPB tests indicate greater percentage increases in the plateau stress than seen in the along the grain direction (Figure 7.23). As in the case of the crushing stress, the plateau stress increases with density.

The effect of the density was minimized by adopting the same normalisation procedure as that followed for the crushing stress. The normalised plateau stresses were plotted against strain rate and impact velocity in Figures 7.24 and 7.25 respectively. The increase in the plateau stress was calculated by comparing the means of the quasi-static and SHPB data shown in Figures 7.24 and 7.25. In the along the grain direction this increase is 11% and in the radial and tangential, 38% and 39% respectively. Note that in Figure 7.24 (a) the SHPB mean and the best fit straight line are almost identical, suggesting that the plateau stress does not increase within the strain rate shown. The same applies for the tangential specimens (Figure 7.24 (c)). Although, the best fit straight line for the radial SHPB test data suggests an increase with strain rate, the amount of scatter in the data points may be the cause of this apparent increase (Figure 7.24 (b)). Figure 7.25 illustrates that the impact velocity has negligible effect on the plateau stress.

The ratio of the crushing stress to plateau stress is plotted for all the quasi-static and SHPB tests against density in Figure 7.26. The dynamic loading of balsa appears to have very little effect on this stress ratio. From Figures 7.26 (a) and (c) dynamic loading clearly has negligible effect in both along and tangential directions. From

Figure 7.26 (b) there maybe a slight effect in the radial direction, although the data is inconclusive.

The strain rate effects on the densification strain were examined as well. Fitting the experimental SHPB data for the densification strain into Equations (7.5) and (7.6) the following relationships were obtained for both along and across the grain specimens:

$$\varepsilon_{d(SHPB)}^{L} = 1 - 2.66\frac{\rho_o}{\rho_S} \quad ; \tag{7.26}$$

$$\varepsilon_{d(SHPB)}^{L} = 0.83(1 - \frac{\rho_o}{\rho_S}) ; \tag{7.27}$$

$$\varepsilon_{d(SHPB)}^{R} = 1 - 3.54\frac{\rho_o}{\rho_S} \quad ; \tag{7.28}$$

$$\varepsilon_{d(SHPB)}^{R} = 0.62(1 - \frac{\rho_o}{\rho_S}) ; \tag{7.29}$$

$$\varepsilon_{d(SHPB)}^{T} = 1 - 3.10\frac{\rho_o}{\rho_S} \quad ; \tag{7.30}$$

$$\varepsilon_{d(SHPB)}^{T} = 0.64(1 - \frac{\rho_o}{\rho_S}) . \tag{7.31}$$

Equations (7.26)-(7.31) were plotted with the data from the SHPB tests in Figure 7.27. In the same figure the densification strains from the quasi-static tests are shown along with the corresponding equations for each direction. As in the case of the quasi-static tests, Equation (7.6) produced the best fit for the SHPB data. The general trend as described from Equation (7.6) is that the densification strain will decrease with density for both quasi-static and SHPB results. The constant C_5 in Equation (7.6) is found to be 0.83 for the SHPB along the grain. Note that the quasi-static

value was 0.82. Given the spread in the test data there is negligible difference between the quasi-static and dynamically loaded specimens. This is at odds with the findings by Vural and Ravichandran [99] who suggested values for the constant C_5 as 0.87 and 0.75 for the quasi-static and SHPB results respectively. This represented a reduction in the densification strain of 14% due to strain-rate effect. Strain-rate also produces negligible effect on densification strain for both radial and tangential directions (Figures 7.27 (b) and (c)).

7.5 Direct Impact Tests

7.5.1 Experiments

The Direct Impact tests were performed using a 40 mm diameter PMMA pressure bar (see Chapter 3). Attenuation and dispersion effects were taken into account as was discussed in Chapter 4. A description of the tests that were carried out to measure the proximal and distal end forces was given in Section 3.4.

7.5.2 Specimens

For the Direct impact tests cylindrical specimens were cut from big blocks of balsa wood along the three principal directions. Their diameter was approximately 23.12 mm and their lengths varied between 6 to 65 mm. As in the case of the quasi-static and SHPB specimens, their moisture content was measured to be less than 7%.

7.5.3 Results

Typical distal end forces for along the grain DI tests are shown in Figures 7.28 (a) and (b). After an initial peak the forces tended to reduce steadily. For some tests the force held steady for a short period, e.g. Figure 7.28 (b) wherein after an initial peak the force remains approximately constant at about 7 kN for a short period. Typical

proximal end force pulses are shown in Figure 7.28 (c) and (d). The shape of the force pulses was similar for both proximal and distal end measurements. Note that the sharp rise in the force at 2.4×10^{-4} seconds for Figure 7.28 (d) is associated with full densification of the specimen.

Figures 7.29 (a) and (b) show typical distal end force pulses for the radial DI tests. The force pulse in Figure 7.29 (a) is similar to a quasi-static load deflection curve and shows that compression to densification has occurred. The difference to a quasi-static curve is the initial peak in the force pulse. Figure 7.29 (b) illustrates a load pulse for a specimen that has not been fully crushed. After an initial peak, the force drops to a minimum before rising again and staying constant for a short period of time.

The proximal force pulses for the DI tests on radial and tangential specimens were difficult to interpret. Representative readings are shown in Figures 7.29 (c) and (d). On impact of the specimen with the Hopkinson pressure bar, an instantaneous rise to a peak load was expected. Instead, the force increased in a series of steps at lower loads than expected. The specimens exhibited global buckling patterns rather than uniform crushing in the loading direction. Consequently, the proximal end forces for radial and tangential DI tests do not represent crushing stresses in the specimens.

The initial peak in the distal load pulses for along the grain DI tests has been converted to stress and normalised by the relative density (see Equations (7.3)) and is plotted against impact velocity in Figure 7.30 (a). The initial peaks show a lot of scatter but no increase with increasing impact velocity. The mean value of these peaks lies between the mean crushing stresses for quasi-static and SHPB tests. The mean of the peak DI stresses is closer in value to the quasi-static mean than the SHPB mean.

The normalised initial peak stresses from along the grain proximal DI tests are plotted in Figure 7.30 (b). The mean value of the initial peaks is slightly lower than the mean value of the SHPB crushing stress. There is no apparent increase in peak

stress with impact velocity. Compaction waves are not considered to have a notable effect and are discussed later in this chapter.

The initial peak normalised distal end stress for the radial specimens is plotted against impact velocity in Figure 7.30 (c). For radial specimens, the mean of the initial peaks is greater than the mean crushing stress for the SHPB specimens. The proximal stresses plotted in Figure 7.30 (d) are actually the maximum stresses before densification rather than the initial peaks. Due to the unexpected deformation of the specimens, little can be said of these results.

7.6 Discussion

The effect of the strain-rate on the properties of balsa compressed in the longitudinal direction is somewhat confusing. The SHPB data of along the grain balsa wood presented by Vural and Ravichandran [99] suggest that the crushing stress is approximately doubled, the plateau stress is unaffected and the densification strain is reduced by 14% when compared with their corresponding quasi-static values. The SHPB results presented herein indicate that strain rate produces an increase in the crushing stress of 16%, an increase in the plateau stress of 11% and negligible change in the densification strain when compared with the analogous quasi-static properties. These increases in the crushing and plateau stress levels are similar to the level of 15% by Zhao et al. [108, 109] for aluminium honeycombs. Zhao et al. [108, 109] proposed that such increases are related to the micro-inertia effect in successive folding mechanisms. Although the results reported here differ to those reported by Vural and Ravichandran [99], it is possible to have confidence in the new data for a number of reasons. First, there was very close agreement between the forces on both specimen faces, indicating that inertia and wave effects within the specimen were insignificant (see Section 2.4). Second, specimens of different lengths were tested and consistent results were obtained in terms of crushing stress and plateau stress, indicating that friction effects were not important (see Section 2.4). Third, initial peak stresses were observed for all along the grain specimens, indicating that the specimens were not strongly influenced by specimen end effects. In contrast, Vural

and Ravichandran [99] did not show any data to confirm stress uniformity within the specimen and only tested one specimen size (length of 5 mm).

The SHPB crushing and plateau stresses of along the grain balsa are greater than the quasi-static values. However, these stresses do not vary with strain rate over the strain rate that the experiments were performed i.e. between 874-3426 s^{-1}. This is indicated in Figures 7.21 (a) and illustrated in Figure 7.16, where a change in strain rate (Figure 7.16 (c)) is not associated with a change in stress (Figure 7.16 (b)).

For the radial and tangential directions there is a greater percentage increase in crushing and plateau stresses associated with the SHPB results than in the case for the along the grain direction. However, the actual magnitude of the increase in stress is smaller in these directions. Note that the concepts of strain and strain rate being applied to a cellular material are average terms. In reality large localised bending will occur in some regions while other regions remain relatively undeformed. Two specimens with different lengths may have similar localised deformation rates if subjected to the same loading wave in the SHPB set-up. Nevertheless, the average strains and strain rates associated with the specimens would be very different. For this reason, a direct relationship between the mechanical properties and strain rate is not to be expected. Note that there is also no direct link between the impact velocity of the SHPB tests and the mechanical properties (Figure 7.22).

It is well known that compaction waves can be present during the dynamic compression of wood and other cellular materials, see ref. [103]. Above a certain critical impact velocity, these compaction waves result in a quadratic relationship between distal end stresses and impact velocity. No such trend is evident in the test data reported in this chapter, e.g. see Figure 7.30(b) and (d). Compaction waves are shown to be of much greater importance for similar tests carried out on Rohacell foam and so will be discussed more fully in the next chapter.

7.7 Conclusions

The high level of agreement between the forces measured at both specimen/bar interfaces and the good agreement in displacements predicted at the ends of each bar

(see Figures 5.7 and 6.8) suggests that the results obtained from the dynamic compression of balsa wood in all three directions are accurate. In general there was an increase of the SHPB stress values as compared with the quasi-static data. The percentage increase was greater for the across the grain balsa wood. On the other hand, no apparent increase was observed with increasing strain rate. It is more difficult to provide general conclusions from the DI tests. The average values for the crushing stresses for along the grain specimens were between the corresponding SHPB and quasi-static values. Across the grain, the average crushing stress values are greater than either the SHPB or quasi-static values. In general, the results of the DI tests showed no increase in stress levels with impact velocity.

Test Number	Mass (gr)	Length (mm)	Density (kgm^{-3})
1	9.172	46.53	124
2	9.468	47.22	126.13
3	3.961	20.23	123.92
4	3.962	20.19	123.49
5	2.054	10.54	122.69
6	2.031	10.26	124.8
8	6.787	45.37	94.66
9	5.473	27.08	128.56
10	5.151	26.06	125.47
11	2.010	12.39	102.87

Table 7.1 Masses, lengths and densities of the along the grain specimens from the unconstrained quasi-static tests.

Test Number	Mass (gr)	Length (mm)	Density (kgm^{-3})
12	9.131	46.92	122.42
13	8.679	46.54	117.46
14	3.980	20.25	123.47
15	3.984	20.40	122.90
16	1.972	10.31	120.48
18	7.151	44.26	102.54
19	6.937	43.91	99.82
20	4.881	24.28	128.79
21	1.847	11.66	100.11
22	1.850	11.50	102.05

Table 7.2 Masses, lengths and densities of the along the grain specimens from the constrained quasi-static tests.

Test Number	Mass (gr)	Length (mm)	Density (kgm^{-3})
15	14.264	45.02	199.57
16	13.639	45.35	187.10
19	10.474	28.82	226.09
20	9.296	29.04	202.08
23	4.840	13.40	225.50
24	4.615	15.77	183.59
25	3.686	12.71	182.26

Table 7.3 Masses, lengths and densities of the radial specimens from the unconstrained quasi-static tests.

Test Number	Mass (gr)	Length (mm)	Density (kgm^{-3})
17	13.477	45.16	187.81
21	10.741	28.98	233.25
22	11.020	29.02	237.39
26	4.294	12.70	211.46
27	5.151	12.70	253.89

Table 7.4 Masses, lengths and densities of the radial specimens from the constrained quasi-static tests.

Test Number	Mass (gr)	Length (mm)	Density (kgm^{-3})
28	14.724	45.39	205.05
29	14.380	45.44	198.80
32	8.716	28.18	195.25
33	8.787	28.04	196.86
36	4.054	12.50	191.48
37	3.831	12.55	194.78

Table 7.5 Masses, lengths and densities of the tangential specimens from the unconstrained quasi-static tests.

Test Number	Mass (gr)	Length (mm)	Density (kgm^{-3})
30	13.931	45.35	193.92
31	14.851	45.03	207.09
34	8.821	28.20	197.55
35	9.085	28.38	200.74
38	3.983	12.47	201.37
39	4.063	12.66	205.15
40	5.689	17.63	204.71

Table 7.6 Masses, lengths and densities of the tangential specimens from the constrained quasi-static tests.

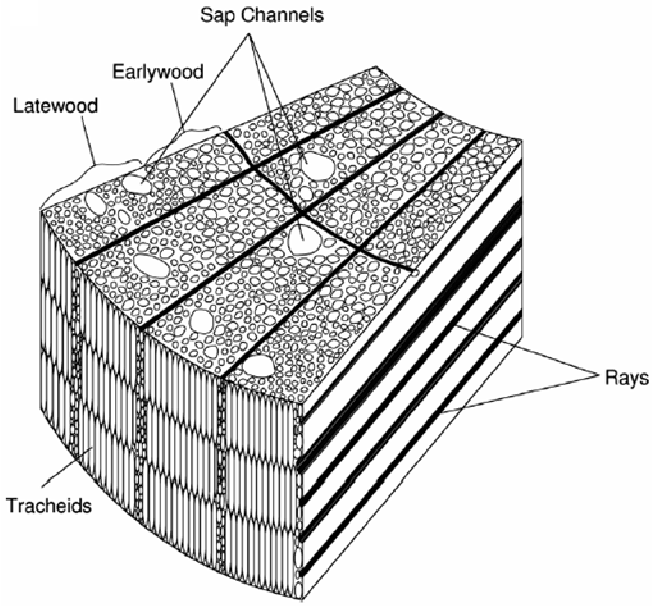

Figure 7.1 Schema showing microstructure of balsa wood [98].

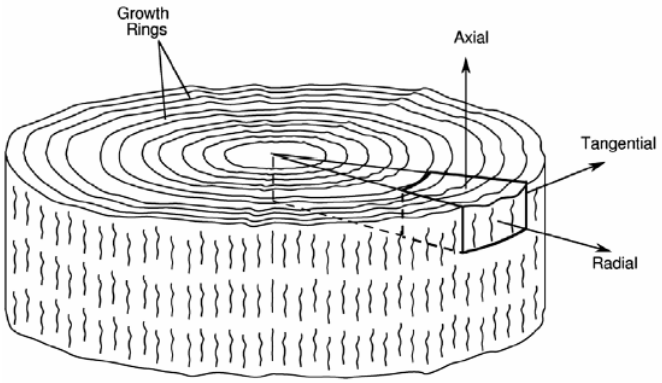

Figure 7.2 Schema showing the three principal directions of balsa wood [98].

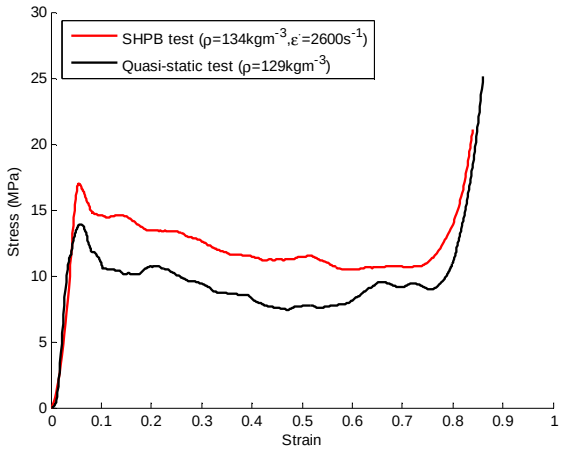

(a)

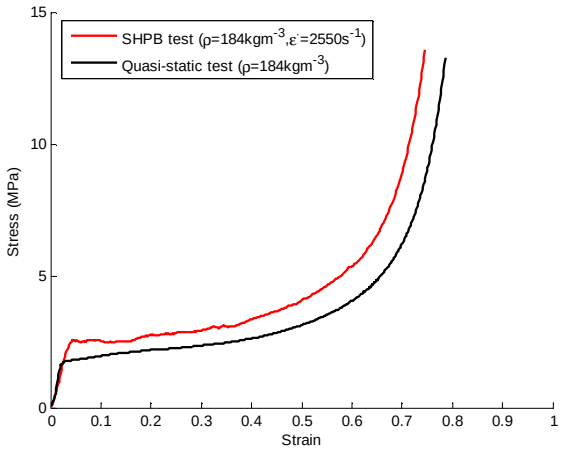

(b)

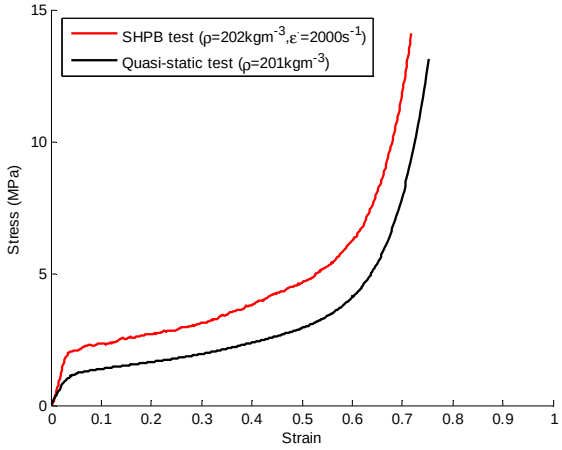

(c)

Figure 7.3 Stress-strain curves from quasi-static and SHPB tests for the (a) L, (b) R and (c) T balsa wood specimens.

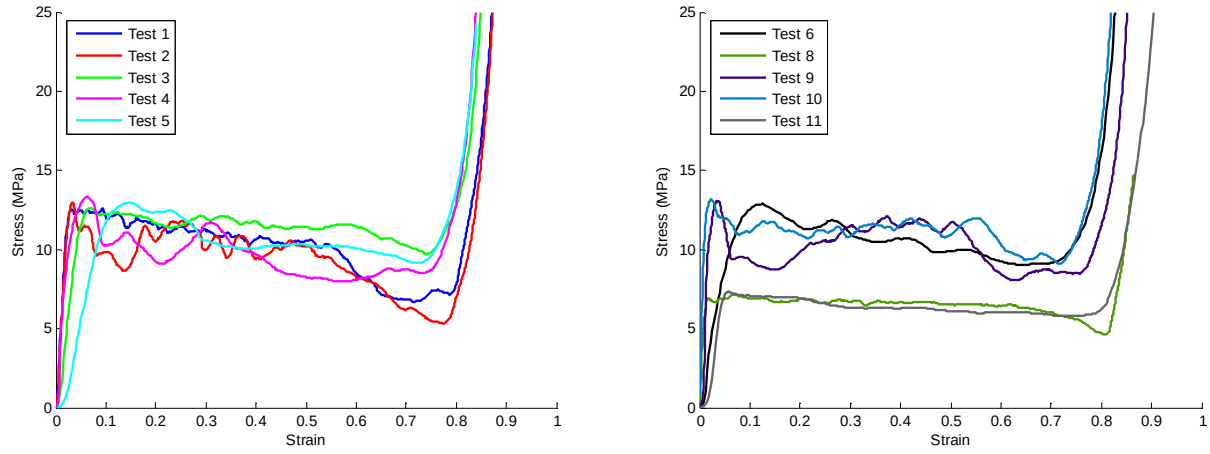

(a) (b)

Figure 7.4 Balsa wood compressed quasi-statically with no constrain in the longitudinal direction (a) Tests 1 to 5, (b) Tests 6 to 11.

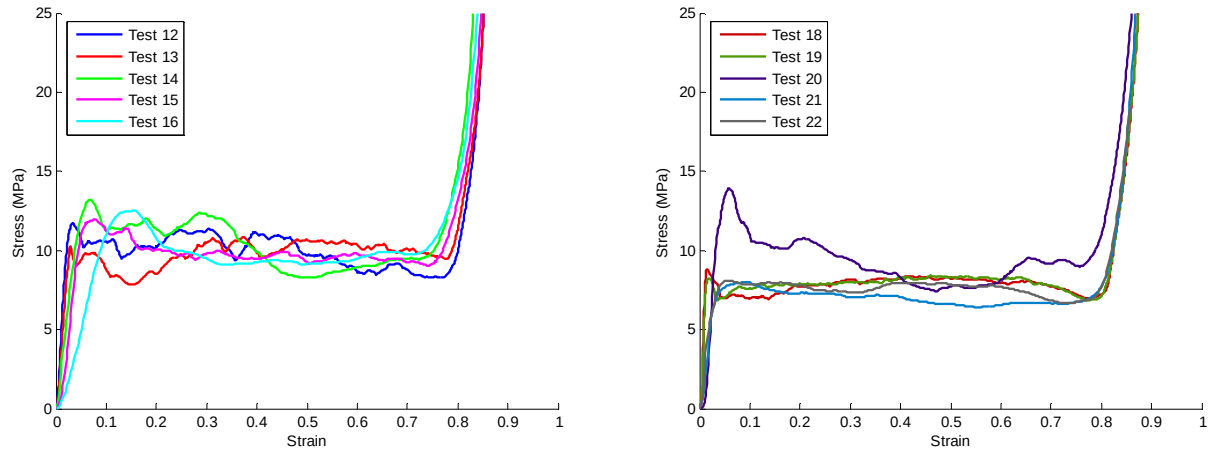

(a) (b)

Figure 7.5 Balsa wood compressesed quasi-statically with lateral constrain in the longitudinal direction (a) Tests 12 to 16, (b) Tests 18 to 22.

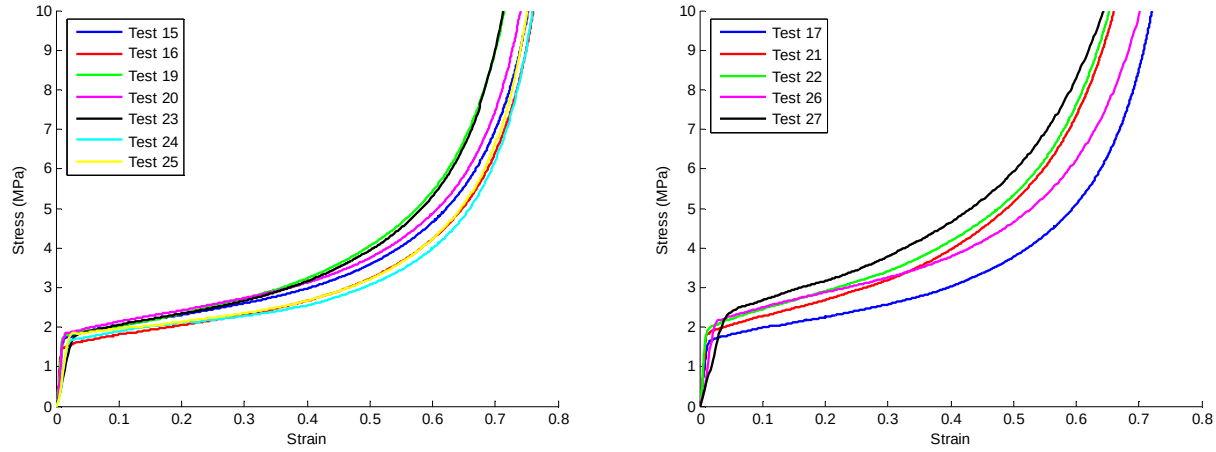

(a) (b)

Figure 7.6 Balsa wood compressed quasi-statically in the radial direction (a) unconstrained, (b) laterally constrained.

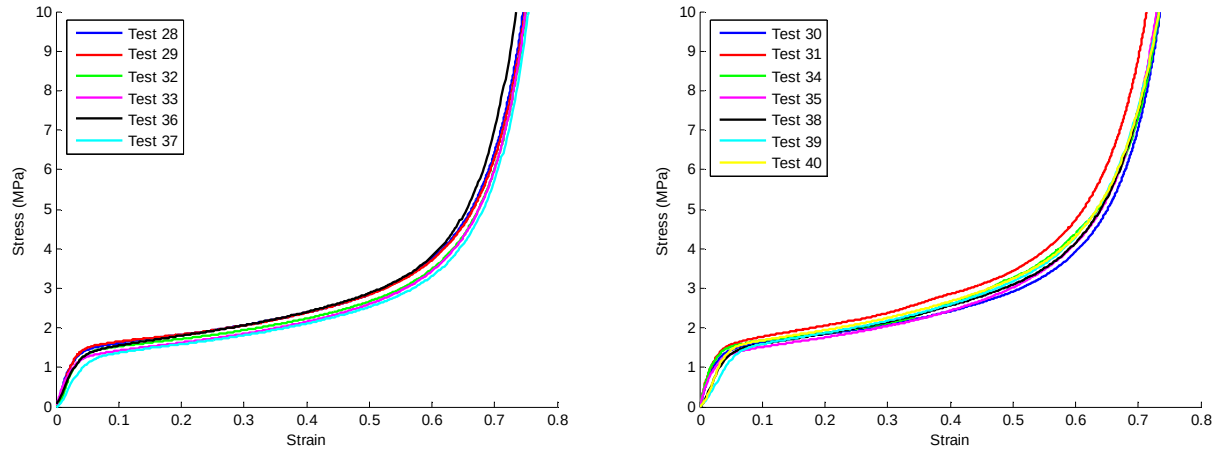

(a) (b)

Figure 7.7 Balsa wood compressed quasi-statically in the tangential direction (a) unconstrained, (b) laterally constrained.

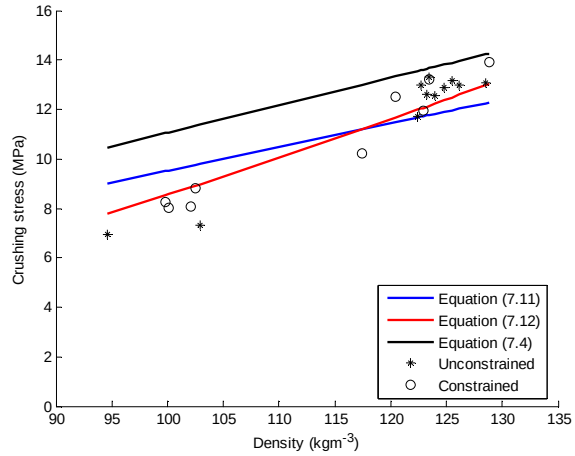

(a)

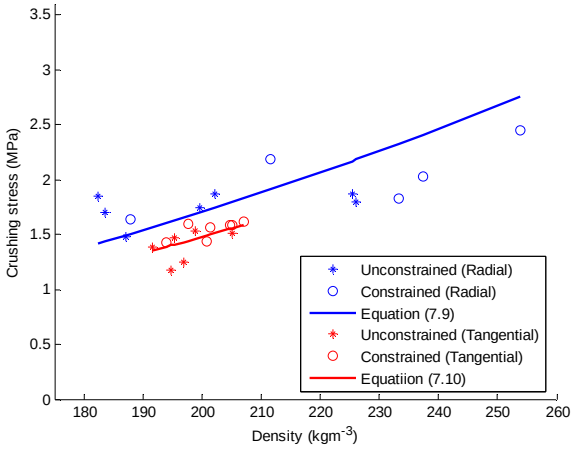

b)

Figure 7.8 Experimental and theoretical crushing stresses (a) along and (b) across the grain.

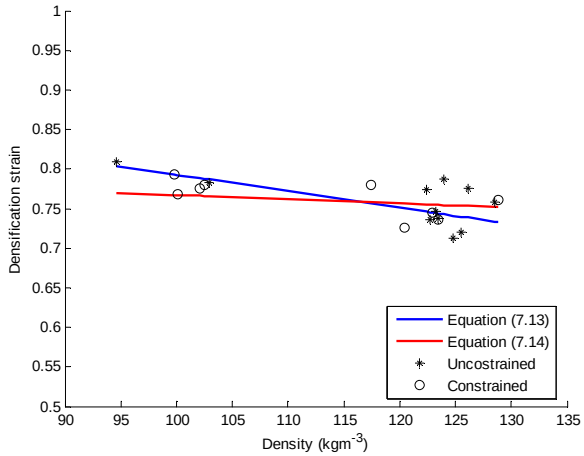

(a)

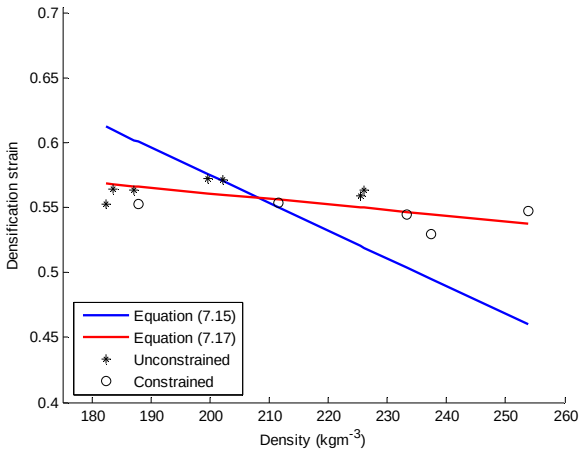

(b)

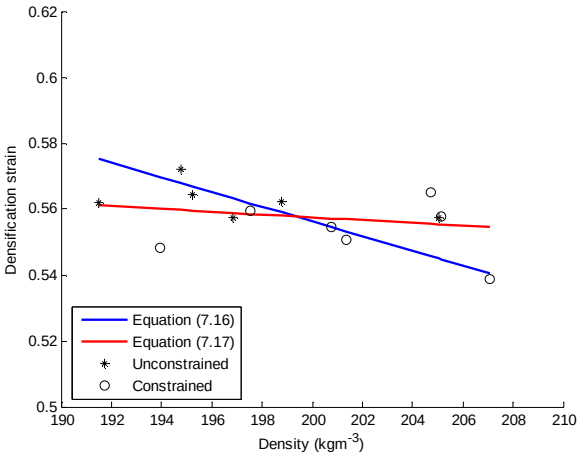

(c)

Figure 7.9 Experimental and theoretical densification strains (a) along and (b) radial and (c) tangential.

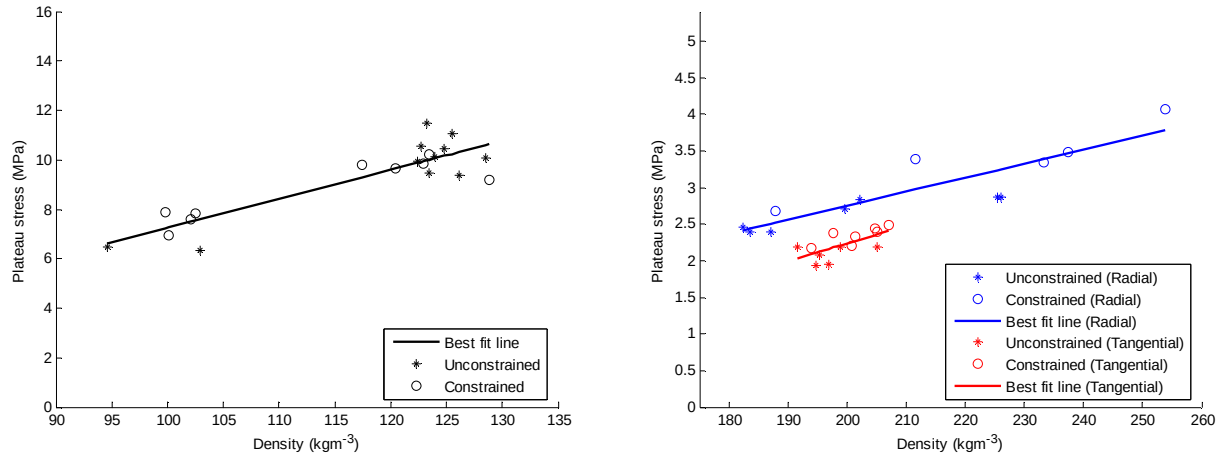

(a) (b)

Figure 7.10 Experimental plateau stresses (a) along and (b) across the grain.

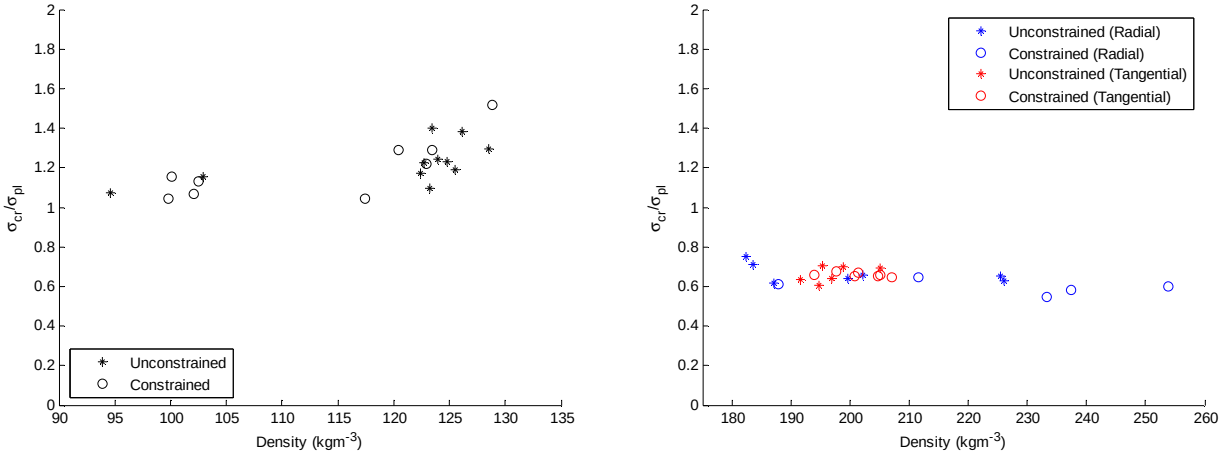

(a) (b)

Figure 7.11 Stress ratio of the crushing to plateau stress for (a) along and (b) across the grain.

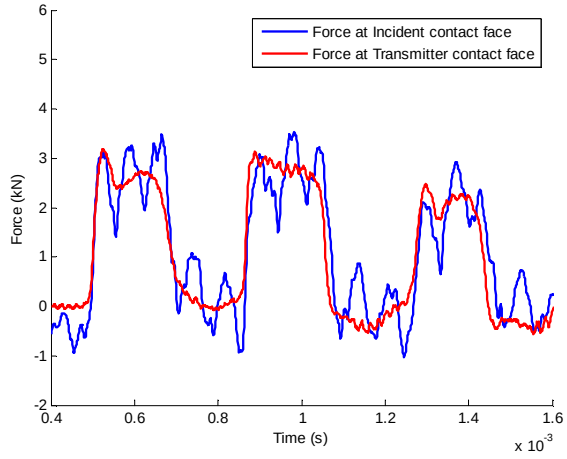

(a)

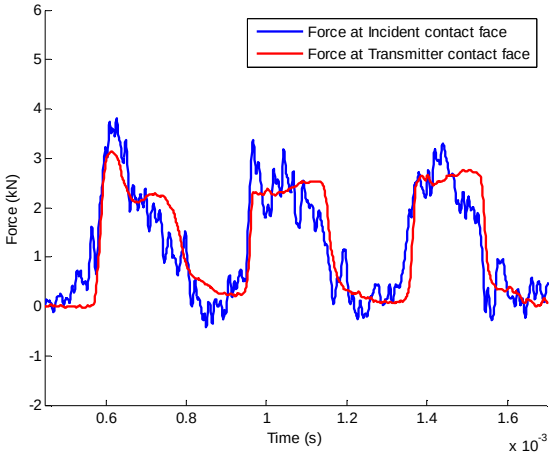

(b)

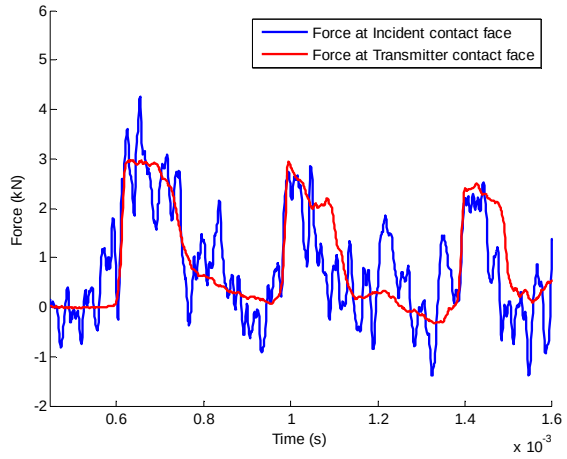

(c)

Figure 7.12 Forces at the incident/specimen and transmitter/specimen interfaces from SHPB tests on along the grain balsa wood specimens with thickness (a) 3 mm, (b) 6 mm and (c) 8 mm using Magnesium pressure bars.

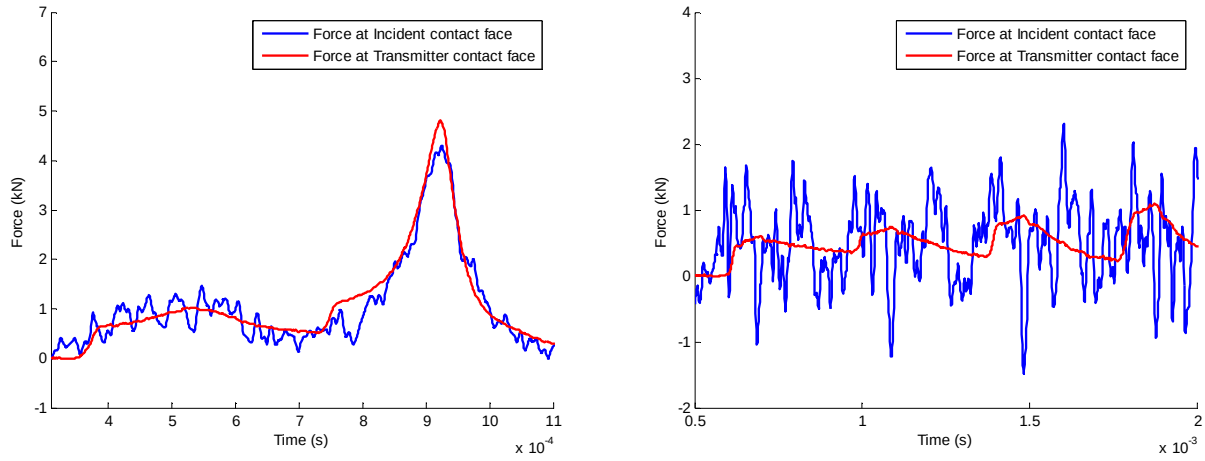

(a) (b)

Figure 7.13 Forces at the incident/specimen and transmitter/specimen interfaces from SHPB tests on tangential balsa wood specimens with thickness (a) 3 mm and (b) 6 mm using Magnesium pressure bars.

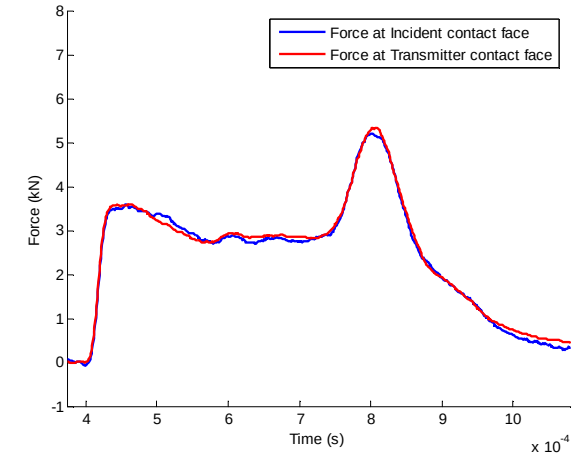

(a)

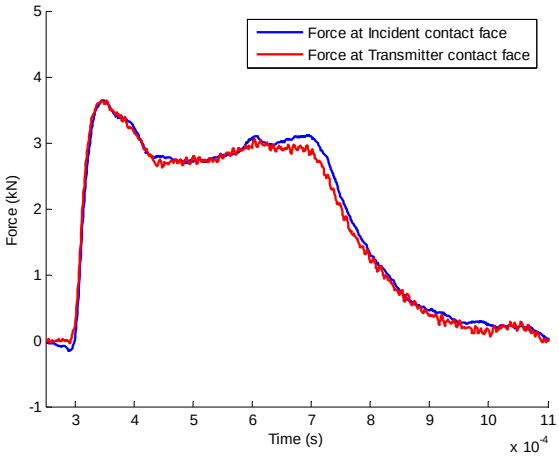

(b)

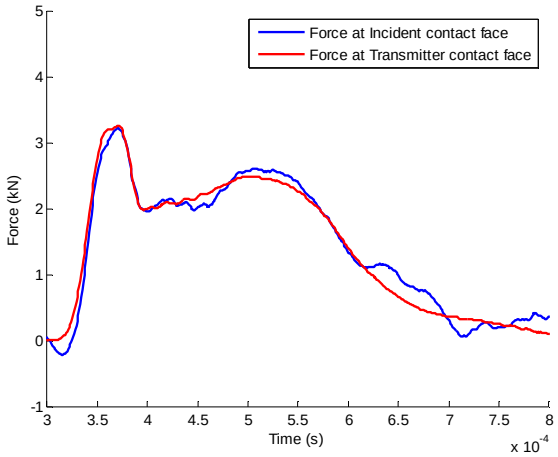

(c)

Figure 7.14 Forces at the incident/specimen and transmitter/specimen interfaces from SHPB tests on along the grain balsa wood specimens with thickness (a) 3 mm, (b) 6 mm and (c) 8 mm using PMMA pressure bars.

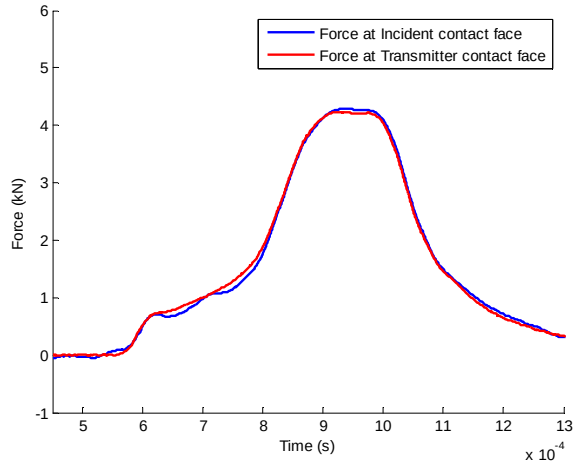

(a)

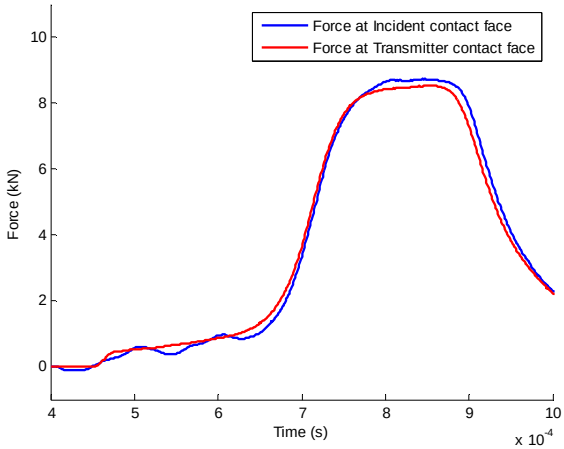

(b)

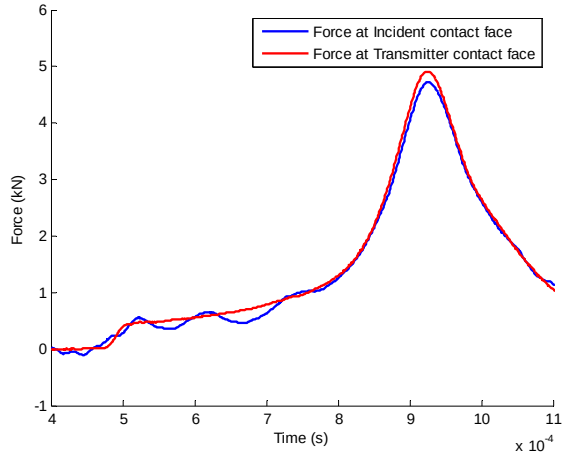

(c)

Figure 7.15 Forces at the incident/specimen and transmitter/specimen interfaces from SHPB tests on tangential specimens with thickness (a) 3 mm, (b) 6 mm and (c) 8 mm using PMMA pressure bars.

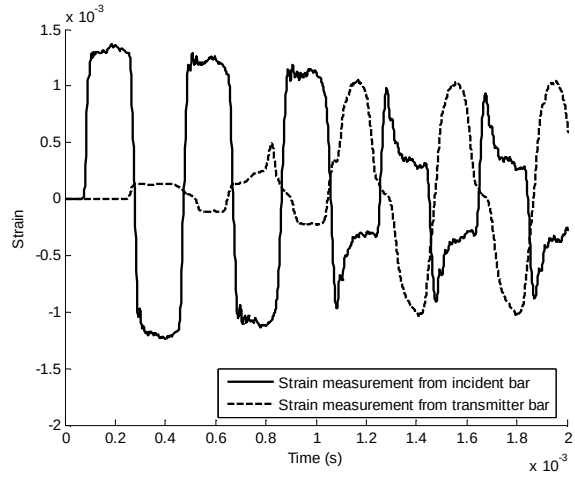

(a)

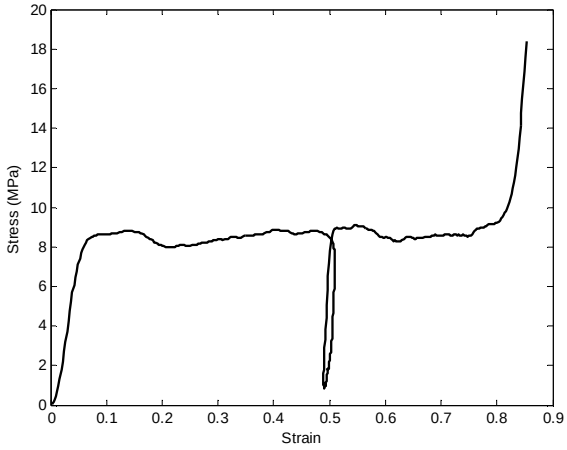

(b)

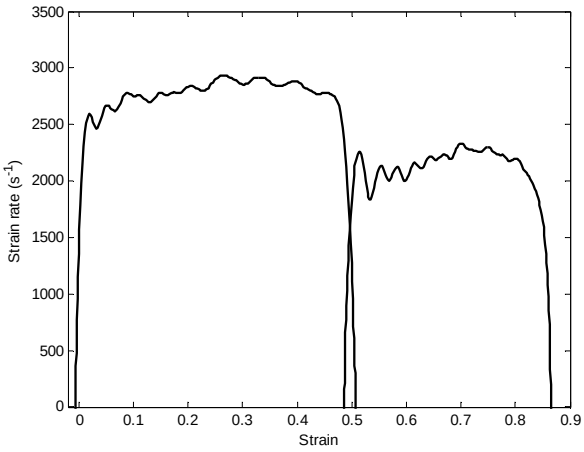

(c)

Figure 7.16 (a) Strain histories from incident and transmitter Magnesium pressure bars and (b) Stress-strain curve and (c) Strain rate from a SHPB test on along the grain balsa (length = 3 mm, density = 95 kgm^{-3}) using the Magnesium pressure bars.

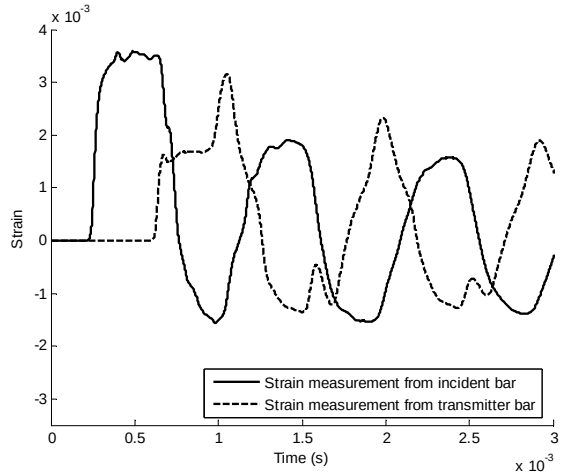

(a)

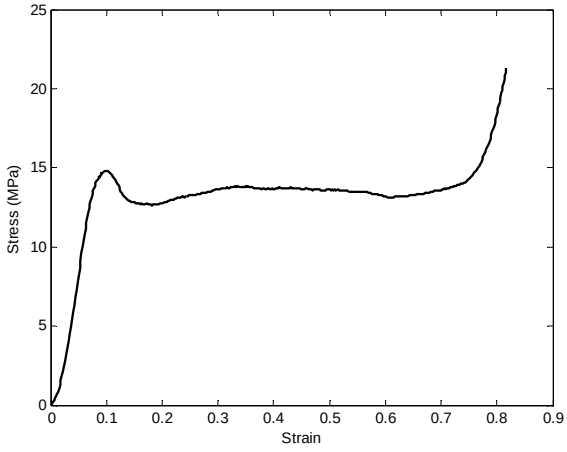

(b)

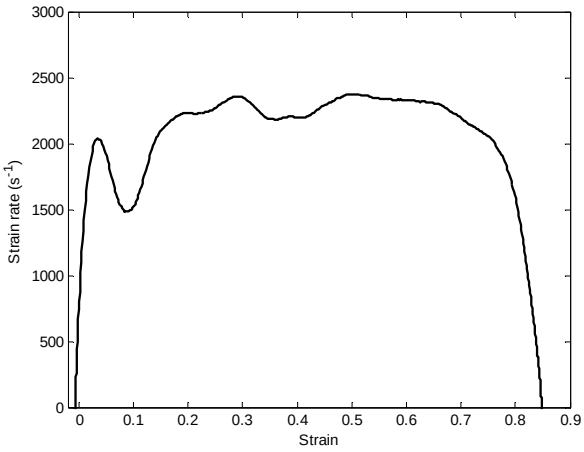

(c)

Figure 7.17 (a) Strain histories from incident and transmitter PMMA pressure bars and (b) Stress-strain curve and (c) Strain rate from a SHPB test on along the grain balsa (length = 3 mm, density = 139 kgm^{-3}) using the PMMA pressure bars.

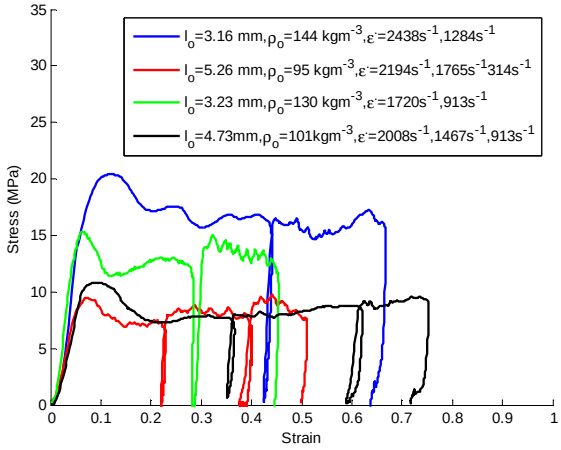

Figure 7.18 Typical stress-strain curves from SHPB tests on along the grain balsa using Magnesium pressure bars.

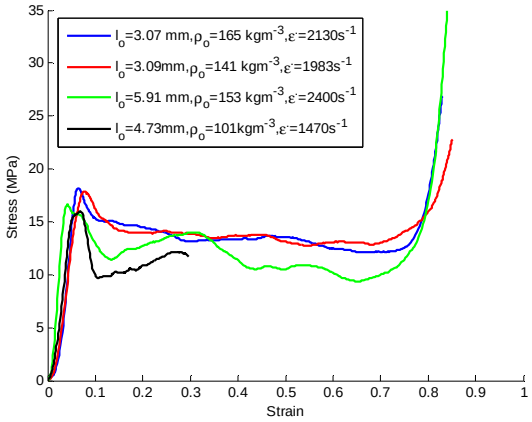

(a)

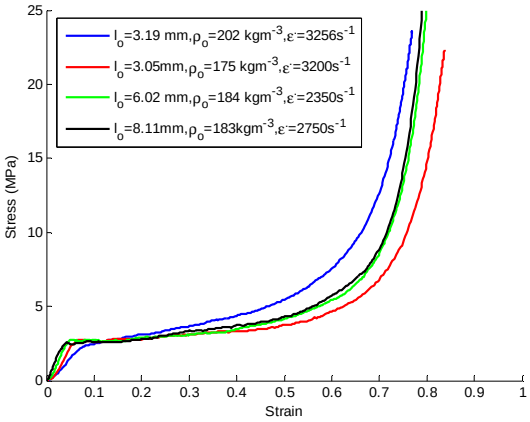

(b)

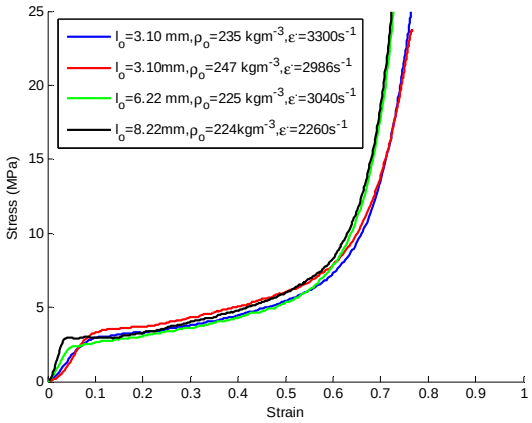

(c)

Figure 7.19 Typical stress-strain curves from SHPB tests on (a) along the grain, (b) radial and (c) tangential balsa using PMMA pressure bars.

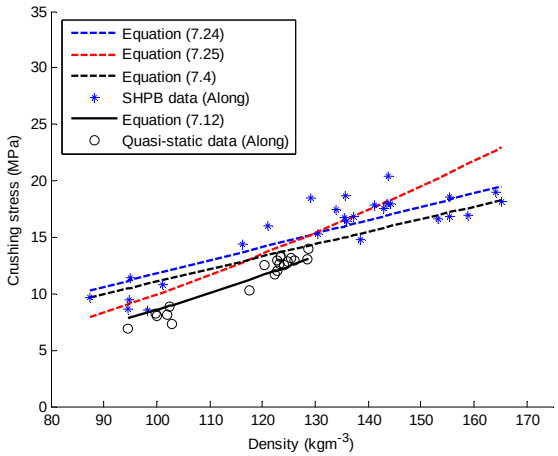

(a)

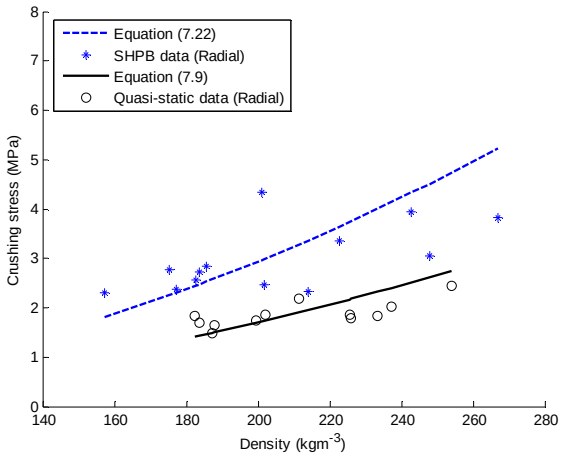

(b)

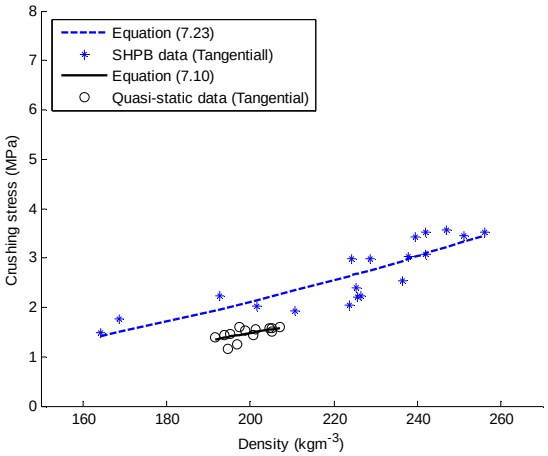

(c)

Figure 7.20 Experimental and theoretical crushing stresses from SHPB and quasi-static tests (a) along, (b) radial and (c) tangential.

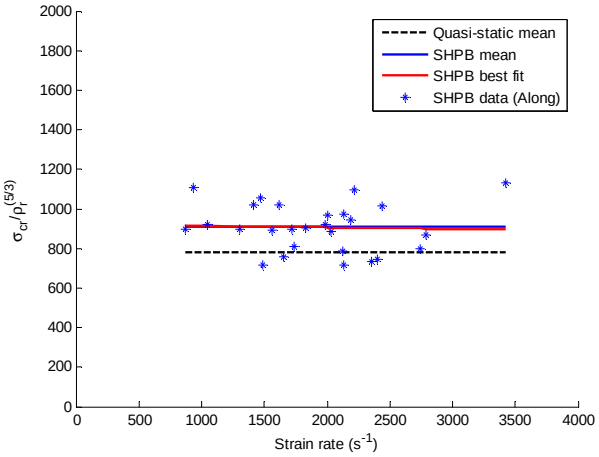

(a)

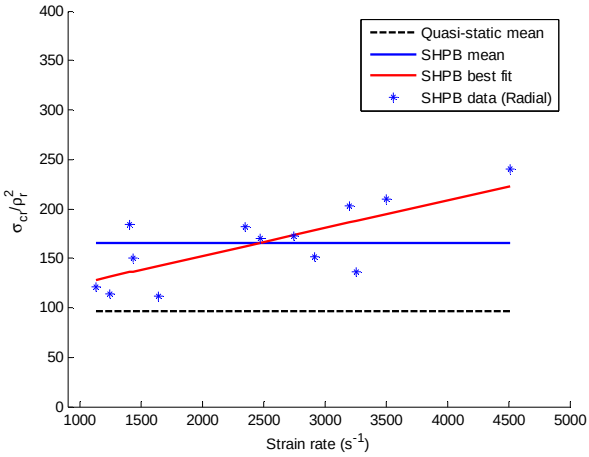

(b)

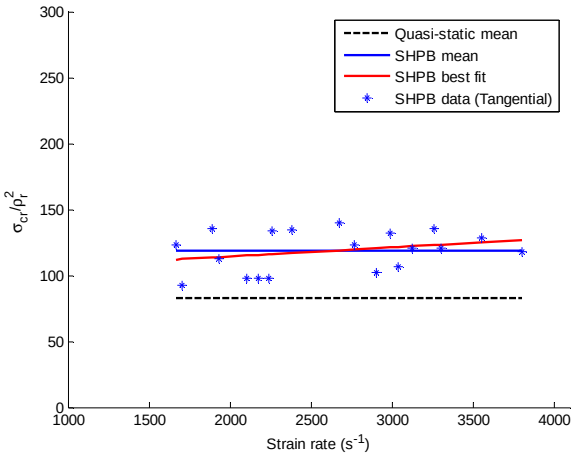

(c)

Figure 7.21 Normalised crushing stress against strain rate (a) along, (b) radial and (c) tangential

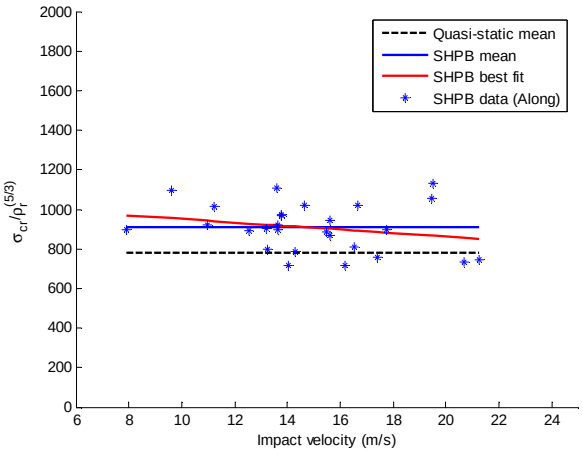

(a)

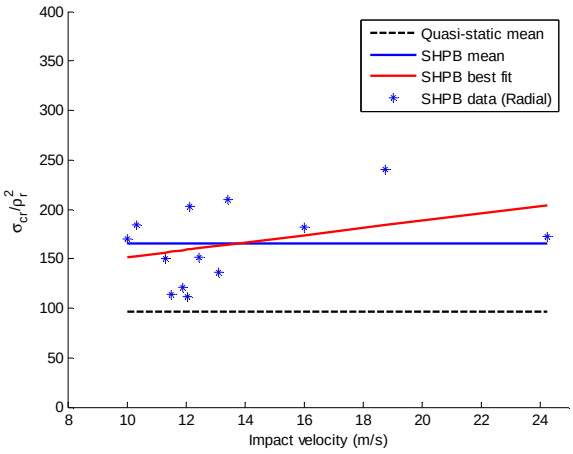

(b)

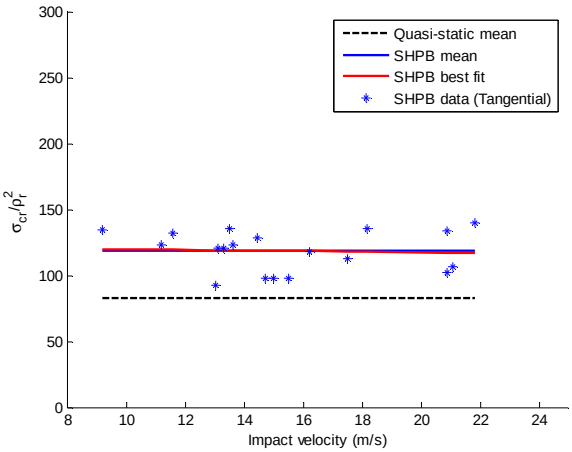

(c)

Figure 7.22 Normalised crushing stress against impact velocity (a) along, (b) radial and (c) tangential

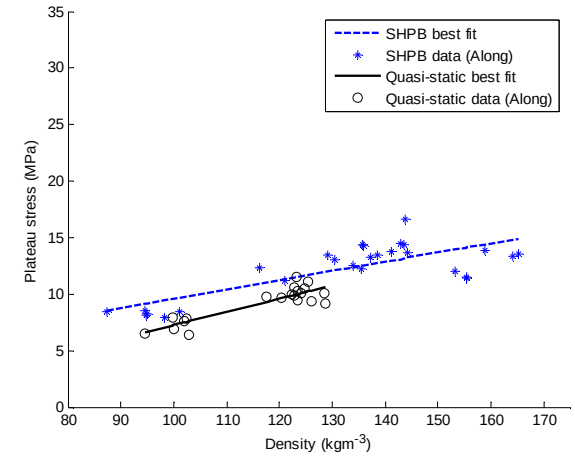

(a)

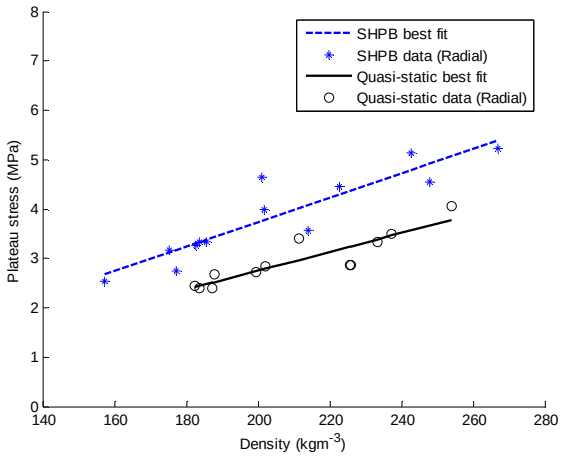

(b)

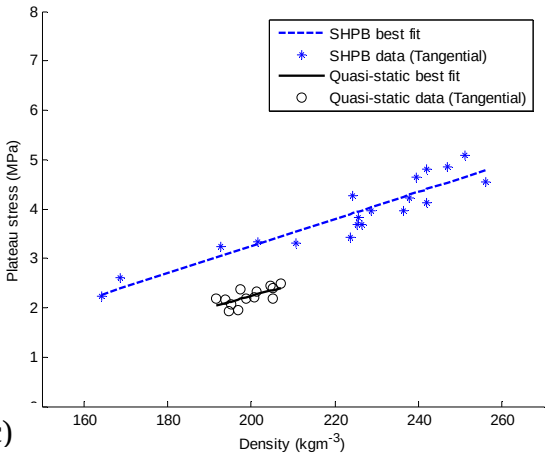

(c)

Figure 7.23 Experimental plateau stresses from SHPB and quasi-static tests (a) along, (b) radial and (c) tangential.

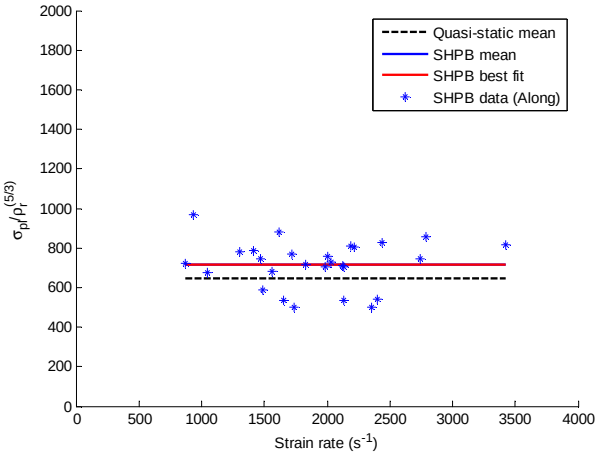

(a)

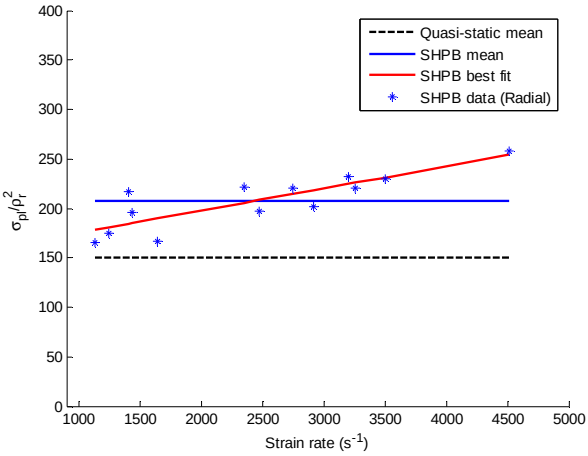

(b)

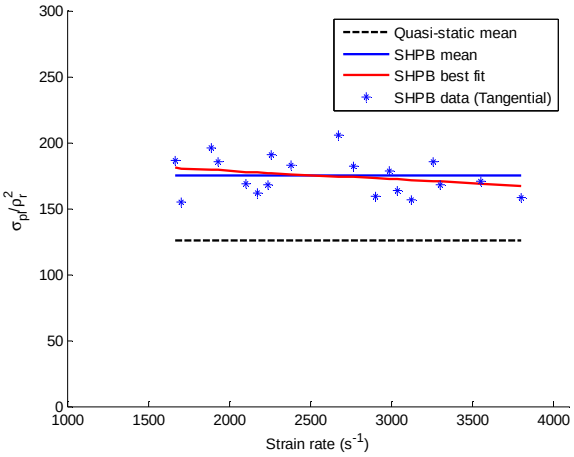

(c)

Figure 7.24 Normalised plateau stress against strain rate from SHPB and quasi-static tests (a) along, (b) radial and (c) tangential.

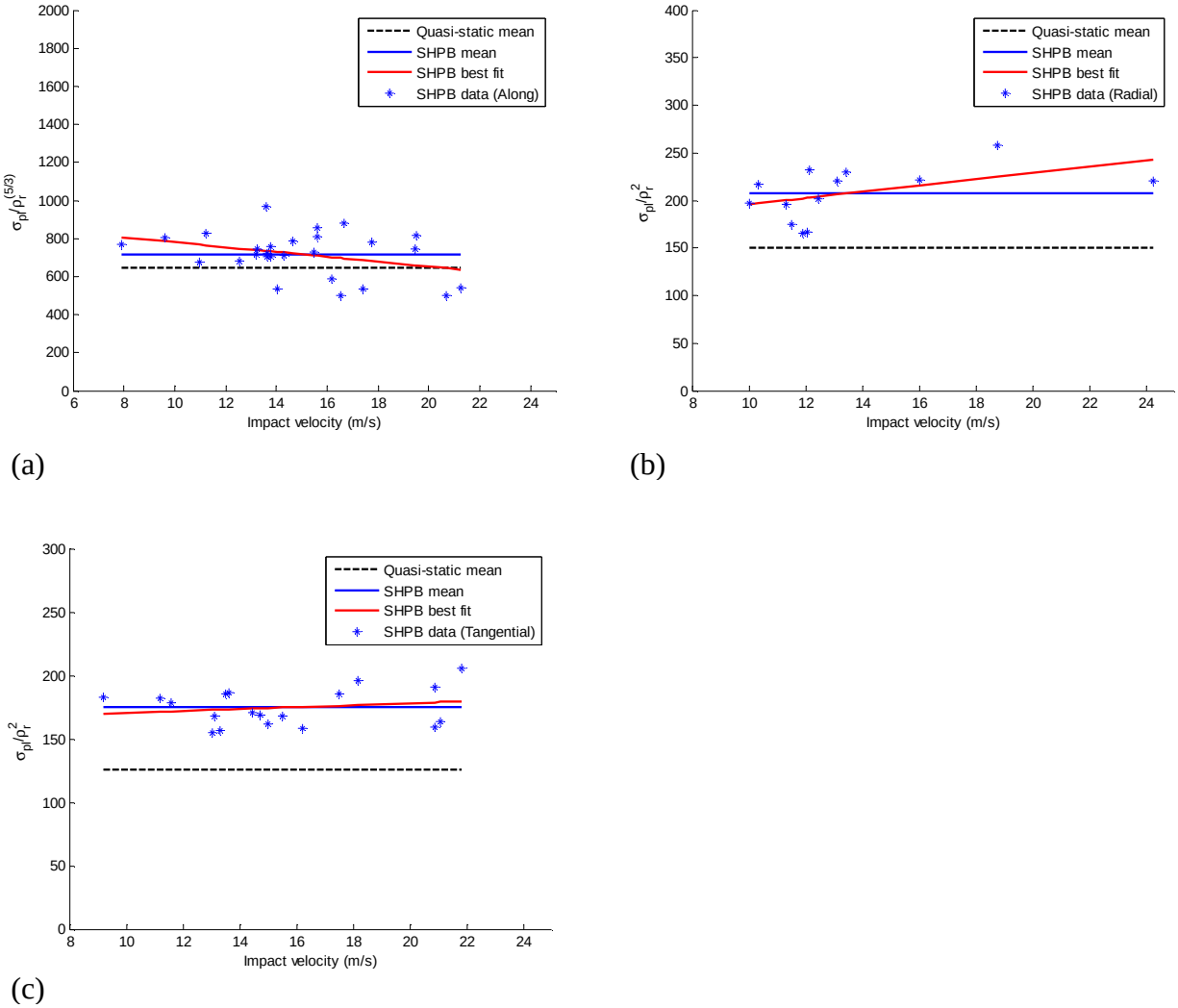

Figure 7.25 Normalised plateau stress against impact velocity from SHPB and quasi-static tests (a) along, (b) radial and (c) tangential.

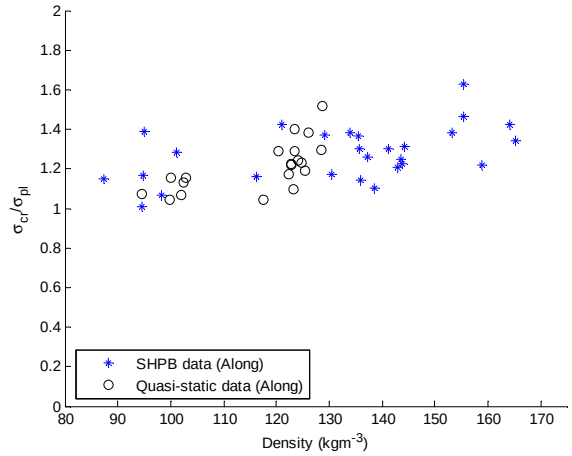

(a)

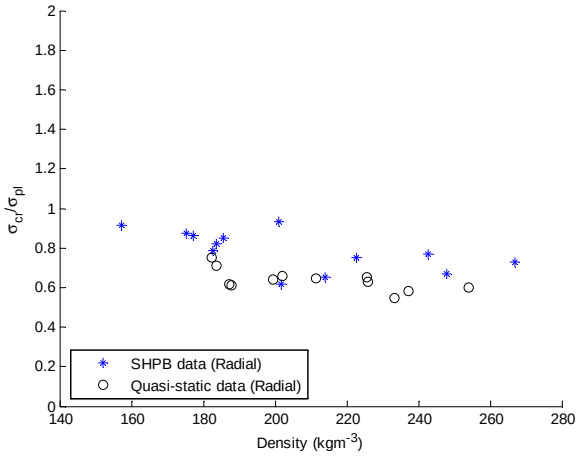

(b)

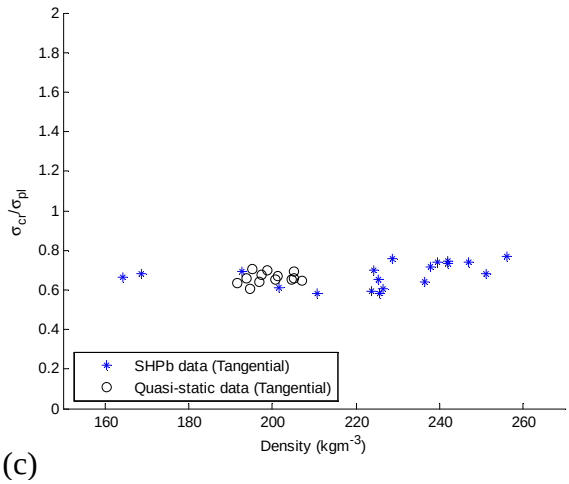

(c)

Figure 7.26 Stress ratio from SHPB and quasi-static tests (a) along, (b) radial and (c) tangential.

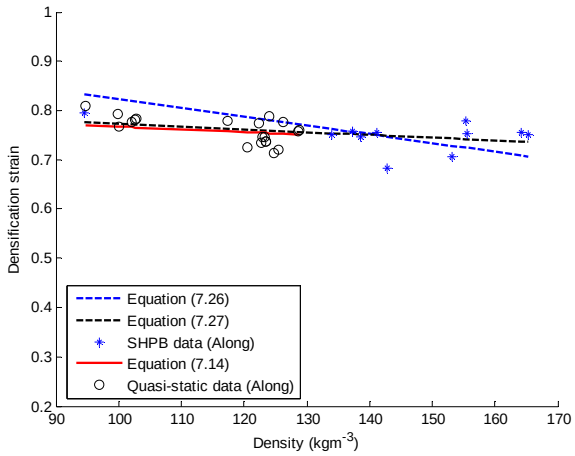

(a)

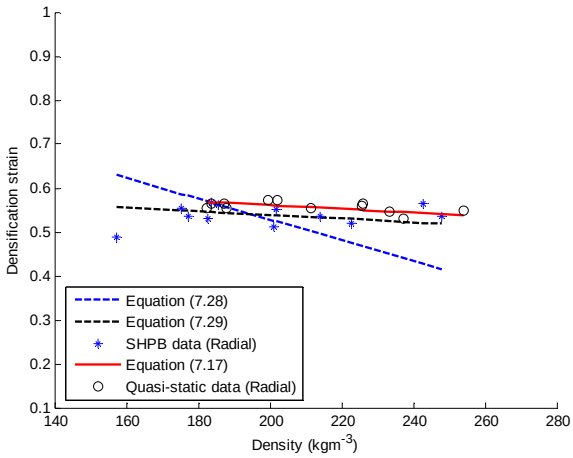

(b)

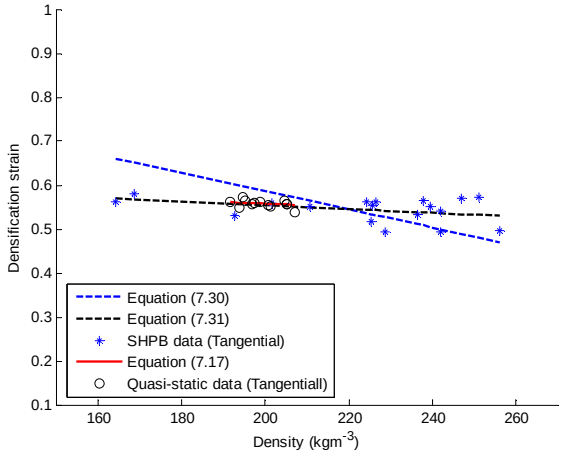

(c)

Figure 7.27 Experimental densification strains from SHPB and quasi-static tests (a) along, (b) radial and (c) tangential.

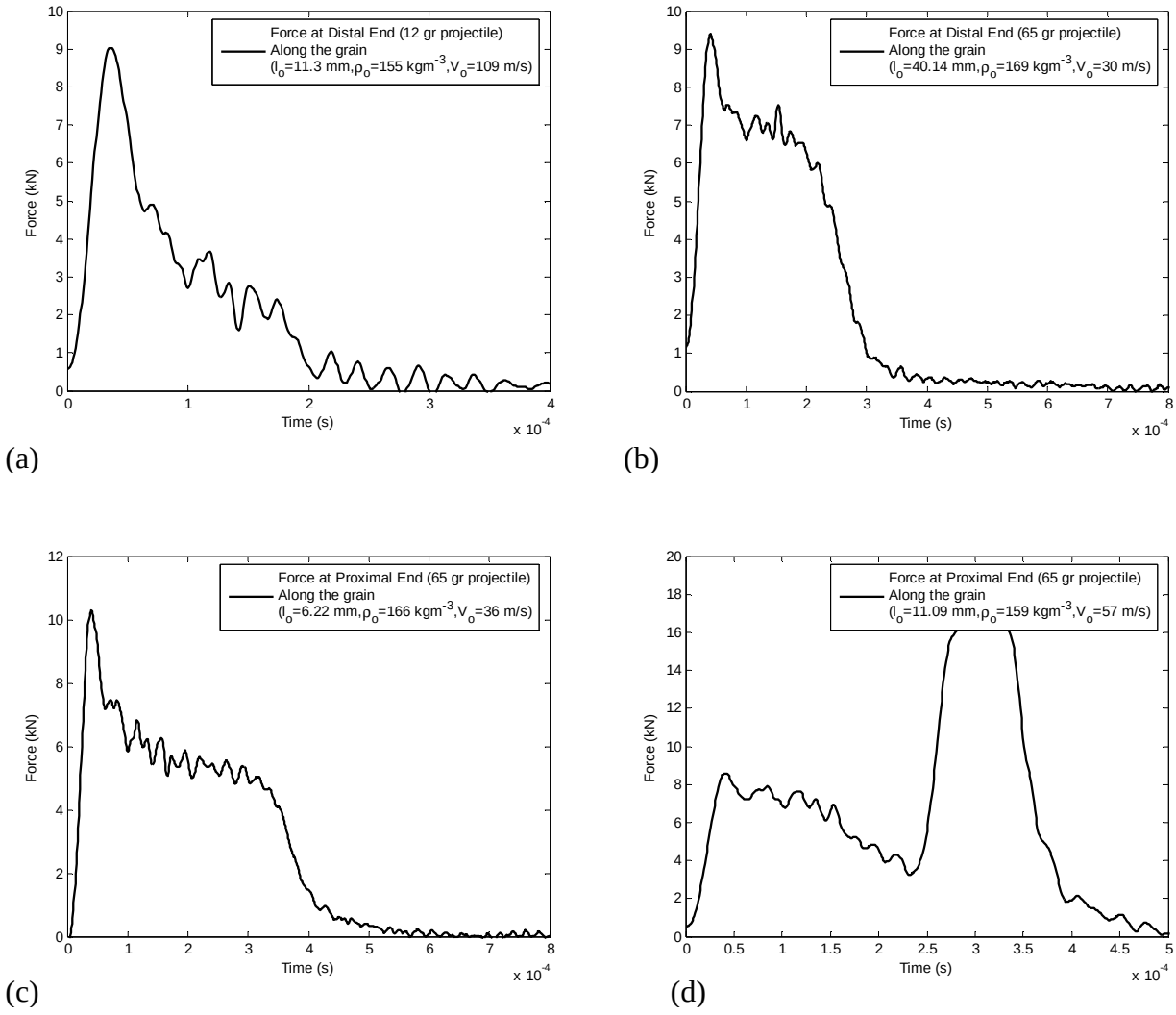

Figure 7.28 Distal ((a), (b)) and Proximal ((c), (d)) end forces for along the grain direct impact tests.

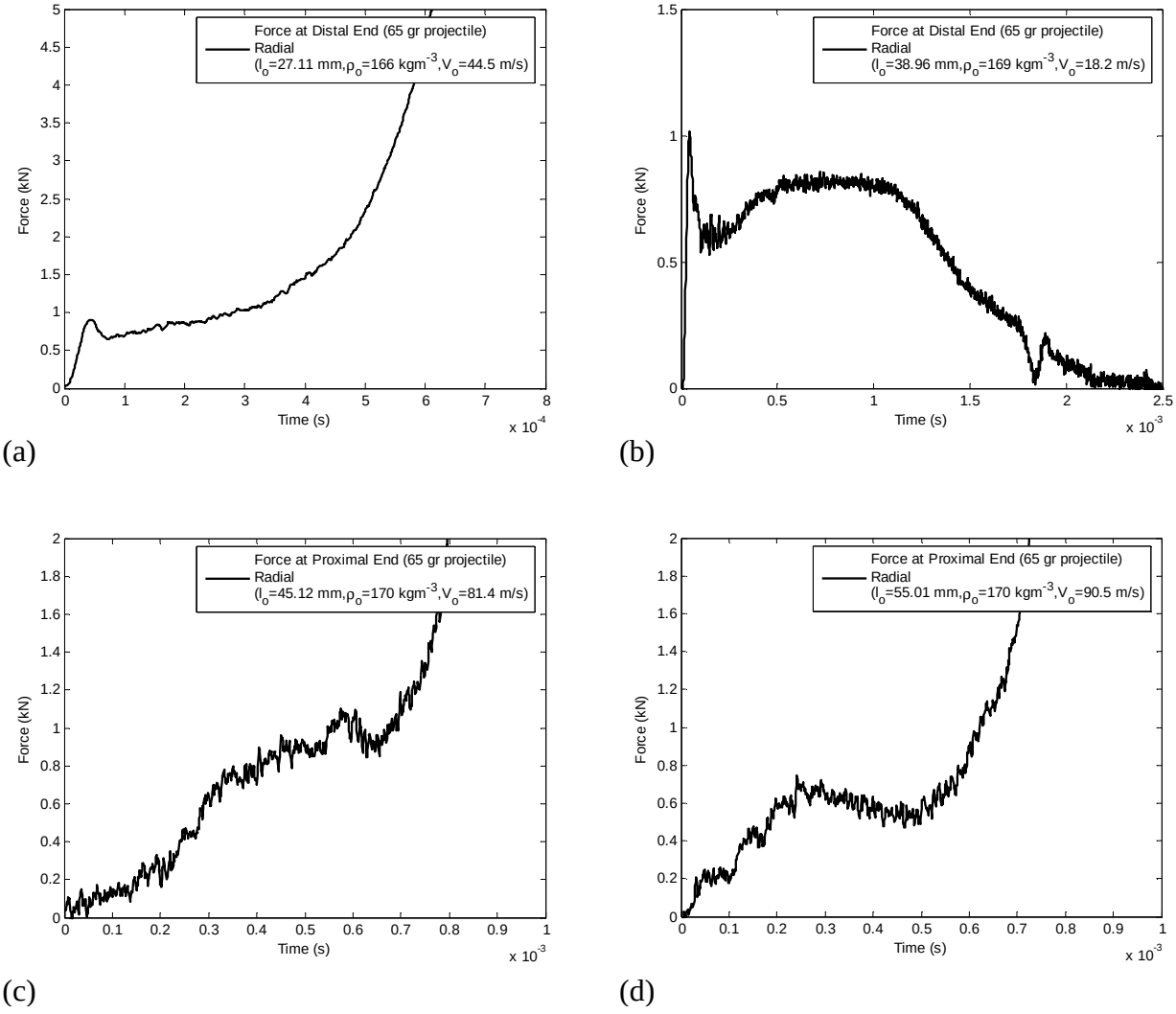

Figure 7.29 Distal ((a), (b)) and Proximal ((c), (d)) end forces for radial direct impact tests.

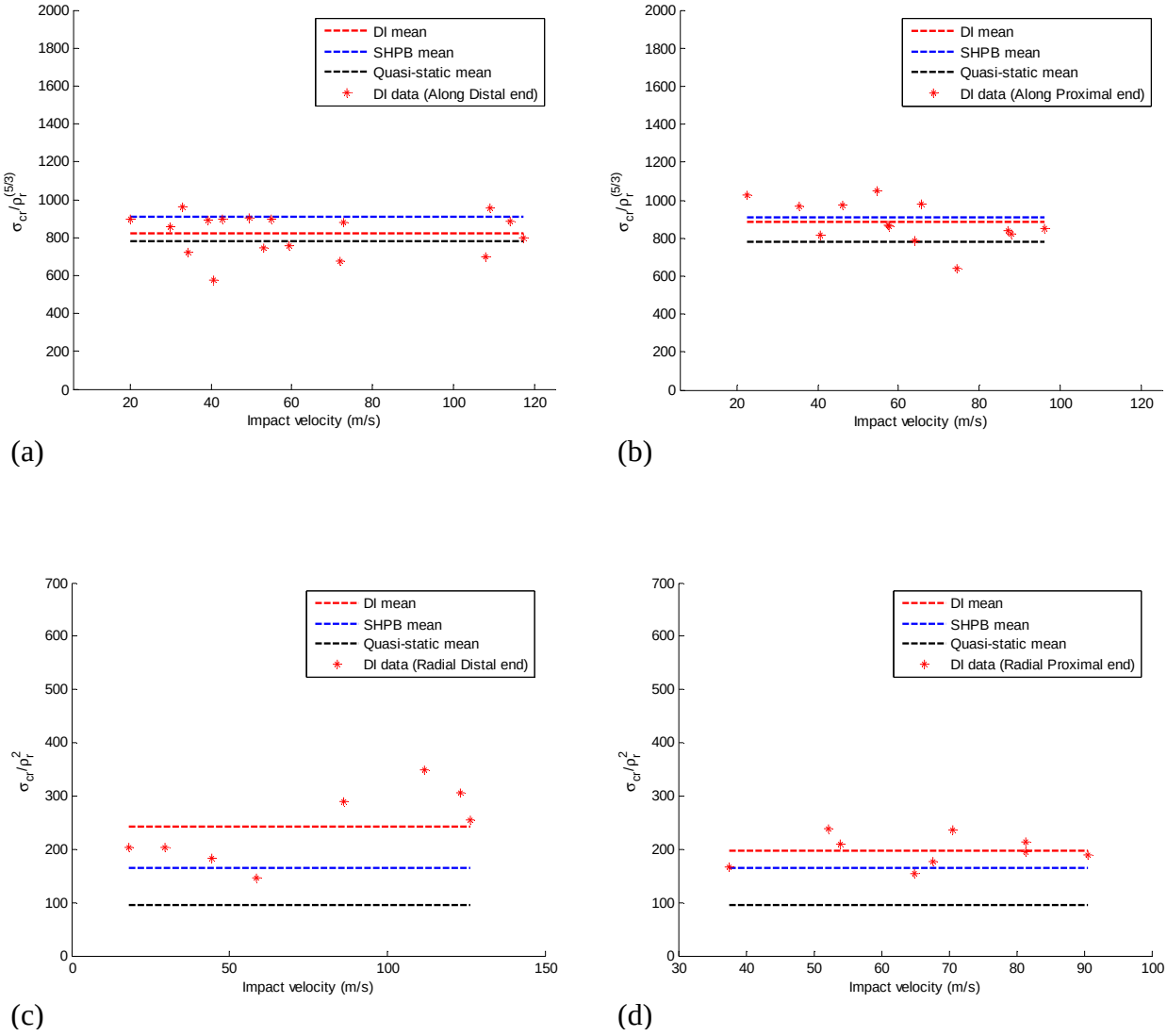

Figure 7.30 Crushing stresses against impact velocity from (a) distal and (b) proximal end DI tests on along the grain balsa wood and from (c) distal and (d) proximal end against DI tests on radial balsa wood.

CHAPTER 8

Rohacell Foam

8.1 Introduction

Rohacell is a low density closed-cell polymethacrylimide rigid foam and is used as a core material in sandwich panels, which are often utilised in aircraft and marine constructions [110]. Although susceptible to changes in humidity, it is sufficiently robust to be used as a support structure material for e.g. silicon strip detectors in the Phenix Multiplicity Vertex Detector [111]. Its strength value is regarded to be one of the highest in its density range.

The damage resulting from low velocity impacts on sandwich panels with Rohacell foam cores has been investigated by various researchers including [112, 113]. Furthermore, Li et al. [110] have examined experimentally the mechanical behaviour and the deformation mechanisms of Rohacell foam under uniaxial tension, compression, pure shear and hydrostatic pressure as well as under a state of multi-axial stress and presented a shear/compression failure relationship.

However, the dynamic behaviour of Rohacell foam has not been investigated. In this chapter the quasi-static and dynamic mechanical properties of Rohacell-51WF and 110WF are investigated experimentally. The dynamic characterisation was carried out by performing SHPB and DI tests utilising PMMA pressure bars.

8.2 Specimen Description

In this study two types of Rohacell foam were examined i.e. Rohacell-51WF and Rohacell-110WF, which represent two different densities (see Table 8.1). Rohacell foam, supplied by Roehm GmbH, is a closed-cell polymethacrylimide (PMI) rigid foam with tetrakaidecahedral cells [114]. According to Anderson and Lakes [115] the average cell size for the Rohacell–51WF and 110WF are 0.67 and 0.5 mm respectively. The mechanical properties of both types of foam given by the manufacturer [116] are shown in Table 8.1, while the properties of the cell wall material according to Chen et al. [114, 117], Maiti et al. [105] and Gibson and Ashby [101] are shown in Table 8.2. It is worth mentioning that the properties of the cell wall material given in [114, 117] differ to the ones that are provided in [101, 105]. This will affect the results of Equations (8.1), (8.3)-(8.5), as described later. In this study the values given by [114, 117] have been used, unless otherwise stated.

For the Quasi-static tests 15 mm cube specimens were used. For the SHPB tests, cylindrical specimens with an average diameter of 16 mm and lengths of 3 mm, 6 mm and 8 mm were used. For the DI tests, the cylindrical specimens had an average diameter of 23.12 mm and lengths of between 10 to 80 mm. Prior to testing, their relative dimensions and their masses were measured with an accuracy of ± 0.001g and ± 0.01 mm respectively. In order to investigate the mechanical properties in all directions, specimens were cut from the foam panel and then compressed along their three principal directions, namely the x and y-directions (which are the in-plane directions) and z-direction representing the out-of-plane direction (Figure 8.1). It should be noted that the base of the foam panel is denser than its core as shown in Figure 8.1. For this reason specimens that were compressed quasi-statically were cut in all directions with and without the denser part of the panel.

8.3 Quasi-static experiments

All specimens were compressed along the in-plane and out-of-plane directions at a constant crosshead speed of 3 mm/min (i.e. at a stain-rate of 3.3×10^{-3} s^{-1}) using an INSTRON 4507 machine. Each sample was placed between the two platens, which were in perfect alignment in order to avoid any shear forces on the specimens.

8.4 Size effects

The ratio of the specimen size to that of the average cell diameter can influence the mechanical properties of cellular solids, termed "size effects". A number of experimental studies have confirmed this [118, 119, 120, 121]. Brezny and Green [118] measured the Young's Modulus, the bending toughness as well as the compressive and bending strength (using a three point bending experiment) of a brittle reticulated vitreous carbon open-cell foam. They concluded that, for constant specimen size, both the Young's Modulus and bending toughness are independent of the cell size while the compressive and bending strength decrease when the cell size is increased. Bastawros et al. [119] investigated the compressive properties of closed-cell Alporas foams by varying the area of the specimen under compression while keeping the height of the samples constant. It was found that both the Young's modulus and compressive strength remain constant only when at-least four cells are present at the shortest dimension of the specimen. Andrews et al. [120] performed uniaxial compressive tests on both closed-cell Alporas and open-cell Duocel foams. For the closed-cell foams different sizes of square cross sectional specimens having a height twice the length of the square were used, while for the open-cell foams variable sizes of cylindrical specimens with a height to diameter ratio of two were tested. It was observed that the Young's modulus reached a stable value for both foams when at least six cells were present in the shortest dimension, and a constant value for the compressive strength was achieved when five and eight cells are present for the closed and open-cell foams respectively. These observations were justified by a recent study on cylindrical closed-cell aluminium foams [121] where it was concluded that the properties obtained truly represent the macroscopic properties

of the examined foam only when the length to the average cell diameter ratio is greater than six. The observed size effects in small specimens can be attributed to the increase in the number of incomplete cells at the boundaries that will carry no load relative to the size of the specimen. This causes an increase of the load that should be carried by the remaining cells resulting in a decrease of the net properties of the material.

According to Anderson and Lakes [115] the average cell size for the Rohacell–51WF and 110WF are 0.67 and 0.5 mm respectively. This gives an average number of cells in any direction of 22 for the Rohacell-51WF and 30 for the Rohacell-110WF quasi-static samples. For the DI tests the smallest sample that was tested had a thickness of 10 mm, which means that approximately 15 and 20 cells are present for the Rohacell-51WF and 110WF specimens respectively. Therefore, the compressive properties obtained from these tests are not influenced by any size effects and are representative of the net properties of the foam. On the other hand, for the case of the SHPB tests the smallest tested specimen had a length of 3 mm, corresponding to an average number of 4.5 and 6 cells for Rohacell–51WF and 110WF respectively. It is clear that for Rohacell-51WF the specimens of this size do not contain the representative number of cells in the loading direction. On the other hand for Rohacell-110WF six cells are regarded to be just sufficient to avoid any size effects. Any possible size effects for the SHPB tests are discussed in section 8.7.2.

8.5 Quasi-static results

Load-displacement curves were obtained for each test, which were then converted to nominal stress and engineering strain. In all cases the displacement recordings were corrected to eliminate the machine compliance. The results that were obtained for each case are shown in Figures 8.2 and 8.3. The dimensions of each specimen are listed in Tables 8.3 and 8.4.

Compression of Rohacell foam results in a typical pattern in the stress-strain curve where three distinct regions can be observed. First at low strain values, the material deforms elastically. Next, cell wall collapse is initiated and is often associated with a

peak stress (see Figures 8.2, 8.3). Note that this is not always the case. Individual specimens will contain cells with a statistical variation in strength so that where weak cells are present, the collapse may initiate at these cells without a notable peak in the stress-strain curve. Then the plateau region follows, where the compressive stress remains almost constant while the strain increases. During this stage gross deformation of the cells can be associated with buckling and breaking of the cell walls, rotation of plastic hinges or by a combination of these [110]. Finally, further compression results in a sharp increase in stress, which corresponds to the interaction between cell walls in cells that have already been compressed to densification [101].

For both the quasi-static and the SHPB tests, the crushing stress (σ_{cr}), plateau stress (σ_{pl}) and densification strain (ε_d) were determined from the experimental stress-strain records in the same way as for the balsa wood specimens (see Section 7.3.3).

The existence of the denser material at the base of the foam panel (Figure 8.1) may affect the properties of the specimens. In order to investigate the effect of this denser region, two specimens with and two specimens without the denser part of the foam were compressed along the x, y and z-directions (Figures 8.2 and 8.3). Note that the black lines correspond to the specimens that contained the denser part.

Observing Figures 8.2 and 8.3 it can be seen that the pattern of the compressive stress-strain curves for the specimens containing the denser part is similar to that of the specimens that do not. As expected, the samples with the denser region have a higher overall specimen density (see Tables 8.3 and 8.4), which contributes to the difference in the stress levels for each case. Also, the denser specimens have an earlier onset of densification. Inspection of Figures 8.2 and 8.3 reveals that the existence of the denser region in any specimen has little effect on the overall shape of the stress-strain relationship. Furthermore, the high level of consistency from one specimen to another is clear.

Observing the shape of the stress-strain curves (Figures 8.2 and 8.3) it can be seen that the stress is almost constant in the plateau region. This implies that individual cells deform following a strain-softening characteristic, which results in an overall

constant plateau region [110]. This is due to the fact that the deformation pattern of a foam specimen is an average of the deformation of each cell. In other words the deformation is localised and is initiated at the weakest regions and then progresses to the remaining cells. Hence, the strain and the strain-rate can be regarded to be discontinuous within the specimen. However, the resulting macroscopic stress-strain curve will follow the same pattern for all specimens.

Li and Mines [122] and Li et al. [116] conducted a series of quasi-static compressive tests along the three principal directions of Rohacell-51WF and reported that the examined material is orthogonal isotropic. Figures 8.2 and 8.3 illustrate that the out-of-plane (z-direction) properties are different to the in-plane (x and y-directions) properties, where x and y have similar properties and are the strongest directions. The results shown in Figures 8.2 and 8.3 reveal a greater anisotropy for the case of the Rohacell-51WF specimens. Taking the mean plateau stress as an example, there is a reduction for specimens crushed in the out-of-plane direction of 21.7% and 7.2% for the 51WF and 110WF foams respectively. As expected, the anisotropy is more pronounced for lower density foams [101, 110]. Such anisotropy is generally attributed to the existence of elongated cells in either the in-plane direction or the out-of plane direction [101].

A simple way to describe the mechanical properties of cellular materials is to use dimensional arguments that produce predictive equations which depend on the relative density and the cell wall properties of the foam [101]. In general, this type of modelling does not take into account the morphology of the cells and assumes that the thickness of the cell edges is uniform and that the cells within the foam are regular and repeated, which is not true in real foam structures. In order to obtain a more accurate representation of the cellular material properties, models that incorporate the unit cell geometry [123] should be employed. This involves the analysis of a repeating unit cell with a more complex structure such as a tetrakaidecahedral using the finite element method. The focus of the study reported here is the measurement of dynamic mechanical properties and the relationship between the global quasi-static and dynamic properties of the foams. As such, an in-depth study of the effect of cellular structure has not been carried out. The scaling law that relates the “plastic collapse stress” to the relative density that was proposed

by Gibson and Ashby [101] is used due to its simplicity. The "plastic collapse stress" defined by Gibson and Ashby in [101] is termed here the crushing stress (σ_{cr}) and defined as the stress at the point of initiation of permanent deformation. According to Gibson and Ashby [101] this crushing stress (σ_{cr}) of closed-cell plastic foam is related to the yield stress of the base material by :

$$\frac{\sigma_{cr}^{qs}}{\sigma_{ys}} = C(\phi\frac{\rho_o}{\rho_s})^{3/2} + C^{"}(1-\phi)\frac{\rho_o}{\rho_s} + \frac{p_o - p_{atm}}{\sigma_{ys}}, \qquad (8.1)$$

where σ_{ys} is the yield stress of the base material, φ is the fraction of the solid material in the cell edges, ρ_o and ρ_s are the densities of the specimen and the cell wall material respectively, C and $C^{"}$ are constants, p_o is the initial pressure of the fluid within the cells of the foam and p_{atm} (equal to 0.1 MPa) is the atmospheric pressure. Assuming that the gas pressure inside the cells is equal to the atmospheric pressure then the last term of Equation (8.1) can be eliminated. Any contributions to the strength of the material due to gas pressure are investigated in Section 8.6.

The first part of Equation (8.1) corresponds to the formation of plastic hinges in the bent cell edges (plastic bending of edges) and the second part to the yielding of the stretched cell faces (plastic stretching of cell faces). By fitting experimental data for open cell foams (where $\varphi = 1$) Gibson and Ashby [101] obtained a value of 0.3 for the constant C. At this point it is worth mentioning that two values of the constant $C^{"}$ appear in two different editions of the Gibson and Ashby book [101, 124]. In the second edition in 1997 [101] for $\varphi = 0$, $C^{"}$ is equal to 1 while in the first paperback of the same edition (with corrections) published in 1999 [124], $C^{"}$ was corrected to 0.44 as obtained by the finite element analysis of tetrakaidecahedral cells. In the current literature Equation (8.1) has been used in both forms (e.g. for $C^{"}$ equal to 1 in [106] and 0.44 in [125]) leading to confusing results regarding the additional contribution of the plastic stretching of the cell faces to the strength of the closed cell foams.

Observing the shape of the stress-strain curves for both Rohacell-51WF and 110WF (see Figures 8.2 and 8.3) it can be said that the material behaviour is very close to perfectly plastic in the plateau region. Hence, the data of the plateau stress can be fitted into Equation (8.1). Figures 8.4 and 8.5 illustrates the normalised quasi-static experimental values of the crushing and plateau stresses respectively for both Rohacell-51WF and 110WF along with the predictions of Equation (8.1) for $C'' = 0.44$. The value of the yield strength of the base material used in Figures 8.4-8.6 is the one given in refs. [117, 114], see Table 8.2.

From Figures 8.4(a) and 8.5(a) it can be seen that for the Rohacell-51WF specimens the data of the normalised crushing and plateau stress values for the x and y-directions is close to φ = 0.5-0.6 and for the z-direction is close to φ = 0.7. On the other hand, the normalised crushing and plateau stress values of the Rohacell-110WF specimens lie between φ = 0 to 0.2 and φ = 0.1 to 0.3 respectively (Figures 8.4(b) and 8.5(b)). For the case of the Rohacell-51WF the above observation implies that apart from plastic bending of the cell edges, plastic stretching of the cell faces contributes to the strength of the foam. However, a value of φ = 0 implies that most of the material within the foam is concentrated on the cell faces, which cannot correspond to real foams as some material must always be present in the cell edges. Nevertheless, from both Figures 8.4 and 8.5 the same conclusion can be made that plastic stretching of cell faces contributes to the strength of the foam. This is in agreement with the findings of Chen et al. [117]. It is worth mentioning that Chen et al. [117] used Equation (8.1) with $C'' = 1$ and determined average values of φ equal to 0.73 and 0.58 for Rohacell-51WF and 110WF specimens respectively. Any discrepancies between the values of φ determined from Figures 8.4 and 8.5 and those quoted by Chen et al. [117] can be attributed to the fact that Chen et al. [117] did not make any distinction between the directions of loading and as well due to the different values of the constant C'' that have been used. If a value of 120 MPa is used for the strength of the base material (see Table 8.2), then the values of φ for Rohacell-51WF would lie between 0.7 and 0.8 for both normalised stresses. For the Rohacell-110WF, using the normalised crushing and plateau stress data to predict φ according to Equation (8.1) would lead values between φ = 0.3 to 0.5 and φ = 0.4 to 0.5 respectively. There is uncertainty in both the use of Equation (8.1) and the yield

stress of the solid material. However, one general conclusion that can be drawn is that the cell wall faces contribute significantly to the strength of the foam. Furthermore, the contribution of these faces is greater for the higher density foam.

Another method for modelling the mechanical properties of foams involves the analysis of a repeating unit cell using the finite element method. This method produces results that predict a dependence of the properties on the unit cell geometry [123, 126]. The results produced by Simone and Gibson [126] for a tetrakaidecahedral foam of relative density less than 0.2 provide a relationship between the relative density, the cell face thickness and edge length:

$$\frac{\rho_o}{\rho_s} = 1.185\frac{t}{l} - 0.4622\left(\frac{t}{l}\right)^2, \tag{8.2}$$

where l is the length of the edge and t is the thickness of the cell face of the tetrakaidecahedral unit cell and both l and t are assumed uniform.

Finite element analysis of the tetrakaidecahedral cell gave the following equation for the crushing stress [123, 126]:

$$\frac{\sigma_{cr}^{qs}}{\sigma_{ys}} = 0.33\left(\frac{\rho_o}{\rho_s}\right)^2 + 0.44\frac{\rho_o}{\rho_s}. \tag{8.3}$$

It was suggested that for the case of low relative densities, the axial yielding of the faces dominates and Equation (8.3) could be approximated as [123,126]:

$$\frac{\sigma_{cr}^{qs}}{\sigma_{ys}} \approx 0.44\frac{\rho_o}{\rho_s}. \tag{8.4}$$

Chen and Lakes [114] proposed a micromechanics model based again on a tetrakaidecahedral unit cell and the following expression was obtained (note that Equation (8.5) has been corrected by Li et al. [110]):

$$\frac{\sigma_{cr}^{qs}}{\sigma_{ys}} = 0.454(\frac{\rho_o}{\rho_s})^2 + 0.189318\frac{\rho_o}{\rho_s}. \quad (8.5)$$

Figure 8.6 shows the predictions of Equations (8.3), (8.4) and (8.5) along with the experimental quasi-static data obtained from both Rohacell-51WF and 110WF specimens. For both the normalised crushing and plateau stresses, Equation (8.5) predicts well the data of the Rohacell-51WF foam. This is in agreement with the results presented by Li et al. [110]. On the other hand, it underestimates the stress values of the Rohacell-110WF specimens. It can be observed (Figure 8.6) that the predictions of Equation (8.4) are close to the experimental values of the 110WF foam. This is in agreement with the conclusion that was made earlier regarding the predictions of Equation (8.1), i.e. that yielding of the cell wall faces dominates the foam strength. However, the predictions of Equations (8.1), (8.3), (8.4) and (8.5) are inconclusive. This can be attributed to the idealisations that were made for the models used (e.g. uniform thickness of the cell walls). Modelling of the foam material properties is beyond the scope of this study. However, it has been demonstrated that further research is required in order to predict the mechanical properties of Rohacell foam.

8.6 Gas contribution to the strength properties of Rohacell foam

During compression of closed cell foams the air that is enclosed within the cells is compressed too. As a result the contribution of the compressed air to the strength of the closed cell foam should be taken into account. This is more important in the case of dynamic compression where the air has little time to escape. Gibson and Ashby [101] assumed an ideal gas in the cells and calculated the elevation in stress $\Delta\sigma$ under isothermal compression as:

$$\Delta\sigma = \frac{p_{atm}\varepsilon_d(1-2\nu_o)}{\left[1-\varepsilon_d(1-2\nu_o)-\rho_o/\rho_s\right]}, \quad (8.6)$$

where ν_o is the Poisson's ratio of the foam, which according to [117] is approximately 0.3 for Rohacell foam. From experimental observations during compression of Rohacell foam there was negligible lateral deformation. Hence, the Poisson's ratio in the plateau region can be assumed to be zero [110].

The elevation in stress assuming adiabatic compression is given as [14]:

$$\Delta\sigma = p_{atm}\left[\left(\frac{1-\rho_o/\rho_s}{1-\varepsilon_d\left(1-2\nu_o\right)-\rho_o/\rho_s}\right)^{\gamma}-1\right], \tag{8.7}$$

where γ is the ratio of specific heat capacities equal to 1.4 for air.

The results that were obtained from both Equations (8.6) and (8.7) by taking the mean average values for the relative densities and densification strains for all the three directions for Rohacell-51WF and 110WF are tabulated in Table 8.5.

For Rohacell-51WF for all directions the estimated average stress elevation due to compression of the entrapped gas in the cells assuming isothermal or adiabatic compression is 0.19 MPa and 0.35 MPa respectively. For the case of the Rohacell-110WF for all the directions the average stress elevation is 0.2 MPa and 0.36 MPa assuming isothermal and adiabatic compression respectively. It can be argued that the contribution of the entrapped air to the elevation of stress cannot be regarded as negligible, especially for the case of Rohacell-51WF. However, such an effect would result in an increasing stress with stain, which is in contrast to the results obtained for both Rohacell-51WF (see Figures 8.2 and 8.11) and 110WF (see Figures 8.3 and 8.12). In fact the stress is reducing with strain for the SHPB tests of Rohacell-110WF (Figure 8.12). Following the work of Deshpande and Fleck [14] and Zhao et al. [109], who performed tests on aluminium foams and honeycombs, it can be suggested that the contribution of the entrapped air to the strengthening of the foam is highly unlikely as this should result in different stress-strain characteristic. A different approach for checking the contribution of the entrapped air in the cells would be experimentally as was performed in ref. [66]. Bouix et al. [66] investigated

the gas contribution to the strengthening of expanded polypropylene foams (EPP) by performing SHPB tests in a water tank and using high speed photography. It was concluded that gas contribution is more pronounced at higher strain rates and for larger size specimens.

The shape of the stress-strain curves obtained for Rohacell-51WF (Figures 8.2 and 8.11) and 110WF (Figures 8.3 and 8.12) suggest that the stress elevation due to the compression of the entrapped air in the cells is unlikely. On the other hand, the stress elevation calculated assuming isothermal (Equation (8.6)) and adiabatic (Equation (8.7)) compression suggest otherwise. Hence, it can be concluded that it is possible that the entrapped air could result in the strengthening of Rohacell foam but that this cannot be evaluated with certainty. Further investigation is required into this matter which is however beyond the scope of this study.

From the investigation performed hitherto, it can be deduced that plastic bending of the edges, stretching of the cell faces and the compression of the entrapped air within the cells are all likely to contribute to the strength of Rohacell foam. A normalisation to the properties of Rohacell-51WF and 110WF foams using the yield stress and density of the base material (Equation (8.1)), in order to minimise any variations as was performed for the case of balsa wood (see Chapter 7) would be challenging. Hence, the data presented in this chapter when comparing the dynamic to the quasi-static values is not normalised.

8.7 SHPB tests on Rohacell foam

8.7.1 Experiments

SHPB tests were carried out in both Rohacell-51WF and 110WF foam specimens utilising a 20 mm diameter PMMA SHPB set-up and a 0.5 m long PMMA projectile, which have been described in Chapter 3. The details of the specimens used for both SHPB and DI tests are shown in Appendix A (Tables A.8-A.25). Attenuation and dispersion effects were taken into account as was explained in Chapter 4. The wave

separation was performed in the frequency domain with the use of a suitable exponential window as was discussed in detail in Chapter 5. The equations used to evaluate the stress, strain and strain rate for each tested specimen are given in Section 7.4.2. In order to minimise any frictional effects, lubrication (Vaseline petroleum jelly) was used in both incident bar/ specimen and transmitter bar/specimen interfaces.

In order to calculate the stress in the specimen with the use of Equation (7.21), the assumption of stress equilibrium within the specimens should be checked first. Figures 8.7 and 8.8 illustrate the forces at the incident bar/specimen interface (front face, shown with blue line) and transmitter bar/specimen interface (back face, shown with red line) for Rohacell-51WF and 110WF respectively, for specimens compressed along the weakest direction (i.e. z-direction) having lengths of 3 mm, 6 mm and 8 mm. The strength of Rohacell-110WF is greater than the strength of Rohacell-51WF, as was shown from the quasi-static experiments. It has already been mentioned in Section 7.4.2 that as a general rule stress equilibrium is achieved if the force at the front face oscillates about the value of the force at the rear face [4, 8]. For the case of Rohacell-110WF for the three thicknesses shown in Figure 8.8, the force at the incident bar/ specimen is very close to the force from the transmitter bar/specimen interface. From Figure 8.7 it can be observed that both forces obtained from the front and rear faces of the specimen are close and follow similar patterns. The above observations give confidence to the results presented in this study from the SHPB tests of Rohacell-51WF and 110WF foam specimens. It is worth mentioning that the forces shown in Figure 8.7 have very low magnitudes of the order of approximately 0.17 kN. It is therefore impossible to be compare the results with data obtained if one used a Magnesium SHPB arrangement, as was the case for compression of across the grain balsa wood.

8.7.2 Results

The stress-strain curves from the SHPB tests on Rohacell-51WF and 110WF specimens were calculated with the use of Equations (7.19) and (7.21). Typical strain measurements from the second strain gauge on the incident bar and first strain gauge

on the transmitter bar from the PMMA SHPB arrangement are illustrated in Figures 8.9 (a) and 8.10 (a). For details of the position of the strain gauges see Table 3.2. A flow chart and the Matlab program that was used to produce the stress-strain curve shown in Figure 8.9 (b) are provided in Appendix B. Wave superposition occurs in both Figures 8.9 (a) and 8.10 (a), especially for the case of the strain measurements from the incident bar. It is obvious that wave separation is essential, so as to obtain an accurate stress-strain curve. The wave separation was performed using all the strain gauge stations mentioned in Table 3.2, although for clarity reasons only two strain measurements are shown in Figures 8.9 (a) and 8.10 (a). In Figure 8.9 it can be seen that the first loading wave was not sufficient long to achieve densification and the second pulse reloaded the specimen from a strain of approximately 0.6 to densification, which occurred at a strain of approximately 0.7 (Figure 8.9 (b)). The tested specimen was loaded at an average strain rate of 1273 s^{-1} and 955 s^{-1} during the first and second pulses respectively (Figure 8.9 (c)). The plateau stress was 1.0125 MPa. Although, it is not clear from Figure 8.9 (b), a small amount of unloading occurred at a strain of about 0.6 and the reloading did not follow the same path. Such unloading and reloading is more evident in Figures 8.12 (a) and (c). This also occurred in the case of the SHPB tests on balsa wood specimens (see for example Figure 7.16 (b)). Figure 8.10 (b) shows the stress-strain curve obtained after the wave separation for a SHPB test on a Rohacell-110WF specimen compressed in the y direction. Densification occurred at a strain of 0.6 and the plateau stress was evaluated to be 2.63 MPa. The average strain rate was 2296 s^{-1}. The strain rates shown in both Figures 8.9 (c) and 8.10 (c) are typical strain rates obtained from all the tests performed on Rohacell foam. It can be observed that these rates are approximately constant. It has already been mentioned in section 7.4.2 that dispersion in PMMA bars leads to longer rise times in the pulse seen at the incident/specimen interface and the strain rate will never be perfectly constant. Furthermore, the shape of the strain rate curve is affected by the deformation characteristics of the tested specimen.

Typical SHPB stress-strain curves from the compression of Rohacell-51WF and 110WF along the three directions are shown in Figures 8.11 and 8.12 respectively. The SHPB tests were performed at a range of strain rates. The tests on Rohacell-51WF compressed along the x- direction covered a range of strain rates of 1273-

4284 s^{-1} and compression in the y and z-directions covered a strain rate range of 1248-5874 s^{-1} and 1060-4413 s^{-1} respectively. For the case of SHPB tests on Rohacell-110WF along the x, y and z-directions the strain rates covered were 983-4620 s^{-1}, 1038-4516 s^{-1} and 972-3945 s^{-1} respectively. The strain rates were calculated as average strain rates with the use of Equation (7.20).

The shortest specimens tested for Rohacell-51WF contain an average of 4.5 cells in the loading direction and this could result in a decrease of the measured properties of the material due to size effects (see Section 8.4). As an example of possible size effects Figure 8.11 (c) shows typical stress-strain curves obtained from three different specimen sizes (z-direction). It can be seen that they follow similar patterns. As a further example, Figures 8.13 (a) and (b) show the crushing and plateau stresses along with their mean values from the SHPB tests against the thickness of the tested specimens for Rohacell-51 WF (x-direction). It can be observed that for the shorter specimens, both the crushing and plateau stress values are slightly lower than those of the thicker specimens. The mean crushing stress of the 3 mm long specimens is approximately 9% lower than the mean crushing stress of the thicker specimens. The mean plateau stress of the 3 mm long specimens is approximately 8% lower than the mean plateau stress of the thicker specimens. There may be a size effect on the results, however for specimens with the same thickness there is typically a scatter of 10% to 20% in both crushing and plateau stress. The variation of the mean stresses of different thicknesses lies within the experimental scatter of each thickness. Standard deviations of the data are also shown in Figure 8.13 (a) and (b). The majority of the data points lie within the range of the standard deviation. Therefore, it is believed that size effects have little influence on the results of Rohacell-51WF specimens and the properties obtained from the SHPB tests represent truly the net properties of the tested foam.

For Rohacell-110WF the shape of the stress-strain curve obtained from the SHPB tests (Figure 8.12) is somewhat different to the one obtained from the quasi-static tests (Figure 8.3). In general, after the initial peak stress the stress-strain curve from the SHPB tests (Figure 8.12) has a negative slope in the “plateau region”, while the stress-strain curve from the quasi-static tests has an almost constant plateau region (Figure 8.3). This difference in shape between the quasi-static and dynamic stress-

strain curves has been noticed previously by Ouellet et al. [127] who performed tests on rigid polyurethane (PU) foams and by Song et al. [128] who performed tests on polymethylene diisocyanate (PMDI)-based rigid polyurethane foams. In both the studies by Ouellet et al. [127] and Song et al. [128] it is clear that the change in shape of the stress-strain curve is more pronounced for denser foams and for higher strain rates. Ouellet et al. [127] attributed the negative slope of the stress-strain curve to the ejection of some material during the SHPB tests. For tests reported herein, there was also some evidence of ejected material during the dynamic tests. Song et al. [128] attributed the negative slope of the stress-strain curve to a change in deformation mode from the quasi-static to dynamic tests. Daphalapurkar et al. [129] performed tomography on Rohacell foam. Although the grade of their foam was not specified, it had a relative density of 0.3, i.e. much greater than the relative density of the samples tested herein. The tomography during the quasi-static compression illustrated that progressive crushing involved the creation of 45° shear bands in the weakest zones [129]. Clearly such shear bands are more difficult to promote in the type of short specimens used for SHPB testing. It is unclear at present whether ejection of the material or changes in the deformation mode causes the difference in shape between the quasi-static and SHPB stress-strain curves for Rohacell-110WF. Further investigations are required to clarify the reasons for this difference.

The shortest specimens used in SHPB tests for Rohacell-110WF contain an average of 6 cells in the loading direction and this is regarded as adequate to avoid any possible size effects [120, 121] (see Section 8.4). Figures 8.14 (a) and (b) show the crushing and plateau stresses along with their mean values from the SHPB tests against the thickness of the tested specimens for Rohacell-110 WF (x-direction). From Figure 8.14 (a) it can be observed that there is negligible effect of the size of the specimen on the crushing stress. On the other hand, it can be observed that for the shorter specimens, the plateau stress values are slightly lower than those of the thicker specimens. The mean plateau stress of the 3 mm long specimens is approximately 16% lower than the mean plateau stress of the thicker specimens. There may be a size effect on the results. However for specimens with the same thickness there is a scatter of up to 28% in plateau stress. The variation of the mean plateau stresses of different thicknesses lies within the experimental scatter and the

majority of the results lie within the range of the standard deviations. Hence, if the size effect is present it is weak for the Rohacell-110WF foam specimens.

Figure 8.15 shows the experimental values of the crushing stress against strain rate obtained from the dynamic compression of Rohacell-51WF foam along x, y and z-directions. It should be noted that a linear best fit line, the standard deviation and the mean of the SHPB data as well as the quasi-static mean are plotted in each of Figures 8.15-8.20. For all three directions it can be observed that there is no apparent increase of the crushing stress with increasing strain rate (Figure 8.15 (a)-(c)). The linear curve fits to the test SHPB data have negative slopes for x and y- directions and a positive slope for the z-direction. In general, for x, y and z-directions the SHPB test data shows an increase in the initial dynamic crushing stress when compared with the quasi-static values. This increase was evaluated by comparing the means of the quasi-static and SHPB crushing stresses shown in Figure 8.15. In the x and y-directions this increase is 2.3% and 7% respectively and in the z-direction it is 18%. Given the scatter in the SHPB data, dynamic enhancement of the crushing stress of Rohacell-51WF appears to be negligible in the x- and y-directions. However, the quasi-static mean is below the bounds of the standard deviation of the SHPB data in the z-direction, suggesting that the enhancement of the crushing stress in this direction is real.

The crushing stresses against strain rate for Rohacell-110WF foam are plotted in Figure 8.16. Similar observations can be made as for Rohacell-51WF specimens, i.e. the crushing stress appears unaffected with increasing strain rate for the x, y and z-directions. For the x and y-directions in particular, the best fit line is very close to the SHPB mean value indicating clearly that there is no increase of the crushing stress with increasing strain rate. For the z-direction the best fit line has a positive slope, but this could be due to experimental scatter. Comparing the SHPB with the means of the quasi-static crushing stresses, an enhancement of 6%, 3% and 11% is revealed for x, y and z-directions respectively.

The plateau stresses for all three directions are illustrated against strain rate for Rohacell-51WF in Figure 8.17. It can be observed that there is no apparent increase of the plateau stress with increasing strain rate for all directions (Figure 8.17(a)-(c)).

In fact the best fit lines are very close to the SHPB means indicating an approximately constant plateau over the strain rate range shown in Figures 8.17 (a)-(c). The mean SHPB values are 6% and 1% less that the quasi-static means for x and y-directions respectively, while for the z-directions the mean of the SHPB data is 5% higher.

For the Rohacell-110WF specimens the plateau stress levels are lower than the quasi-static plateau values (Figure 8.18). This is expected as a decrease of the stress with strain in the “plateau region” was observed in the SHPB stress-strain curves, as discussed previously in this section. This decrease in the plateau stress obtained from the SHPB tests was estimated to be 17%, 9% and 11% for x, y and z-directions respectively.

The strain rate effect on the densification strain was examined as well for both Rohacell-51WF and 110WF foams (Figures 8.19 and 8.20). The general trend indicated by the best fit lines is that the densification strain remains approximately constant for the strain rate ranges shown in Figures 8.19 and 8.20. When comparing the SHPB with the quasi-static mean values an increase in densification strain values is present for all directions for both foams. For the Rohacell-51WF this increase is 4%, 10% and 11% for x, y and z-directions respectively (Figure 8.19). For the Rohacell-51WF this enhancement is 8%, 13% and 14% for x, y and z-directions respectively (Figure 8.20).

8.8 DI tests on Rohacell foam

8.8.1 Experiments

Distal end and proximal end forces were measured using a 40 mm diameter PMMA pressure bar. Attenuation and dispersion effects of the PMMA bar were taken into account as discussed in Chapter 4. A description of the DI tests that were carried out is given in Section 3.4.

8.8.2 Specimens

Rohacell-51WF and 110WF cylindrical specimens of all x, y and z-directions were used for the DI tests. Their diameter was approximately 23.12 mm and their lengths varied from 10 mm to 80 mm.

8.8.3 Results

Figures 8.21, 8.22 and 8.23 show typical distal and proximal end forces for the x, y and z-directions respectively for Rohacell-51WF, while Figure 8.24, 8.25 and 8.26 show again typical distal and proximal end forces for the x, y and z-directions of Rohacell-110WF.

For proximal end forces the shape of the force pulses obtained from the DI tests is similar to the shape of the SHPB stress-stain curves (Figures 8.11 and 8.12) for both Rohacell-51WF and 110WF in all directions (part (b) of Figures 8.21-8.26). The proximal end forces of Rohacell-51WF in x, y and z-directions have an initial peak after a sharp increase of the load that is followed by an approximately constant load. Then the force increases sharply due to full compaction of the specimen during the test (Figures 8.21 (b), 8.22 (b) and 8.23 (b)). For the Rohacell-110WF foam samples the force increases sharply to an initial peak and then reduces in the “plateau region” (Figures 8.24 (b), 8.25 (b) and 8.26 (b)) as occurred in the SHPB tests in all directions (see Figure 8.12).

For distal end forces for both foams in all directions the load increases more gradually to an initial peak, followed by an almost constant plateau region until full densification of the tested specimens, where the load increases sharply (part (a) of Figures 8.21-8.26). For the majority of the tests, in the early stages of the load history the load increased in a series of steps at lower levels than the crushing stress.

The initial peak loads are defined as the first maximum in the load pulses, defined as crushing stress in Figures 8.27-8.32. The average stress corresponds to the mean stress calculated from the “plateau region” following the initial peak and before

densification. The initial peak and average forces from both distal and proximal ends were converted to stress and were plotted against impact velocities for all directions for both foams in Figures 8.27-8.32. The mean values of the crushing and plateau (timed averaged) stresses from the quasi-static, SHPB and DI data are also shown in each of Figure 8.27-8.32.

The distal end stresses (both crushing and average) of Rohacell-51WF foam in all directions appear to remain fairly constant with increasing impact velocity (parts (a) and (c) of Figures 8.27-8.29). Although there may be a slight reduction of the crushing and time-averaged stresses with impact velocity (see e.g. Figure 8.29 (a) and (c)) the data is inconclusive. The mean values of both the crushing and average stresses at the distal end are greater than either the quasi-static or SHPB mean values. Note that for consistency reasons with previous comparisons the DI mean values are compared with the quasi-static values. It was estimated that the crushing stress increases by 27%, 50% and 39% in the x, y and z directions respectively and the average stress increases by 28%, 44% and 40% for the x, y and z-directions respectively.

The proximal end stresses show a different trend. For all three directions of Rohacell-51WF it is evident that the proximal end crushing stress increases with impact velocity as the impact velocity increases from approximately 20 m/s to approximately 70 m/s (see part (b) of Figures 8.27-8.29). The time-averaged proximal end stresses, however, remain very constant over the range of the impact velocities tested (see part (d) of Figure 8.27-8.29). For all three directions the mean of the timed-averaged proximal end stress is similar to the mean of the timed-average distal end stress as can be seen by comparing parts (c) and (d) of Figures 8.27-8.29. Again the mean values of the timed-averaged stress are higher than both the means of the quasi-static and SHPB plateau stresses. The average stress increases by 23%, 22% and 39% for the x, y and z-directions respectively.

The results of the DI tests on Rohacell-110WF foam specimens are summarised in Figures 8.30-8.32. The overall trends in the data are similar to those derived for the Rohacell-51WF foam. For all directions the mean values of both the crushing and time-averaged distal end stresses are greater than both the quasi-static and SHPB

means (see parts (a) and (c) of Figures 8.30-8.32). The distal end mean crushing stress is 15% higher in all directions and the mean timed-average stress is 16.5%, 32% and 16% higher for the x, y and z-directions respectively when compared with the corresponding quasi-static mean stresses. The trends of the variation of the distal end stresses with increasing impact velocity are more difficult to specify. For the y and z-directions there may at first be an increase of the distal stresses up to velocities of 60 m/s, followed by a reduction in distal stresses as the impact velocity increases further to 90 m/s (parts (a) and (c) of Figures 8.31 and 8.32). This trend is not seen in the x-directiion (Figure 8.30 (a) and (c)) but the majority of the data are for impact velocities below 70 m/s for this direction.

The proximal end crushing stresses increase with impact velocity for all directions of Rohacell-110WF (see part (b) of Figures 8.30-8.32). However the timed-averaged proximal stresses remain fairly constant and at similar levels to the distal end forces (see parts (c) and (d) of Figures 8.30-8.32). Again the mean of the time-averaged stresses are higher than both the quasi-static and SHPB means. It was estimated that the mean time-average stress increases by 22%, 15% and 14% for the x, y and z-directions respectively.

It is interesting to note that for the Rohacell-110WF specimens the force-time traces from the DI tests (see part (b) in Figures 8.24-8.26) do not exhibit the same level of reduction in stress in the “plateau region” as was noted for the SHPB tests (Figure 8.12). This is illustrated by comparing the means of the timed-average stresses, which were above the corresponding quasi-static means in contrast to the SHPB mean values (parts (c) of Figures 8.30-8.32).

8.9 Discussion

The SHPB tests on Rohacell foam produced results that can be treated with confidence. This is supported by the fact that force equilibrium was considered to be satisfactory for all tests (Figures 8.7 and 8.8). Additionally, the strain rate was approximately constant during each test so that any inertia effects present in axial compression could be neglected (Figures 8.9 (c) and 8.10 (c)) (see Section 2.4).

Hence all the data presented herein are believed to reflect accurately the effects of strain rate. Furthermore, the crushing and plateau stress values and the densification strain remain approximately constant with increasing strain rate for both foams and in all directions (Figures 8.15-8.20). Similar conclusions have been made for rigid polyurethane foams [127]. Given the scatter in the SHPB data for both Rohacell-51WF and 110WF foams the enhancement in the crushing stress appears negligible in the x and y-directiions (parts (a) and (b) of Figures 8.15 and 8.16). Nevertheless an increase of 18% and 11% was found in the z-direction for both foams when comparing the SHPB and quasi-static means of the crushing stress (part (c) of Figures 8.15 and 8.16). For Rohacell-51WF the plateau stress mean values are approximately equal to the mean quasi-static plateau stress. On the other hand, for the Rohacell-110WF the mean plateau stress is less than the quasi-static mean due to the decrease of the stress with strain in the "plateau region" in the SHPB stress-strain curves. This is attributed to the ejection of the material during the dynamic compression of the foam [127] and to the change of the collapse mechanism of the cell structure for higher density foams under dynamic compression [128]. The dynamic mean densification strain is greater than the quasi-static densification strain for both foams, which may be the result of material ejection.

During quasi-static and low speed compression of a cellular material, regions with weak cells will tend to collapse first. However, for DI testing with increasing impact speeds, the deformation is governed by stress waves and is less random in nature. Finite element (FE) studies of honeycomb materials compressed in the in-plane direction have highlighted the different deformation patterns that are dominant at different impact velocities (e.g. [130, 131]). With increasing impact velocity the deformation of cells becomes localised at the compaction front. This has been noted in both FE models [131] and experimental studies [132]. Reid and Peng [103] predicted the stress at the compaction wave using a rate-independent rigid-perfectly-plastic-locking (r-p-p-l) idealisation of the cellular material stress-strain characteristics. Using this material model Reid and Peng [103] proposed that the compaction wave compression will be dominant beyond a certain "critical impact velocity" (V_{cr}), defined as:

$$V_{cr} = \sqrt{\frac{2\sigma_{cr}\varepsilon_d}{\rho_o}}, \tag{8.8}$$

where σ_{cr} is the crushing stress, ε_d is the densification strain and ρ_o is the specimen's density.

Furthermore, the stress at the front of the compaction wave (σ^*) was predicted according to the "shock wave" theory as:

$$\sigma^* = \sigma_{cr} + \frac{\rho_o V^2}{\varepsilon_d}, \tag{8.9}$$

where V is the change in velocity across the compaction wavefront.

For distal end tests reported here, the force measured by the Hopkinson bar load cell is that at the interface between the distal end of the specimen and the load cell. The force at this end is the result of the reflection of an elastic precursor wave at the specimen/load cell boundary. Because elastic waves are dispersive in cellular materials, the measured force (and specimen stress) increases gradually as seen in parts (a) of Figures 8.21-8.26. As the impact velocity increases, stresses in the compaction wave will increase according to Equation (8.9). However, the elastic precursor should be unaffected by increasing velocity. For this reason distal end forces are expected to remain fairly constant and approximately equal to the crushing stress as the impact velocity increases.

Taking the material properties of the SHPB tests, and the elastic moduli (E_o) given in [133] as 77.4 MPa and 181.9 MPa for Rohacell-51WF and 110WF respectively, the impact velocities V_Y that should produce plastic compression on impact can be predicted using:

$$\sigma_{cr} = \rho_o c_o V_Y = V_Y \sqrt{\rho_o E_o}, \tag{8.10}$$

where c_o is the elastic wave speed of the foam. The predicted impact velocities for plastic compression in the x-direction are therefore approximately 16 m/s and 27 m/s for Rohacell-51WF and 110WF respectively. For DI distal end tests at velocities greater than V_Y, an elastic precursor could be reflected at the distal end as a compaction wave, giving an increase in the crushing stress for Rohacell-51WF and 110WF foam specimens of approximately 2% and 4% respectively.

However, the mean crushing and timed-averaged stresses for Rohacell-51WF in all three directions are substantially higher that the corresponding SHPB mean values (see parts (a) and (c) of Figures 8.27-8.29). This suggests that there is some strength enhancement in the Rohacell-51WF foam during impact loading that cannot be attributed directly to the strain rate. Rather, the enhancement is inertial in origin and is associated with wave effects in the material. There may be a change in deformation mode during impact loading and the fact that strength enhancements are seen in the time-averaged mean stress values suggests that this impact deformation mode is not restricted to a small number of cells. For the Rohacell-110WF the mean values of the crushing and time-averaged stress at the distal end are also greater than the equivalent quasi-static and SHPB means. The enhancement in crushing stress is less than the enhancement in the timed-averaged stress.

For proximal end tests, both elastic and compaction waves will be initiated on impact with the load cell, which measures the force associated with the compaction wave. The stress at the interface is expected to rise to a maximum on impact (see e.g. Figure 8.24 (b)) and to be predicted by Equation (8.9). The "shock theory" predictions of Equation (8.9) are plotted along with the experimental data in part (b) of Figures 8.27-8.32. "Shock theory A" in part (b) of Figures 8.27-8.32 refers to the predictions of Equation (8.9) using the SHPB mean crushing stresses and SHPB mean densification strains, while for "Shock theory B" the mean values of the distal end crushing stress were used for σ_{cr} in Equation (8.9).

Overall, in some cases (e.g. part (b) of Figures 8.27 and 8.30) the use of the distal end mean crushing stress values in Equation (8.9) gives better predictions for the proximal end stress measurements than the use of the SHPB crushing stresses. This

supports the proposal of the inertial enhancement of crushing stresses for specimens subjected to impact loading. However, for e.g. low velocity impacts of Rohacell-110WF in the y-direction (Figure 8.31 (b)) the SHPB properties give a better prediction for the proximal end crushing stresses. This highlights the need to perform both SHPB and distal end DI tests so as to assess the dynamic properties of cellular materials. Unfortunately, it is not obvious which tests provide the relevant data for the prediction of the stresses within a compaction wave.

Applying the SHPB data to Equation (8.8), the prediction of the "critical impact velocity" (V_{cr}) at which a "steady shock" [103] can be generated is approximately 154 m/s and 210 m/s for Rohacell-51WF and 110WF respectively. However, FE analysis [131] and experimental data [55] suggests that Equation (8.8) overestimates the impact velocity required to cause deformation modes associated with compaction waves. As Equation (8.9) is derived from conservation of mass and momentum it should be applicable when compaction waves are present.

8.10 Conclusions

The quasi-static and dynamic properties of Rohacell-51WF and 110WF foams for all three directions were investigated. The dynamic response of Rohacell foam was examined by performing SHPB and DI tests utilising PMMA pressure bars. From the quasi-static stress-strain curves it was revealed that both Rohacell foams are orthogonal isotropic, with the z-direction being the weakest direction (Figures 8.2 and 8.3). Rohacell-110WF had a crushing stress of about 76% higher than Rohacell-51WF. Different ways to predict the quasi-static stresses for both foams were investigated (Equations (8.1), (8.3)-(8.5)), but their predictions were regarded as unsatisfactory. A general conclusion that could be drawn from this investigation was that plastic bending of the cell edges, stretching of the cell faces and compression of the entrapped air within the cells can contribute to the strength of Rohacell-51WF and 110WF foams.

Possible size effects on the results obtained in this chapter were also examined. For the quasi-static and DI tests the length of the specimens was regarded as sufficient to

avoid any size effects. For the shortest specimens used in the SHPB tests it was found that size effects would have little influence in the results.

The assumption of “stress equilibrium” was regarded to be valid for the SHPB tests on Rohacell foam (see Figures 8.7 and 8.8). In addition, an approximately constant strain rate was achieved during each test (Figures 8.9 (c) and 8.10 (c)). Therefore, the results obtained from the SHPB tests in all three directions for both foams were regarded as valid. For the Rohacell-51WF, the shape of the SHPB stress-strain curves (Figure 8.11) was similar to that for quasi-static compression (Figure 8.2). On the other hand, for the Rohacell-110WF the SHPB stress-strain curve had a negative slope in the “plateau region” (Figure 8.12), while the quasi-static stress-strain curves had an almost constant plateau region (Figure 8.3). This was attributed to the ejection of the material during the SHPB testing and to the change of the deformation mode from quasi-static to dynamic tests. For both foams the crushing stress, the plateau stress and the densification strain remain approximately constant with increasing strain rate (Figures 8.15-8.20). When comparing the mean values of the crushing stresses for the SHPB tests with the quasi-static mean values negligible increase was observed in the x and y-directions for both foams (parts (a) and (b) of Figures 8.15 and 8.16). A noticeable increase was observed only in the z-direction of Rohacell-51WF and 110WF (part (c) of Figures 8.15 and 8.16). For the Rohacell-51WF specimens the mean SHPB plateau stress was very close to the mean of the quasi-static plateau stress value for all directions (Figure 8.17). On the other hand, for the Rohacell-110WF a decrease of the SHPB mean plateau stress was observed when compared with the quasi-static mean in all directions (Figure 8.18). The densification strain was found to be slightly higher than the quasi-static mean densification strain for both foams and in all directions (Figures 8.19 and 8.20).

Properties	**Rohacell-51WF**	**Rohacell-110WF**
Density (kgm^{-3})	52	110
Compressive Strength (MPa)	0.8	3.6
Tensile Strength (MPa)	1.6	3.7
Shear Strength (MPa)	0.8	2.4
Shear Modulus (MPa)	24	70
Elongation at break (%)	3	3

Table 8.1 Mechanical properties of Rohacell-51WF and Rohacell-110WF foam as supplied by the manufacturer [116].

Properties	**PMI [114, 117]**	**PMI [105,101]**
Compressive Young's Modulus (MPa)	5200	3600
Compressive Yield stress (MPa)	90	120 [101], 360 [105]
Density (kgm^{-3})	1200	1200

Table 8.2 Mechanical properties of polymethacrylimide (PMI) [114, 117, 101, 105]

Specimen	Mass (gr)	Area (mm^2)	Height (mm)	Density (kgm^{-3})
x1	0.233	251.5035	15.67	59.1212
x2	0.230	246.4884	15.61	59.7762
x4	0.233	262.523	15.68	56.6034
x5	0.235	260.9064	15.62	57.6636
y1	0.238	240.2451	16.64	59.5346
y2	0.234	240.7122	16.44	59.1311
y4	0.232	241.1745	16.74	57.4647
y5	0.231	241.645	16.63	57.4833
z1	0.192	219.3972	15.12	57.8786
z2	0.190	219.1761	15.20	57.0318
z3	0.191	220.704	15.10	57.3121
z4	0.188	216.7613	15.13	57.3241

Table 8.3 Masses, dimensions and densities of the Rohacell-51WF specimens from the quasi-static tests.

Specimen	Mass (gr)	Area (mm^2)	Height (mm)	Density (kgm^{-3})
x1	0.534	257.9227	15.80	131.0372
x2	0.522	250.114	15.91	131.1784
x4	0.474	256.6368	16.18	114.1513
x5	0.457	249.3225	15.94	114.9917
y1	0.540	252.4896	16.33	130.9677
y2	0.548	254.88	16.45	130.7010
y3	0.483	249.6384	15.86	121.9923
y4	0.504	256.9465	16.35	119.9693
z1	0.512	250.272	15.86	128.9895
z2	0.457	248.5262	15.63	117.6481
z3	0.450	248.2158	15.70	115.4738
z4	0.468	236.315	15.52	127.6036

Table 8.4 Masses, dimensions and densities of the Rohacell-110WF specimens from the quasi-static tests.

Rohacell-51WF	**x-direction**	**y-direction**	**z-direction**
Equation (8.6) (MPa)	0.2118	0.2007	0.1590
Equation (8.7) (MPa)	0.3913	0.3671	0.2790
Rohacell-110WF	**x-direction**	**y-direction**	**z-direction**
Equation (8.6) (MPa)	0.2128	0.1905	0.1889
Equation (8.7) (MPa)	0.3936	0.3450	0.3417

Table 8.5 Results of Equations (8.6) and (8.7) for Rohacell-51WF and 110WF foam.

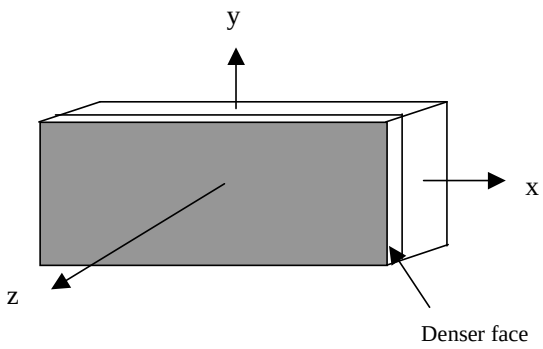

Figure 8.1 Rohacell foam panel.

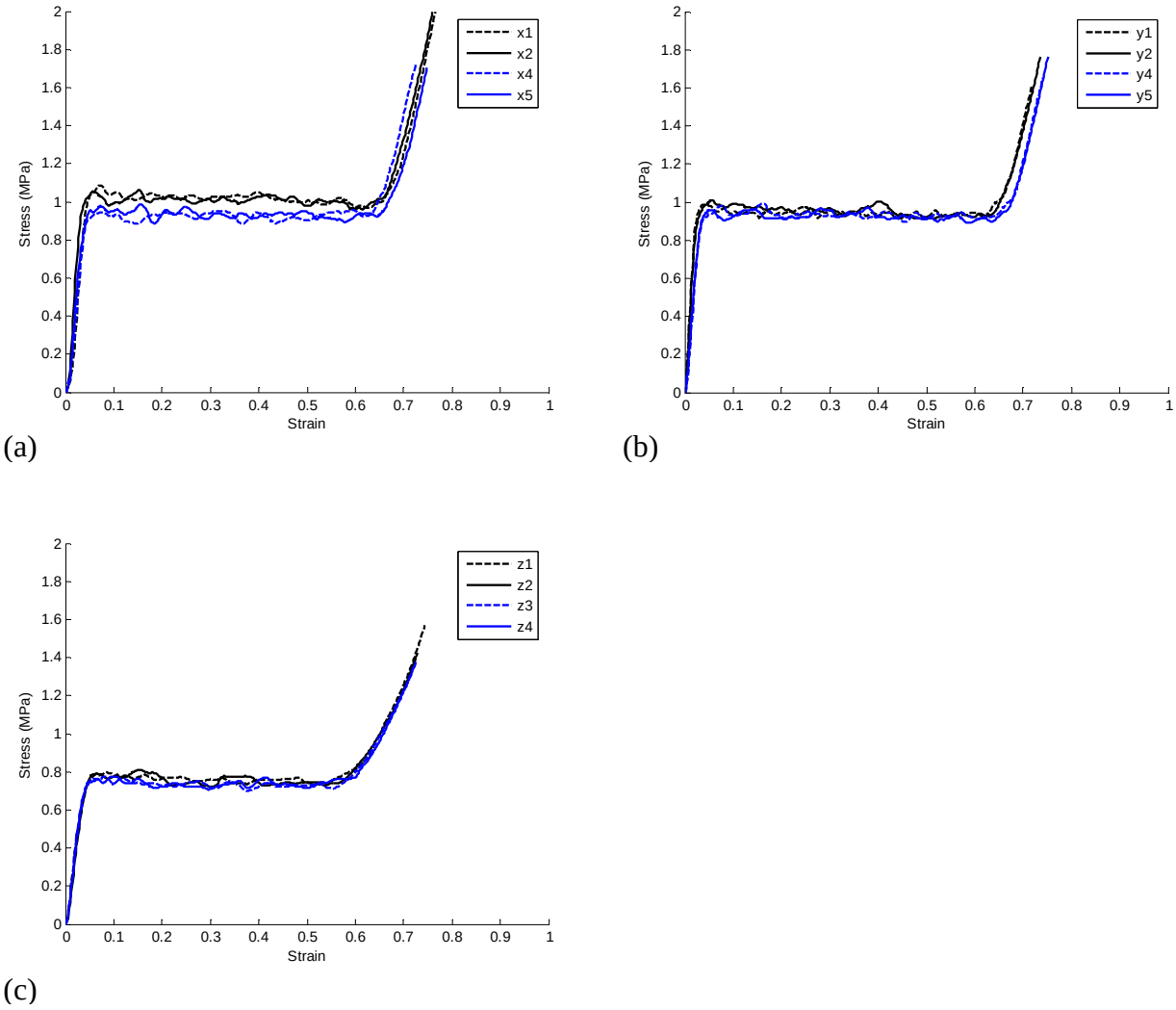

Figure 8.2 Quasi-static compressive stress-strain curves along (a) x, (b) y and (c) z directions for Rohacell-51WF specimens with (black lines) and without (blue lines) the denser part of the foam.

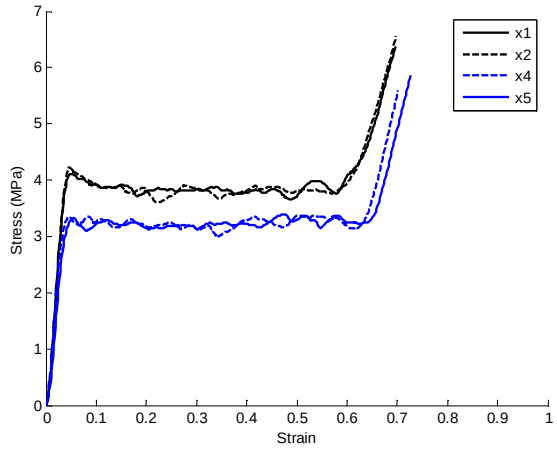

(a)

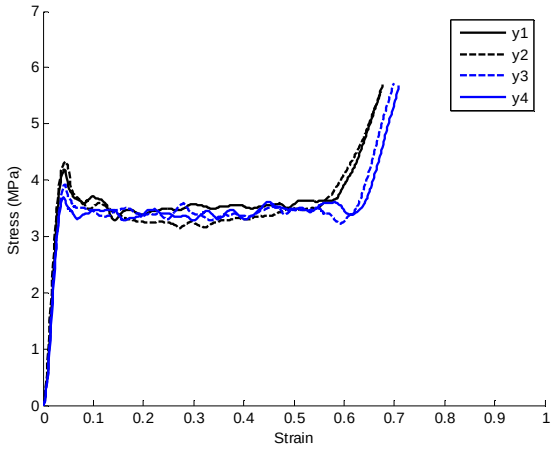

(b)

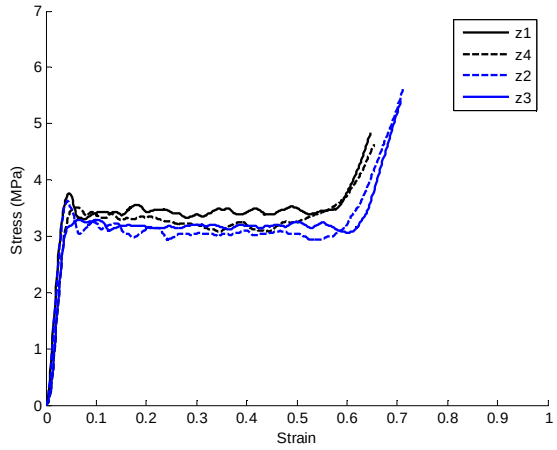

(c)

Figure 8.3 Quasi-static compressive stress-strain curves along (a) x, (b) y and (c) z directions for Rohacell-110WF specimens with (black lines) and without (blue lines) the denser part of the foam.

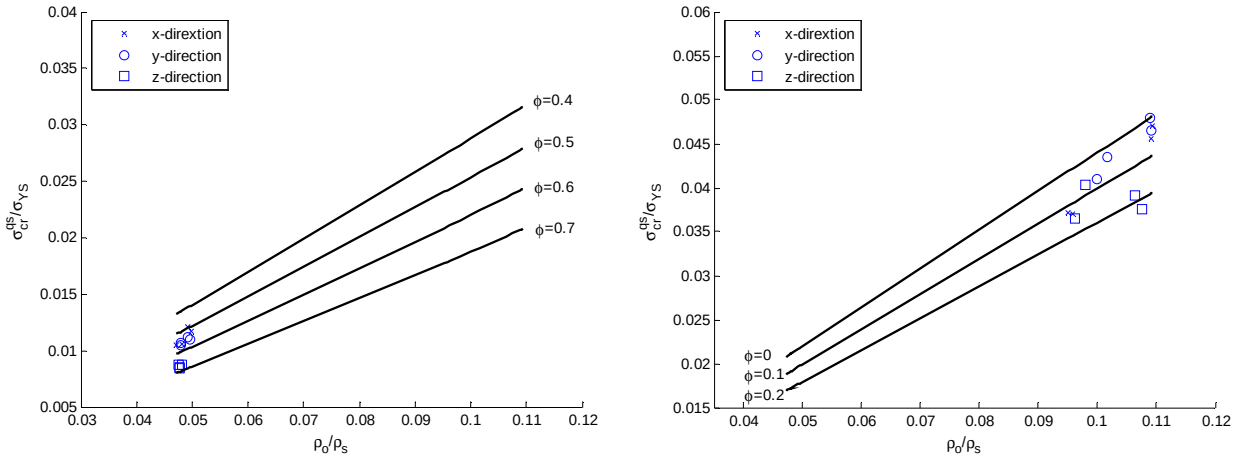

(a) (b)

Figure 8.4 Crushing over yield stress of the solid material against relative density for (a) Rohacell-51WF and (b) Rohacell-110WF specimens (Equation (8.1)).

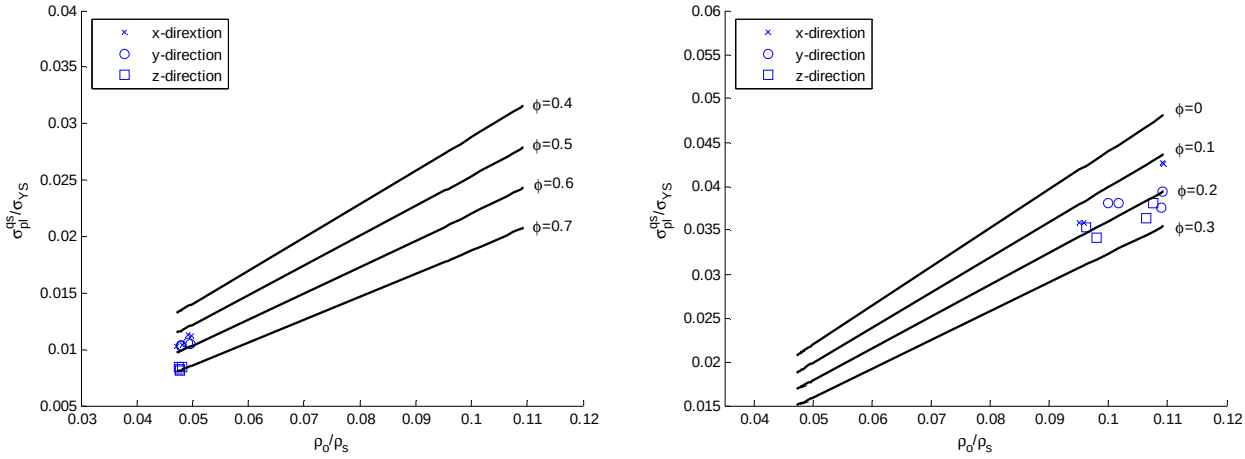

(a) (b)

Figure 8.5 Plateau over yield stress of the solid material against relative density for (a) Rohacell-51WF and (b) Rohacell-110WF specimens (Equation (8.1)).

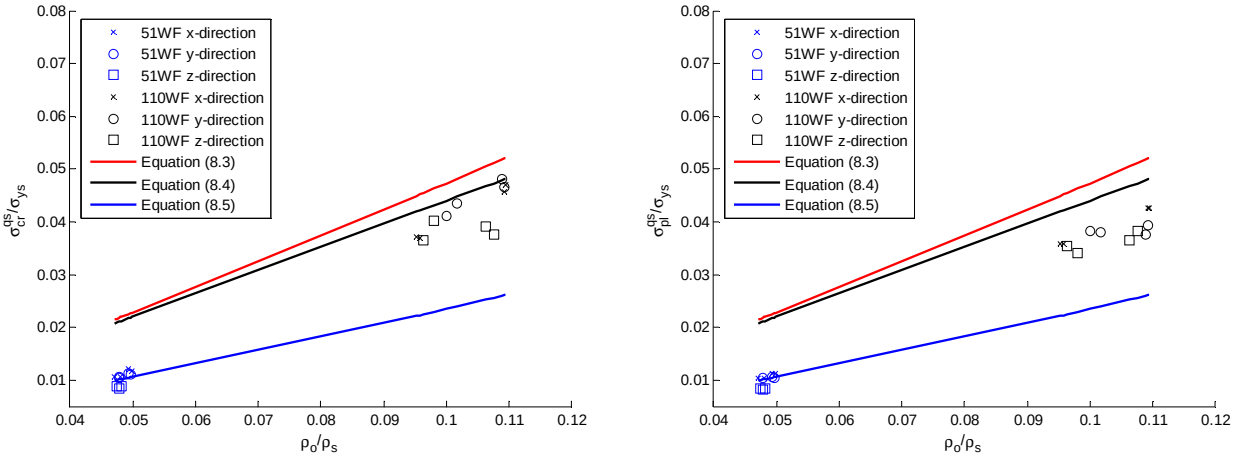

(a) (b)

Figure 8.6 (a) Crushing over yield stress of the solid material and (b) Plateau over yield stress of the solid material against relative density for Rohacell-51WF and 110WF along with predictions of Equations (8.3), (8.4) and (8.5).

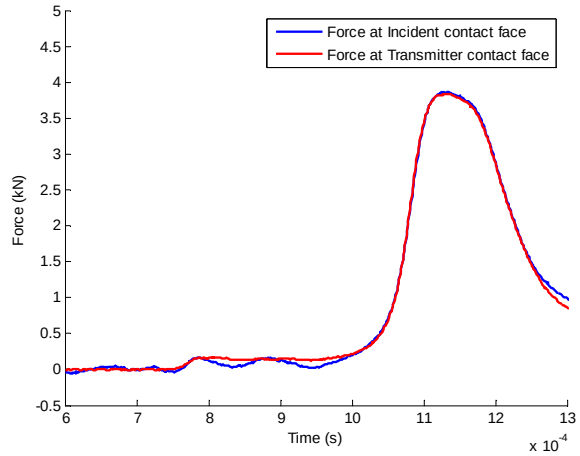

(a)

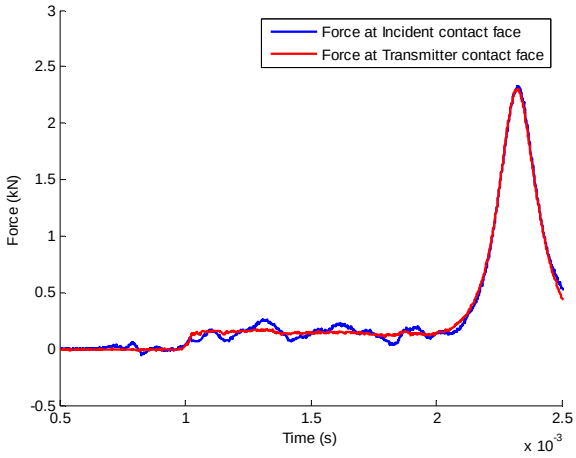

(b)

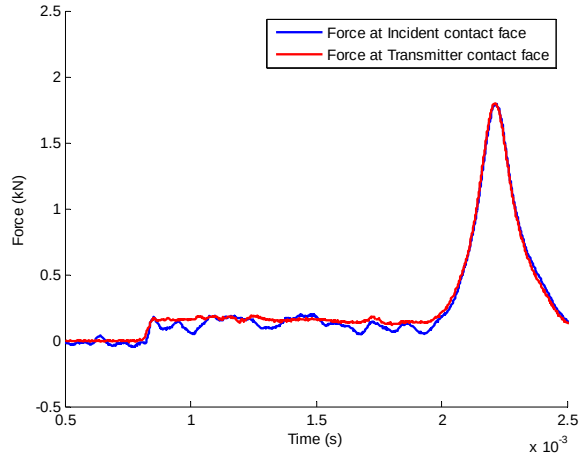

(c)

Figure 8.7 Forces at the incident/specimen and transmitter/specimen interfaces from SHPB tests on Rohacell-51WF z direction specimens with thickness (a) 3mm, (b) 6 mm and (c) 8 mm using PMMA pressure bars.

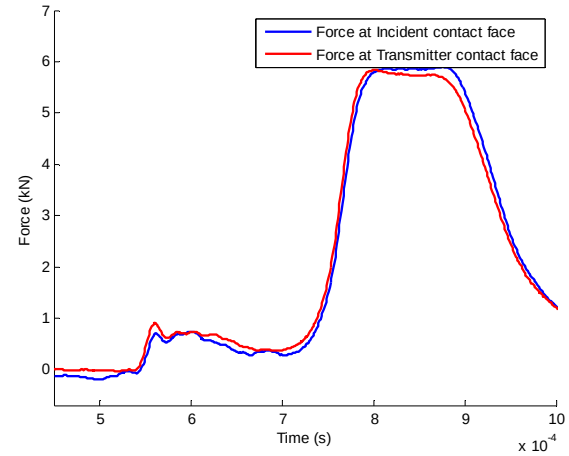

(a)

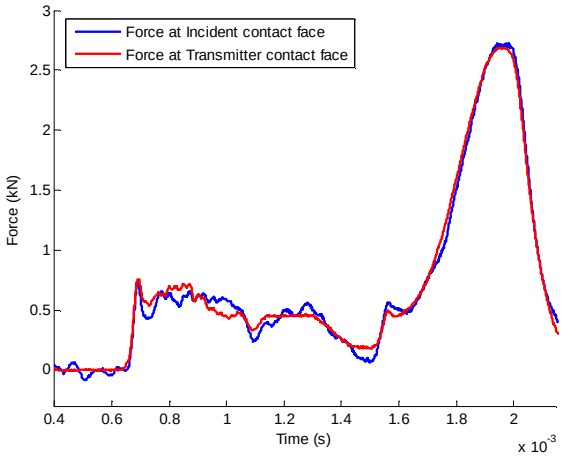

(b)

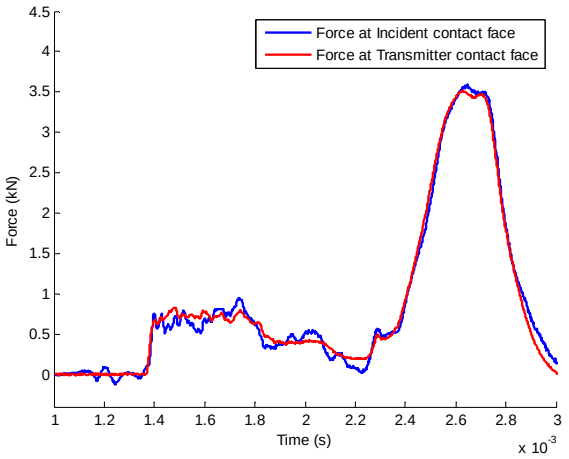

(c)

Figure 8.8 Forces at the incident/specimen and transmitter/specimen interfaces from SHPB tests on Rohacell-110WF z direction specimens with thickness (a) 3mm, (b) 6 mm and (c) 8 mm using PMMA pressure bars.

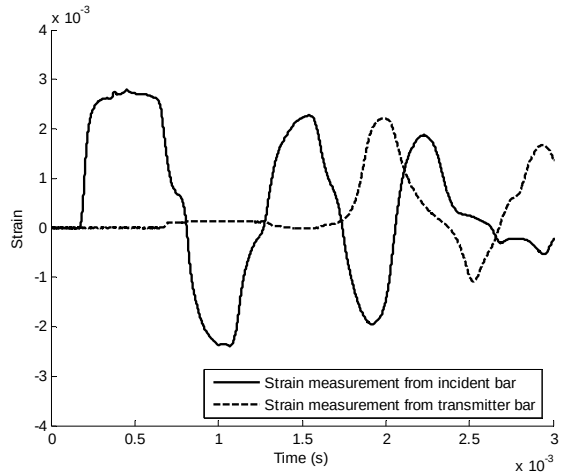

(a)

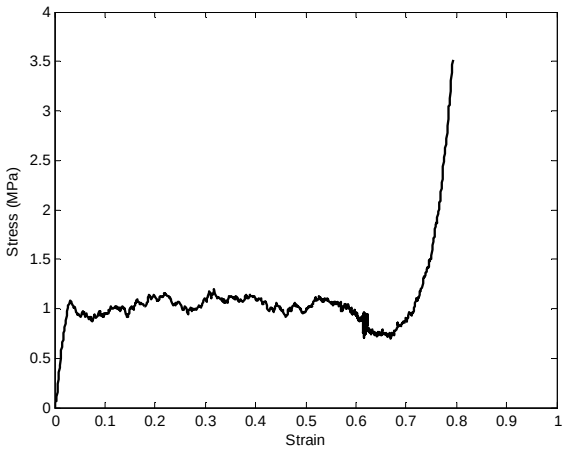

(b)

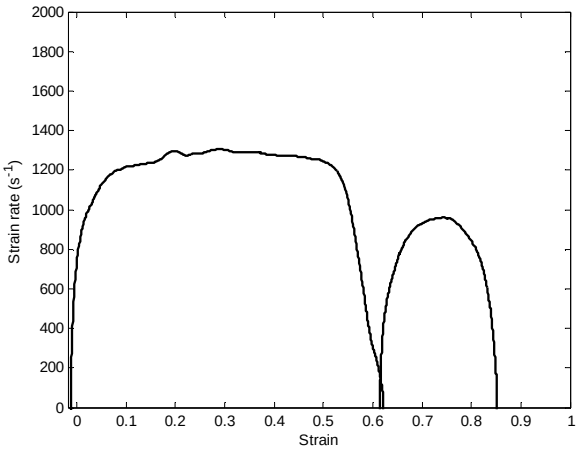

(c)

Figure 8.9 (a) Strain histories from incident and transmitter PMMA pressure bars and (b) Stress-strain curve and (c) Strain rate from a SHPB test on Rohacell-51WF (x direction, length = 8 mm, density = 59 kgm^{-3}) using the PMMA pressure bars.

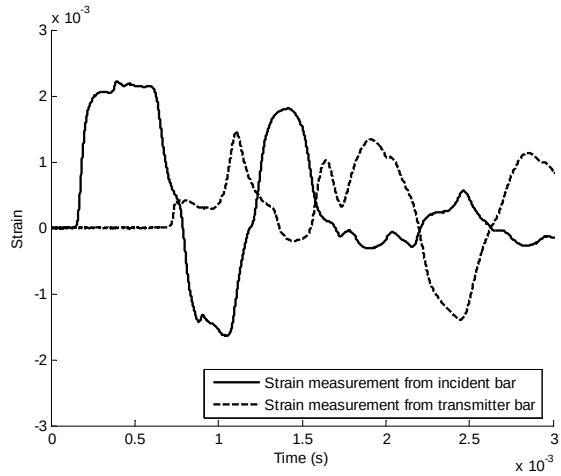

(a)

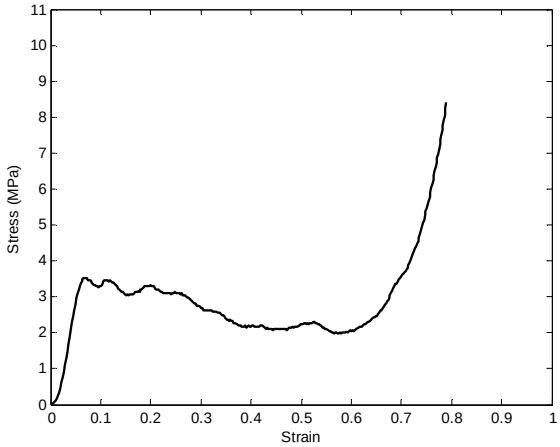

(b)

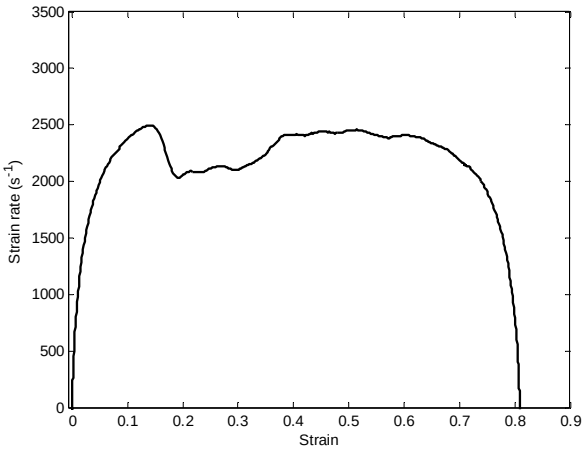

(c)

Figure 8.10(a) Strain histories from incident and transmitter PMMA pressure bars and (b) Stress-strain curve and (c) Strain rate from a SHPB test on Rohacell-110WF (y direction, length = 3mm, density = 122 kgm^{-3}) using the PMMA pressure bars.

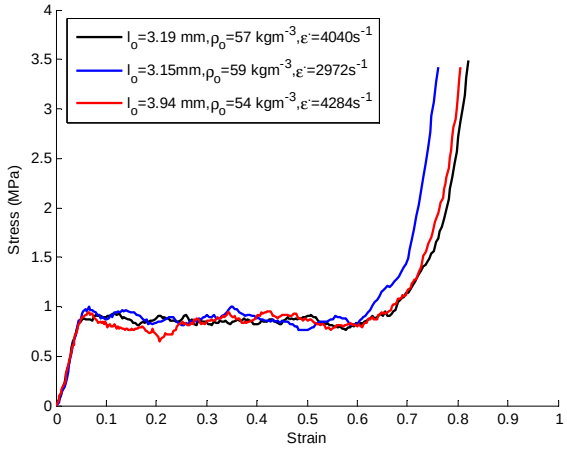

(a)

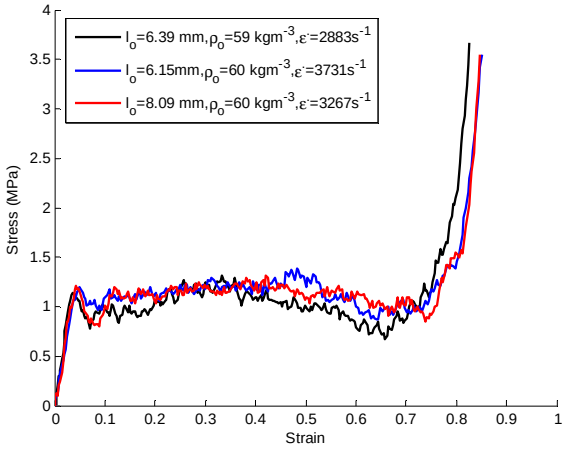

(b)

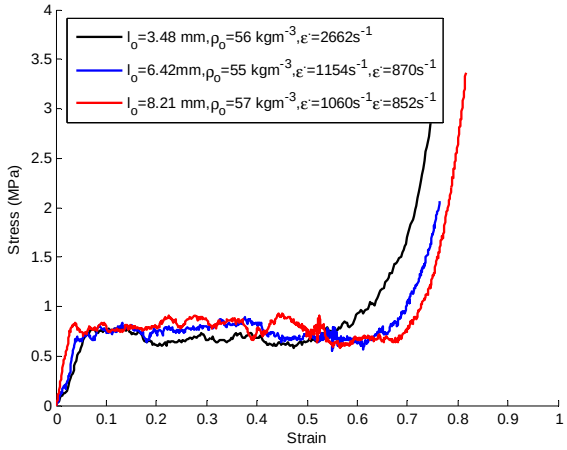

(c)

Figure 8.11 Typical stress-strain curves from a SHPB test on Rohacell-51WF (a) x direction, (b) y direction and (c) z direction using PMMA pressure bars.

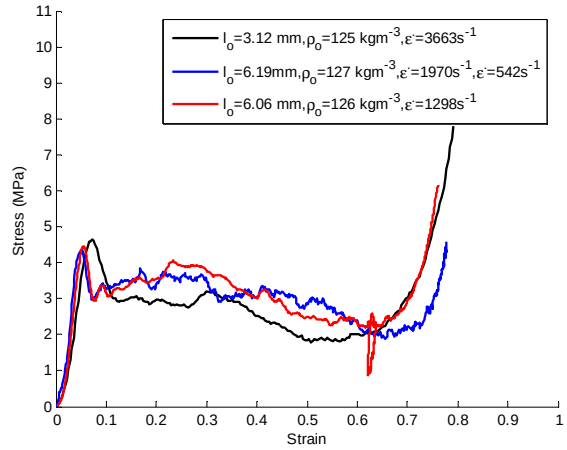

(a)

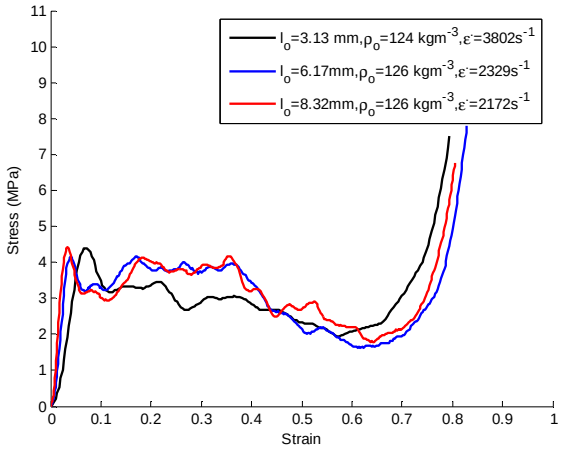

(b)

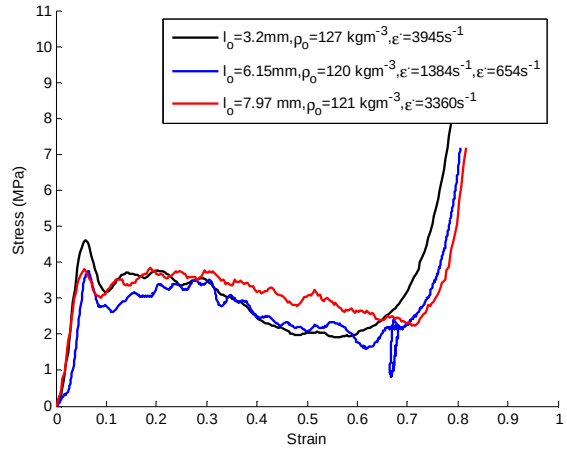

(c)

Figure 8.12 Typical stress-strain curves from a SHPB test on Rohacell-110WF (a) x direction, (b) y direction and (c) z direction using PMMA pressure bars.

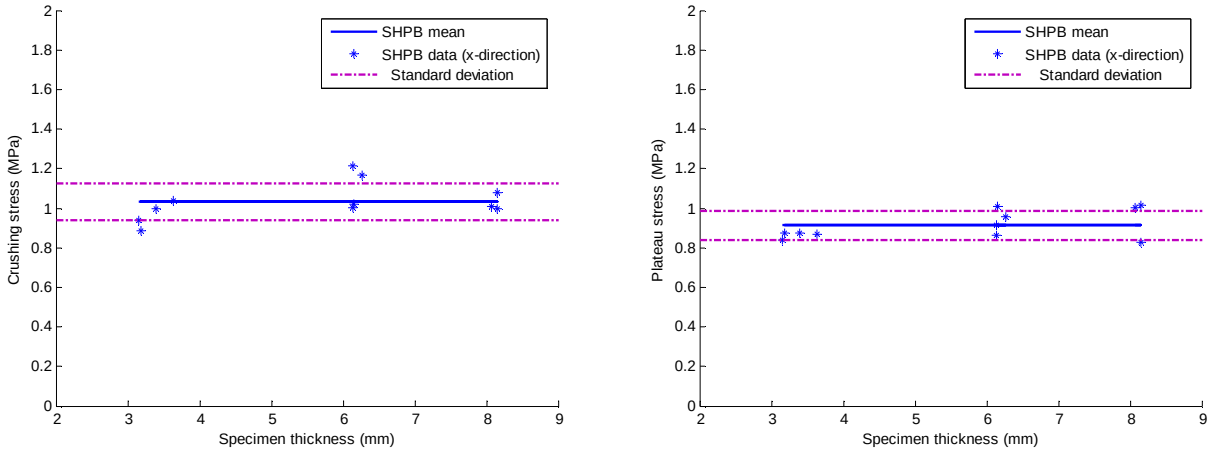

(a) (b)

Figure 8.13 (a) Crushing stress and (b) plateau stress against specimen's thickness for Rohacell-51WF specimens (x-direction).

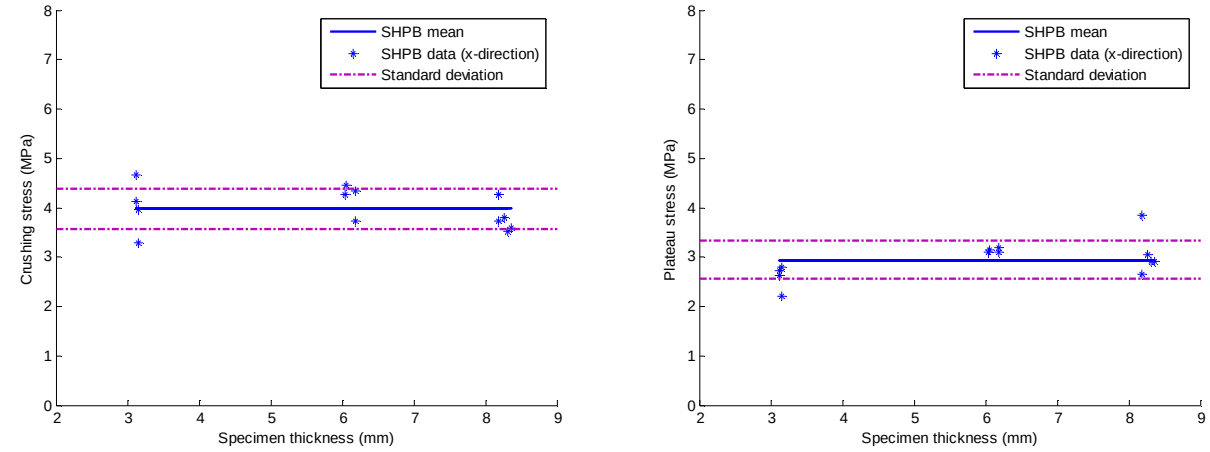

(a) (b)

Figure 8.14 (a) Crushing stress and (b) plateau stress against specimen's thickness for Rohacell-110WF specimens (x-direction).

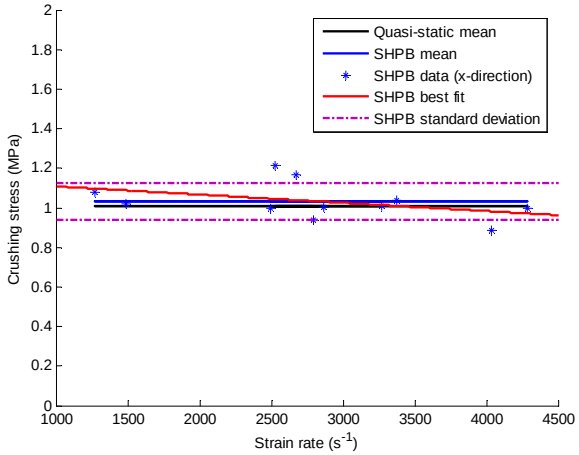

(a)

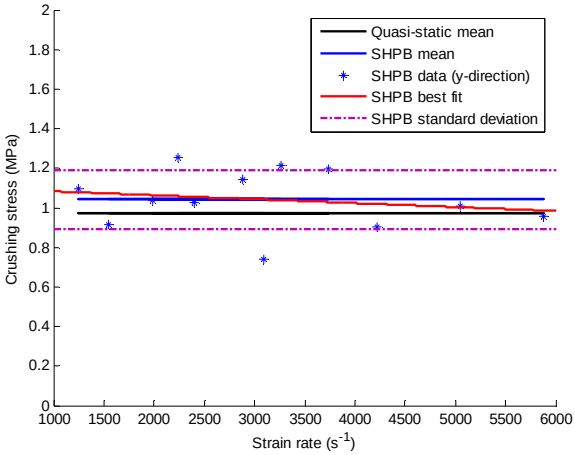

(b)

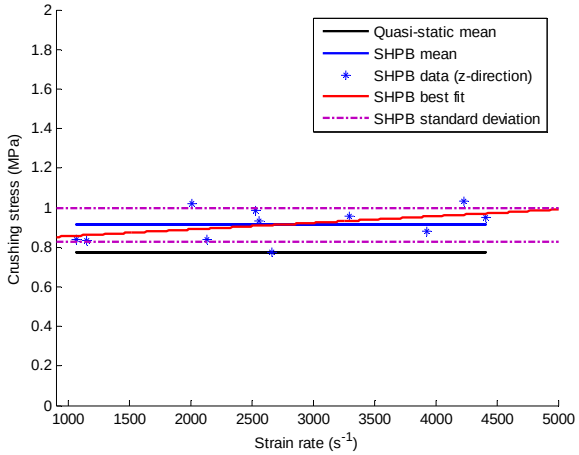

(c)

Figure 8.15 Crushing stress against strain rate for Rohacell-51WF specimens (a) x, (b) y and (c) z directions.

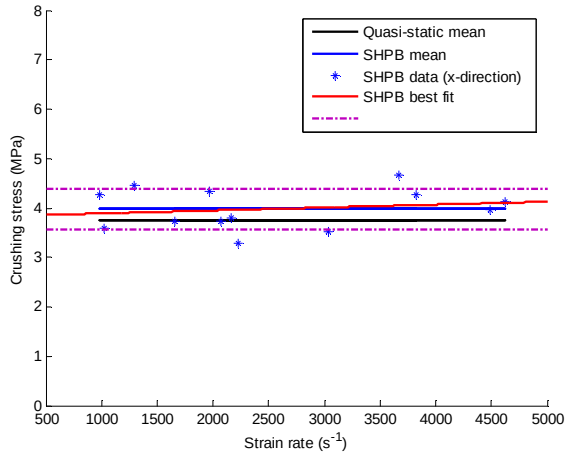

(a)

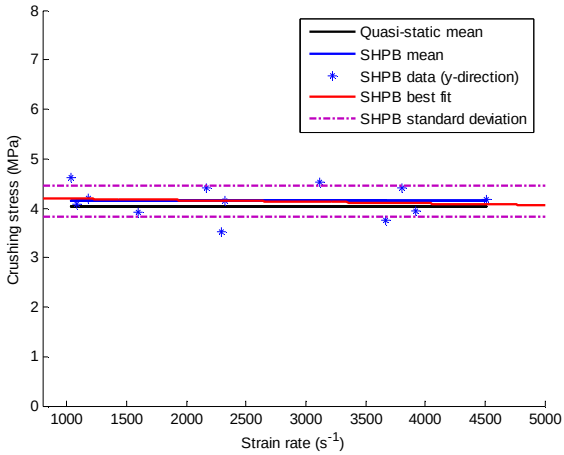

(b)

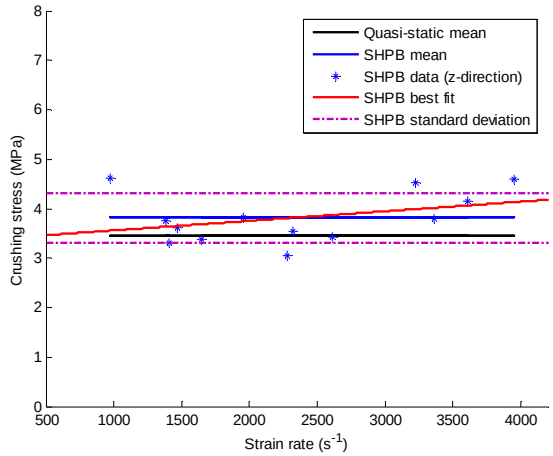

(c)

Figure 8.16 Crushing stress against strain rate for Rohacell-110WF specimens (a) x, (b) y and (c) z directions.

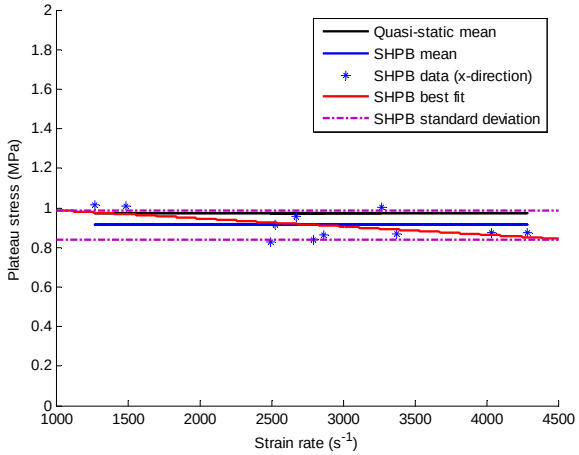

(a)

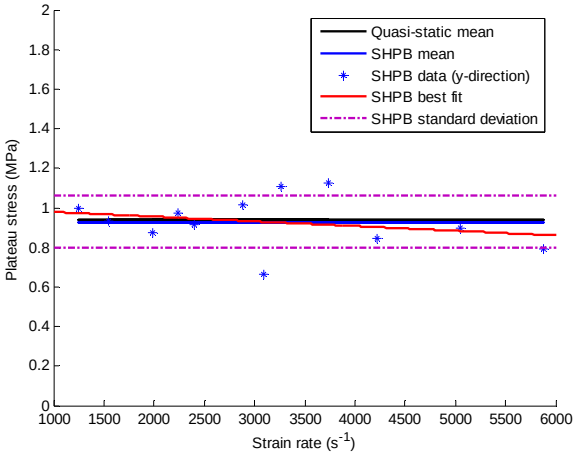

(b)

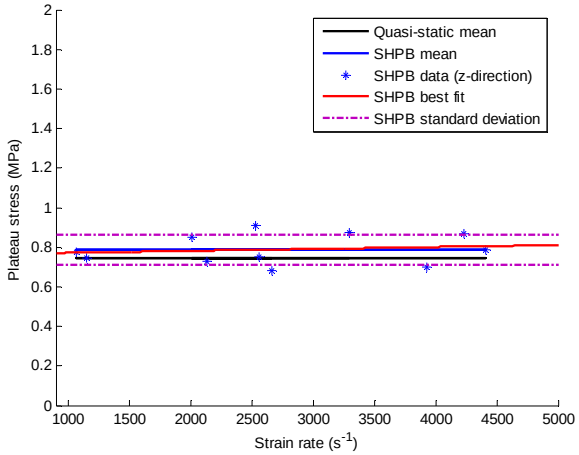

(c)

Figure 8.17 Plateau stress against strain rate for Rohacell-51WF specimens (a) x, (b) y and (c) z directions.

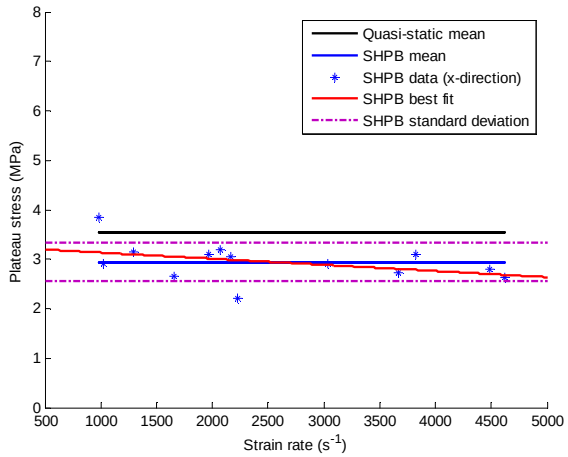

(a)

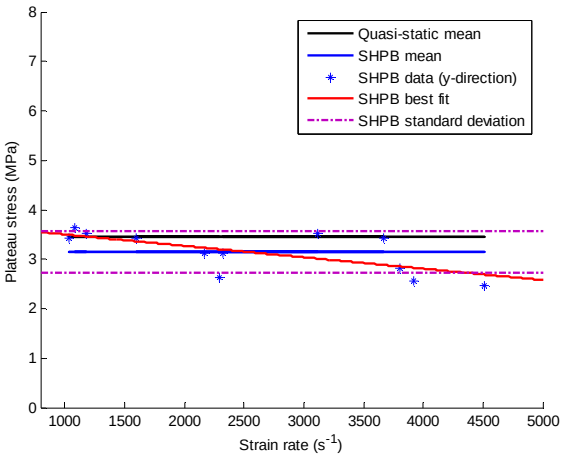

(b)

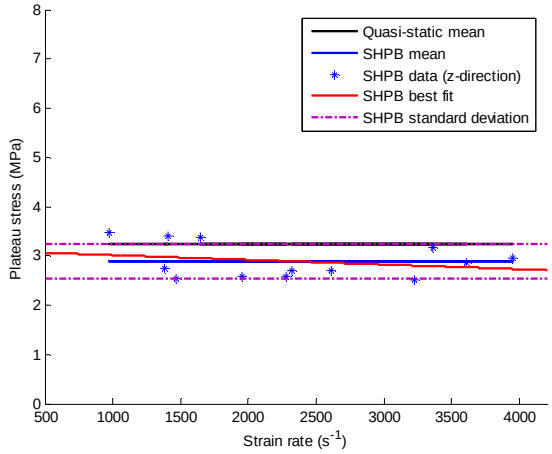

(c)

Figure 8.18 Plateau stress against strain rate for Rohacell-110WF specimens (a) x, (b) y and (c) z directions.

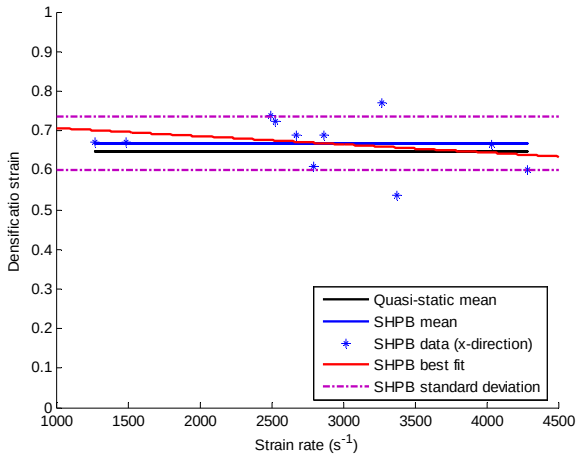

(a)

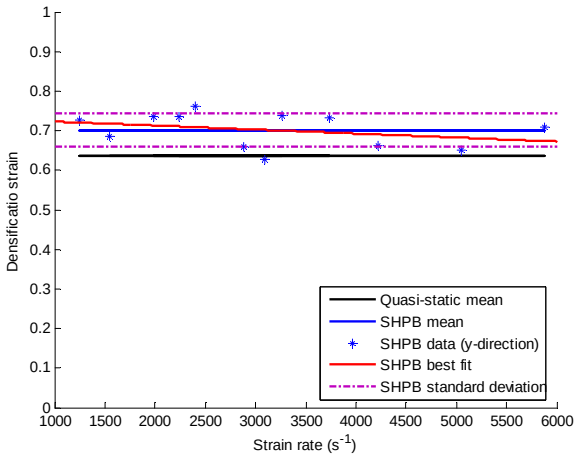

(b)

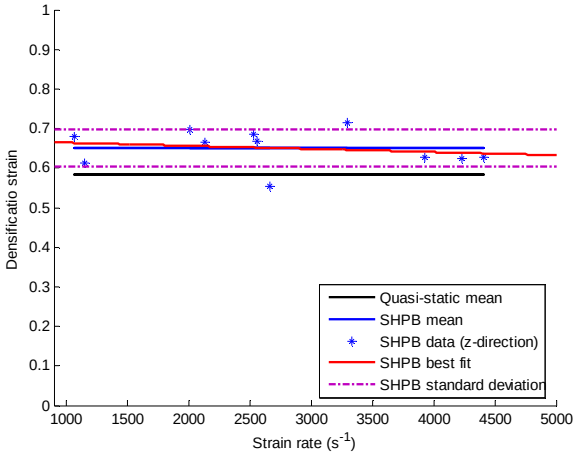

(c)

Figure 8.19 Densification strain against strain rate for Rohacell-51WF specimens (a) x, (b) y and (c) z directions.

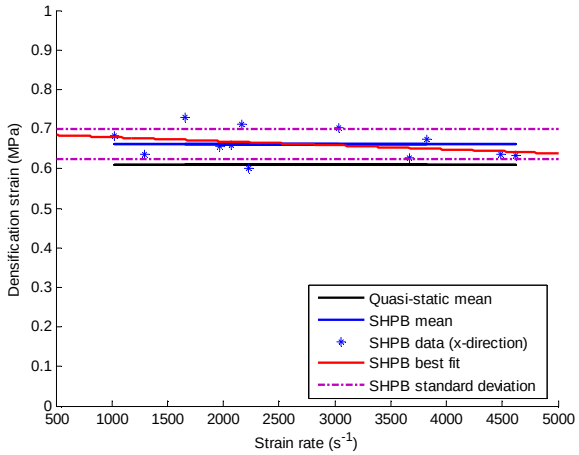

(a)

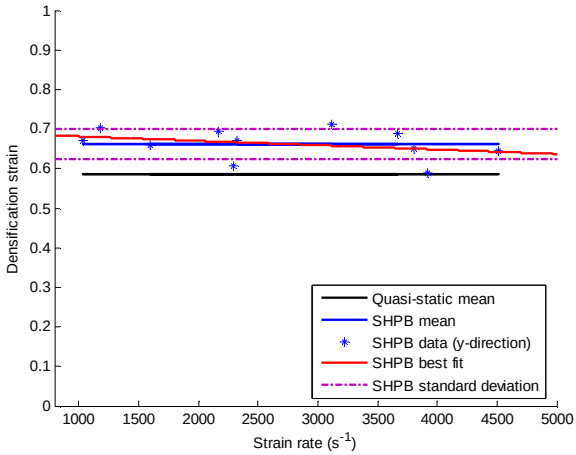

(b)

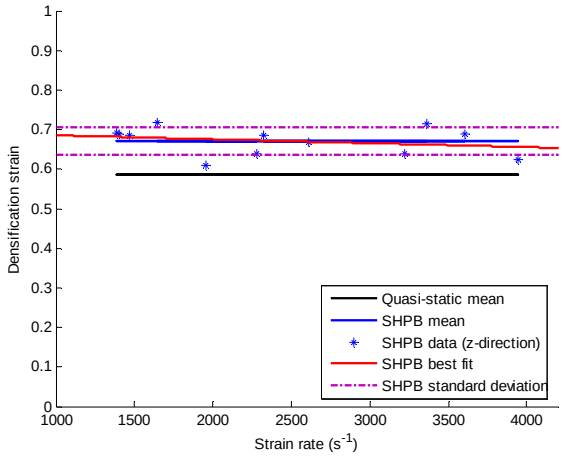

(c)

Figure 8.20 Densification strain against strain rate for Rohacell-110WF specimens (a) x, (b) y and (c) z directions.

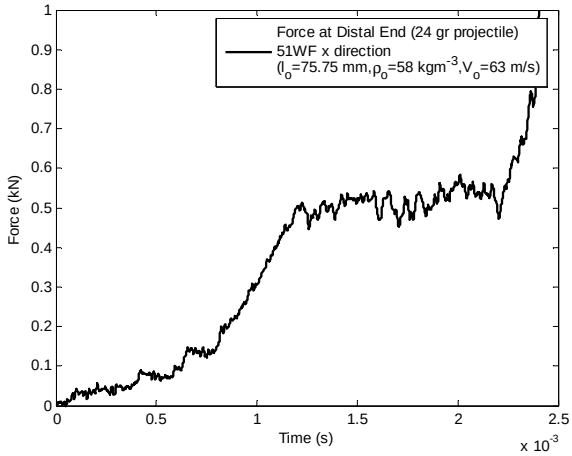

(a)

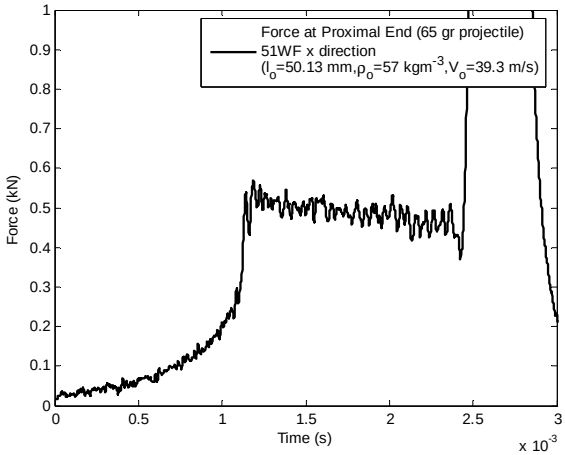

(b)

Figure 8.21 (a) Distal and (b) Proximal end forces from DI tests on Rohacell-51WF x direction.

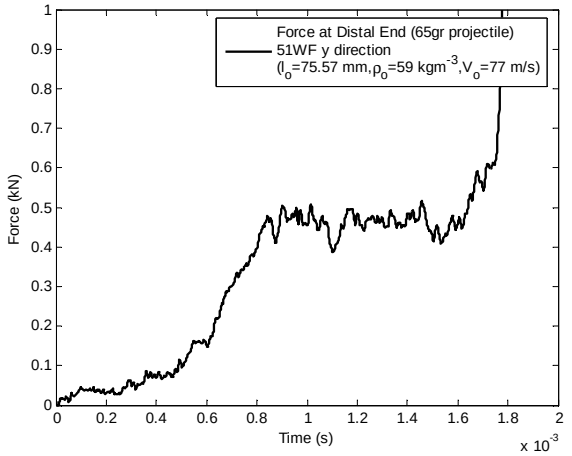

(a)

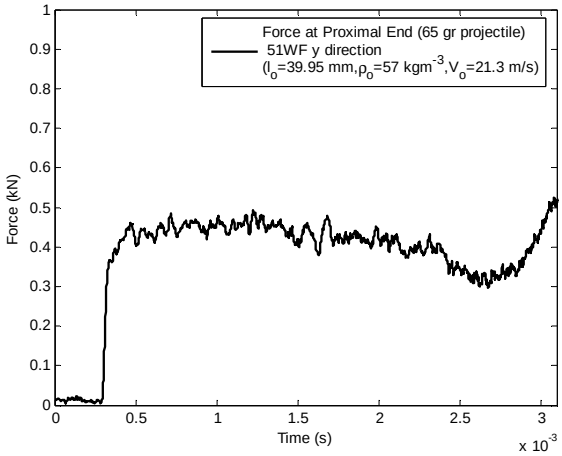

(b)

Figure 8.22 (a) Distal and (b) Proximal end forces from DI tests on Rohacell-51WF y direction.

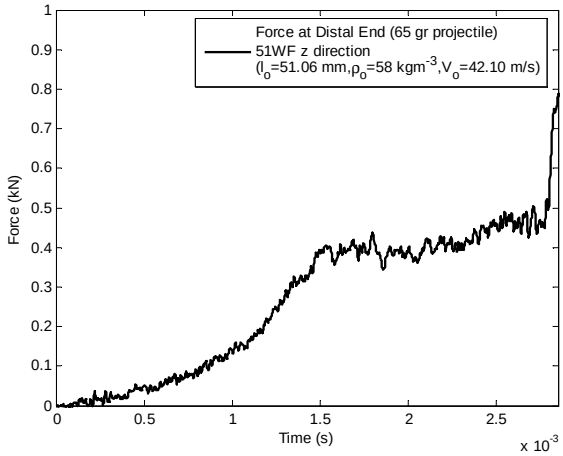

(a)

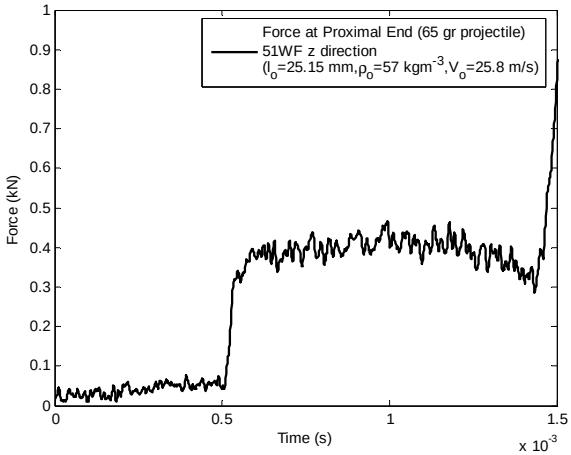

(b)

Figure 8.23 (a) Distal and (b) Proximal end forces from DI tests on Rohacell-51WF z direction.

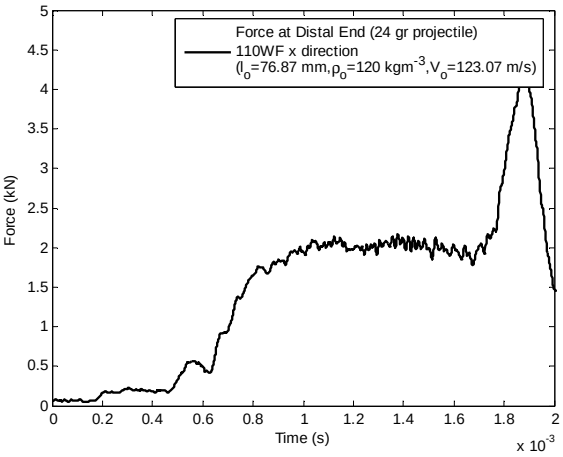

(a)

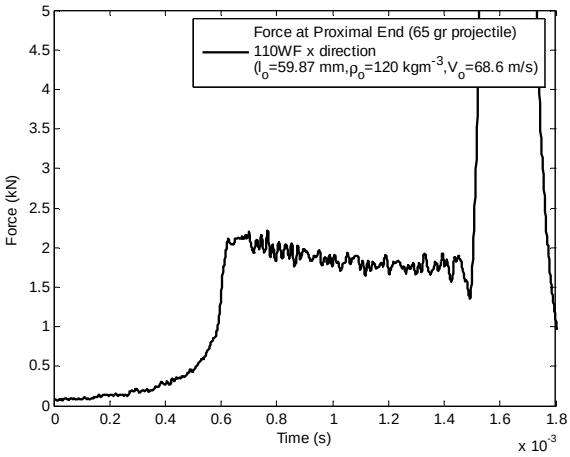

(b)

Figure 8.24 (a) Distal and (b) Proximal end forces from DI tests on Rohacell-110WF x direction.

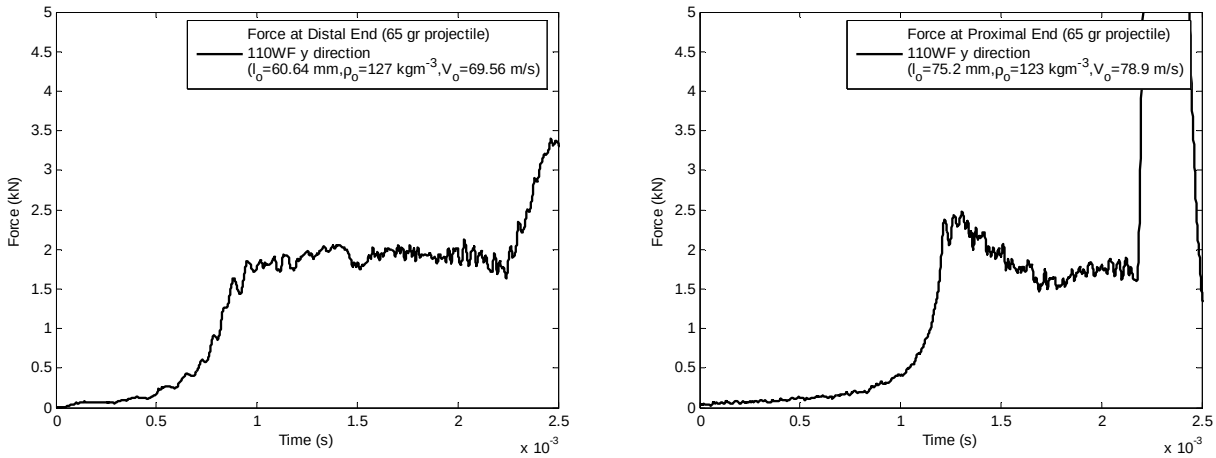

(a) (b)

Figure 8.25 (a) Distal and (b) Proximal end forces from DI tests on Rohacell-110WF y direction.

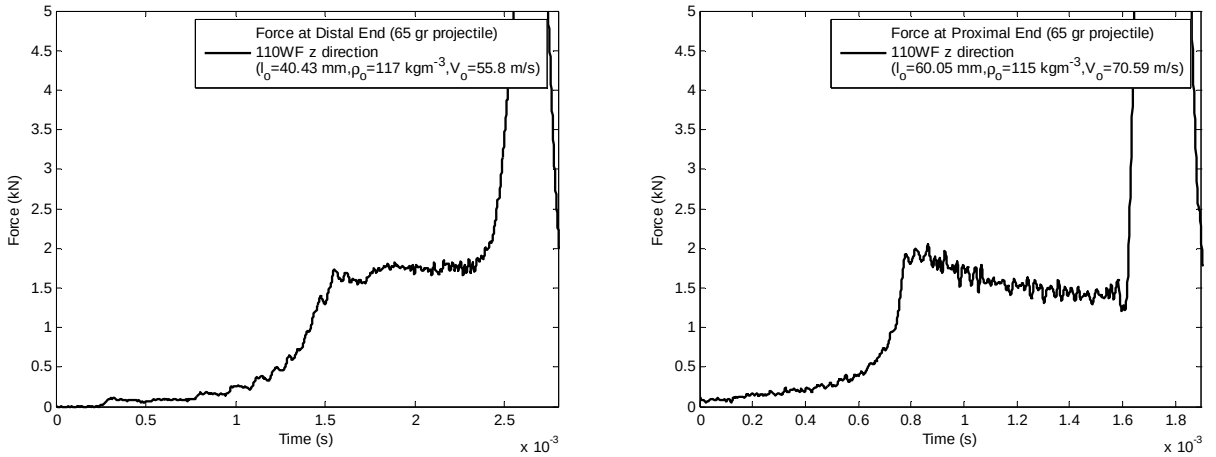

(a) (b)

Figure 8.26 (a) Distal and (b) Proximal end forces from DI tests on Rohacell-110WF z direction.

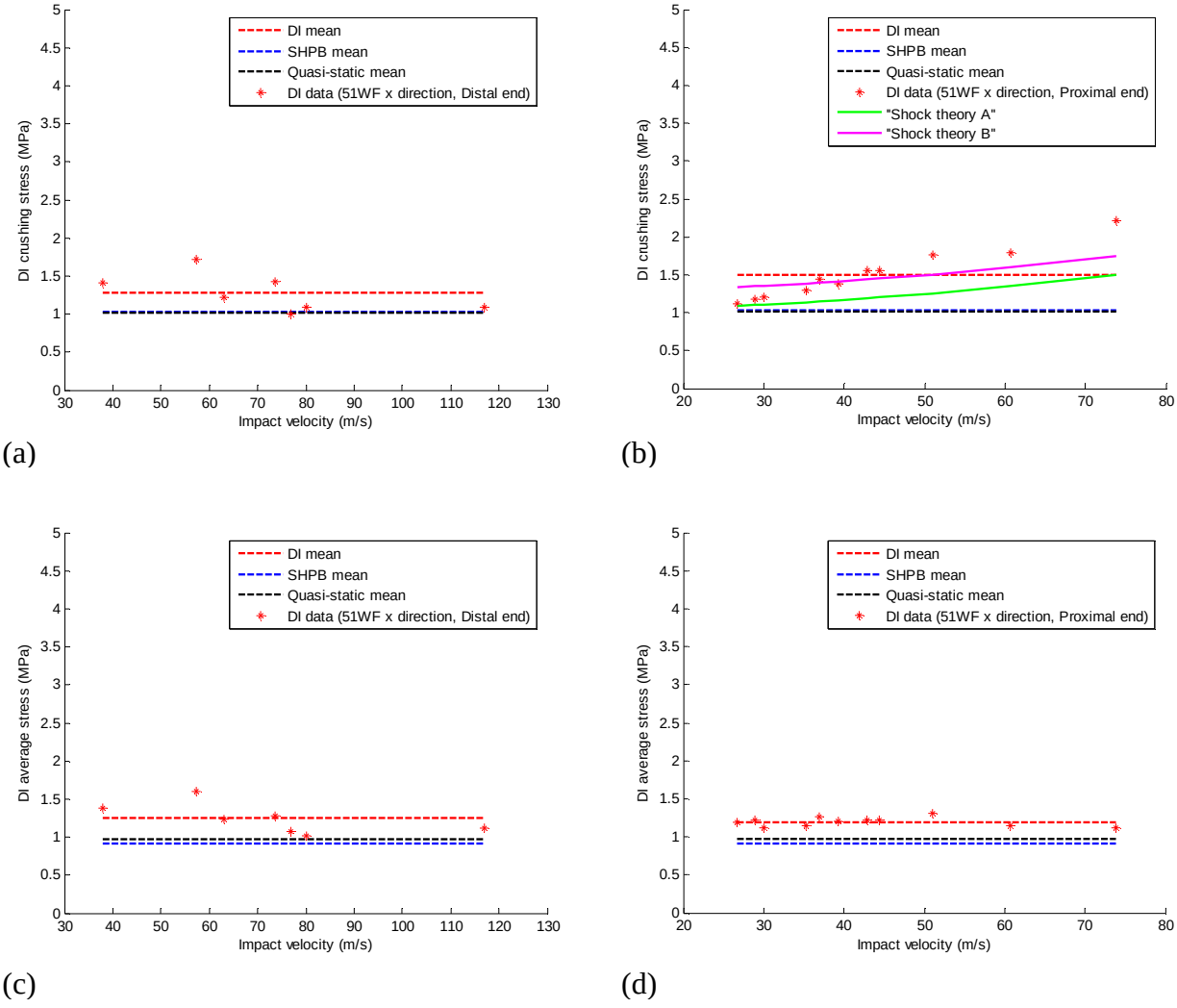

Figure 8.27 (a) Crushing, (c) average stresses against impact velocity from distal ends and (b) crushing, (d) average stresses against impact velocity from proximal ends from DI tests on Rohacell-51WF x direction.

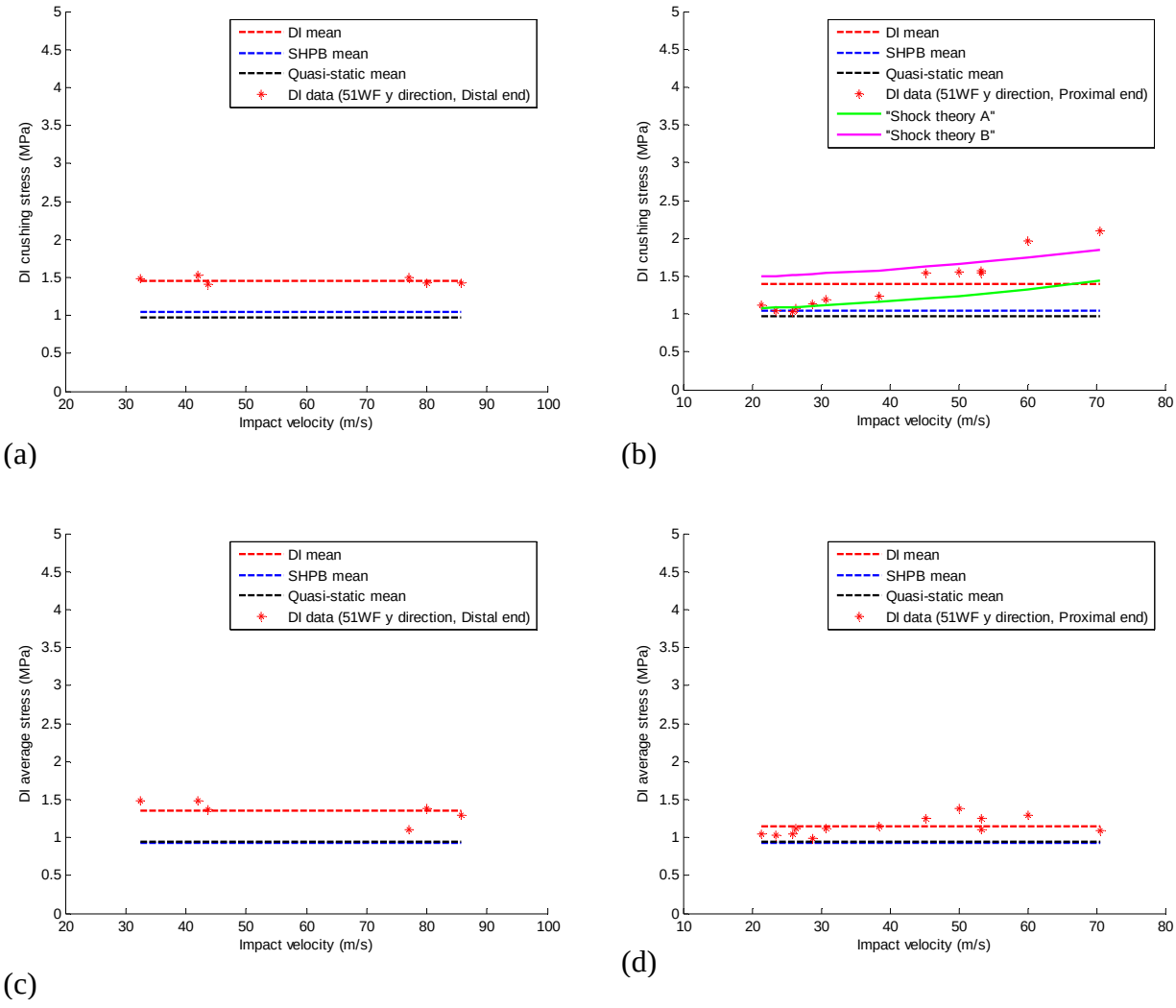

Figure 8.28 (a) Crushing, (c) average stresses against impact velocity from distal ends and (b) crushing, (d) average stresses against impact velocity from proximal ends from DI tests on Rohacell-51WF y direction.

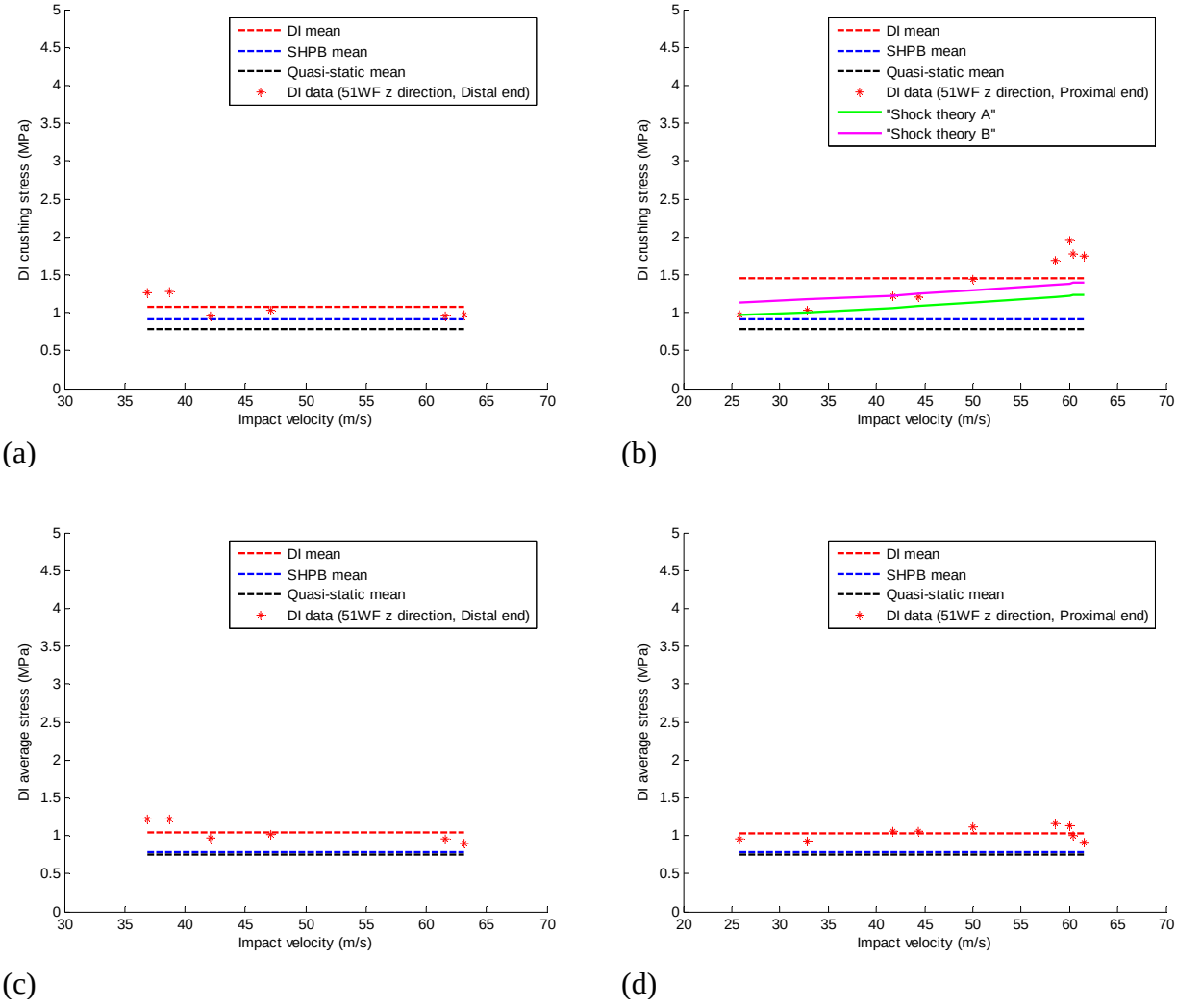

Figure 8.29 (a) Crushing, (c) average stresses against impact velocity from distal ends and (b) crushing, (d) average stresses against impact velocity from proximal ends from DI tests on Rohacell-51WF z direction.

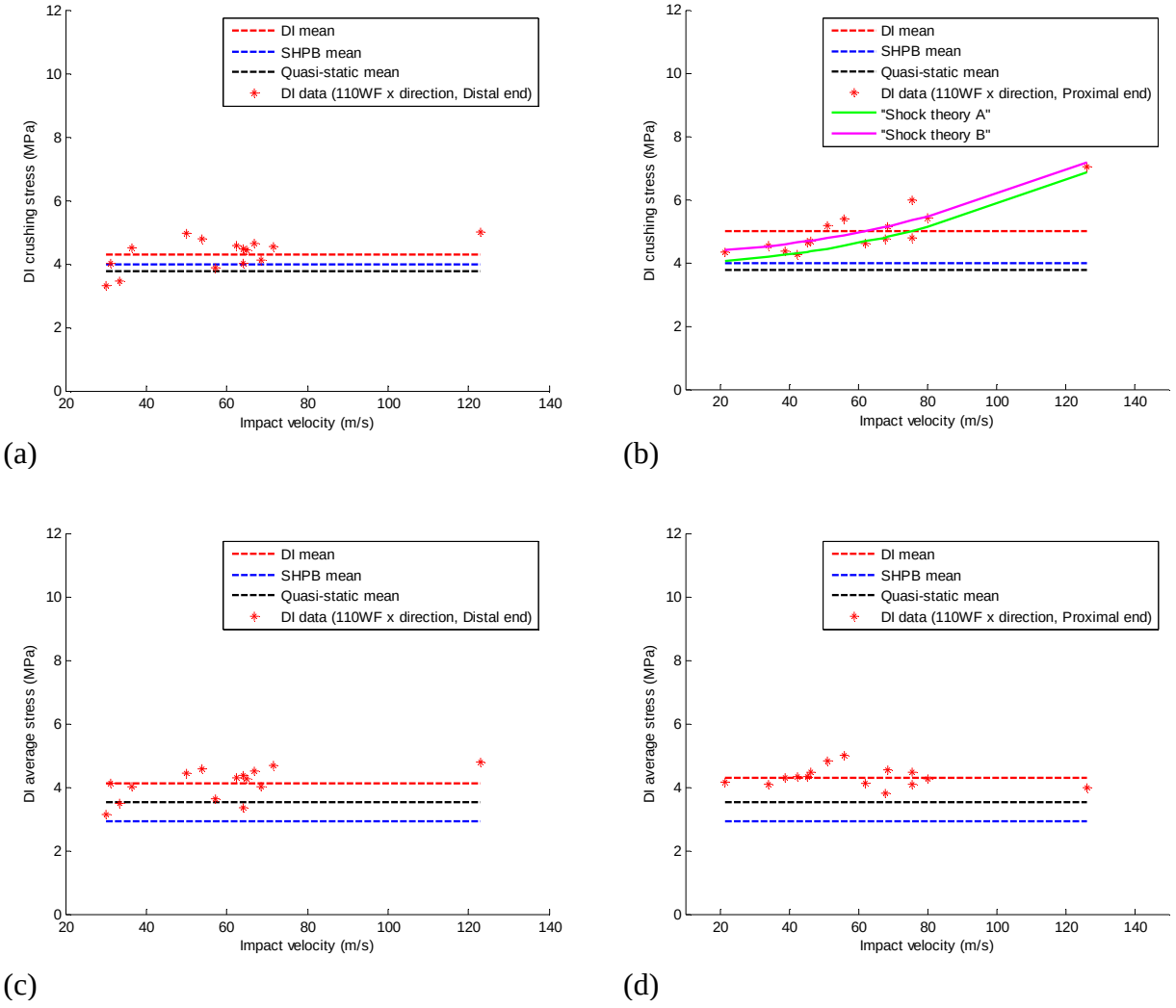

Figure 8.30 (a) Crushing, (c) average stresses against impact velocity from distal ends and (b) crushing, (d) average stresses against impact velocity from proximal ends from DI tests on Rohacell-110WF x direction.

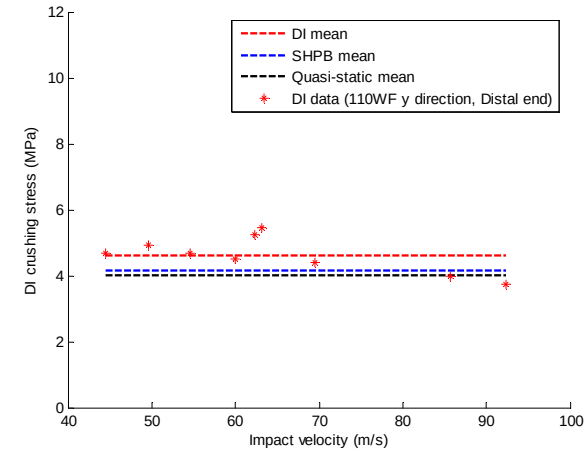

(a)

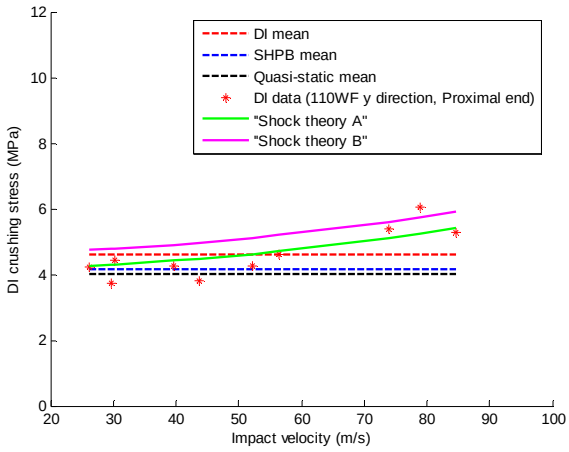

(b)

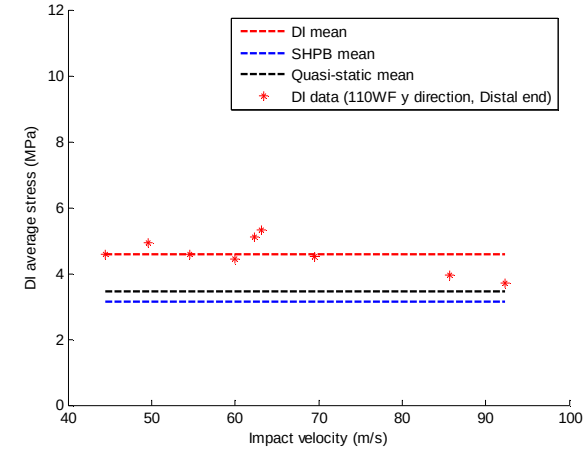

(c)

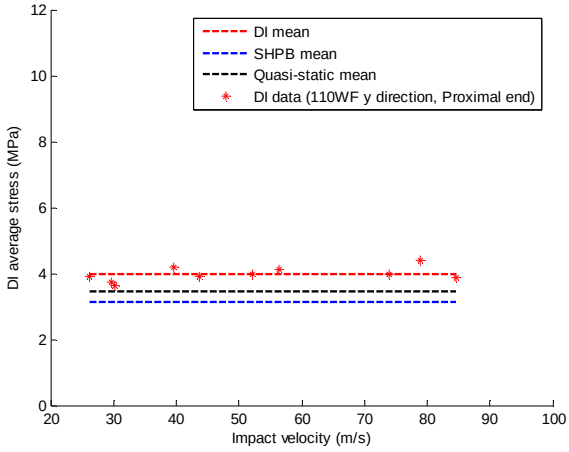

(d)

Figure 8.31 (a) Crushing, (c) average stresses against impact velocity from distal ends and (b) crushing, (d) average stresses against impact velocity from proximal ends from DI tests on Rohacell-110WF y direction.

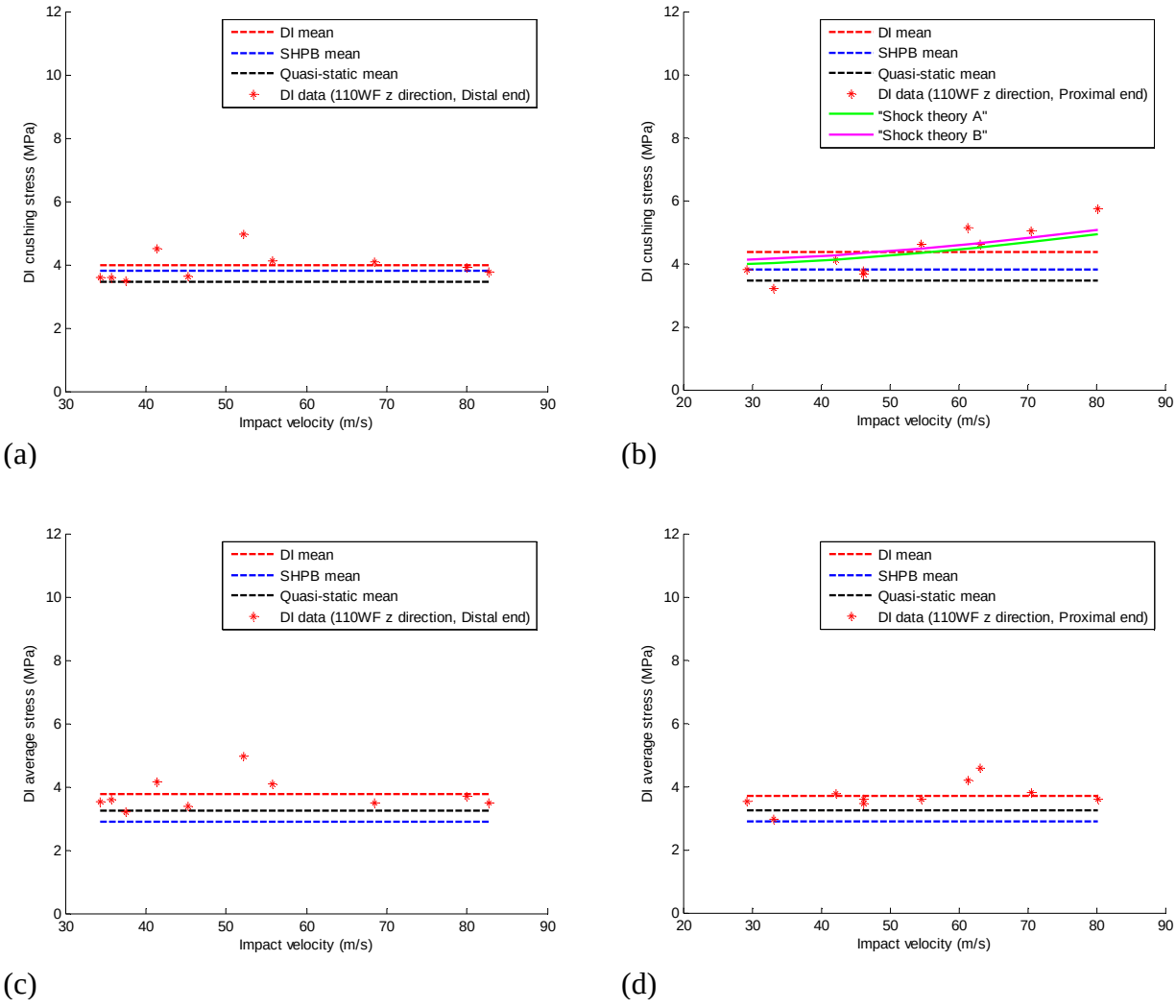

Figure 8.32 (a) Crushing, (c) average stresses against impact velocity from distal ends and (b) crushing, (d) average stresses against impact velocity from proximal ends from DI tests on Rohacell-110WF z direction.

CHAPTER 9

Concluding Remarks and Further Research

9.1 Conclusions

The limitations of traditional SHPB arrangements for testing of low density, soft materials were discussed (Section 2.2). One of the main difficulties is that it becomes impossible to check for stress uniformity in the specimen. The use of elastic low impedance bars is attractive due to the simple analysis involved in the processing of the bar strain histories. However, there exists a class of materials (e.g. across the grain balsa wood, Rohacell foam) wherein the use of viscoelastic (e.g. PMMA) pressure bars is regarded as essential to perform SHPB tests. For example Magnesium bars proved suitable for checking forces at both specimen/bar interfaces for along the grain balsa specimens with a maximum length of 6 mm. On the other hand, the PMMA bars allowed stress equilibrium to be checked for all three directions of balsa wood and for specimens of lengths varying between 3 mm to 8 mm. This indicates the superiority of the use of viscoleastic pressure bars for testing soft materials to large strains.

A literature review was carried out on previous techniques that have been used to overcome the difficulties involved when testing soft materials. The method presented by Bacon [33] was adopted in this study as it was regarded as rather advantageous over the other techniques, due to the fact that it is simple from a mathematical point of view and easy to implement. Accurate results were achieved when the method was applied to impact tests that involved the use of viscoelastic or elastic bars. Also, a discussion on the validity of the assumption of stress uniformity within the specimen in SHPB tests was presented (Section 2.4). It was concluded that stress equilibrium within the specimen should never be assumed for soft materials and

should always be checked during SHPB testing, even if using the proposed optimal lengths presented in Section 2.4.

An experimentally determined propagation coefficient was evaluated from a series of impact tests using axial strain measurements according to Equation (4.13) for two different diameter PMMA bars (20 mm and 40 mm) and for Magnesium pressure bars. The experimentally determined propagation coefficient is representative of both the dispersion and attenuation and can be used to describe waves at any point of the bar. The Elastic Modulus of both PMMA bars and Magnesium bars was evaluated using the elementary theory (Equation (4.7)). Although, the method is based on the one-dimensional theory it was proven to be accurate for the impact tests performed in this study. For the case of the PMMA bars it was concluded that the elementary theory is accurate for frequencies up to between 10 to 15 kHz and 6 to 8 kHz for the 20 mm and 40 mm diameter bars respectively. For the Magnesium bars it was concluded that the elementary theory is accurate for frequencies up to between 20 to 30 kHz. It should be noted that for the impact tests performed in this study no energy was detected above these frequencies (see Figures 4.4, 4.5 and 6.3).

For the case of the 20 mm diameter PMMA pressure bar, direct measurements of both axial and lateral strains on an impacted PMMA rod led to the determination of complex Poisson's ratio. Furthermore, the complex Shear and Bulk moduli were determined. It was found that Poisson's ratio and the complex Shear and Young's moduli agreed well with the data reported by Mousavi et al. [62] for the same material and the same diameter bar. It is worth mentioning that the method adopted herein utilised bars with shorter lengths than the 2 m long bars used in ref. [62]. Also, the method adopted herein to determine the Shear modulus was simpler than the method of Mousavi et al. [62], since no torsion tests were carried out.

Wave separation techniques were also discussed. In order to measure to large strains without the need for impractically long bars, wave separation is essential (see for example Figure 7.16). Both time-domain and frequency-domain wave separation are possible. A review of the existing wave separation techniques was presented together with the advantages and disadvantages of each method (Section 5.6). It was

concluded that the method that is computationally efficient and avoids problems associated with truncation of the measured signals and critical frequencies is the use of more than two strain measurements and the application of a suitable exponential window. The method was applied successfully to both 20 mm and 40 mm diameter PMMA pressure bars as well as to the Magnesium pressure bars. Both the accuracy of the wave separation method and the accuracy of the propagation coefficients adopted in this study for analysing data obtained from SHPB and DI tests were verified experimentally (see Figures 5.6, 5.7 and 6.8).

The quasi-static and dynamic compressive properties of two types of cellular materials were investigated, i.e. balsa wood and Rohacell foam. The quasi-static and dynamic compressive properties of balsa wood were investigated along its three principal directions. From the quasi-static compression of balsa wood it was revealed that the along the grain direction is the strongest direction due to the elongated shape of the cells in this direction. The other two directions had similar properties with the radial balsa wood being stronger than the tangential due to the presence of rays in this direction that act as reinforcement. Quasi-static tests were performed with and without lateral constraint. It was observed that the lateral constraint had negligible affect on the results obtained for all directions (Figure 7.8). It is proposed that the reason is the same for any direction, i.e. the plastic compression of the cells takes place in the loading direction without the need of gross expansion in the perpendicular to loading direction. It is worth mentioning that the effect of the lateral constraint has not been reported previously for radially or tangentially compressed balsa wood. Furthermore, the general trend observed in Figures 7.8 (a) and (b) is that when balsa wood is compressed in any of the three principal directions, the crushing stress increases with density. Different relationships, corresponding to different failure modes, were used to predict the crushing stress of the along the grain specimens. It was found that the plastic buckling failure mode prediction gave the best fit to experimental data. Furthermore, the quasi-static densification strain and plateau stress values were evaluated for all directions.

SHPB tests were performed on balsa samples over a range of strain rates utilising both PMMA and Magnesium pressure bars. Prior to analysing the SHPB test data,

the assumption of stress equilibrium was checked. Wave separation was performed for all tests. As was the case for the quasi-static tests, both the crushing and plateau stresses increased for increasing density samples. For all directions, the crushing stress, the plateau stress and the densification strain did not vary with increasing strain rates for the SHPB tests. For the along the grain balsa wood it was found that the plastic buckling deformation mechanism again gave the best fit to the experimental crushing stresses. The SHPB tests revealed an enhancement in both the crushing stress and the plateau stress when compared with their quasi-static values for all directions. This enhancement was greater in percentage for the across the grain balsa, although the actual magnitude of the increase in stress was greatest for the along the grain direction. The crushing stress of the along, radial and tangential specimens increased by 16%, 72% and 43% respectively. The increase in the plateau stress for the along the grain direction was 11% and in the radial and tangential directions, the increase was 38% and 39% respectively. On the other hand, there was negligible difference in terms of the densification strains between the quasi-static and SHPB results for all directions. It is worth pointing out that there is currently no published data for SHPB tests of across the grain balsa.

DI tests were performed on along and across the grain balsa wood in order to measure distal and proximal end forces. In should be noted that the proximal force pulses for the DI tests on radial and tangential specimens were difficult to interpret. The force increased in a series of steps at lower loads than expected and the specimens exhibited global buckling patterns rather than uniform crushing in the loading direction. For the along the grain balsa the initial peak stresses of the distal and proximal ends showed no increase with increasing impact velocity. Similar conclusions were made for the radial specimens. Compaction waves were not considered to have a notable effect on crushing stresses over the range of impact velocities used in this study.

Two types of Rohacell foam were examined i.e. Rohacell-51WF and Rohacell-110WF, which represent two different densities. The quasi-static and dynamic compression behaviour was investigated for both types of foam along the three principal directions, namely the x and y-directions (which are the in-plane directions)

and z-direction representing the out-of-plane direction (Figure 8.1). No previous studies of the dynamic behaviour of Rohacell foam have been reported in the open literature. The dynamic response of Rohacell foam was examined by performing SHPB and DI tests utilising PMMA pressure bars.

From the quasi-static experiments it was revealed that both density foams are orthogonal isotropic with the in-plane-directions having similar properties and being the strongest directions (Figures 8.2 and 8.3). The crushing stress of Rohacell-110WF was about 76% greater than Rohacell-51WF. The quasi-static crushing stress values of both foams were predicted using different equations based on simplified cell geometries (Equations (8.1), (8.3)-(8.5)), but their predictions were regarded as unsatisfactory. One general conclusion that could be drawn from the test data is that the plastic bending of the edges, stretching of the cell faces and the compression of the entrapped air within the cells are all likely to contribute to the strength of Rohacell foam

Possible size effects on the compressive properties of both foams were examined. It was found the results obtained from the quasi-static and DI tests were not influenced by size effects and were representative of the net properties of the foam. For the case of the shortest specimens used in the SHPB tests, it was concluded that size effects had little influence on the results.

The assumption of stress equilibrium within the specimens was checked for all SHPB tests and was regarded to be valid (see Figures 8.7 and 8.8). In addition, an approximately constant strain rate was achieved during each test (Figures 8.9 (c) and 8.10 (c)). The above observations gave confidence in the results presented for the SHPB tests of Rohacell-51WF and 110WF foam specimens. It is worth mentioning that the forces shown in Figure 8.7 had very low magnitudes of the order of approximately 0.17 MPa. It is therefore impossible to compare the results with data obtained if one used a Magnesium SHPB arrangement, as was the case for compression of across the grain balsa wood.

For the Rofacell-51WF the SHPB stress-strain curves (Figure 8.11) were similar to those obtained form the quasi-static tests (Figure 8.2). On the other hand, for Rohacell-110WF the stress-strain curve obtained from the SHPB tests (Figure 8.12) had a negative slope in the "plateau region", while the stress-strain curve from the quasi-static tests had an almost constant plateau region (Figure 8.3). This negative slope for the SHPB "plateau region" could be attributed to ejection of the material or changes in the deformation mode during the dynamic compression of Rohacell-110WF.

For all three directions of Rohacell-51WF and 110WF it was observed that there is no variation of the crushing stress, the plateau stress nor the densification strain with increasing strain rate (Figures 8.15-8.20). When comparing the SHPB mean crushing stresses with the quasi-static mean values it appeared that for the x and y-directions there was negligible increase (parts (a) and (b) of Figures 8.15 and 8.16), while a noticeable increase of the order of 18% and 11% was observed in the z-direction for Rohacell-51WF and 110WF respectively (parts (c) of Figures 8.15 and 8.16). For the Rohacell-51WF specimens the mean SHPB plateau stress was very close to the mean of the quasi-static plateau stress values for all directions (Figure 8.17). On the other hand, for the Rohacell-110WF a decrease of the SHPB mean plateau stress was observed when compared with the quasi-static mean in all directions (Figure 8.18). This decrease in the plateau stress was estimated to be 17%, 9% and 11% for the x, y and z-directions respectively. When comparing the SHPB with the quasi-static values, an increase in densification strain is present for all directions for both foams (Figures 8.19 and 8.20).

For proximal end forces, the shape of the force pulses obtained from the DI tests is similar to the shape of the SHPB stress-stain curves (Figures 8.11 and 8.12) for both Rohacell-51WF and 110WF in all directions (part (b) of Figures 8.21-8.26). For distal end forces for both foams and in all directions, the load increases more gradually to an initial peak, followed by an almost constant plateau region until full densification of the tested specimens, where the load increases sharply (part (a) of Figures 8.21-8.26).

The distal end stresses (both crushing and average) of Rohacell-51WF foam in all directions appeared to remain fairly constant with increasing impact velocity (parts (a) and (c) of Figures 8.27-8.29). The mean values of both the crushing and average stresses at the distal end were greater than either the quasi-static or SHPB mean values. It was estimated that the crushing stress increases by 27%, 50% and 39% in the x, y and z directions respectively and the average stress increases by 28%, 44% and 40% for the x, y and z-directions respectively when compared with the corresponding quasi-static mean values. The proximal end stresses showed a different trend, with the crushing stress for all three directions of Rohacell-51WF increasing with impact velocity (see part (b) of Figures 8.27-8.29). On the other hand, the time-averaged proximal end stresses remained constant over the range of the impact velocities tested (see part (d) of Figure 8.27-8.29). For all three directions the mean of the timed-averaged proximal end stress was close to the mean of the timed-average distal end stress as can be seen by comparing parts (c) and (d) of Figures 8.27-8.29. Again the mean values of the timed-averaged stresses are higher than both the means of the quasi-static and SHPB plateau stresses. The average stress increases by 23%, 22% and 39% for the x, y and z-directions respectively.

The overall trends in the data obtained for the DI tests of Rohacell-110WF were similar to those derived for the Rohacell-51WF foam. For all directions the mean values of both the crushing and time-averaged distal end stresses were greater than both the quasi-static and SHPB means (see parts (a) and (c) of Figures 8.30-8.32). The distal end mean crushing stress is 15% higher in all directions and the mean timed-average stress is 16.5%, 32% and 16% higher for the x, y and z-directions respectively when compared with the corresponding quasi-static mean stresses. The proximal end crushing stresses increase with impact velocity for all directions of Rohacell-110WF (see part (b) of Figures 8.30-8.32). However the timed-averaged proximal stresses remain fairly constant and at similar levels to the distal end stresses (see parts (c) and (d) of Figures 8.30-8.32). Again the mean of the time-averaged stresses were higher than both the quasi-static and SHPB means. It was estimated that the mean time-average stress increases by 22%, 15% and 14% for the x, y and z-directions respectively. It is interesting to note that for the Rohacell-110WF specimens the force-time traces from the DI tests (see part (b) in Figures 8.24-8.26)

do not exhibit the same level of reduction in stress in the “plateau region” as was noted for the SHPB tests (Figure 8.12). This is illustrated by comparing the means of the timed-average stresses, which were above the corresponding quasi-static means in contrast to the SHPB mean values (parts (c) of Figures 8.30-8.32).

During quasi-static and low speed compression of a cellular material, regions with weak cells will tend to collapse first. However, for DI testing with increasing impact speeds, the deformation is governed by stress waves and is less random in nature. With increasing impact velocity the deformation of cells becomes localised at the compaction front. Overall, in some cases (e.g. part (b) of Figures 8.27 and 8.30) the use of the distal end mean crushing stress values in Equation (8.9) gives better predictions for the proximal end stress measurements than the use of the SHPB crushing stresses. This supports the proposal of the inertial enhancement of crushing stresses for specimens subjected to impact loading. However, for e.g. low velocity impacts of Rohacell-110WF in the y-direction (Figure 8.31 (b)) the SHPB properties give a better prediction for the proximal end crushing stresses. This highlights the need to perform both SHPB and distal end DI tests so as to assess the dynamic properties of cellular materials. Unfortunately, it is not obvious which tests provide the relevant data for the prediction of the stresses within a compaction wave.

9.2 Further research

The experimental method presented in this study was regarded as accurate so the data obtained from both SHPB and DI tests are presented with confidence. However, there are numerous aspects of the dynamic mechanical properties of balsa wood and Rohacell foam that would benefit from further investigations, in particular:

- It was noticed that the proximal force pulses for the DI tests on radial and tangential specimens were difficult to interpret. Further experimental work needs to be carried out so to measure distal and proximal end forces for across the grain balsa wood.

- It was demonstrated that further research is required in order to predict the mechanical properties of Rohacell foam and further investigation is required to quantify the contribution in the strengthening of Rohacell foam due to the compression of the entrapped air within the cells. In addition, further investigations are required to clarify the reasons for the difference in shape between the quasi-static and SHPB stress-strain curves for Rohacell-110WF.

References

1. Davies, R.M., *A critical study of the Hopkinson pressure bar,* Roy Soc Lond - Philosophical Trans Series A, 1948, **240**, pp. 375-457.
2. Kolsky, H., *Investigation of mechanical properties of materials at very high rates of loading,* Proc. Phys. Soc. B, 1949, **62**, pp. 676-700.
3. Al-Mousawi, M.M., Reid, S.R., Deans, W.F. , *The use of the split Hopkinson pressure bar techniques in high strain rate materials testing,* Proc. Inst. Mech. Eng. Part C, 1997, **211**, pp. 273-292.
4. Gray III, G.T., *Classic Split-Hopkinson Pressure Bar testing,* ed. H. Kuhn, Medlin, D. Vol. 8. 2000: ASM handbook:mechanical testing and evaluation. 462-476.
5. Chen, W., Lu, F., Frew, D.J., Forrestal, M.J., *Dynamic compression testing of soft materials,* J. Appl. Mech. Trans. ASME, 2002, **69**, pp. 214-223.
6. Chen, W., Lu, F., Zhou, B., *A Quartz-crystal-embedded Split Hopkinson Pressure Bar for soft materials,* Exp. Mech., 2000, **40**, pp. 1-6.
7. Chen, W., Zhang, B., Forrestal, M.J., *A Split Hopkinson Bar Technique for low-impedance materials,* Exp. Mech., 1999, **39**, pp. 81-85.
8. Gray III, G.T., Blumenthal, W.R., *Split-Hopkinson Pressure Bar testing for soft materials*, ed. H. Kuhn, Medlin, D. Vol. 8. 2000: ASM handbook:mechanical testing and evaluation. 488-496.
9. Mahfuz H., W.A.M., A. Harque, S. Turner, H. Mohamed, S. Jeelani, *An innovative technique for measuring the high strain rate response of sandwich composites,* Compos. Struct., 2000, **50**, pp. 279-385.
10. Chen, W., Lu, F., Chen, M. , *Tension and compression tests of two polymers under quasi static and dynamic loading,* Polym. Test., 2002, **21**, pp. 113-121.
11. Song, B., Chen, W. , *One-dimensional dynamic compressive behavior of EPDM rubber,* J Eng Mater Technol Trans ASME, 2003, **125**, pp. 294-301.
12. Song, B., Chen, W. , *Dynamic stress equilibration in the Split Hopkinson Pressure Bar Tests on soft materials,* Exp. Mech., 2004, **44**, pp. 300-312.
13. Casem, D., Weerasooriya, T., Moy, R. , *Inertial effects of quartz force transducers embedded in a split Hopkinson pressure bar,* Proc. Soc. Exp. Mech., 2005, **52**, pp. 368-376.
14. Deshpande, V.S., Fleck, N.A. , *High strain rate compressive behaviour of aluminium alloy foams,* Int. J. Impact Eng., 2000, **24**, pp. 277-298.
15. Chen, W., Zhou, B., *Constitutive behaviour of Epon 828/T-403 at various strain rates,* Mech. Time-Depend. Mater. (Netherlands), 1998, **2**, pp. 103-111.
16. Gray III, G.T., Idar, D.J., Blumenthal, W.R., Cady, C.M., Paterson, P.D., . *High- and low- strain rate compression properties of several energetic material composites as a function of strain rate and temperature*. in *11th Detonation Symposium, (Snow Mass, CO)*. 2000: Amperstand Publishing
17. Shergold, O.A., Fleck, N.A.,Radford, D., *The uniaxial stress versus strain response of pig skin and silicone rubber at low and high strain rates,* Int. J. Impact Eng., 2006, **32**, pp. 1384-1402.
18. Tagarielli, V.L., Deshpande, V.S. Fleck, N.A. , *The high strain rate response of PVC foams and end-grain balsa wood,* Compos. B, 2008, **39**, pp. 83-91.

19. Bacon, C., *An experimental method for considering dispersion and attenuation in a viscoelastic Hopkinson Bar,* Exp Mech, 1998, **38**, pp. 242-249.
20. Casem, D.T., Fourney, W.L., Chang, P. , *A polymeric Split Hopkinson Pressure Bar instrumented with velocity gages,* Exp Mech, 2003, **43**, pp. 420-427.
21. Cheng, Z.Q., Crandall, J.R., Pilkey, W.D. , *Wave dispersion and attenuation in viscoelastic Split Hopkinson Pressure Bar,* Shock. Vib., 1998, **5**, pp. 307-315.
22. Lundberg, B., Blanc, R.H. , *Determination of mechanical properties from the two-point response of an impacted linearly viscoelastic rod specimen,* J Sound Vibr, 1988, **126**, pp. 97-108.
23. Sawas, O., Brar, N.S., Brockman, R.A., *Dynamic characterization of compliant materials using an all-polymeric Split Hopkinson Bar,* Exp. Mech., 1998, **38**, pp. 204-210.
24. Sharma, A., Shuckla, A., Prosser, R.A. , *Mechanical characterization of soft materials using high speed photography and Split Hopkinson Pressure Bar technique,* J. Mater. Sci., 2002, **37**, pp. 1005-1017.
25. Wang, L., Labibes, K., Azari, Z., Pluvinage, G. , *Generalization of Split Hopkinson Technique to use viscoelastic bars,* Int J Impact Eng, 1994, **15**, pp. 669-686.
26. Zhao, H., Gary, G. , *A three dimensional analytical solution of the longitudinal wave propagation in an infinite linear viscoelastic cylindrical bar. Application to experimental techniques,* J. Mech. Phys. Solids, 1995, **43**, pp. 1335-1348.
27. Zhao, H., Gary, G.,Klepaczko, J.R. , *On the use of a viscoelastic Split Hopkinson Pressure Bar,* Int. J. Impact Eng., 1997, **19**, pp. 319-330.
28. Liu, Q., Subhash, G., *Characterization of viscoelastic properties of polymer bar using iterative deconvolution in the time domain,* Mech Mater 2006, **38**, pp. 1105-1117.
29. Bacon, C., Brun, A. , *Methodology for a Hopkinson test with a non-uniform viscoelastic bar,* Int. J. Impact Eng., 2000, **24**, pp. 219-230.
30. Gary, G., Klepaczko, J.R., Zhao, H. , *Letter to the editor Generalization of Split Hopkinson Technique to use viscoelastic bars,* Int. J. Impact Eng., 1995, **16**, pp. 529-530.
31. Zhao, H., Gary, G., *Crushing behaviour of aluminium honeycombs under impact loading,* Int. J. Impact Eng., 1998, **21**, pp. 827-836.
32. Zhao, H., Gary, G. , *A New method for the separation of waves. Application to the SHPB technique for an unlimited duration of measurement,* J Mech Phys Solids, 1997, **45**, pp. 1185-1201.
33. Bacon, C., *An experimental method for considering dispersion and attenuation in a viscoelastic Hopkinson Bar,* Exp. Mech., 1998, **38**, pp. 242-249.
34. Palamidi, E., Harrigan, J.J., *An investigation of balsa wood over a range of strain-rates and impact velocities,* J. Phys. IV, Proc., 2006, **134**, pp. 225-230.
35. Subhash, G., Liu, Q., Gao, X.L. , *Quasistatic and high strain rate uniaxial compressive response of polymeric structural foams,* Int. J. Impact Eng., 2006, **32**, pp. 1113-1126.
36. Zhao, H., *A study of specimen thickness effects in the impact tests on polymers by numeric simulations,* Polymer, 1998, **39**, pp. 1103-1106.

37. Bertholf, L., Karnes, C. H. , *Two-dimensional analysis of the Split Hopkinson Pressure Bar system,* J. Mech. Phys. Solids 1975, **23**, pp. 1-19.
38. Ravichandran, G., Subhash, G. , *Critical appraisal of limiting strain rates for compression testing of ceramics in a split Hopkinson pressure bar,* J. Am. Ceram. Soc., 1994, **77**, pp. 263-267.
39. Yang, L.M., Shim, V.P.W. , *An analysis of stress uniformity in Split Hopkinson Bar test specimens,* Int J Impact Eng 2005, **31**, pp. 129-150.
40. Meng, H., Li, Q.M., *Correlation between the accuracy of a SHPB test and the stress uniformity based on numerical experiments,* Int. J. Impact Eng., 2003, **28**, pp. 537-555.
41. Davies, E.D.H., Hunter, S.C. , *The dynamic compression testing of solids by the method of the Split Hopkinson Pressure Bar,* J. Mechanics Physics Solids, 1963, **11**, pp. 155-179.
42. Malinowski, J.Z., Klepaczko, J.R. , *A unified analytic and numerical approach to specimen behaviour in the Split-Hopkinson Pressure Bar,* Int. J. Mech. Sci., 1986, **28**, pp. 381-391.
43. Gorham, D.A., *Specimen inertia in high strain-rate compression,* J Phys D, Appl Phys 1989, **22**, pp. 1888-1893.
44. Zencker, U., Clos, R., *Limiting conditions for compression testing of flat specimens in the Split Hopkinson Pressure Bar,* Exp. Mech., 1999, **39**, pp. 343-348.
45. Klepaczko, J., Malinowski, Z. , *Dynamic frictional effects as measured from the Split Hopkinson Pressure Bar,* 1978, pp. 403-416.
46. Chen, W., Lu, F., Winfree, N. , *High-strain-rate compressive behavior of a rigid polyurethane foam with various densities,* Exp. Mech., 2002, **42**, pp. 65-73.
47. Gorham, D.A., *The effect of specimen dimensions on high strain rate compression measurements of copper,* J. Phys. D, Appl. Phys., 1991, **24**, pp. 1489-1492.
48. Gorham, D.A., Pope, P.H., Field, J.E., *An improved method for compressive stress-strain measurements at very high strain rates,* Proc. R. Soc. Lond. A, Math. Phys. Sci., 1992, **438**, pp. 153-170.
49. Gorham, D.A., *Specimen inertia in high strain-rate compression,* J. Phys. D, Appl. Phys. , 1989, **22**, pp. 1888-1893.
50. Jia, D., Ramesh, K.T. , *A rigorous assessment of the benefits of miniaturization in the Kolsky bar system,* Exp. Mech., 2004, **44**, pp. 445-454.
51. Dioh, N.N., Leevers, P.S.,Williams, J.G., *Thickness effects in split Hopkinson pressure bar tests,* Polymer, 1993, **34**, pp. 4230-4234.
52. Dioh, N.N., Ivankovic, A., Leevers, P.S., Williams, J.G. , *Stress wave propagation effects in split Hopkinson pressure bar tests,* Proc. R. Soc. Lond. A, Math. Phys. Sci., 1995, **449**, pp. 187-204.
53. Lindholm, U.S., *Some experiments with split Hopkinson pressure bar,* J Mechanics Physics Solids, 1964, pp. 317-335.
54. Frew, D.J., Forrestal, M.J., Chen, W., *Pulse shaping techniques for testing brittle materials with a Split Hopkinson Pressure Bar,* Exp. Mech., 2002, **42**, pp. 93-106
55. Harrigan, J.J., Reid, S.R., Tan, P.J., Reddy, T.Y. , *High rate crushing of wood along the grain,* Int. J. Mech. Sci., 2005, **47**, pp. 521-544.
56. Follansbee, P.S., Frantz, C., *Wave propagation in the split Hopkinson pressure bar,* J. Eng. Mater. Technol. Trans. ASME, 1983, **105**, pp. 61-66.

57. Benatar, A., Rittel, D., Yarin, A.L., *Theoretical and experimental analysis of longitudinal wave propagation in cylindrical viscoelastic rods,* J. Mech. Phys. Solids, 2003, **51**, pp. 1413-1431.
58. Davies, R.M., *A critical study of the Hopkinson pressure bar,* Philos. Trans. R. Soc. Lond. A, Math. Phys. Sci., 1948, **240**, pp. 375-457.
59. Anderson, S.P., *Higher-order rod approximations for the propagation of longitudinal stress waves in elastic bars,* J. Sound Vib., 2006, **290**, pp. 290-308.
60. Blanc, R.H., *Transient wave propagation methods for determining the viscoelastic properties of solids,* Trans. ASME, J. Appl. Mech., 1993, **60**, pp. 763-768.
61. Hillström, L., Mossberg, M., Lundberg, B., *Identification of complex modulus from measured strains on an axially impacted bar using least squares,* J. Sound Vib., 2000, **230**, pp. 689-707.
62. Mousavi, S., Nicolas, D.F., Lundberg, B. , *Identification of complex moduli and poisson's ratio from measured strains on an impacted bar,* J. Sound Vib., 2004, **277**, pp. 971-986.
63. Sogabe, Y., Kishiba, K., Nakagama, K., *Wave propagation analysis for determining the dynamic properties of high damping alloys,* Bull JSME, 1982, **25**, pp. 321-327.
64. Sogabe, Y., Tsuzuki, M. , *Identification of the dynamic properties of linear viscoelastic materials by wave propagation testing,* Bull. Jpn. Soc. Mech. Eng. , 1986, **29**, pp. 2410-2419.
65. Mahata, K., Mousavi, S., Söderström, T. , *On the estimation of complex modulus and Poisson's ratio using longitudinal wave experiments,* Mech. Syst. Signal Process., 2006, **20**, pp. 2080-2094.
66. Bouix, R., Viot, P., Lataillade, J. L. , *Polypropylene foam behaviour under dynamic loadings: Strain rate, density and microstructure effects,* Int. J. Impact Eng., 2009, **36**, pp. 329-342.
67. Lundberg, B., Blanc, R.H. , *Determination of mechanical properties from the two-point response of an impacted linearly viscoelastic rod specimen,* J. Sound Vibr., 1988, **126**, pp. 97-108.
68. Lundberg, B., Ödeen, S., *In situ determination of the complex modulus from strain measurements on an impacted structure,* J. Sound Vib., 1993, **167**, pp. 413-419.
69. Pritz, T., *Frequency dependences of complex moduli and complex Poisson's ratio of real solid materials,* J. Sound Vibr., 1998, **214**, pp. 83-104.
70. Pritz, T., *Measurement methods of the complex Poisson's ratio of viscoelastic materials,* Appl. Acoust. , 2000, **60**, pp. 279-292.
71. Pritz, T., *The Poisson's loss factor of solid viscoelastic materials,* J. Sound Vibr., 2007, **306**, pp. 790-802.
72. Caracciolo, R., Gasparetto, A., Giovagnoni, M., *An experimental technique for complete dynamic characterization of a viscoelastic material,* J. Sound Vib., 2004, **272**, pp. 1013-1032
73. Read, B.E., Duncan, J.C., *Measurement of dynamic properties of polymeric glasses for different modes of deformation,* Polym. Test., 1981, **2**, pp. 135-150.
74. Bacon, C., *Separation of waves propagating in an elastic or viscoelastic Hopkinson pressure bar with three-dimensional effects,* Int. J. Impact Eng., 1999, **22**, pp. 55-69.

75. Zhao, H., Gary, G., *A new method for the separation of waves. Application to the SHPB technique for an unlimited duration of measurement,* J. Mech. Phys. Solids, 1997, **45**, pp. 1185-1201.
76. Lynn, P.A., *An Introduction to the Analysis and Processing of Signals*. 3rd ed. 1989: Macmillan Education.
77. Bracewell, R.N., *The Fourier Transform and its Application*. 2nd ed. 1978: McGraw-Hill.
78. Brigham, E.O., *The Fast Fourier Transform and its Applications*. 1988: Englewood Cliffs, N.J. ,Prentice Hall.
79. Carlson, G.E., *Signal and Linear System Analysis*. 2nd ed. 1998: John Wiley & Sons.
80. Fladung, W., Rost, R., *Application and correction of the exponential window for frequency response functions,* Mech. Syst. Signal Process., 1997, **11**, pp. 23-26.
81. Wilcox, D.J., *Numerical Laplace transformation and inversion,* Int. J. Electr. Eng. Educ., 1978, **15**, pp. 247-265.
82. Lundberg, B., Henchoz, A., *Analysis of elastic waves from two-point strain measurement,* Exp. Mech., 1977, **17**, pp. 213-218.
83. Yanagihara, N., *New measuring method of impact force,* Bull. Jpn. Soc. Mech. Eng., 1978, **21**, pp. 1085-1088.
84. Park, S.W., Zhou, M., *Separation of elastic waves in split Hopkinson bars using one-point strain measurements,* Exp. Mech., 1999, **39**, pp. 287-294.
85. Zhao, P.J., Lok, T.S., *A new method for separating longitudinal waves in a large diameter Hopkinson bar,* J. Sound Vib., 2002, **257**, pp. 119-130.
86. Bussac, M.-N., Collet, P., Gary, G., Othman, R. , *An optimisation method for separating and rebuilding one-dimensional dispersive waves from multi-point measurements. Application to elastic or viscoelastic bars,* J. Mech. Phys. Solids, 2002, **50**, pp. 321-349.
87. Jacquelin, E., Hamelin, P., *Force recovered from three recorded strains,* Int. J. Solids Struct. , 2003, **40**, pp. 73-88.
88. Casem, D.T., Fourney, W.L., Chang, P., *Wave separation in viscoelastic pressure bars using single-point measurements of strain and velocity,* Polym. Test. , 2003, **22**, pp. 155-164.
89. Jacquelin, E., Hamelin, P., *Block-bar device for energy absorption analysis,* Mech. Syst. Signal Process., 2001, **15**, pp. 603-617.
90. Meng, H., Li, Q.M. , *An SHPB set-up with reduced time-shift and pressure bar length,* Int. J. Impact Eng., 2003, **28**, pp. 677-696.
91. Pochhammer, L., *Uber die fortpflanzungsgeschwindigkeiten kleiner schwingungen in einem unbergrensten isotropen kreiszylinder,* J. Reine. Angew. Math., 1876, **81**, pp. 324-326.
92. Chree, C., *The equations of an isotropic elastic solid in polar and cylindrical coordinates, their solutions and applications,* Trans. Camb. Phil. Soc., 1889, **14**, pp. 250-369.
93. Bancroft, D., *The velocity of longitudinal waves in cylindrical bars,* Phys. Rev., 1941, **59**, pp. 588-593.
94. Gong, J.C., Malvern, L.E., Jenkins, D.A. , *Dispersion investigation in the split Hopkinson pressure bar,* Trans. ASME, J. Eng. Mater. Technol. , 1990, **112**, pp. 309-314.
95. Gorham, D.A., *A numerical method for the correction of dispersion in pressure bar signals,* J. Phys. E. Sci. Instrum., 1983, **16**, pp. 477-479.

96. Lifshitz, J.M., Leber, H. , *Data processing in the split Hopkinson pressure bar tests,* Int. J. Impact Eng., 1994, **15**, pp. 723-733.
97. Vural, M., Ravichandran, G. , *Failure mode transition and energy dissipation in naturally occurring composites,* Compos. B, 2004, **35B**, pp. 639-646.
98. Da Silva, A., Kyriakides, S., *Compressive response and failure of balsa wood,* Int. J. Solids Struct., 2007, **44**, pp. 8685-8717.
99. Vural, M., Ravichandran, G. , *Dynamic response and energy dissipation characteristics of balsa wood: experiment and analysis,* Int. J. Solids Struct., 2003, **40**, pp. 2147-2170.
100. Vural, M., Ravichandran, G. , *Microstuctural aspects and modeling of failure in naturally occurring porous composites,* Mech. Mater., 2003, **35**, pp. 523-536.
101. Gibson, L.J., Ashby, M.F., *Cellular Solids: Structures and Properties*. 2nd ed. 1997: Cambridge University Press.
102. Easterling, K.E., Harrysson, R., Gibson, L.J., Ashby, M.F., *On the mechanics of balsa wood and other woods,* Proc. R. Soc. London Ser. A, 1982, **383**, pp. 31-41.
103. Reid, S.R., Peng, C., *Dynamic uniaxial crushing of wood,* Int. J. Impact Eng., 1997, **19**, pp. 531-570.
104. Cave, I.D., *The longitudinal Young's modulus of Pinus radiata,* Wood Sci. Technol., 1969, **3**, pp. 40-48.
105. Maiti, S.K., Gibson, L.J., Ashby, M.F., *Deformation and energy absorption diagrams for cellular solids,* Acta Metall., 1984, **32**, pp. 1963-1975.
106. Tan, P.J., Harrigan, J.J., Reid, S.R. , *Inertia effects in uniaxial dynamic compression closed cell aluminium alloy foam,* Mater. Sci. Technol., 2002, **18**, pp. 480-488.
107. Dinwoodie, J.M., *Timber: a review of the structure-mechanical property relationship,* J. Microsc., 1975, **104**, pp. 3-32.
108. Zhao, H., Elnasri, I., HuiJian, Li, *The mechanism of strength enhancement under impact loading of cellular materials,* Adv. Eng. Mater. , 2006, **8**, pp. 877-883.
109. Zhao, H., Elnasri, I., Abdennadher, S. , *An experimental study on the behaviour under impact loading of metallic cellular materials,* Int. J. Mech. Sci. , 2005, **47**, pp. 757-774.
110. Li, Q.M., Mines, R.A.W., Birch, R.S., *The crush behaviour of Rohacell-51WF structural foam,* Int. J. Solids Struct., 2000, **37**, pp. 6321-6341.
111. Bosze, E., Simon-Gillo, J. ,Boissevain, J., Chang, J., Seto, R., *Rohacell foam as a silicon support structure material for the PHENIX multiplicity vertex detector,* Nucl. Instrum. Methods Phys. Res. A, 1997, **400**, pp. 224-232.
112. Wu, C.L., Sun, C.T., *Low velocity impact damage in composite sandwich beams,* Compos. Struct., 1996, **34**, pp. 21-27.
113. Shipsha, A., Hallstrom, S., Zenkert, D., *Failure mechanisms and modelling of impact damage in sandwich beams – A 2D approach: Part I – experimental investigation,* J. Sandwich Struct. and Mat., 2003, **5**, pp. 5-29.
114. Chen, C.P., Lakes, R.S., *Analysis of the structure-property relations of foam materials,* Cell. Polym., 1995, **14**, pp. 186-202.
115. Anderson, W.B., Lakes, R.S. , *Size effects due to Cosserat elasticity and surface damage in closed-cell polymethacrylimide foam,* J. Mater. Sci., 1994, **29**, pp. 6413-6419.

116. Li, Q.M., Magkiriadis, I., Harrigan, J.J. , *Compressive strain at the onset of densification of cellular solids,* J. Cell. Plast., 2006, **42**, pp. 371-392.
117. Chen, C.P., Anderson, W.B., Lakes, R.S., *Relating the properties of foam to the properties of the solid from which it is made,* Cell. Polym., 1994, **13**, pp. 16-32.
118. Brezny, R., Green, D.J., *Effect of cell size on the mechanical behavior of cellular materials,* Acta Metall. Mater., 1990, **38**, pp. 2517-2526.
119. Bastawros, A.-F., Bart-Smith, H., Evans, A.G., *Experimental analysis of deformation mechanisms in a closed-cell aluminum alloy foam,* J. Mech. Phys. Solids 2000, **48**, pp. 301-322.
120. Andrews, E.W., Gioux, G., Onck, P., Gibson, L.J. , *Size effects in ductile cellular solids.Part II: experimental results,* Int. J. Mech. Sci. , 2001, **43**, pp. 701-713.
121. Yu, H., Guo, Z., Li, B., Yao, G., Luo, H., Liu, Y. , *Research into the effect of cell diameter of aluminum foam on its compressive and energy absorption properties,* Mater. Sci. Eng. A, 2007, **454-455**, pp. 542-546.
122. Li, Q.M., Mines, R.A.W., *Strain measures for rigid crushable foam in uniaxial compression,* Strain, 2002, **38**, pp. 132-140.
123. Gibson, L.J., *Mechanical behavior of metallic foams,* Annu. Rev. Mater. Sci., 2000, **30**, pp. 191-227.
124. Gibson, L.J., Ashby, M.F., *Cellular solids:Structures and properties*. 2nd ed. 1999: Cambridge University press.
125. Konstantinidis, I.C., Papadopoulos, D.P., Lefakis, H., Tsipas, D.N. , *Model for determining mechanical properties of aluminum closed-cell foams,* Theor. Appl. Fract. Mech. , 2005, **43**, pp. 157-167.
126. Simone, A.E., Gibson, L.J. , *Effects of solid distribution on the stiffness and strength of metallic foams,* Acta Mater., 1998, **46**, pp. 2139-2150.
127. Ouellet, S., Cronin, D., Worswick, M. , *Compressive response of polymeric foams under quasi-static, medium and high strain rate conditions,* Polym. Test., 2006, **25**, pp. 731-743.
128. Song, B., Lu, W-Y., Syn, C.J., Weinong, C., *The effects of strain rate, density, and temperature on the mechanical properties of polymethylene disocyanate (PMDI)-based rigid polyurethane foams during compression,* J. Mater. Sci., 2009, **44**, pp. 351-357.
129. Daphalapurkar, N.P., Hanan, J.C., Phelps, N.B., Bale, H., Lu, H. , *Tomography and simulation of microstructure evolution of a closed-cell polymer foam in compression,* Mech. Adv. Mater. Struct., 2008, **15**, pp. 594-611.
130. Ruan, D., Lu, G., Wang, B., Yu, T.X. , *In-plane dynamic crushing of honeycombs - A finite element study,* Int. J. Impact Eng., 2003, **28**, pp. 161-182.
131. Zou, Z., Reid, S.R., Tan, P.J., Li, S., Harrigan, J.J. , *Dynamic crushing of honeycombs and features of shock fronts,* Int. J. Impact Eng., 2009, **36**, pp. 165-176.
132. Radford, D.D., Deshpande, V.S., Fleck, N.A. , *The use of metal foam projectiles to simulate shock loading on a structure,* Int. J. Impact Eng., 2005, **31**, pp. 1152-1171.
133. Wang, J., Wang, H., Chen, X., Yu, Y. , *Experimental and numerical study of the elastic properties of PMI foams,* J. Mater. Sci., 2010, **45**, pp. 2688-2695.

APPENDIX A

Details of the Balsa Wood and Rohacell Foam Specimens from the Impact Tests

Specimen Mass (gr)	Specimen Length (mm)	Specimen Density (kgm^{-3})	Projectile Length (mm)	Impact Velocity (ms^{-1})	Strain rate (s^{-1})
0.096	3.07	165.29	500	14.03	2129.25
0.184	5.91	158.99	500	16.2	1492.45
0.180	5.94	155.34	500	16.55	1733.96
0.178	5.91	153.22	500	21.24	2398.113
0.191	5.92	164.137	500	17.39	1654.99
0.181	5.84	155.50	500	20.69	2356.13
0.088	3.16	138.50	500	14.3	2123.49
0.088	3.09	141.11	500	13.63	1982.45
0.084	3.14	133.48	500	13.79	2134.81
0.087	3.11	137.24	500	13.186	1827.26
0.091	3.11	144.27	500	12.56	1561.6
0.088	3.20	135.75	250	14.63	1412.2
0.087	3.16	135.4	450	10.98	1044
0.093	3.19	142.84	450	15.48	2030.4
0.173	5.91	143.6	450	13.63	873.618
0.163	5.96	135.85	250	17.75	1305.4
0.185	7.51	121.3	250	19.48	1469.7
0.092	3.16	143.9	450	11.22	2438, 1283.3
0.184	7.84	116.29	250	16.66	1613.8, 1266.6, 932.7
0.138	4.73	101.4	450	13.76	2008.1, 1466.9, 912.63
0.114	4.19	94.56	450	15.6	2787.2, 2158.3

0.194	7.14	95.029	250	19.52	3425.7, 2791.7, 2143.4
0.102	3.65	98.355	250	13.26	2739.9, 2144.1, 1514.1
0.143	5.26	94.88	250	15.6	2193.4, 1764.8, 1313.5
0.148	5.92	87.25	250	13.6	932.363, 733.025, 516.0756
0.085	3.23	130.39	450	7.9	1720.4, 912.84
0.083	3.18	129.167	450	9.6	2216.8, 1312.5

Table A. 1 Details of the along the grain balsa wood SHPB tests.

Specimen Mass (gr)	**Specimen Length (mm)**	**Specimen Density (kgm^{-3})**	**Projectile Length (mm)**	**Impact Velocity (ms^{-1})**	**Strain rate (s^{-1})**
0.136	3.19	201.83	500	13.11	3256.5
0.109	3.05	175.33	500	12.12	3201.42
0.306	6.15	242.9	500	11.32	1433.2
0.313	6.06	247.822	500	12.06	1644.34
0.225	6.02	183.57	500	16	2351.038
0.226	6.22	185.78	500	10.35	1403.87
0.451	8.41	267.05	500	11.88	1127.17
0.367	8.12	213.96	500	11.5	1246.98
0.300	8.11	182.84	500	24.24	2748.113
0.131	3.15	201.176	250	18.75	4510.4
0.117	3.16	177.26	450	10	2472.4
0.101	3.10	157.28	450	13.44	3499.7
0.143	3.11	222.8	450	12.43	2916.3

Table A. 2 Details of the radial balsa wood SHPB tests.

Specimen Mass (gr)	**Specimen Length (mm)**	**Specimen Density (kgm^{-3})**	**Projectile Length (mm)**	**Impact Velocity (ms^{-1})**	**Strain rate (s^{-1})**
0.149	3.05	251.066	500	11.21	2764.34
0.140	3.10	237.77	500	13.11	3303.5
0.146	3.10	247.04	500	11.6	2986.32
0.269	6.22	225.4	500	21.05	3039.9
0.261	6.25	210.81	500	15.5	2238.68
0.293	6.17	226.45	500	15	2174.62
0.305	6.25	236.46	500	20.87	2902.64
0.283	6.24	225.26	500	14.72	2102.264
0.254	7.69	164.27	500	13.63	1670.566
0.327	8.12	201.55	500	17.5	1932.93
0.368	8.22	224.34	500	20.86	2261.038
0.283	8.32	168.75	500	21.8	2677.55
0.331	8.61	192.64	500	18.18	1886.7
0.157	3.17	242.07	250	16.2	3802.4
0.159	3.13	256.17	450	13.3	3126.9
0.145	3.12	241.9	450	13.5	3263.2
0.147	3.14	228.535	450	14.46	3552.8
0.151	3.11	239.4	450	9.2	2379.1, 1979.8
0.282	6.28	223.61	250	13.04	1700.3, 1573.6, 1442.4 1270.8

Table A. 3 Details of the tangential balsa wood SHPB tests.

Specimen Mass (gr)	**Specimen Length (mm)**	**Specimen Density (kgm^{-3})**	**Projectile Mass (gr)**	**Projectile Length (mm)**	**Impact Velocity (ms^{-1})**
0.447	6.14	174.16	65.085	35.18	34.3
4.055	65.08	149.70	65.085	35.18	54.94
0.456	6.17	177.11	65.085	35.18	40.8
0.723	11.17	155.25	65.085	35.18	39.4
0.785	13.14	142.92	65.085	35.18	43
1.296	22.28	138.56	65.085	35.18	53
1.259	22.25	136.43	65.085	35.18	49.36
1.410	25.19	133.33	65.085	35.18	59.2
1.363	25.33	128.73	65.085	35.18	72.7
2.303	35.17	155.84	65.085	35.18	72
1.959	35.07	135.30	65.085	35.18	20
2,817	40.14	169.20	65.085	35.18	30
4.703	65.20	173.92	65.085	35.18	33
0.421	6.11	164.409	23.798	38.06	107.816
0.784	13.17	141.80	23.798	38.06	113.9
0.726	11.39	154.77	23.798	38.06	109.09
2.334	40.14	138.9834	23.798	38.06	117.073

Table A. 4 Details of the along the grain balsa wood distal end DI tests.

Specimen Mass (gr)	Specimen Length (mm)	Specimen Density (kgm^{-3})	Projectile Mass (gr)	Projectile Length (mm)	Impact Velocity (ms^{-1})
0.431	6.22	165.77	65.085	35.18	35.6
1.255	22.09	136.27	65.085	35.18	57.7
0.447	6.15	174.33	65.085	35.18	40.8
0.736	11.09	158.5	65.085	35.18	57.34
0.910	13.09	166.02	65.085	35.18	64.1
1.392	25.41	130.83	65.085	35.18	74.4
2.223	35.18	151.7	65.085	35.18	87.08
2.345	40.31	139.65	65.085	35.18	87.9
4.751	65.18	175.44	65.085	35.18	96.2
0.479	6.12	186.65	65.085	35.18	22.64
0.778	13.18	140.5	23.798	38.06	65.75
2.327	35.12	157.69	65.085	35.18	46.15
4.573	65.1	168.48	65.085	35.18	54.54

Table A. 5 Details of the along the grain balsa wood proximal end DI tests.

Specimen Mass (gr)	Specimen Length (mm)	Specimen Density (kgm^{-3})	Projectile Mass (gr)	Projectile Length (mm)	Impact Velocity (ms^{-1})
1.568	25.10	151.4	23.798	38.06	111.67
1.769	25.24	170.615	23.798	38.06	86.145
3.023	45.12	161.68	23.798	38.06	123.08
3.746	55.08	165.85	23.798	38.06	126.316
1.811	25.94	174.84	65.085	35.18	58.53
0.982	17.16	140.53	65.085	35.18	29.63
1.815	27.11	166.08	65.085	35.18	44.44
2.587	38.96	168.65	65.085	35.18	18.18

Table A. 6 Details of the radial balsa wood distal end DI tests.

Specimen Mass (gr)	Specimen Length (mm)	Specimen Density (kgm^{-3})	Projectile Mass (gr)	Projectile Length (mm)	Impact Velocity (ms^{-1})
2.007	25.17	192.08	65.085	35.18	54
1.010	15.13	172.93	65.085	35.18	37.5
1.556	25.63	152.42	65.085	35.18	52.17
2.265	40.35	140.369	65.085	35.18	70.5
1.976	25.06	195.52	65.085	35.18	64.86
3.828	55.03	166.125	65.085	35.18	67.6
1.546	25.13	146.92	65.085	35.18	81.36
3.184	45.12	170.29	65.085	35.18	81.36
3.855	55.01	170.74	65.085	35.18	990.5

Table A. 7 Details of the radial balsa wood proximal end DI tests.

Specimen Mass (gr)	Specimen Length (mm)	Specimen Density (kgm^{-3})	Projectile Length (mm)	Impact Velocity (ms^{-1})	Strain rate (s^{-1})
0.035	3.64	48.06	410	13.63	3377.74
0.036	3.19	56.409	410	14.16	4040
0.036	3.4	53.2	410	16.107	4283.9
0.071	6.14	57.8	410	16.1	2526
0.073	6.27	59.08	410	18.113	2669.8
0.073	6.14	59.35	410	18.9	2870.75
0.094	8.15	56.37	410	22.02	2496.22
0.096	8.07	60.443	410	29.6	3273.113
0.037	3.15	59.60	500	9.4	2972
0.071	6.16	58.27	500	9.09	1486
0.094	8.16	59.133	500	10.4	1273

Table A. 8 Details of the x-direction Rohacell-51WF SHPB tests.

Specimen Mass (gr)	**Specimen Length (mm)**	**Specimen Density (kgm^{-3})**	**Projectile Length (mm)**	**Impact Velocity (ms^{-1})**	**Strain rate (s^{-1})**
0.037	3.21	57.399	410	15	4222.64
0.036	3.14	58.4748	410	17.6	5047.17
0.034	3.11	54.306	410	20.7	5873.6
0.076	6.39	58.932	410	20.52	2883.2
0.074	6.15	59.25	410	15	2233.113
0.075	6.15	60.276	410	24.24	3730.85
0.093	8.09	56.537	410	21.05	2396.32
0.094	8.03	57.643	410	17.14	1980.66
0.099	8.09	60.334	410	28.6	3267.26
0.076	6.18	60.10	500	8.98	1544.7
0.034	3.20	52	500	9.5	3088.5
0.098	8.04	60.32	500	9.9	1248, 960

Table A. 9 Details of the y-direction Rohacell-51WF SHPB tests.

Specimen Mass (gr)	**Specimen Length (mm)**	**Specimen's Density (kgm^{-3})**	**Projectile's Length (mm)**	**Impact Velocity (ms^{-1})**	**Strain rate (s^{-1})**
0.037	3.45	52.61	410	15	3927.7
0.037	3.31	55.25	410	16.107	4413.2
0.038	3.43	54.015	410	16	4230.18
0.074	6.66	54.92	410	18.18	2560.75
0.072	6.27	57.113	410	14.55	2135
0.102	8.09	61.55	410	17.7	2011.6
0.099	8.13	59.44	410	22.5	2527.17
0.094	8,23	56.44	410	30	3292.07
0.040	3.48	56.042	500	9.125	2661.5
0.071	6.42	55	500	7.633	1154.11, 870.19
0.095	8.21	57.34	500	8.5	1060.7, 852.34

Table A. 10 Details of the z-direction Rohacell-51WF SHPB tests.

Specimen Mass (gr)	**Specimen Length (mm)**	**Specimen Density (kgm^{-3})**	**Projectile Length (mm)**	**Impact Velocity (ms^{-1})**	**Strain rate (s^{-1})**
0.080	3.12	125.17	410	14.4	3663.20
0.080	3.12	125.016	410	17.26	4620.4
0.080	3.15	124.44	410	17.5	4486
0.161	6.19	126.97	410	14.73	1969.8, 542.4
0.160	6.18	127.16	410	15.5	2071.8
0.156	6.04	126.55	410	26.66	3825.1
0.191	8.18	114.7	410	16	1659.9, 1018
0.192	8.27	114.04	410	20.7	2164.6, 1029.9
0.194	8.31	113.67	410	28.6	3034
0.081	3.15	125.99	500	8	2221.7
0.156	6.06	125.98	500	9.61	1298.1
0.193	8.36	113.39	500	9.8	1026.2
0.214	8.18	128.83	500	9.17	983.1928

Table A. 11 Details of the x-direction Rohacell-110WF SHPB tests.

Specimen Mass (gr)	**Specimen Length (mm)**	**Specimen Density (kgm^{-3})**	**Projectile Length (mm)**	**Impact Velocity (ms^{-1})**	**Strain rate (s^{-1})**
0.079	3.13	124.28	410	14.5	3801.8
0.077	3.21	118.27	410	15.2	3921.3
0.079	3.12	126.34	410	16.6	4516
0.157	6.17	126.55	410	16.9	2328.8
0.157	6.22	124.76	410	26.08	3673.7
0.213	8.57	124.097	410	16.32	1597, 955
0.212	8.32	125.63	410	20.86	2171.6
0.209	8.27	124.74	410	29.3	3118
0.078	3.16	122	500	7.8	2296
0.158	6.19	125.8	500	7.9	1085
0.213	8.26	126.98	500	11.11	1179.9, 671.45
0.213	8.21	126.61	500	9.5	1038.2, 559.8

Table A. 12 Details of the y-direction Rohacell-110WF SHPB tests.

Specimen Mass (gr)	Specimen Length (mm)	Specimen Density (kgm^{-3})	Projectile Length (mm)	Impact Velocity (ms^{-1})	Strain rate (s^{-1})
0.079	3.19	120.31	410	12.6	3220.9
0.082	3.2	127.70	410	15.09	3945.2
0.147	6.17	117.019	410	16.55	2320
0.145	6.20	114.17	410	18.45	2608.2
0.149	6.16	118.66	410	25.26	3606.4
0.194	8.04	117.64	410	15.5	1646.5
0.199	7.97	121.14	410	30	3360.1
0.083	3.18	126.78	500	7.7	1955
0.077	3.16	120.15	500	8.16	2279.2
0.148	6.14	118.95	500	9.95	1470.3, 606.7
0.150	6.15	119.8	500	9.8	1383.7, 653.95
0.212	8.07	127.18	500	12.6	1404.2, 688.84
0.218	8	131.7	500	8.8	971.97, 378.0631

Table A. 13 Details of the z-direction Rohacell-110WF SHPB tests.

Specimen Mass (gr)	Specimen Length (mm)	Specimen Density (kgm^{-3})	Projectile Mass (gr)	Projectile Length (mm)	Impact Velocity (ms^{-1})
0.499	21.10	56.283	65.085	35.18	38
0.971	40.68	56.85	65.085	35.18	73.6
0.993	40.38	58.67	65.085	35.18	57.3
1.883	75.53	59.127	23.798	38.06	117
1.865	75.59	58.516	23.798	38.06	77
1.785	75.93	55.99	65.085	35.18	80
1.843	75.75	58.255	65.085	35.18	63

Table A. 14 Details of the x-direction Rohacell-51WF distal end DI tests.

Specimen Mass (gr)	Specimen Length (mm)	Specimen Density (kgm^{-3})	Projectile mass (gr)	Projectile length (mm)	Impact Velocity (ms^{-1})
0.468	20.05	56.92	65.085	35.18	28.9
0.447	19.97	54.68	65.085	35.18	30
0.466	20.08	56.79	65.085	35.18	26.66
0.902	39.43	56.43	65.085	35.18	35.29
0.943	40.03	57.45	65.085	35.18	36.93
1.137	49.96	56.036	65.085	35.18	44.4
1.154	50.13	56.78	65.085	35.18	39.3
1.321	57.20	56.72	65.085	35.18	51.06
1.731	75.18	56.197	65.085	35.18	42.86
1.726	74.81	57.209	65.085	35.18	60.78
1.788	74.56	58.53	65.085	35.18	73.85

Table A. 15 Details of the x-direction Rohacell-51WF proximal end DI tests.

Specimen Mass (gr)	Specimen Length (mm)	Specimen Density (kgm^{-3})	Projectile Mass (gr)	Projectile Length (mm)	Impact Velocity (ms^{-1})
0.523	21.38	58.57	65.085	35.18	32.43
0.957	40.44	56.52	65.085	35.18	42.105
0.951	40.37	55.96	65.085	35.18	43.63
1.001	40.47	58.713	23.798	38.06	80
1.870	75.31	58.79	23.798	38.06	85.72
1.869	75.57	58.91	65.085	35.18	77

Table A. 16 Details of the y-direction Rohacell-51WF distal end DI tests.

Specimen Mass (gr)	Specimen Length (mm)	Specimen Density (kgm^{-3})	Projectile Mass (gr)	Projectile Length (mm)	Impact Velocity (ms^{-1})
0.452	20.12	54.735	65.085	35.18	23.4
0.455	20.08	54.97	65.085	35.18	30.77
0.446	19.89	54.35	65.085	35.18	25.9
0.926	39.95	56.47	65.085	35.18	21.3
0.910	39.99	55.15	65.085	35.18	26.35
0.914	40.08	56.25	65.085	35.18	50
1.133	50.08	55.66	65.085	35.18	45.28
1.116	49.82	54.72	65.085	35.18	38.4
1.117	49.92	54.95	65.085	35.18	53.33
1.690	74.94	55.235	65.085	35.18	53.33
1.711	74.91	55.6	65.085	35.18	60
1.686	75.08	55.93	65.085	35.18	28.75
1.646	75.10	54.44	65.085	35.18	70.58

Table A. 17 Details of the y-direction Rohacell-51WF proximal end DI tests.

Specimen Mass (gr)	Specimen Length (mm)	Specimen Density (kgm^{-3})	Projectile Mass (gr)	Projectile Length (mm)	Impact Velocity (ms^{-1})
0.615	25.14	57.45	65.085	35.18	36.9
0.609	25.15	57.48	65.085	35.18	38.7
1.232	51.09	57.34	65.085	35.18	47.06
1.244	51.06	57.534	65.085	35.18	42.10
1.968	80.66	58.217	65.085	35.18	63.16
1.982	80.70	58.45	65.085	35.18	61.53

Table A. 18 Details of the z-direction Rohacell-51WF distal end DI tests.

Specimen Mass (gr)	**Specimen Length (mm)**	**Specimen Density (kgm^{-3})**	**Projectile Mass (gr)**	**Projectile Length (mm)**	**Impact Velocity (ms^{-1})**
0.572	25.07	55.64	65.085	35.18	32.87
0.586	25.15	56.92	65.085	35.18	25.8
0.891	40.05	55.76	65.085	35.18	44.4
0.890	39.94	55.35	65.085	35.18	41.73
1.123	49.87	56.036	65.085	35.18	50
1.127	49.95	56.847	65.085	35.18	58.5
1.797	79.98	55.52	65.085	35.18	60
1.825	80.05	55.55	65.085	35.18	61.54
1.243	51.31	57.8	65.085	35.18	60.33

Table A. 19 Details of the z-direction Rohacell-51WF proximal end DI tests.

Specimen Mass (gr)	**Specimen Length (mm)**	**Specimen Density (kgm^{-3})**	**Projectile Mass (gr)**	**Projectile Length (mm)**	**Impact Velocity (ms^{-1})**
0.525	10.86	115.15	65.085	35.18	31.33
0.529	10.98	114.96	65.085	35.18	50
0.456	10.61	102.63	65.085	35.18	33.33
0.518	10.59	116.51	65.085	35.18	36.36
0.930	20.65	107.37	65.085	35.18	66.9
0.942	20.81	108.57	23.798	38.06	57.3
1.037	20.91	117.823	65.085	35.18	54
2.047	41.23	118.26	65.085	35.18	64.86
2.052	41.14	119.22	65.085	35.18	62.33
2.054	41.45	118.24	65.085	35.18	71.65
2.790	61.07	109.10	65.085	35.18	64
2.795	61.27	108.66	65.085	35.18	30.2
3.059	61.07	120.038	65.085	35.18	64
3.726	75.20	118.22	65.085	35.18	68.6
3.872	76.87	119.77	23.798	38.06	123.07

Table A. 20 Details of the x-direction Rohacell-110WF distal end DI tests.

Specimen Mass (gr)	**Specimen Length (mm)**	**Specimen Density (kgm^{-3})**	**Projectile Mass (gr)**	**Projectile Length (mm)**	**Impact Velocity (ms^{-1})**
2.780	60.82	109.06	23.798	38.06	126.44
2.784	60.51	109.97	65.085	35.18	67.87
1.886	41.12	109.63	65.085	35.18	75.66
3.811	75.47	120.49	65.085	35.18	75.57
2.108	40.42	129.54	65.085	35.18	55.81
1.564	30.5	127.15	23.798	38.06	51.064
0.513	10.16	122.37	65.085	35.18	34.033
0.513	10.07	123.559	65.085	35.18	38.95
0.955	20.20	120.18	65.085	35.18	46.15
0.947	20.23	118.15	65.085	35.18	42.54
1.907	39.83	120.84	65.085	35.18	45.25
1.833	40.24	111.18	65.085	35.18	61.95
3.034	60.02	122.625	65.085	35.18	21.6
2.955	59.87	119.94	65.085	35.18	68.6
3.464	75.08	112.01	65.085	35.18	80.26

Table A. 21 Details of the x-direction Rohacell-110WF proximal end DI tests.

Specimen Mass (gr)	Specimen Length (mm)	Specimen Density (kgm^{-3})	Projectile Mass (gr)	Projectile Length (mm)	Impact Velocity (ms^{-1})
0.560	10.76	124.183	65.085	35.18	44.44
1.055	19.96	126.33	65.085	35.18	63.16
1.055	21.79	116.028	65.085	35.18	54.62
1.119	21.28	125.03	65.085	35.18	49.63
2.013	41.38	115.88	65.085	35.18	59.98
2.163	40.48	126.95	65.085	35.18	62.33
3.268	60.64	127.814	65.085	35.18	69.56
3.718	76.17	116.77	65.085	35.18	92.307
4.026	75.28	127.16	65.085	35.18	85.71

Table A. 22 Details of the y-direction Rohacell-110WF distal end DI tests.

Specimen Mass (gr)	Specimen Length (mm)	Specimen Density (kgm^{-3})	Projectile Mass (gr)	Projectile Length (mm)	Impact Velocity (ms^{-1})
0.495	10.14	120.08	65.085	35.18	29.63
0.497	10.31	118.07	65.085	35.18	30.32
0.954	20.22	115.26	65.085	35.18	43.63
1.003	20.03	123.63	65.085	35.18	26.087
1.004	20.04	123.25	65.085	35.18	39.67
1.884	40.49	114.87	65.085	35.18	56.47
1.877	40.77	113.49	65.085	35.18	52.174
2.841	60.27	114.49	65.085	35.18	73.84
3.791	75.20	123.15	65.085	35.18	78.9
3.530	75.31	115.3	65.085	35.18	84.7

Table A. 23 Details of the y-direction Rohacell-110WF proximal end DI tests.

Specimen Mass (gr)	Specimen Length (mm)	Specimen Density (kgm^{-3})	Projectile Mass (gr)	Projectile Length (mm)	Impact Velocity (ms^{-1})
0.501	10.32	115.137	65.085	35.18	37.5
0.508	10.76	112.166	65.085	35.18	35.8
0.484	10.04	114.73	65.085	35.18	34.3
1.061	20.74	121.54	65.085	35.18	41.38
1.063	20.64	123.33	65.085	35.18	52.17
1.977	40.43	116.175	65.085	35.18	55.814
1.985	40.70	115.07	65.085	35.18	68.57
2.872	59.88	113.85	65.085	35.18	45.28
2.872	60.58	112.93	65.085	35.18	80
3.708	75.97	118.124	65.085	35.18	82.76

Table A. 24 Details of the z-direction Rohacell-110WF distal end DI tests.

Specimen Mass (gr)	Specimen Length (mm)	Specimen Density (kgm^{-3})	Projectile Mass (gr)	Projectile Length (mm)	Impact Velocity (ms^{-1})
0.474	10.18	114.044	65.085	35.18	33.2
0.514	10.23	121.56	65.085	35.18	29.27
0.894	20.19	107.7	65.085	35.18	46.15
0.956	20.14	116.26	65.085	35.18	46.15
0.992	20.31	119.526	65.085	35.18	42.1
1.975	40.12	119.62	65.085	35.18	61.4
1.983	40.02	119.88	65.085	35.18	63.16
2.801	60.05	114.44	65.085	35.18	70.59
2.770	60.06	113.86	65.085	35.18	54.54
3.485	75.03	114.263	65.085	35.18	80.27

Table A. 25 Details of the z-direction Rohacell-110WF proximal end DI tests.

APPENDIX B

Flow Chart and Matlab Programs Describing the Procedure to Produce Stress-Strain Curves for SHPB Tests.

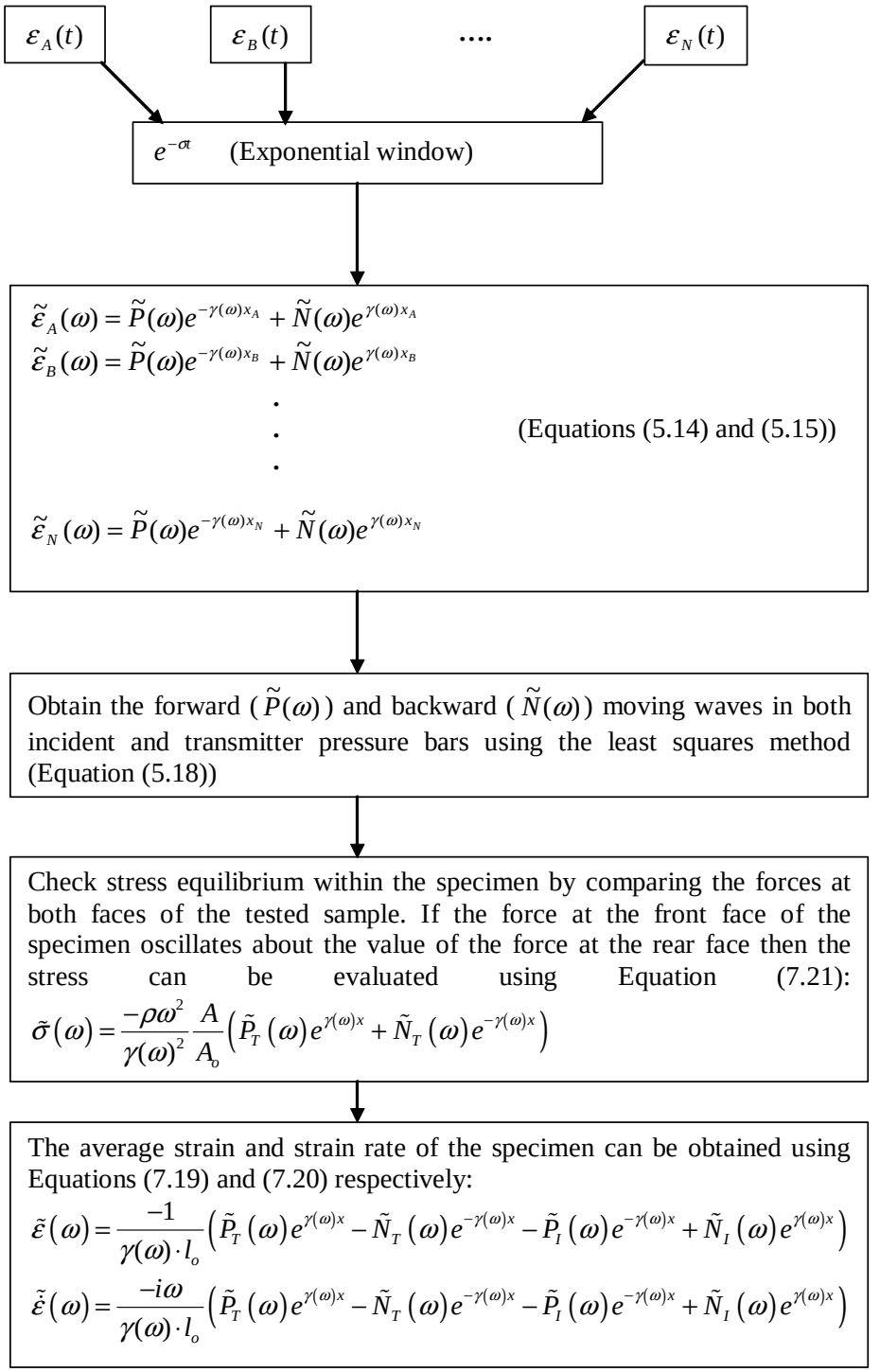

Figure B. 1 Flow Chart describing the procedure to produce stress-strain curves for SHPB tests.

Appendix B

Matlab program used to calculate the stress-strain curve from a SHPB test on along the grain balsa wood using the Magnesium SHPB set up (shown in Figure 7.16):

```
%%%%%%%%Forward and backward moving waves for both incident
and transmitter Magnesium pressure bars
load P1c.dat
load N1c.dat
load P3a.dat
load N3a.dat
N=2^13;
ei=P1c;
er=N1c;
et=P3a;
etr=N3a;
%%%%%%%%Propagation coefficient defined in complex domain
load alpha.dat
load kappa.dat
N=2^13;                                    %Number of sampling
points
gamma1=alpha+i.*kappa;
gamma2=fliplr(conj(gamma1(2:N/2)));
gamma8=[gamma1,gamma2];
%%%%%%%%Time and frequency vectors%%%%%%%%
dt=1e-6;
t=0:dt:N*dt-dt;
T=dt*N;
df=1/T;
f=0:df:1/(2*dt);
w1=2*pi*f;
w2=fliplr(-w1(2:N/2));
w=[w1,w2];
n=2*pi/(N*dt);
h1=exp(-n*t);
h2=exp(n*t);
%%%%%%%%%%%%%%%%%%%%%%%%%%%%%%%%%%%%%%%%%%%%%%%%%%%%%%%%%%%%%%%%
%%%%
%%%%%%%Dimensions of specimen and bars%%%%
```

```
rho=1770;   %density of bar material
d1=0.60986;  %distance  of  the  incident  strain  gauge  from
interface
d2=0.3277;   %distance of the transmitter strain gauge from
interface
Ab=4.1547563e-4; %area of the bar
As=2.8772245e-4; %area of the specimen
thickness=4.19e-3; %specimen's length
%%%%%%%%Shift the waves at the interfaces%%%%%
inter_ei1=fft(ei.*h1).*(exp(-d1.*gamma8));
inter_er1=fft(er.*h1).*(exp(d1.*gamma8));
inter_et1=fft(et.*h1).*(exp(d2.*gamma8));
inter_etr1=fft(etr.*h1).*(exp(-d2.*gamma8));

inter_ei=real(ifft(inter_ei1).*h2);
inter_er=real(ifft(inter_er1).*h2);
inter_et=real(ifft(inter_et1).*h2);
inter_etr=real(ifft(inter_etr1).*h2);

figure
hold on
plot(inter_ei)
plot(inter_er)
plot(inter_et,'black')
plot(inter_etr,'black')
plot(ei,'r')
plot(er,'r')
plot(et,'r')
%%%%%%%%%Stress%%%%%%%%%%
stressT1=(Ab/As).*((-rho.*(w-
i*n).^2)./(gamma8.^2)).*(inter_et1+inter_etr1) ;
stressT2=ifft(stressT1).*h2;
stressT=real(stressT2);
stressT=stressT/1e6;
figure
hold on
plot(t,stressT)
```

```
xlabel('Time (s)')
ylabel('Nominal Stress')

%%%%Velocity%%%%%%%%
v=((-i.*(w-i*n))./gamma8).*(inter_et1-inter_etr1-
inter_ei1+inter_er1);
v1=ifft(v).*h2;
velo=real(v1);

figure
hold on
plot(t,velo)
xlabel('Time (s)')
ylabel('Velocity')

%%%%%Displacement%%%%%%%
displacementI1=-(inter_et1-inter_etr1-
inter_ei1+inter_er1)./(gamma8);
displacementI2=ifft(displacementI1).*h2;
displacementI=real(displacementI2);

%%%%%Strain%%%%%%%
strain=displacementI./thickness;

%%%Plot of the stress-strain curve

figure
plot(strain,stressT)
xlabel('Strain')
ylabel('Stress (MPa)')

%%%%%%Strain rate%%%%%%

strainrate=velo./thickness;

figure
plot(t,strainrate)
```

```
xlabel('Time (s)')
ylabel('Strain rate (s^-^1)')


figure
plot(strain,strainrate)
xlabel('Strain')
ylabel('Strain rate (s^-^1)')
```

Matlab program used to calculate the stress-strain curve from a SHPB test on Rohacell-51WF (x-direction) using the PMMA SHPB set up (shown in Figure 8.9):

```
%%%%%%%%Forward and backward moving waves for both incident
and transmitter PMMA pressure bars
load P1c.dat
load N1c.dat
load P3a.dat
load N3a.dat
N=2^13;
ei=P1c;
er=N1c;
et=P3a;
etr=N3a;

%%%%%%%%Propagation coefficient defined in complex domain
load alpha.dat
load kappa.dat
N=2^13;   %Number of sampling points
gamma1=alpha+i.*kappa;
gamma2=fliplr(conj(gamma1(2:N/2)));
gamma8=[gamma1,gamma2];
%%%%%%%%Time and frequency vectors%%%%%%%%
dt=1e-6;
t=0:dt:N*dt-dt;
```

```
T=dt*N;
df=1/T;
f=0:df:1/(2*dt);
w1=2*pi*f;
w2=fliplr(-w1(2:N/2));
w=[w1,w2];
n=2*pi/(N*dt);
h1=exp(-n*t);
h2=exp(n*t);
%%%%%%%%%%%%%%%%%%%%%%%%%%%%%%%%%%%%%%%%%%%%%%%%%%%%%%%%%%%%%%%%%%%%%%%
%%%%
%%%%%%%Dimensions of specimen and bars%%%%
rho=1190;   %density of bar material
d1=0.85238;  %distance  of  the  incident  strain  gauge  from
interface
d2=0.32403; %distance  of  the  transmiteer  strain  gauge  from
interface
Ab=3.1416e-4;  %area of the bar
As=1.97808e-4; %area of the specimen
thickness=8.16e-3; %specimen's length
%%%%%%%%Shift the waves at the interfaces%%%%%
inter_ei1=fft(ei.*h1).*(exp(-d1.*gamma8));
inter_er1=fft(er.*h1).*(exp(d1.*gamma8));
inter_et1=fft(et.*h1).*(exp(d2.*gamma8));
inter_etr1=fft(etr.*h1).*(exp(-d2.*gamma8));

inter_ei=real(ifft(inter_ei1).*h2);       %incident  strain  at
interface
inter_er=real(ifft(inter_er1).*h2);      %reflected  strain  at
interface
inter_et=real(ifft(inter_et1).*h2);     %trasmitted strain at
interface
inter_etr=real(ifft(inter_etr1).*h2);

figure
hold on
plot(inter_ei)
```

```
plot(inter_er)
plot(inter_et,'black')
plot(inter_etr,'black')
plot(ei,'r')
plot(er,'r')
plot(et,'r')
%%%%%%%%%Stress%%%%%%%%%%
stressT1=(Ab/As).*((-rho.*(w-
i*n).^2)./(gamma8.^2)).*(inter_et1+inter_etr1) ;
stressT2=ifft(stressT1).*h2;
stressT=real(stressT2);
stressT=stressT/1e6;
figure
hold on
plot(stressT)
xlabel('Time (s)')
ylabel('Stress')
%%%%Velocity%%%%%%%%
v=((-i.*(w-i*n))./gamma8).*(inter_et1-inter_etr1-
inter_ei1+inter_er1);
v1=ifft(v).*h2;
velo=real(v1);

figure
hold on
plot(t,velo)
xlabel('Time (s)')
ylabel('Velocity')
%%%%Displacement%%%%%%%%
displacementI1=-(inter_et1-inter_etr1-
inter_ei1+inter_er1)./(gamma8);
displacementI2=ifft(displacementI1).*h2;
displacementI=real(displacementI2);

%%%%%Strain%%%%%%%
strain=displacementI./thickness;
```

Appendix B

```
%%%Plot of the stress-strain curve
figure
plot(strain,stressT)
xlabel('Strain')
ylabel('Stress (MPa)')

%%%%%%Strain rate%%%%%
strainrate=velo./thickness;

figure
plot(t,strainrate)
xlabel('Time (s)')
ylabel('Strain rate')

figure
plot(strain,strainrate)
xlabel('Strain')
ylabel('Strain rate (s^-^1)')
```